UNIVERSITÀ
DEGLI STUDI
FIRENZE

PhD in
Earth Science

CYCLE XXXIII

COORDINATOR Prof. Lorella Francalanci

Kinematics, non-coaxial flow and rheological constraints on the Main Central Thrust zone and the South Tibetan Detachment System in central Himalaya

Doctoral Candidate
Dr. Nania Laura

Supervisor
Prof. Montomoli Chiara

Co-Supervisor
Dr. Iaccarino Salvatore

Coordinator
Prof. Francalanci Lorella

Years 2017/2020

Table of contents

List of figures

4. Kali Gandaki valley

5. Lower Dolpo Region

6. Microchemistry and ^{40}Ar–^{39}Ar geochronology on the Tethyan Himalaya Sequence

7. Discussion

List of Tables

Abstract

Long-lasting regional shear zones accommodate most of the crustal shortening of orogenic collisional settings. During their evolution, they involve large crustal volumes, that are buried or exhumed under various conditions of pressure, temperature, differential stress, etc. over time. Investigating the evolution of such structures is crucial to understand how mountain belts reach their final assets and to decipher the geodynamic of the continental crust. This Ph.D. thesis aims to correlate deformation at different observation scales to constrain the rheological evolution of two regional shear zones responsible for the current Himalayan setting: the Main Central Thrust zone and the South Tibetan Detachment System. Both tectono-metamorphic discontinuities are natural laboratories for tectonic and micro-tectonic studies as: (1) they display an impressive lateral continuity for over 2400 km and (2) they accommodate great amounts of displacement. Most of the current rheological studies for the two shear zones focus on quartz-bearing lithologies. Particularly, a composite architecture of the South Tibetan Detachment System, a prime example of a syn-collisional low-angle normal fault, has been described around the Everest area (Eastern Nepal), where a lower normal ductile- and an upper brittle- branch of the detachment have been recognized. Nevertheless, the lithologies affected by the Main Central Thrust zone and the South Tibetan Detachment System vary along the Himalaya, and both shear zones are not characterized by equal evolutionary stories through their whole extension. Moreover, minor work has been done on the South Tibetan Detachment System in central Himalaya, where marble is the widespread lithology, and where the upper brittle- branch is not always cropping out.

In this work, the Main Central Thrust zone and the South Tibetan Detachment System were characterized in three study areas of Western Nepal (central Himalaya): the Budhi Gandaki valley and the Marsyandi valley (around the Manaslu Massif), the Kali Gandaki valley (around the Mustang-Myagdi region), and the Lower Dolpo Region. A suite of seventy-two oriented samples from different transects perpendicular to the strike of the two shear zones were carefully investigated at the microscale combining optical microscopy, X-ray texture goniometry, crystal fabric analyzer, chemical analyses with electron microprobe, ^{40}Ar–^{39}Ar step-heating and laser *in-situ* geochronological analyses. Such techniques, coupled with image analyses, enabled to determine crystals grain size distributions, crystal shape, crystallographic preferred orientation (CPO, texture), twin density, and therefore parameters as differential stress, strain rate, finite strain, and kinematic vorticity, with implications on their variation over time.

The studied samples of the Main Central Thrust zone from the Manaslu area and the Lower Dolpo region show comparable microstructures, metamorphic facies, and kinematic indicators, pointing out a top-to-the-south/southwest non-coaxial ductile flow. Quartz and dolomite textures, and quartz, dolomite, and feldspar microstructures support an increase of deformation temperature from ~400–450 °C up to ~700 °C, moving toward higher structural levels along the investigated profiles through the Main Central Thrust zone. Kinematic vorticity estimates in the Manaslu area indicate a general shear flow with 44–60% of simple shear (including the statistical uncertainty) at high-temperature conditions (>550 °C) at the top of the Main Central Thrust zone. The comparison with literature data for the Himalaya supports a non-steady-state flow and a “decelerating strain-path”, where the highest simple shear components are recorded at deeper structural levels of the thrust hanging wall.

The South Tibetan Detachment System shows a dominant ductile shear zone, occurring in all the study areas. Data comparison for calcite and quartz CPO, grain sizes and shapes, and *e*-twin in pure and impure marbles, coupled with petrographic observations, allowed us to reconstruct a complex tectono-metamorphic history with two stages of shearing occurring during the footwall

exhumation, characterized by different thermal and lithospheric stress regimes. The early stage of normal shearing occurred at low differential stress, ca. 10 MPa, and at temperatures ranging from 650 °C to 400 °C moving up-section. This stage is recorded in all study areas, and is characterized by simple-shear dominated flow with (84-91% simple shear). The late stage of normal shearing, along the STDS, occurred at higher differential stress conditions (>100 MPa) and lower temperatures (T=300-400 °C) in all study areas, under a general shear flow with only 20-35% of simple shear in the Manaslu area and in the Lower Dolpo. On the other hand, in the Kali Gandaki valley minor kinematic vorticity variations provide a general shear flow during both early- and late-stage of shearing, confirming that the STDS does not have an equal evolution along the belt. The shortening perpendicular to the shear plane obtained for the bulk deformation of the South Tibetan Detachment System (14-30%) in both the Manaslu area and the Kali Gandaki valley implies telescoping of the deformed rock packages and this confirms a strong paleo-isotherm condensation. Decreasing temperatures from an early-stage of shearing to a late-stage of normal shearing, coupled with increasing recorded differential stress at comparable strain rates (c. 10^{-11}-10^{-12} s^{-1}) in all study areas, support strain hardening of the ductile South Tibetan Detachment System. This path, associated with a temporal (rather than spatial) decreasing simple shear contribution, also indicates a not-steady-state flow and a "decelerating strain-path" as highlighted for the Main Central Thrust zone. Indeed, the component of pure shear progressively replaced high-temperature simple shear flow during cooling and exhumation of the South Tibetan Detachment System toward shallower structural levels. The main implication of this work is that, as marbles can plastically deform even at lower temperature conditions than quartz-dominated lithologies, when calcite-bearing tectonites dominate (as in central Himalaya) the ductile shearing of South Tibetan Detachment System protracted to upper structural levels, without localizing a prominent upper brittle fault.

Microstructural, chemical, thermobarometric, and ^{40}Ar–^{39}Ar (step-heating and *in-situ*) geochronological analyses were conducted on static micas recrystallized in the South Tibetan Detachment System hanging wall rocks, overprinting the mylonitic foliation, in the Lower Dolpo area. Their tectonic meaning was not previously deeply explored even if post-kinematic mica occurrence is widespread in the Himalaya. Samples from the South Tibetan Detachment System hanging wall up to almost one km of vertical thickness above, were analysed for three populations of micas, defining two overprinting foliations and a post-kinematic crystallization event. ^{40}Ar–^{39}Ar analyses on these populations indicate static (re)equilibration at 14–11 Ma, with an age rejuvenation from lower to higher structural levels. This data and thermobarometric results support a late thermal event at T=500-550 °C occurred at low structural levels (~15-18 km depth), below the South Tibetan Detachment System, after the cessation of the ductile activity. This inferred thermal event is not spatially associated to any outcropping intrusion in this specific area. In this thesis, the thermal event in the Lower Dolpo has been associated to the late Himalayan deformation stage related to orogen parallel E-W extension accommodated by N-S striking normal faults and coupled with crustal anatexis and crustal doming.

Introduction

A fascinating question in tectonics regards the exhumation of deep-seated rocks. In several tectonic settings, thrust and low-angle normal fault (i.e. LANF) allow the exhumation of high-grade metamorphic rocks, from deeper to shallower structural levels. During the exhumation process, confining pressure, pore pressure, temperature, and fluid circulation can change, as well as other geological parameters such as strain rate and kinematic of the flow. These parameters, and their interplay, control the rheology of the rocks involved at different structural levels. Understanding such parameters is necessary to define tectonic models for the deep-seated rocks exhumation, but requires a multidisciplinary approach linking geological mapping, structural analysis, texture analysis, mineral chemistry, pressure (P), temperature (T) estimates, and geochronological investigation. A natural laboratory for such studies is the Himalaya, commonly regarded as the classic example of collisional belt (Hodges, 2000; *Fig. I*). The Himalaya is characterized by ongoing rapid convergence and exhumation rates (e.g. Hodges, 2000; Robert et al., 2011). Due to the high peaks and deep valleys developed for hundreds of km, natural sections of middle- to upper crust, not always accessible in orogenetic settings, are well exposed. This feature makes it possible to laterally compare the main structures geometry and kinematic along the belt, and several balanced geological cross sections show minor lateral variation of main units and structures (Le Fort, 1975; Fuchs, 1981; Hodges, 2000; Law et al., 2004; Yin, 2006; Weinberg, 2016; Carosi et al., 2018, 2019). However, the orogen structure (Yin, 2006), convergence rates (Larson et al., 1999; Paul et al., 2001), and climate-induced erosion/denudation (Garzanti et al., 2007, 2020; Gemignani et al., 2018) are not uniform from west to east (see also Robert et al., 2011 with references). Therefore, studying the main shear zones in different areas, comparing each section, is necessary to unravel how deep-seated rocks are exhumed over time and space.

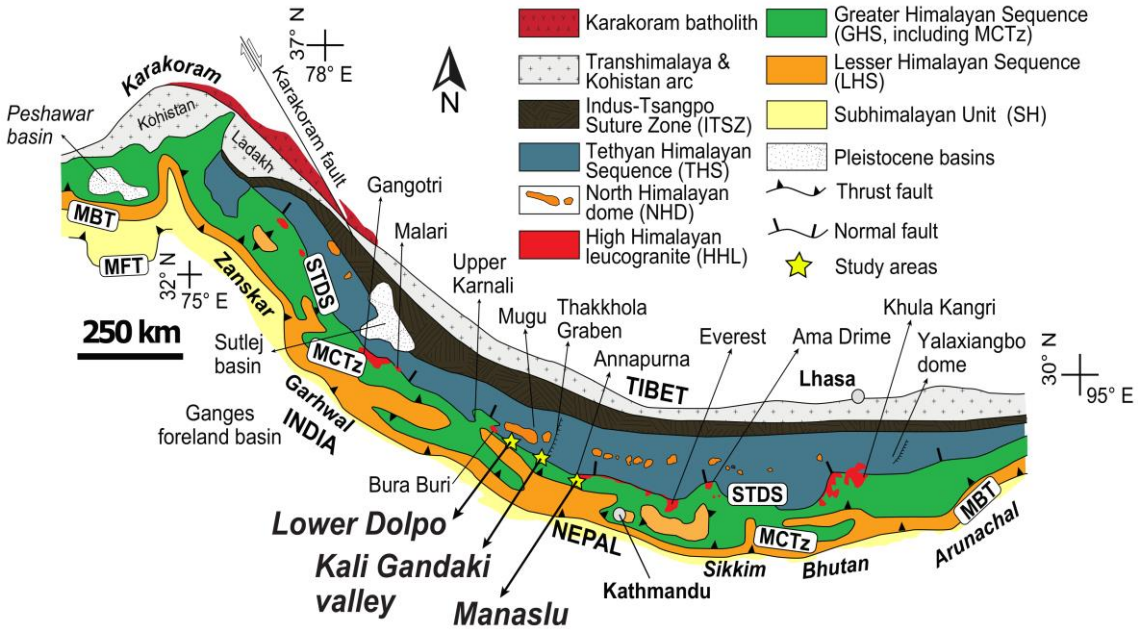

Figure I. *Schematic geological map of the Himalayan belt (redrawn after Law et al., 2004; Guillot et al., 2008; Carosi et al., 2018).*

The Himalaya derives from the diachronic collision, and the ongoing indentation, of the Indian and Eurasian Plates, which started around 54-61 Ma (Hu et al., 2016; Najman et al., 2017; An et al., 2021). After the collision, crustal thickening and shortening occurred through folding and north-dipping regional-scale shear zones along the northern margin of India (Hodges, 2000; Godin et al., 2001; Searle et al., 2009). The development of the shear zones, striking parallel to the Himalayan trend, led to the southward imbrication of the main litho-tectonic units, including the metamorphic core of the belt, commonly referred to as Greater Himalayan Sequence (GHS). Throughout the Late Oligocene-Miocene, exhumation of the previously underthrusted units was mainly led by: a low-angle ductile top-to-the-north/northeast extensional system (i.e. LANF), known as the South Tibetan Detachment System (STDS) (Caby et al., 1983; Burg and Chen, 1984; Burchfiel et al., 1992; Brown and Nazarchuk, 1993; Carosi et al., 1998; Searle et al., 2003; Kellett et al., 2019), and by the progressive development of south-directed thrust-sense shear zones and brittle faults (Carosi et al., 2019 for a review). In the northern sector of the belt, the south-directed tectonics suffered a switch to an E-W, still ongoing, orogen parallel tectonics, associated with the development of N-S trending grabens (e.g. Thakkhola Graben, *Fig. 1*), partial melting and doming (Coleman, 1996; Colchen, 1999; Blisniuk et al., 2001; Jessup et al., 2008, 2019).

During the last 20 years, to explain the exhumation of the GHS from mid-crustal levels, most authors have focused their studies on kinematics, geometry, pressure-temperature paths and the ages of activity of the main tectonic boundaries that affected the unit and on shear zones located in its core. They are (*Fig. 1*): the STDS, at the top; the High Himalayan Discontinuity (HHD), within the GHS (Carosi et al., 2010; Montomoli et al., 2013, 2015); and the Main Central Thrust zone (MCTz), at the base of the GHS (Brunel and Kienast, 1986; Hubbard, 1989; Pêcher et al., 1991; Schelling and Arita, 1991; Searle et al., 2008; Martin, 2017). These shear zones experienced ductile activity barely during the same span of time (Hodges et al., 1992; Godin et al., 2006b; Leloup et al., 2010; Kellett et al., 2019), even if recent works suggest a southward temporal propagation of discontinuities and a not always contemporaneous activity (Chambers, et al., 2011; Montomoli et al., 2013; Montemagni et al., 2018). Detailed reviews of available data present lateral variability of structures linked to the diachronic collision, with variations in the geochronological and rheological dataset (e.g. Godin et al., 2006b with references; Parsons et al., 2016a, 2020 with references). Indeed, a clear identification of the shear zones is required to constrain tectonic models, but different authors do not always agree on the spatial position of the MCTz and the STDS limits (e.g. Searle et al., 2008). This problem is complicated as both shear zones involve different lithologies along-strike. On the base of different criteria, including lithological, metamorphic, structural, kinematic, strain gradient or timing of the ductile activity of the shear zones, the MCTz and the STDS limits are shifted by various kilometers (Searle et al., 2008; Martin, 2017, Starnes et al., 2020, and Godin et al., 2021 for the MCTz; Kellett et al., 2019 for the STDS). For the STDS, a further complication occurs since it shows a complex geometry and architecture, with an upper brittle detachment fault and a lower ductile shear zone, involving also the top of the GHS (Carosi et al., 1998; Searle et al., 2003; Iaccarino et al., 2017b; Kellett et al., 2019). For the lower ductile branch of the STDS, one still open question regards the occurrence of a high apparent temperature field gradient, varying from ~160–260 °C/km (Waters et al., 2019; Long et al., 2019) up to 300–400 °C/km (Jessup et al., 2008; Cottle et al., 2011; Law et al., 2011; Kellett and Grujic, 2012), which is one order of magnitude higher than the typical ones (i.e. 30°C/km). The reasons for the development of the strong isotherm condensation are still debated, requiring a comprehensive microstructural and petrographic

database (Kellett et al., 2019). Most of current ideas on the STDS architecture and behavior come from the well exposed outcrops around the Everest area, in Eastern Nepal (Carosi et al., 1998; Searle, 1999; Law et al., 2011, 2013; Waters et al., 2019). In this area, both brittle and ductile branches of the STDS are present, where the ductile shearing affects quartz-bearing lithologies (Carosi et al., 1998; Searle, 1999; Searle et al., 2003; Jessup et al., 2008), such as sheared paragneiss or Miocene leucogranites. On the contrary, in Central-Western Nepal where the STDS also involved carbonate-bearing lithologies, despite this structure being mapped, the definition of the exact shear zone boundaries, architecture and structural evolution is still controversial (e.g. Guillot et al., 1995; Coleman and Hodges, 1998; Carosi et al., 2002; Searle and Godin, 2003). This Ph.D. thesis contributes to these research topics by analyzing the MCTz and the STDS in the same areas along different sections of the belt. Indeed, it is essential to unambiguously define the spatial and temporal limits of the tectonic-discontinuities at the base and the top of the GHS. Adopting for both shear zones the same structural approach, rheological data at the base and at the top of the GHS can be compared. Furthermore, investigating the temporal limit of the STDS and the initiation of the orogen parallel extension provides an additional constraint to understand the timing, and possible coupled activity, of the two shear zones.

The study areas are located in Western Nepal and are from east to west (*Fig.1.I*): the Budhi Gandaki valley and the Marsyandi valley around the Manaslu Massif, the Kali Gandaki valley, and the Lower Dolpo Region. A multidisciplinary approach is adopted on field-oriented samples, studying the deformation at different scales. Kinematic and rheology of field structures were investigated through microstructural and texture analyses, focusing on calcite- and quartz-rich tectonites, on seventy-two samples from different structural levels collected in previous geological expeditions by Montomoli, C., Carosi, R. and Iaccarino, S.

For the MCTz, microstructural, texture and kinematic vorticity analyses enabled constraining temperatures and kinematic flow conditions in the Lower Dolpo Region and in the Manaslu area. The results are supported by consistent data present in the literature, indicating a temporal deceletaring strain path of the shear zone during heterogeneous ductile shearing.

For the STDS, data comparison for different areas led to define the tectonic evolution of this shear zone, allowing us to recognize a composite structural evolution during its activity and two progressive stages of shearing. Microstructural and texture analysis of pure and impure marble proved to be useful for characterizing the STDS spatial location, architecture, and temporal variation. The combination of different paleopiezometers, kinematic vorticity gauges, and geothermometers, coupled with finite strain analysis, allows us to infer a complex evolution of the STDS. When the upper-brittle fault did not develop, the ductile shearing likely persisted at high structural levels due to the rheology of the involved rocks.

Finally, new geochronological data, complemented with structural and chemical analysis, were collected through step heating ^{40}Ar–^{39}Ar laser probe analysis and *in-situ* ^{40}Ar–^{39}Ar analysis on white mica and dark mica porphyroblasts from the hanging wall of the STDS in the Lower Dolpo (Midwestern Nepal). Age and thermobarometric results, coupled with microstructure evidences, have been linked to the onset of the tectonic transition from NS, orogen orthogonal, to EW, orogen parallel, tectonics in the study area.

1. Himalayan overview and tectonic setting

The Himalaya is an active collisional orogen that extends for over 2400 km in length in a large area of Central Asia, which includes India, Pakistan, Nepal, Tibet, China and Bhutan (*Fig. I*). The belt resulted from the convergence between the Indian and Eurasian Plates, which led to closure of the Neo-Tethys Ocean, to the north, and the opening of the Indian Ocean, to the south (Stampfli and Borel, 2002). After the ocean closure and, therefore, the subduction of the passive margin of the Indian Plate, collision and indentation occurred diachronically during the middle Paleocene (Dewey and Bird, 1970; Hodges, 2000), starting between 59-61 Ma in the central-eastern Himalaya (Hu et al., 2016; Parsons et al., 2020; An et al., 2021) and 54 Ma in the north-western part of the belt (Najman et al., 2017). The collisional stage, often indicated as D1 or Eohimalayan stage (Hodges 2000), resulted in diachronic crustal shortening, thickening and in prograde metamorphism between 48/43-32 Ma in the central Himalaya (Godin et al., 2001; Carosi et al., 2010) and 44 Ma in SW Tibet (Dunkl et al., 2011). Crustal shortening devolved through folding and regional-scale shear zones with a southward imbrication of north-dipping slabs, derived from the northern margin of India (Hodges, 2000). The exhumation stage, or D2 phase, occurred during the late Oligocene-Miocene associated with an isothermal to retrograde Neohimalayan metamorphic stage. This tectonic phase resulted into folding and regional-scale shear zones. The main active discontinuities are (from bottom to top) the Main Central Thrust zone (MCTz), the High Himalayan Discontinuity (HHD), and the South Tibetan Detachment System (STDS) (*Fig. 1.1*). The D2 phase was followed by a switch to crustal thinning through an E-W orogen parallel extension (hereafter referred to as D3), mainly recorded in the northern sector of the belt (within central to southern Tibet). The main structures related to this phase are the regional-extended grabens, such as the Tibrikot fault system and the Thakkhola Graben in Central Nepal (*Fig. I*, Godin et al., 1999; Blisniuk et al., 2001; Garzione et al., 2003; Godin, 2003; Larson et al., 2019; Brubacher et al., 2020), the Kung Co Graben (Lee et al., 2011), the Yadong Gulu Graben (Dunkl et al., 2011), and the Cona Graben in Bhutan (east of the Yalaxiangbo Dome, Dunkl et al., 2011; *Fig. I*). Further structures are doming associated with partial melting (Blisniuk et al., 2001; Godin, 2003; Larson et al., 2019; Brubacher et al., 2020; see Jessup et al., 2019 for a review). Several attempts to date this tectonic switch from south-directed- to E-W directed flow suggest that the orogen parallel extension started in the Miocene, between 20 Ma and 10 Ma (Molnar and Stock, 2009; Iaffaldano et al., 2013; Xu et al., 2013), coinciding with the elevation increase of the Tibetan Plateau and two drops in the convergence rate between India and Eurasia, at ca. 20 Ma and 13-11 Ma (Larson et al., 2019). For example, in the Karnali valley of Western Nepal and southern Tibet, the Gurla Mandhata–Humla fault overprints the STDS deformation, marking the initiation of D3 at 15-13 Ma (Murphy et al. 2002; Murphy and Copeland 2005; Nagy et al. 2015 with references). The causes for the tectonic switch are still debated (e.g. Sundell et al., 2013; Larson et al., 2019; Brubacher et al., 2020). It has been suggested that the first drop of convergence rate at ca. 20 Ma, that is coeval with the ending of the ductile STDS shearing and the onset of the Karakoram fault zone (*Fig. I*, see Valli et al., 2007), is linked to the break-off of the Indian Plate (Replumaz et al., 2010). A second convergence rate drop, coeval to the cooling of the STDS and the major development of the (D3 phase) N-S graben (Ratschbacher et al., 2011), occurred due to the coupling between the upper crust and the mid-crust in the upper section of the belt (e.g. Clark and Royden, 2000; Larson et al., 2019).

After a significant tectonic exhumation prior to ca. 8 Ma, much of the denudation has been induced by the combined activity of climate-related erosion and tectonics (Huntington et al.,

2006; Garzanti et al., 2007; Gemignani et al., 2018; Govin et al., 2020). Rapid exhumation through surface erosion during the Late Miocene is well documented by detrital minerals within foreland basin deposits in the syntaxial terminations (Nanga Parbat massif, to the west, and Namche Barwa massif to the east, see Lang et al., 2016; Govin et al., 2020). Specifically, the onset of rapid exhumation rates of >5 km/Ma have been suggested starting at 5 Ma in the Namche Barwa region (Lang et al., 2016), with an acceleration of erosion rates during the Pliocene, at 2.5-0.9 Ma (Huntington et al., 2006; Gemignani et al., 2018; Govin et al., 2020). Pliocene focused erosion of the southern part of the belt coincides with the dramatic destabilization in climate on a global scale (Huntington et al., 2006). According to Huntington et al. (2006), the increase in erosive rates induced by climate change, for those considered constant tectonic processes, is responsible for the abrupt increase in exhumation rate of the belt, especially southward, along the MCTz front. Therefore, climate-induced erosion is a fundamental element for modelling the Himalayan landscape and in the tectonic denudation to be taken into account in the exhumation models (Garzanti et al., 2007).

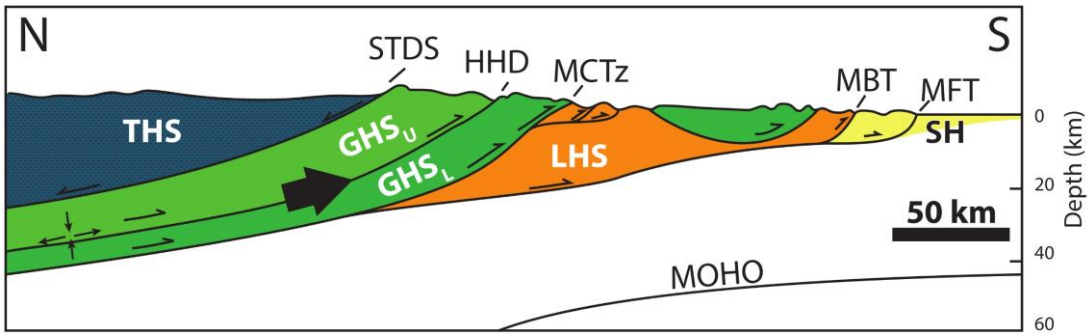

Figure 1.1. *Schematic geological cross section of the Himalaya (modified after Law et al., 2004). THS, Tethyan Himalayan Sequence; GHS$_U$, upper Greater Himalayan Sequence; GHS$_L$, lower Greater Himalayan Sequence; LHS, Lesser Himalayan Sequence; SH, Sub-Himalayan unit; STDS, South Tibetan Detachment System; HHD, High Himalayan Discontinuity; MCTz, Main Central Thrust zone; MBT, Main Boundary Thrust; MFT, Main Frontal Thrust.*

From bottom to top (or along a south to north profile), the main units that crop out are (*Fig. 1.1*): the Subhimalayan Unit or Siwalik Group (SH), the Lesser Himalayan Sequence (LHS), the Greater Himalayan Sequence (GHS), and the Tethyan Himalayan Sequence (THS).

- The SH consists of late Miocene-Pleistocene molasse deposit formed in the foreland basin during the flexural downwarping of the Indian plate (Burbank et al., 1996).
- The LHS is made up of a thick sequence of middle- to low-grade metamorphic phyllite and metasediments, which passes upward to medium-metamorphic rock quartzite, marble, orthogneiss and minor amphibolite, spanning from Precambrian to upper Palaeozoic in age (Hodges, 2000; Upreti et al., 2003; DeCelles et al., 2004; Kohn et al., 2010).
- The GHS consists of 5-to-30 km-thick medium-to high-grade metasediments, with minor metabasite and orthogneiss, Precambrian to lower Palaeozoic in age (Le Fort, 1971; Pêcher, 1975; Vannay and Hodges, 1996; Larson and Godin, 2009). Before recognition of the High Himalayan Discontinuity (see Carosi et al., 2010), the GHS was described as a single coherent tectonic unit, divided into three formations (Le Fort, 1971, 1975), now more properly referred as units (Searle and Godin, 2003). Unit 1, at the bottom, is made of paragneiss and mica schist; Unit 2, in the middle part of GHS, is dominated by calc-silicates-rich marble, gneiss, and psammitic rocks; Unit 3, at the top, is formed by orthogneiss and migmatite. After the discovery of intra-GHS discontinuities (*Fig. 1.1*), it became possible to better define the

GHS architecture, identifying a lower GHS unit (GHS_L) and an upper GHS unit (GHS_U) characterized by different P-T-D-t paths (Montomoli et al., 2013, 2015; Iaccarino et al., 2015, 2017a). The GHS_L includes gneiss and mica schist of Unit 1 (Montomoli et al., 2013, 2015; Carosi et al., 2018), showing an inverse metamorphism (Searle and Rex, 1989; Goscombe et al., 2006; Searle et al., 2008; Imayama et al., 2010), whereas the GHS_U is composed of calc-silicates-rich rocks and metasediments of Unit 2, and the orthogneiss and migmatite of Unit 3 (Carosi et al., 2010, 2018). The upper part of the GHS_U is frequently intruded by two main groups of Oligo-Miocene leucogranite (Fuchs et al., 1988; Guillot et al., 1993; Carosi et al., 2002, 2013; Visonà and Lombardo, 2002; Montomoli et al., 2017), known as Higher Himalayan Leucogranites (Visonà et al., 2012).

- The THS is a nearly continuous sequence of marine (meta)sediments (Frank and Fuchs, 1970; Fuchs, 1977; Garzanti, 1999). From the base to the top, the THS varies from greenschist facies marble and metapelite of Cambrian-Ordovician age, to low-to-non-metamorphic sediments, of the Palaeozoic to the Cenozoic (Eocene) (Gaetani and Garzanti, 1991).

As briefly introduced above, the main tectonic boundaries separating the lithotectonic units (*Fig. I, Fig. 1.1*) are, from bottom to top: the Main Frontal Thrust (MFT), the Main Boundary Thrust (MBT); the Main Central Thrust zone (MCTz); the High Himalayan Discontinuity (HHD), and the South Tibetan Detachment System (STDS). The MFT, between the Siwalik Group and the north Indian Plain, has been the active front of the belt since the late Pleistocene, with a top-to-the-south sense of shear (Gansser, 1981; Burgess et al., 2012; Kaushal et al., 2017). The MBT, with the same sense of shear, juxtaposes the LHS above the uppermost part of the SH (Hodges, 2000). The MCTz, dividing the LHS from the structurally upper GHS_L, is a north-dipping thick zone of heterogeneously distributed south-directed ductile to brittle shear (*Fig. 1.1, Fig. 1.2a-b*).

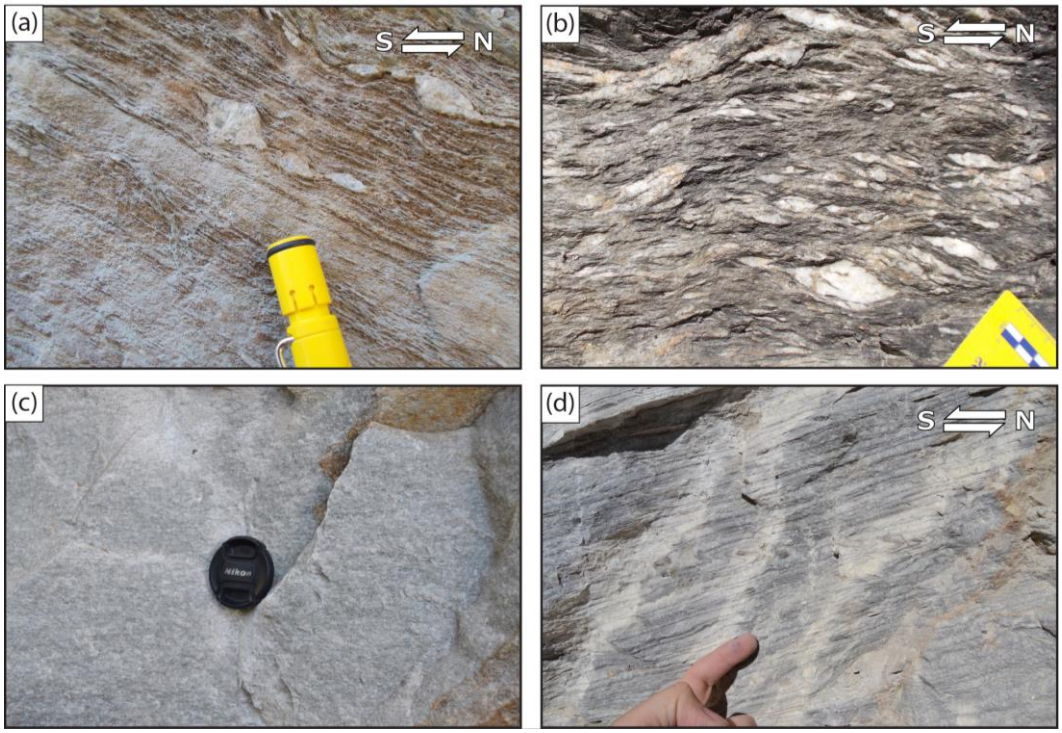

Figure 1.2. *(**a-b**) Outcrop photos of sheared rocks involved by the MCTz in Garhwal, NW India. Kinematic indicators are consistent with the top-to-south sense of shear. (**c-d**) Outcrop photos of sheared rocks involved by the STDS, respectively from the GHSu and the THS, in the Masryandi valley (photo c-d, credit: Carosi, Iaccarino, Simonetti, 2017).*

The MCTz has accommodated a great quantity of shortening (Brunel and Kienast, 1986; Hubbard, 1989; Pêcher et al., 1991; Schelling and Arita, 1991; Searle et al., 2008; Martin, 2017), e.g. from 52 km in the Arunachal Himal (Ningthoujam et al., 2015) to 253 km in the Kumaun-Garhwal region (Srivastava and Mitra, 1994; see also Parsons et al., 2020). Approaching the sillimanite isograde, close to the migmatite zone of the GHS, the HHD occurs. It is a high-temperature contractional ductile top-to-the-south shear zone (Carosi et al., 2007; Montomoli et al., 2013, 2015; Carosi et al., 2016 with references; Wang et al., 2016; Waters, 2019).
The STDS, at the top, is a top-down-to-the-north km-thick shear zone with a major lower ductile detachment zone, involving also the uppermost part of the GHS_U (*Fig. 1.2c*) and the base of the THS (*Fig. 1.2d*). This feature is well-described by e.g. the Lhotse Detachment in the Everest area (*Fig. 1.3a-c*, see Carosi et al., 1998; Searle, 1999; 2010; Searle et al., 2003; Cottle et al., 2011). A brittle upper branch of the STDS is a further element (e.g. Qomolangma Detachment, QD, *Fig. 1.3b, c*, see Lombardo et al., 1993; Carosi et al., 1998; Searle et al., 2003; Corthouts et al., 2016; Waters et al., 2019; Larson et al., 2020) that does not crop out continuously along the belt (Carosi et al., 2002, 2013, 2014; Cottle et al., 2011; Kellett et al., 2019).

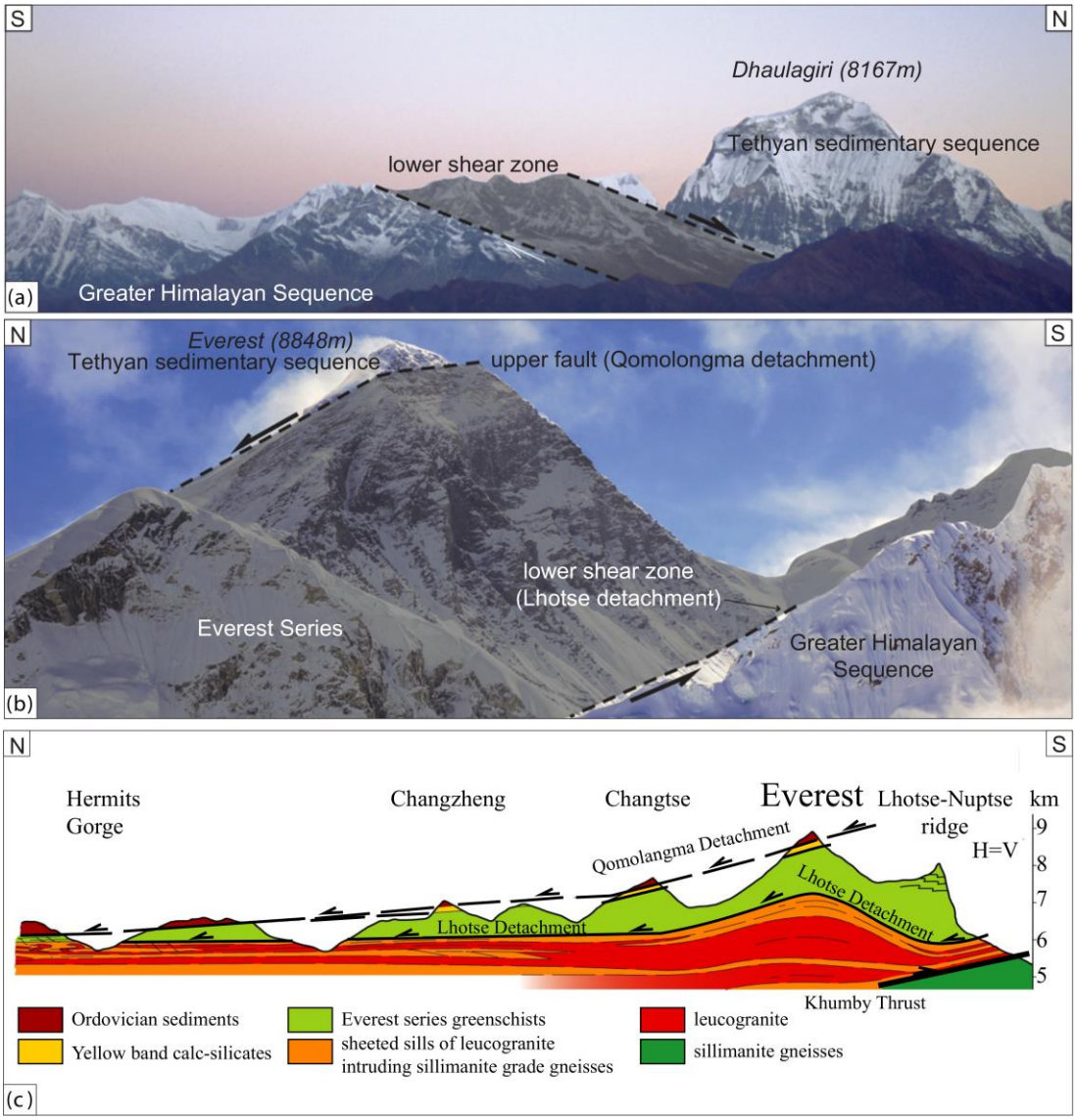

Figure 1.3. *Outcrop photos of the South Tibetan Detachment System from the (**a**) Dhaulagiri (Western Nepal) and from the (**b**) Everest area (Eastern Nepal) (Kellett et al., 2019). (**c**) Example of cross-section across the Everest massif, showing the composite architecture of the South Tibetan Detachment System (after Searle et al., 2003).*

1.1. Tectonic models for the metamorphic core exhumation

In recent decades, several tectonic models have been proposed to explain how the medium-to high metamorphic rocks of the GHS were exhumed from mid-crust levels (e.g. Burchfiel and Royden, 1985). Most of the models focused on the (coupled) role of the MCTz and the STDS, prominently active between 24/17 Ma. The opposite kinematics of the two (considered) contemporaneous shear zone led to developing tectonic models in which the GHS was squeezed, or extruded, southward as a single body (see Montomoli et al., 2013 and Parsons et al., 2016a for a review). These models (*Fig. 1.4*) differ in terms of the interpreted geometry of the MCTz and the STDS, and the rheological behavior of the GHS itself. The “Wedge extrusion” model by Burchfiel and Royden (1985) and Hodges et al. (1992) ruled that the MCTz and the STDS connected in-depth, delimiting the GHS as a wedge of mid-crustal material (*Fig. 1.4a*). The former model was then re-adapted by Grujic et al. (1996), in a "ductilely deformed wedge" where the GHS wedge extrusion was dominated by simple shear flow, or the "wedge deformed by non-coaxial general flow" proposed by Vannay and Grasemann (2001) where the GHS is deformed under general shear conditions. Later, Webb et al. (2007) proposed the "Wedge insertion" model (*Fig. 1.4b*). They considered the STDS as a back-thrust system rather than a detachment system, attributing to the GHS a wedge geometry thinned toward the south, at higher structural levels.

Nevertheless, recognition of the STDS in seismic profiles below the Tibet (Nelson et al., 1996) as a flat lying detachment separating a partially melted mid-crust encouraged other models (*Fig. 1.4c-e*). The MCTz and the STDS are there regarded as the sub-parallel boundaries of a channel of rheological weak material (i.e. the GHS). Among them, the first most successful model was the "Channel Flow" of Beaumont et al. (2001, 2004), which account the GHS as a single ductile body, with widespread *in-situ* partial melting (Searle et al., 2009), that reached the actual position through a hot "channel" delimited by the MCTz and the STDS (*Fig. 1.4c*). For this model, the southward movement is driven by a lateral pressure gradient due to the differences in potential energy between the Tibetan Plateau and the India Plate. The model, with its variants (i.e. Godin et al., 2006b), is based on and requires the synchronous activity of the STDS and the MCTz, and the intense erosion at the Himalayan front, which would have fueled the upwelling process of the GHS, removing materials upward. With a similar geometry for the MCTz and the STDS, the "Critical taper wedge" of Kohn (2008), is based on a non-contemporaneous activity of the two bounding shear zones. This model proposes that the Himalayas behaved as a “modified” Coulomb wedge (Davis et al., 1983; Platt, 1993) and suggests that the GHS was exhumed by alternating periods of shortening and extension (*Fig. 1.4d*). However, Fraser et al. (2000) already found it doubtful to define the GHS as a single block considering at the kilometric thickness of the unit and its significant, at least vertical, internal heterogeneity. After the first recognition of the high-temperature HHD within the GHS in the Lower Dolpo (Western Nepal) by Carosi et al. (2010), and the discovery that the MCTz ductile activity protracted after the end of the STDS (e.g. Montemagni et al., 2018 with references), authors proposed new models (e.g. Montomoli et al., 2013 in *Fig. 1.4e*; Larson et al., 2015 in *Fig. 1.4f*), even if not all the previous theories were rejected (see Parsons et al., 2016a; Searle et al., 2017; Marques et al., 2018). The recent “in-sequence shearing” model of Montomoli et al. (2013) considers that the almost simultaneous activity of the MCTz and the STDS is not the only engine of the GHS exhumation. Rather, it suggests the GHS exhumed at least as two main slices (*Fig. 1.4e*), the GHS_U and GHS_L, divided by

the HHD (active before the MCTz and contemporaneous with the STDS) through a temporal and spatial propagation of the active front of the belt toward the south (see also Carosi et al., 2010; Corrie and Kohn, 2011; Montomoli et al., 2013; Cottle et al., 2015; Iaccarino et al., 2015; Larson et al., 2015; Wang et al., 2015, 2016; Khanal et al., 2020). Indeed, the GHS_U and GHS_L, show diachronic metamorphic peaks occurred at different P-T conditions (Iaccarino et al., 2015). The upper GHS slice reached the metamorphic peak at ca. 0.7 GPa and 600-700 °C before the lower GHS, but at structural levels relatively shallower than the GHS_L which reached a pressure of 0.9-1.0 GPa at similar temperatures (Montomoli et al., 2015; Iaccarino et al., 2015; Carosi et al., 2016, 2019). The "in-sequence shearing" model then proposes that the exhumation occurred starting from HT-ductile intra-GHS discontinuities, with a southward imbrication of the tectonic slices over time (Carosi et al., 2010; Corrie and Kohn, 2011; Cottle et al., 2015; Iaccarino et al., 2015; Wang et al., 2015, 2016; Khanal et al., 2020).

However, due to the lateral variability of structures, geochronological database, convergence rates, and thermobarometric data collected from W-to-E along the belt, some authors do not agree on the non-contemporaneous activity of the MCTz and the STDS. Indeed, it has been suggested the need for high-resolution geochronology to resolve deformation episodes in orogenic systems, that may explain the timing discrepancies over long-lasting activities (e.g. Braden et al., 2018). The debate is still ongoing, focusing on how and when the tectonic discontinuities were effectively active.

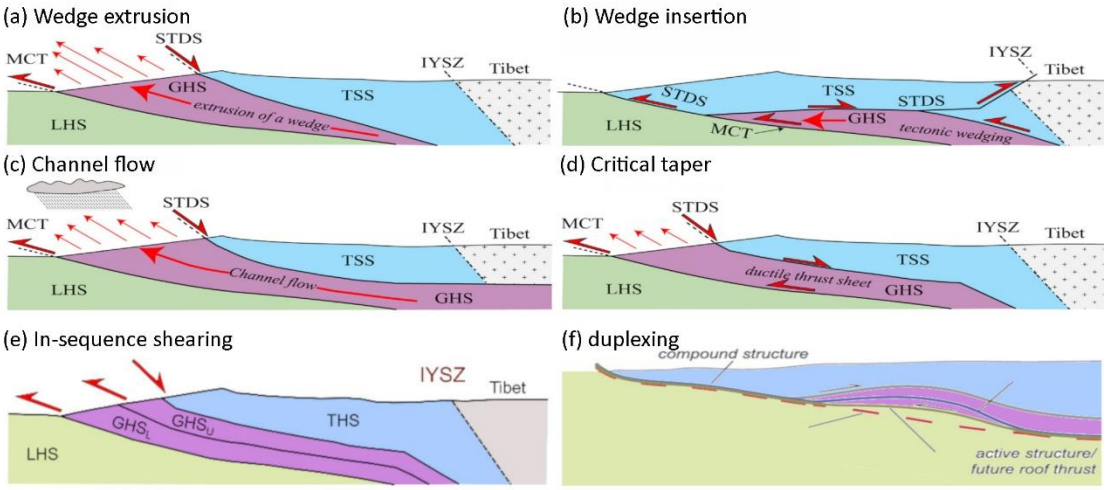

***Figure 1.4**. Schematic sketches of the main tectonic models proposed over time to define the exhumation of the Himalayan metamorphic core (GHS in violet); modified after Montomoli et al. (2013). (**a**) The MCTz and the STDS connect in depth with opposite kinematics, exhuming the GHS as a rigid wedge. (**b**) The MCTz and the STDS are connected in depth with thrust kinematics. (**c**) MCTz and the STDS run subparallel with opposite kinematics, exhuming the ductile and hot GHS though weathering-assisted processes. (**d**) MCTz and the STDS run subparallel with opposite, not strictly contemporary kinematics, exhuming the alternating GHS shortening and extension. (**e**) The GHS is exhumed by the MCTz, HHD and the STDS, the latter having opposite kinematics, with a southward propagation of the subparallel thrusts over time. (**f**) The GHS is exhumed by the MCTz, HHD and by the STDS, the latter with opposite kinematics, with a southward propagation of the thrusts that connect in depth with duplex type geometry.*

2. Analytical methods adopted for the shear zones characterization

In order to define a shear zone, it is essential to understand its geometry, kinematics and type of flow. Viscous-like to brittle-like behaviour (e.g. rheological behaviour) of heterogeneous rocks within a shear zone is strongly affected by the structural level where the deformation occurs. Particularly, the constituent mineral phases, the fluids contained in pores, and the type of fabric play a fundamental role in the rheological behaviour. In the geological and non-geological (materials science) literature, there are different terminologies for the fabric elements (e.g. see Passchier and Trouw, 2005). In this thesis, fabric (or petrofabric, Turner, 1949) is defined as the combination of structures (or "microstructures" at the microscale) and textures of rock-forming minerals (e.g. *Fig. 2.1a, b*; see Hobbs et al., 1976 and Passchier and Trouw, 2005). Microstructures are all the reciprocal spatial arrangements, geometric factors and topology of rock-forming minerals developed within the rock volume. They comprise foliation and lineation, but also the mineral grain shape, grain size and crystal shape preferred orientation (SPO). On the other hand, textures are here defined (as in material science) by all the intra-crystalline features like the crystallographic preferred orientations (CPO, *Fig. 2.1a, b*, e.g. Bunge, 1969, 1982; Mainprice et al., 2015). It is worthy of note that the two concepts of microstructure and texture are strongly related and a distinction is here provided only to make the type of analysis conducted more articulated in the text. Hereafter, textures are displayed in equal area lower hemisphere projections (pole figures), using foliation and lineation as reference frames. Pole figures observation makes it possible to interpret texture (e.g. quartz [*c*]-axis) in terms of "slip system" (e.g. *Fig. 2.1c*, after Schmid and Casey, 1986; Toy et al., 2008, and Parsons et al., 2016a).

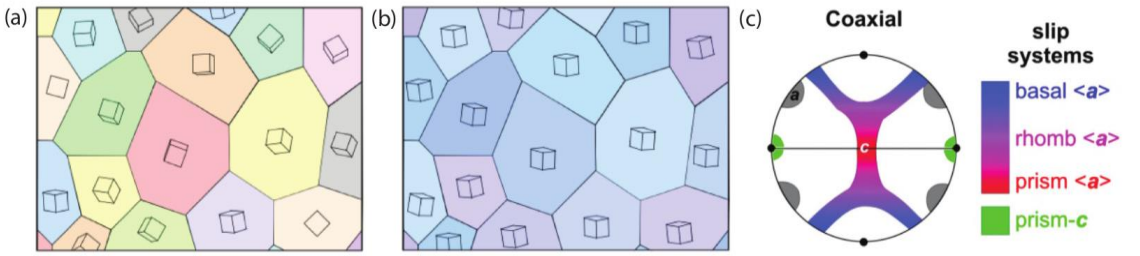

Figure 2. 1. *Examples of elements derived from texture analysis, given similar microstructures (). **(a)** example of lack of mineral CPO. Different colours of crystals correspond to different lattice orientations, showed by the small cubes dyesplayed for each crystal. **(b)** strong CPO (similar colour of crystals correspond to similar crystallographic orientation). **(c)** example of quartz [c]-axis pole figure (for strong CPO) for a plane strain coaxial defamation (redrawn by Parsons et al., 2016a).*

2.1. Microstructural analysis

Microstructural analyses were carried out on oriented samples (varying from marble to orthogneiss, quartzite and mica schist) from different structural levels along the STDS and the MCTz profiles, from different areas (*Fig. I*). Seventy-two samples were analyzed on thin sections cut parallel to the lineation and perpendicular to the main foliation (approximating the XZ plane of the finite strain ellipsoid). Several calcite-bearing samples were stained with alizarine to highlight the occurrence of dolomite.

Geometrical and topological aspects such as grain shape and arrangement (i.e. oblique foliations) and grain size distribution were studied on thin sections approximating the XZ plane of the finite strain ellipsoid (parallel to the object lineation and perpendicular to the main foliation). Stacked images of the full thin sections were acquired with a resolution of 5.08 µm

per pixel, through the crystal fabric analyzer hosted in Göttingen. Stacked images consist of ten light microscopy digital photographs (for each sample) of the full thin section acquired under crossed nicols with different orientations of the two polarizers. Comparing stacked images, it is possible to distinguishing clear subgrains and grain boundaries of crystals (*Fig. 2.2a, b*) for their relative misorientation angle (see also Trimby and Prior, 1999; Humphreys, 2001). Using a vector-graphics application, calcite grains were semi-automatically defined as closed polygon.
By adopting the ImageJ software (1.47v by Wayne Rasband) on stacked images of full thin sections, grain size maps were derived to achieve the grain size of over 1000 crystals for each sample (*Fig. 2.2a, b*). Apparent grain size was therefore derived as equivalent circular diameters starting from the corresponding maps (e.g. *Fig. 2.2b*) of each sample, calculating in 2-D as the square root mean (RMS) as [√(1/n·Σ xi2)] by GrainSizeTools v2.0.2 (Lopez-Sanchez and Funez, 2015). Twin frequency and density were measured on section micro-photos for appropriate oriented grains (checked optically) using ImageJ software.

2.1.1. Paleostress analysis on marbles

Calcite paleopiezometers aim to quantify the differential stress occurring during the deformation of marble (Schmid et al., 1980; Rutter, 1995; Barnhoorn et al., 2004; Platt and De Bresser, 2017). Paleopiezometers using the grain size of recrystallized grains are based on the (experimental) observations carried out on different (homogeneous) materials (including minerals, ceramics, metals, salts). According to such paleopiezometers, during dynamic recrystallization processes induced by deformation, the differential stress decreases with the increase in grain size (d) with no influences from other parameters, including deformation temperatures (e.g. see Rutter, 1995; Barnhoorn et al., 2004). Given a deformation temperature, the strain rate path which produced the differential stress is calculated as predicted by the Hall-Petch relation for pure marbles deformed in the dislocation creep field (Renner et al., 2002). For this Ph.D. thesis work, the differential stress conditions were derived from the 2-D apparent grain sizes using different flow laws. The Barnhoorn et al. (2004) piezometer, designed for GBM and SGR regime in non-coaxial flow, was adopted:

$$\text{Log}\sigma = (-0.82 \pm 0.15)\ \log(d) + 2.73 \pm 0.11$$

where σ is the differential stress, and d is the root-mean-square of equivalent diameter of grains. All results from the Barnhoorn et al. (2004) equation fall on the Rutter (1995) regression line, as recently confirmed by Platt and De Bresser (2017). The empirical Rutter (1995) piezometer for dislocation creep regime (originally derived for coaxial deformation regime) for grain boundary migration (GBM) mechanisms, is:

$$\sigma_{(GBM)} = 10^{3.43} * d^{-0.89}$$

The differential stress derived for subgrain rotation recrystallization (SGR) through the Rutter (1995) piezometer, is:

$$\sigma_{(SGR)} = 10^{2.91} * d^{-0.88}$$

Strain rate ($\dot{\varepsilon}$) was calculated for the estimated temperatures in accordance with the Renner et al. (2002) equation, as:

$$\dot{\varepsilon} = A\sigma^{n} \exp(\sigma/\sigma_0) \exp(-Q/RT)$$

where *A* is a material constant, possibly containing the chemical fugacity, *n* is stress sensitivity (n=2), σ is the differential stress (here derived by the Barnhoorn et al., 2004 piezometer), σ_0 is the resistance to glide, *Q* is the apparent activation energy for the process, *R* the universal gas constant, and *T* is the deformation temperature. The resistance to glide was estimated through the Renner et al. (2002) equation, as follows:

$$\sigma_0 = (\sigma + Kd^{-m})\,(T_m - T) / 1000$$

Within the equation, $(Kd^{-m})(T_m - T)$ is the backstress generated by dislocation pileups in front of grain boundaries (grain size and temperature dependent). *K* is a pre-exponential constant, *m* is the Hall-Petch exponent (m=0.5), and *Tm* is the melting temperature. Apparently, the following parameters apply to all calcite rocks: A=270; Q=200 kJ/mol; K=115 MPa kK^{-1} $\mu m^{0.5}$; Q=200 kJ/mol; Tm=1600 °K (Renner et al., 2002).

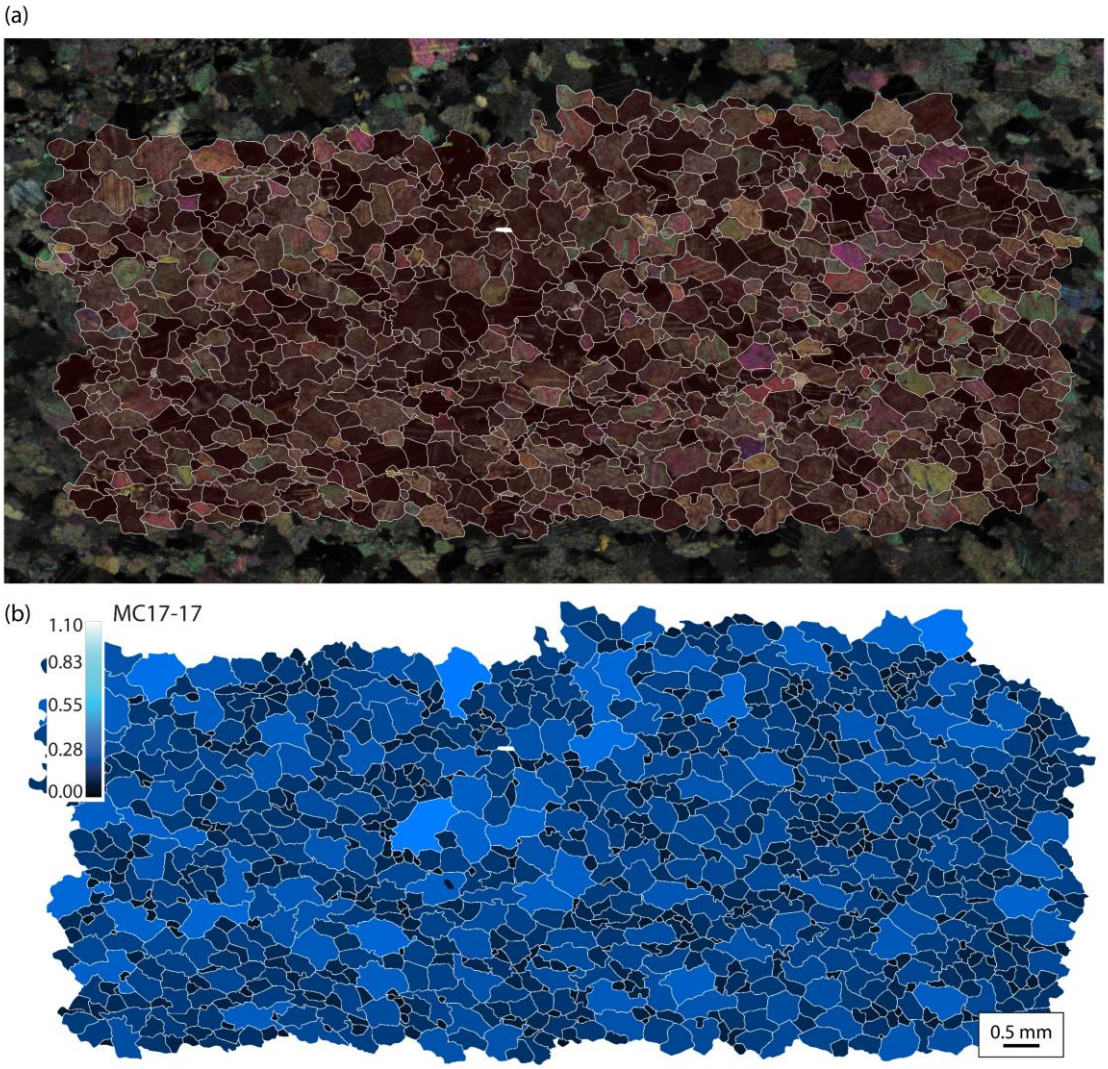

Figure 2. 2. *Example of analysed area for deriving the calcite grain size distribution of a deformed marble (sample MC17-17, from the Manaslu area).* ***(a)*** *Over 1000 of interconnected calcite crystals (in semi-transparent red) selected from a representative area of the thin section (one out of ten stacked images is here displayed in background).* ***(b)*** *Grain size distribution map processed by ImageJ software. Up-left scalebar corresponds to crystals equivalent radius.*

In the case of calcite, paleostress conditions can be also inferred using {*e*}-twins, applying twin density-based piezometers (Rowe and Rutter, 1990; Rybacki et al., 2011, 2013). In this thesis, twin lamellae were checked with the aid of an optical microscopy and/or with a Universal Stage at the Pisa University (e.g. *Fig. 2.3a, b*). The Universal Stage was adopted to recognize the type of twin set, measuring the angle between the pole of the twin plane and the [*c*]-axis. *E*-twins (for which this angle is of 26°, see Lacombe, 2010 with references) were investigated as their width, morphology and density correlate with temperature and differential stress (e.g. Rowe and Rutter, 1990; Burkhard, 1993; Ferrill et al., 1998, 2004; Rybacki et al., 2011, 2013).

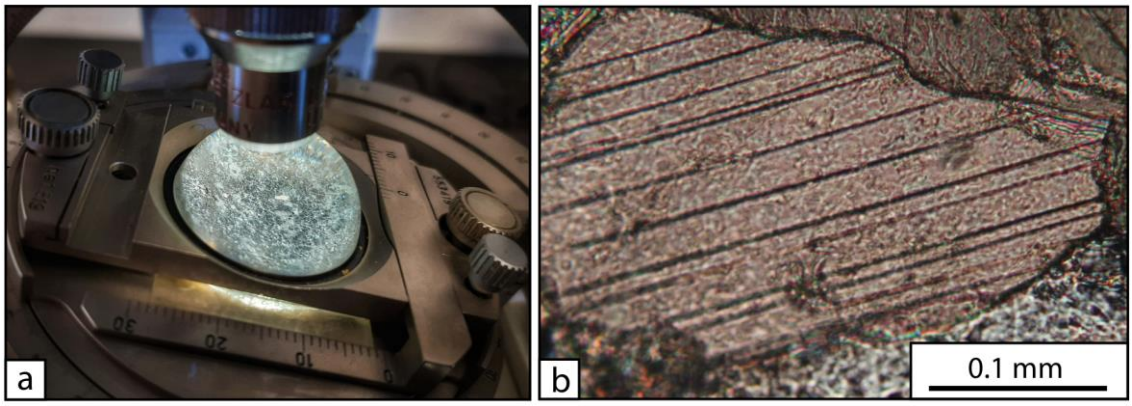

Figure 2. 3. (a) *Universal Stage.* ***(b)*** *example of one analysed crystal checked for e-twin density on the plane normal to the trace of the twin lamellae (e.g. sample MC17-18 from the Manaslu area).*

According to Rowe and Rutter (1990), the rate of twin lamellae of a given set with respect to grain diameter (normalized for 1 mm length and measured normal to the trace of the twin lamellae) is the twin density (D). This parameter depends on the differential stress recorded by calcite crystals (Rowe and Rutter, 1990; Rybacki et al., 2011, 2013). In this thesis work, twin densities were measured on over 20 crystals in each thin section and estimated using ImageJ software (1.47v by Wayne Rasband). Differential stress recorded by twinning was calculated from the Rowe and Rutter (1990) paleopiezometer and two calibrations after Rybacki et al. (2011) and Rybacki et al. (2013), with the assumption that temperature, strain and grain size have no major influence on twin incidence, and that the critical resolved shear stress of {*e*}-twin is constant (Rowe and Rutter, 1990; Rybacki et al., 2011). According to Rowe and Rutter (1990):

$$\sigma_{(TWIN)}=-52.0+171.1\mathrm{Log}(D)$$

with a minimum standard deviation of 43 MPa. *Vice versa*, according to the Rybacki et al. (2011) piezometer (still based on the mean twin density on natural samples from San Andreas Fault):

$$\sigma_{(TWIN)}=10^{1.29\pm0.02}\,D^{0.5\pm0.05}$$

A further calibration of Rybacki et al. (2013), based on laboratory experiments on pure marbles deformed between 20-350 °C, under confining pressures of 50–400 MPa, and at strain rates of ~10^{-4}–10^{-6} s^{-1}, was adopted, as:

$$\sigma_{(TWIN)} = (19.5 \pm 9.8)\sqrt{D}$$

Rybacki et al. (2011, 2013) calibrations from natural samples and experimental investigations provide essentially the same results. Strain rates from twinning mechanisms were calculated for the inferred deformation temperatures by the Exponential Law of Rutter (1974), which states:

$$\text{Log } \dot{\varepsilon}_{(TWIN)}=5.8-(250000/2.303RT)+0.038\ \sigma_{(TWIN)}$$

2.1.2. Finite strain analysis on marbles

Among the various parameters that influence rock deformations, the final distribution of internal objects can depend on the finite strain. The 'center-to-center' method of strain analysis introduced by Fry (1979) provides a two-dimensional finite strain ellipse estimation (strain equivalent ellipse ratio, R_{XZ}) through the measurements of the object centers distances in naturally deformed rocks. In this thesis, the center-to-center method of Fry (1979) was applied using EllipseFit 3.6.2 software (by Frederick W. Vollmer). Analyzed thin sections approximate the XZ plane of the finite strain ellipsoid. Selected strain markers are deformed calcite crystals (*Fig. 2.4a*). Results are displayed in Fry (1979) plots, in which dots denote the distances between pairs of objects centroids, placed at the same distance and direction to the graph origin. Low-density areas (vacancy field ellipse) within the plot approximate the finite strain equivalent ellipse (*Fig. 2.4b*). For an objective shaping of the field ellipse, the exponential edge detection (EED) method of Waldron and Wallace (2007) was applied (*Fig. 2.4b*).

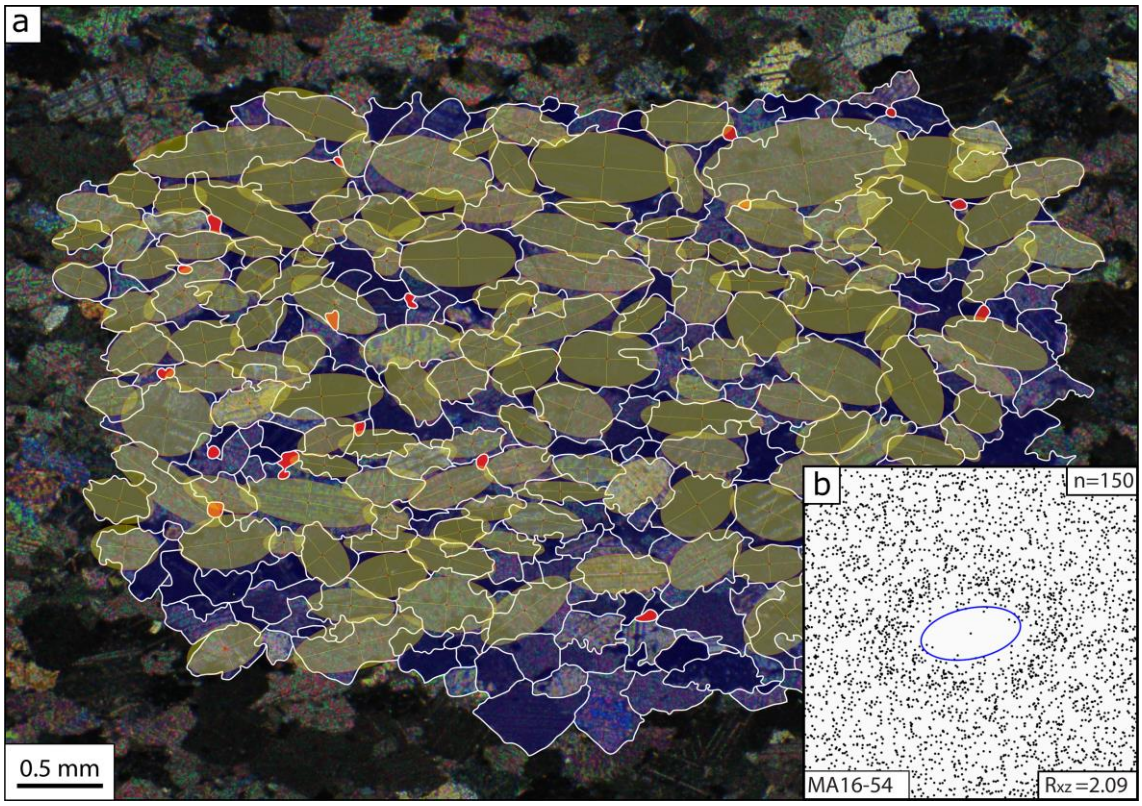

Figure 2. 4. *Example of finite strain analysis of one selected sample (Manaslu area).* ***(a)*** *Lobate calcite grain boundaries, highlighted in white, are approximated to ellipsoids by EllipseFit 3.6.2 software.* ***(b)*** *Fry plot for 150 ellipses. The low-density area, highlighted in blue, is defined applying the exponential edge detection method (EED) of Waldron and Wallace (2007).*

2.2. Texture analysis

Texture analyses were performed on suitable samples, measuring the crystallographic directions of calcite, dolomite, quartz and micas through different apparatus.

X-RAY TEXTURE GONIOMETER

Analyses were carried out with an X-ray Texture Goniometer (XTG), model X'Pert Pro MRD_DY2139 (by PANalytical), at the Georg-August University of Göttingen, Germany (*Fig. 2.5*). The adopted XTG uses the lattice diffraction pattern of X-rays (40 kV/40 mA) channeled from an X-ray generator by a polycapillary tube (350 ranked capillary tubes, each of 100 µm in diameter) on a specimen. A cross slit system determines the conical beam size (7 mm in diameter) to minimize the defocusing effects in function of the sample size, grain size and homogeneity of the area to be analyzed.

Measurements were made on tabular samples cut parallel to the XZ planes and possibly on YZ planes of the finite strain ellipsoid, to acquire the full crystal fabrics. A 2Θ standard diffraction pattern of 5-75° was used with a tilt angle Chi of 5°.

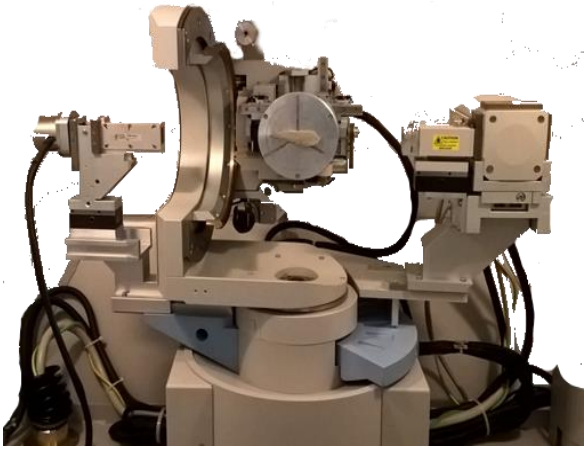

Figure 2.5. *X-ray Texture Goniometer (XTG) by PANalytical (model X'Pert Pro MRD_DY2139) hosted at the Georg-August University of Göttingen*

MTEX Toolbox (available for download here: https://mtex-toolbox.github.io/) of Matlab software was used for processing and calculating the orientation distribution function (ODF) from acquired data. Complete pole figures were provided for the cell parameters a, b, c, α, β, γ and the symmetry code for each mineral. 3D-ODF, inverse pole figures, CPO intensity and misorientation angles (in degrees) were also produced. In order to reduce artefacts linked to data acquisition (coarse grain crystals are investigated several times during X-ray diffraction, producing more intense peaks), the radially symmetric de la Vallee Poussin kernel function (Schaeben, 1997) was applied on ODFs calculation, with a halfwidth of 10° and a resolution of 5° (Hielscher and Schaeben, 2008). For both calcite and dolomite, the planes (001), (110), (104) and (112) were selected to obtain the main crystallographic elements. In calcite and dolomite, poles to the (001) plane are parallel to the [*c*]-axis ([0001] using the hexagonal structural cell) trend, the direction of which is a function of tectonics and kinematics recorded during the deformation (Wenk et al., 1987). The other elements provide respectively the <*a*>-axis <11$\bar{2}$0> and the poles to the rhombic faces *r* {10$\bar{1}$4}, *f* {01$\bar{1}$2}. For calcite data processing, the adopted lattice parameters were a=b=4.988, c=17.062; α=β=90°, λ=120° and, as calcite is trigonal, crystal

symmetry '312' (corresponding to '3m' for the hexagonal structural cell). Through the ODF, calcite poles to {*e*}-planes {01$\bar{1}$8} were determined.

For dolomite, the selected lattice parameters were a=b=4.801 Å, c=16.002 Å; α=β=90°, λ=120°. As it is trigonal, crystal symmetry (from Laue groups) is of '312' (corresponding to '-3'). Prismatic planes, poles to {*m*}-planes {10$\bar{1}$0}, were recalculated from the ODF.
The chosen crystallographic planes for quartz where {11$\bar{2}$0}, {10$\bar{1}$0}, {10$\bar{1}$1}, {01$\bar{1}$1}. Adopting a=b=4.913 Å, c=5.405 Å and α=β=90°, λ=120° and crystal symmetry '312' (corresponding to '321'), the following quartz elements were projected: [*c*]-axis as the pole to the basal plane [0001]; <*a*>-*ax*is as pole to {11$\bar{2}$0}; poles to {*m*}-planes {10$\bar{1}$0}; poles to {*r*}-planes {10$\bar{1}$1}; and poles to {*z*}-planes {01$\bar{1}$1}.
For one sample, biotite was investigated for (001), (110), (200) and (202), adopting as cell parameters a=5.3860 Å, b=9.3241 Å, c=10.2683 Å, α=λ =90°, β = 100.6°, and Z = 1 (space group C2/m). From the ODF, *a*-axis (100), *b*-axis <010>, and *c*-axis <001> were recalculated together with the poles to (101) and (011). The pole to the (001) for biotite, almost parallel to their [*c*]-axis, was used to define how a foliation is oriented in the 3D space and to correct for quartz CPO asymmetries.

FABRIC ANALYZERS

Quartz textures were determined on standard thin sections using a G60+ automated crystal fabric analyzer from Russell-Head Instruments at the University of British Columbia, Kelowna, Canada (*Fig. 2.6*) and at the Georg-August University of Göttingen, Germany. A Fabric Analyzer consists of a computer-controlled microscope equipped with rotating polarizing filters above and below the stage. A CCD camera acquires the images from the microscope during an analysis session with a selected resolution down to 5.08 µm/pixel. The computer controls the acquisition of axial images at stepped rotations of the polarizers and the light source direction. Using the *Crystal Imaging System - Instrument G60 (v.4.1)* software, the fabric analyzer selects the area of the thin section (from single tile up to the full thin section area).

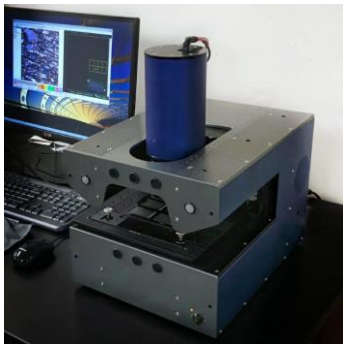

Figure 2.6. *G60+ automated crystal fabric analyser from Russell-Head Instruments at the University of British Columbia, Kelowna, Canada.*

On the base of the crystal birefringence, one analytical session provides Image files with several elements of information, where the main elements are:

- *Azimuth/orientation/trend maps*, consisting of AVA (German: 'Achsenverteilungsanalyse' – analysis of orientation of axes) maps (Sander, 1950; Heilbronner and Pauli, 1993). AVA maps are images of the thin section where pixels, defining each grain, are colored in function of the three-dimensional [*c*]-axis orientation (plunge direction of [*c*]-axes).
- *Overall quality map,* which is an image of the thin section where crystals are colored on a color scale, as a function of their correspondence to the selected mineral phase. *Overall quality* maps enable distinguishing the different phases even if they have similar birefringence colors, as long as they have differences in the other optical properties, e.g. the shape of the optical indicatrix, and therefore in extinction angles (if quartz is the selected

phase in a B/N color scale, quartz crystals are colored in white, whereas second-phase minerals like feldspars and micas are darker).

- *Retardation map,* an image with the average of birefringence colors for each crystal.
- *Xpol maps*, images, under crossed nicols, acquired with variable angle of incidence of light.

Combining the stack of images, pixel by pixel for each grain, and their linked information, the Matlab-based automatized FAME©2017 software (https://peternell.org/archive.html; see Hammes and Peternell, 2016) recalculates the [*c*]-axis orientations of chosen uniaxial mineral. For each thin section, an "angle grain criterion" for the data acquisition was selected in function of the grain size, to remove feldspars from the count when feldspars and quartz had different grain size. The "angle grain criterion" is a parameter that makes it possible to identify the boundary between different subgrains within a crystal. In this case, using a minimum and maximum angle grain criterion allowed us to eliminate unwanted coarse-grained feldspar from the dataset. However, the automated FAME©2017 software is not always able to distinguish quartz crystals from feldspars in heterogeneous rocks, because of the similar birefringence and, in some cases, because of the similar angle of the optical indicatrix. Therefore, during this work, the G50 (v5.12) software Investigator was adopted for manually selecting (and picking) the quartz crystals to be analyzed. Data were reprocessed manually for a critical approach.

2.2.1. CPO intensity and quartz opening angle

ODF plots (e.g. *Fig. 2.7a*) from pole figures, obtained through diffraction analyses, display complete three-dimensional representations of the crystallographic texture relative to the Bunge Euler angle space φ1, ϕ, φ2. Their calculation allows a CPO intensity estimation (e.g. see Schaeben et al., 2007), which has been used in recent years to localize regional-scale shear zones (i.e. whether the deformation is intense and/or long-lasting, crystals orient themselves consistently with the type of the flow; see Hunter et al., 2016; Larson et al., 2017; Starnes et al., 2020 for examples in natural shear zones). The CPO intensity can be visualized, in first order, through misorientation angles versus their frequency plots (*Fig. 2.7b*). These plots allow us to compare an ideal uniform misorientation distribution with the calculated uncorrelated: the greater the difference between the two curves the stronger is CPO intensity.

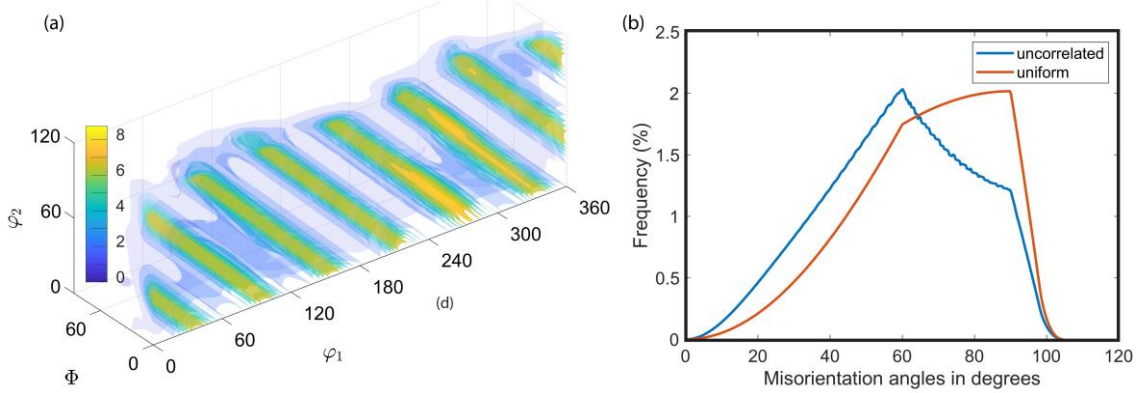

Figure 2. 7. (a) *3D ODF example after quartz texture analysis (XTG-analysis, sample MA16-102, Manaslu area). Orientation density (d) is the plot in the Eulerian space, relative to the Eulerian angles φ1, ϕ, φ2. The range of φ1, ϕ, φ2 depends on the crystal symmetry of the mineral phase.* ***(b)*** *example of misorientation angle plot to derive the CPO intensity (sample MA16-102, Manaslu area).*

The most adopted indexes for CPO intensity from ODFs are the J-Index, or "texture index" (Bunge, 1982; Schaeben, 2007), and the M-Index (Skemer et al., 2005, see also Mainprice et al., 2015). From a crystallographic random orientation to a single-fiber orientation, the J-index ideally increases from 0 to infinity; whereas the M-index ranges from 0 to 1 (Bunge, 1982; Skemer et al., 2005). As long as a well-defined CPO is present, texture patterns can be interpreted in terms of slip systems (e.g. *Fig. 2.1c* for quartz, see Passchier and Trouw for a review). Slip systems can be active singularly or simultaneously with other slip systems, reorienting the deformed crystals in function of the flow type, strain field, conditions of fluids and temperature, if a certain critical stress - the critical resolved shear stress - is reached (e.g. see De Bresser and Spiers, 1993 for calcite).

Slip systems have been widely adopted as geothermometers. Moreover, for quartz [*c*]-axis patterns, when a crossed girdle is recognized, different geothermometers have been proposed (Krhul, 1998; Morgan and Law, 2004; Faleiros et al., 2016), namely the fabric opening-angle method (*Fig. 2.8*). This method assumes that in a crossed girdle the angle defined by the leading edge and the trailing edge of the pole figures is related to the mixed <*a*> slip and varies according to the temperature. According to Faleiros et al. (2016), for a deformation temperature regime below 650 °C we can apply the following equation:

$$T°C=6.9*(OA)+48$$

where OA is the fabric opening-angle. For a deformation temperature regime above 650 °C:

$$T°C=4.6*(OA)+258$$

From fabric analyzer output, quartz fabric opening-angles were automatically recalculated through an independent script (https://osf.io/ays5w/) designed for this purpose. For ODF-based pole figures, quartz fabric opening-angles were measured manually.

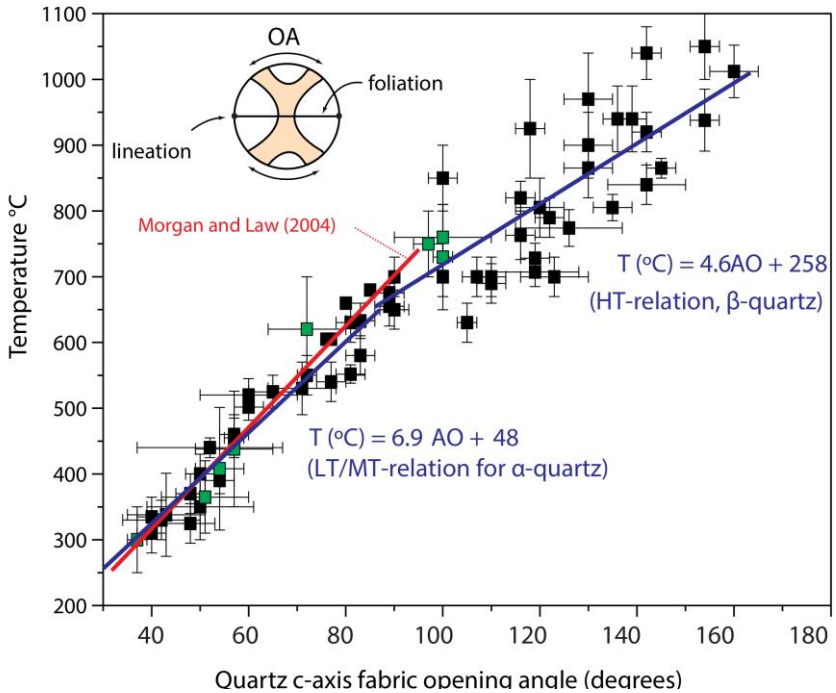

Figure 2. 8. *Graph of quartz [c]-axis fabric opening angles versus estimated temperatures of deformation presenting linear fits for different suites of naturally deformed samples (after Morgan and Law, 2004 and Faleiros et al., 2016).*

2.2.2. Kinematic vorticity and shortening

Flow within shear zones often deviates from simple shear conditions (Xypolias, 2010; Fossen and Cavalcante, 2017) and has a variable contribution of pure shear (Truesdell, 1954, 2018; Ramberg, 1975; Means et al., 1980; Passchier, 1997). On the basis of coaxial and non-coaxial deformation contribution, a kinematic flow can be described as pure shear dominated (Behyari and Shahbazi, 2019), or simple shear dominated (e.g. *Fig. 2.9a*, Fossen and Cavalcante, 2017). The aim of kinematic vorticity analyses is quantifying the contemporaneous relative contribution of simple shear and pure shear during the plastic flow of mylonitic rocks (Xypolias, 2010).

The kinematic vorticity number (Wk) is a dimensionless number for the vortical flow, defined as the ratio between the angular velocity and the instantaneous stretching rate (Truesdell, 1954; Means et al., 1980). The instantaneous stretching axes, ISA1 and ISA2, correspond respectively to the incremental shortening direction and the incremental extensional direction. The angle between the Instantaneous Stretching Axes is always 90° (*Fig. 2.9b*), while their orientations with respect to the shear plane define the kinematic vorticity. During kinematic flow, the material lines can rotate synthetically and antithetically. The sense of rotation of the material lines depends on their orientation, and the limits between the fields of synthetic and antithetic rotation define two "flow apophyses": A1 and A2. In pure shear deformation (Wk=0, *Fig. 2.9a, b*), the flow apophyses are orthogonal to each other and, they are parallel to the Instantaneous Stretching Axis, ISA1 and ISA2, respectively. In simple shear, (Wk=1, *Fig. 2.9a, b*) the flow apophyses are parallel to each other, and ISA2 is at 45° to the flow apophysis A2, always oriented parallel to the shear plane. In general shear, the flow apophyses will be conjugated at different angles as a function of the kinematic vorticity of the flow (*Fig. 2.9a, b*) with the A2 parallel to the shear plane. If the deformation occurs under a monoclinic plane strain regime (2D flow), Wk corresponds to the sectional vorticity number (Wn) which is a function of the angle between the flow apophyses: $Wn = \cos(\alpha)$ (*Fig. 2.9c*). Wn represents the instantaneous vorticity of the flow occurring during a single deformation increment (Passchier, 1997). In long-lasting deformations, the Wn can vary highly in function of the tectonic setting. The average Wn recorded in a shear zone is referred to as mean kinematic vorticity (Wm) (Xypolias, 2010, and reference therein). Different kinematic vorticity estimation methods can quantify either the Wn or the Wm depending on the strain memory of the analyzed structure. In this work, Wn estimations were applied through the CPO-based Wenk et al. (1987) method on calcite in marbles and through the "orientation of oblique grain shape fabrics method" of Wallis (1995) for impure marbles and dolomitic marbles. Both methods require knowing the orientation of the shear plane, which is often unknown in regional-scale shear zones.

The Wenk et al. (1987) method uses the Taylor theory and the viscoplastic self-consistent model to predict the simple shear contribution on calcite crystals deformed by twinning and intercrystalline slip. Analytically, the method requires measuring the angle (ω) between the [c]-axis point maximum and the normal axis to the shear plane. In such a method, 100% of simple shear is realized at an angle of ω~36°, and a pure coaxial deformation is suggested for ω = 0°. The sectional vorticity number, Wn, can be calculated as the cosine of the angle between the flow apophyses (see Law et al., 2004). Therefore, from the simple shear estimations, it is possible to estimate the complementary angle α and the angle between A1 and A2 flow apophysis $Wn=\sin(\alpha)$.

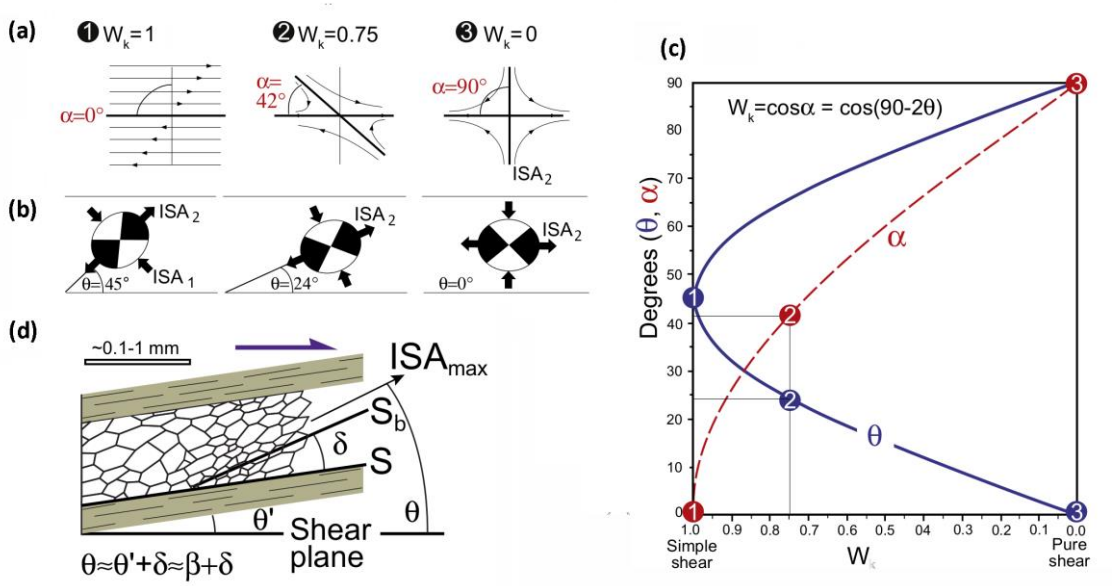

Figure 2.9. *Schematic illustrations modified after Fossen and Cavalcante (2017).* ***(a)*** *The particle paths and orientations of flow apophyses (α) illustrated for simple shear (Wk=1), general shear (0<Wk<1) and pure shear flow (Wk=0), from left to right.* ***(b)*** *ISA orientations for simple shear, general shear and pure shear flows. Black areas are fields of instantaneous extension; white are fields of instantaneous contraction.* ***(c)*** *The orientations of ϑ and α defining the kinematic flow (e.g. in case of simple shear, 1, general shear, 2, or pure shear, 3).* ***(d)*** *Angular relationships between the shear plane (horizontal), the mylonitic foliation, S (at ϑ' angle respect to the shear plane), and oblique foliation (Sb) forming a δ angle to S.*

The Wallis (1995) method, on the other hand, assumes that in a shear zone, when new blasts nucleate obliquely to the shear zone boundaries (*Fig. 2.8d*), their long axes are parallel to the direction of the extensional instantaneous axes, ISA2, during the progressive deformation (see also Xypolias, 2009, 2010). The greatest recorded angle between the oblique foliation and the shear plane represents the angle δ between the ISA2 and the flow apophysis A2 (*Fig. 2.8b*), and the kinematic vorticity is Wm=sin(2δ).

In general shear, the shortening orthogonal with respect to the shear plane is connected to the coaxial component of deformation. Non-coaxial component is associated with the rotational component of the deformation. For this reason, the shortening (S) can be calculated knowing the equivalent ellipse ratio of the finite strain (Rxz) (*par. 2.1.2*) though the Wallis et al. (1993) equation:

$$S = \left\{\frac{1}{2}\sqrt{(1-Wm^2)}\left[\sqrt{\left(Rxz+\frac{1}{Rxz}+2\frac{(1+Wm^2)}{(1-Wm^2)}\right)}+\sqrt{\left(Rxz+\frac{1}{Rxz}-2\right)}\right]\right\}^{-1}$$

2.3. Microchemical and geochronological analysis

Geochronological investigations are crucial for defining the tectonic evolution of orogens, helping to distinguish episodic and progressive deformation in polydeformed rocks (Fossen et al., 2019). However, structural and microstructural observations, coupled with microchemical and petrological analyses, are crucial for clarifying to what event the minerals dated are related to (Müller, 2003; Di Vincenzo et al., 2004; Villa, 2006; Engi et al., 2017; Kohn et al., 2017; Bosse and Villa, 2019).

In this thesis, the mica mineral chemistry was analyzed through an Electron Microrobe, JEOL 8200 Super Probe equipped with 5 WDS spectrometers at Dipartimento di Scienze della Terra "Ardito Desio", Università di Milano Statale (Italy). Dark mica and white mica atoms per formula unit (a.p.f.u.) and structural formulas were recalculated on the basis of 11 oxygens. Full chemical datasets are given in supplementary materials (*Appendix – Electron microprobe analyses*). For geochronological analyses, ^{40}Ar–^{39}Ar step-heating and laser *in-situ* ^{40}Ar–^{39}Ar analyses were adopted on white and dark micas. Samples selected for step-heating analysis were crushed at room temperature; dark mica was then separated through standard separation techniques (e.g. Franz magnetic separator and separators based on the 3D grain shape) at the IGG-CNR of Pisa (Institute of Geosciences and Earth Resources of National Research Council of Italy). For ^{40}Ar–^{39}Ar *in-situ* analysis, a rock chip was drilled from sample D20-10-49 (ca. 9 mm in diameter and ca. 0.4 mm in thickness) using a diamond core drill. In this sample (D20-10-49), the thickness of the dark mica flakes was checked in a mineral separate, resulting to be in the order of ca. 0.1 mm. Both the mica separates and the rock chip were cleaned by alternating deionized water and methanol. Samples were then wrapped in aluminium foil and irradiated along with the Fish Canjon Tuff (FCs) sanidine monitor in the TRIGA reactor (Mark II) at the University of Pavia (Italy) during three different irradiations. Sample D20-10-69 was irradiated for 5 hours, the rock chip from sample D20-10-49 for 60 hours, and D18-10-64 for 2 hours. The neutron flux was determined by total fusion analyses of the Fish Canyon Tuff sanidine grains using a continuous wave CO_2 laser (New Wave Research MIR10–30 CO_2 laser system). For each sample, parabolic interpolation between the analysed standards was used to derive the irradiation parameter J. ^{40}Ar–^{39}Ar analyses were performed in collaboration with the IGG-CNR of Pisa (Italy) through ^{40}Ar–^{39}Ar step-heating and *in-situ* ^{40}Ar–^{39}Ar geochronology (*Fig. 2.10*).

Figure 2. 10*. The ^{40}Ar–^{39}Ar laboratory at IGG-CNR of Pisa (photo and information available at: https://www.igg.cnr.it/en/laboratories/analytical-laboratories/ar-ar-geochronology-laboratory/).*

^{40}Ar–^{39}Ar step-heating analysis was performed by heating the dark mica separates with a continuous wave infrared diode-pumped Nd:YAG (neodymium-doped yttrium aluminum garnet) laser (beam defocused to ca. 2 mm of spot size; power ~20 W). 16 heating cycles were carried out for sample D20-10-69, whereas 13 cycles of heating were performed for sample D18-10-64. Argon isotope compositions were investigated through a MAP215–50 single-collector noble gas mass spectrometer, equipped with a Secondary Electron Multiplier detector, with an instrumental sensitivity of approximately 3 x 10^{-14} mol/V.

Gas purification was achieved every 10-12 minutes, including 2 minutes of lasering by: two SAES AP10 GP MK3 getters held at 400 °C; one SAES C-50 getter held at room temperature, and a liquid nitrogen cold trap. Blanks were analyzed every three-four analyses. A polynomial function was fit to blanks analysed during the day of acquisition, and unknown analyses were corrected based on the time of measurement. Maximum blanks are given in (*Appendix – Electron microprobe analyses*).

In-situ ^{40}Ar–^{39}Ar analyses were performed on the rock chip (on a computer-controlled x–y stage) based on detailed back-scattered electron (BSE) imaging. By heating the micas, three different structural domains were investigated with an ultraviolet Nd:YAG UV laser beam (frequency quadrupled and Q-switched), operating at 20 Hz and 0.5–1 mJ per pulse. The laser beam was focused to ca. 10 µm on areas of ca. 100x100 μm^2 for a few tens of micrometers in depth. Argon isotope compositions were investigated through an ARGUS VI (Thermo Fisher Scientific) multi-collector noble gas mass spectrometer. Ar isotopes ^{40}Ar, ^{39}Ar, ^{38}Ar, ^{37}Ar were measured by Faraday detectors (10^{12} Ω resistors for the ^{40}Ar and ^{38}Ar isotopes, and 10^{13} Ω resistors for ^{39}Ar and ^{37}Ar), cross calibrated for the slight offset with ~4000 fA air shots), whereas the Ar isotope ^{36}Ar was acquired by a Compact Discrete Dynode (CDD) detector, previously calibrated daily by measuring four to six air pipettes. Gas purification was achieved every 4 minutes, including ~3 min of lasering, using three SAES NP10 getters (one water cooled, held at ~400 C, and two at room temperature). Blanks, monitored every two runs, were subtracted from succeeding sample results (see *Appendix – Electron microprobe analyses*).

For both step-heating and *in-situ* analyses, data were corrected also for post-irradiation decay, mass discrimination effects and isotope derived from interfering neutron reactions. In-run statistics and uncertainties on single runs, discrimination factor, interference corrections, and procedural blanks were propagated and reported as 2σ through the ArArCALC (Koppers, 2002) software. ^{40}Ar–^{39}Ar ages were calculated assuming 28.201 Ma for the standard FCs (Kuiper et al., 2008), whereas uncertainties on the total gas ages, the error-weighted means and ages derived from isochron plots were estimated, also including the uncertainty on the fluence monitor (as internal errors, 2σ).

3. Manaslu area (Annapurna region)

The Manaslu range of Western Nepal is a key area of the Himalaya. Extensive field-based research work, particularly by French geologists over the last 50 years, is well organized and summarized in a detailed geological map (scale 1:200,000) comprising the Annapurna-Manaslu-Ganesh Himalaya proposed by Colchen et al. (1986). This work offers an overview of the stratigraphical, metamorphic and tectonic setting of the area. Larger-scale, and more recent, tectonic studies (e.g. Brown and Nazarchuk, 1993; Schneider and Masch, 1993; Coleman, 1996; Vannay and Hodges, 1996; Godin et al., 1999a, b, 2001; Godin, 2003) report ductile detachments belonging to the STDS, not documented in the Colchen et al. (1986) map. Recently, the 1:200,000 Dhaulagiri-Annapurna-Manaslu-Himal geological map by Parsons et al. (2016b) integrates this structure with the available cartography. This recent map simplifies the Colchen et al. (1981, 1986) stratigraphic division, including the works of Garzanti (1999), Paudel and Arita (2000), Godin (2003), Godin et al. (2006a) and Searle et al. (2008). By integrating the stratigraphy of Colchen et al. (1986) with the Parsons et al. (2016b) geological maps and recent investigations (e.g. Schneider and Masch, 1993; Walters and Kohn, 2017), and original unpublished mapping from Carosi, Iaccarino, Montomoli, Simonetti and Visonà during two field expeditions (2016 and 2017), a simplified geological map is provided in *Fig. 3.1*. The purpose of this map is to take advantage of past research to localize the MCTz and the STDS with the micro tectonic and texture investigations made during the work for this thesis.

Two major N-S trending valleys cross the study area (*Fig. 3.1*). From east to west, these are the Budhi Gandaki valley, around the Manaslu Massif, and the Marsyandi valley. From south to north, both valleys expose the upper LHS, a complete section of the GHS and THS rocks. From the Himalchuli peak (7893 m) toward the north, an impressive Oligocene-Miocene leucogranite body, the Manaslu pluton (*Fig. 3.1*), is a prime example of High Himalayan leucogranites. It was originally interpreted as intruding into both the GHS_U and the Triassic rocks of the THS (Le Fort, 1975, 1981; Colchen et al., 1986; Guillot et al., 1993, 1995). More recently, it has been suggested that the Manaslu pluton only intrudes into the GHS_U (Searle and Godin, 2003; Searle, 2010; Parsons et al., 2016b). Several geochronological investigations (e.g. white mica, biotite, hornblende, and K-feldspar Ar–Ar dating; monazite U–Th–Pb dating) indicate that the Manaslu pluton intruded at the STDS base at 23-19 Ma and cooled down at ca. 14-13 Ma at a depth of 18 ± 2 km (Copeland et al., 1990; Guillot et al., 1994; Cottle et al., 2019).

From south to north, the LHS of Colchen et al. (1986) comprises a complete section of 6 km of greenschist facies quartzite and minor pelite (garnet-zone) and schist (staurolite-zone) (*Fig. 3.2*) to amphibolite facies quartzite, paragneiss (kyanite-zone) and impure marble (Colchen et al., 1981, 1986). Upward, the MCTz affects the LHS and the GHS (Colchen et al., 1986, Pêcher, 1991). According to Colchen et al. (1986), the GHS consists of about 7 km of medium- to high-grade metamorphic rocks, divided into the classical three units (or formations). Unit 1 consists of micaschist and paragneiss, with lenses of orthogneiss and calc-silicate-rich rocks, from the staurolite-zone to the sillimanite-zone. Unit 2 is made of calc-silicate rich metasiltstone and marble in the scapolite-zone. At the top, Unit 3 consists of migmatitic orthogneiss (Colchen et al., 1981, 1986; Searle, 2010; Walters and Kohn, 2017). Structurally above, the THS encompasses a continuous sequence of about 10 km of marine metasediments (Cambrian-Ordovician) and unmetamorphosed sediments (up to Cretaceous in age, Colchen et al., 1981, 1986; Godin, 2003).

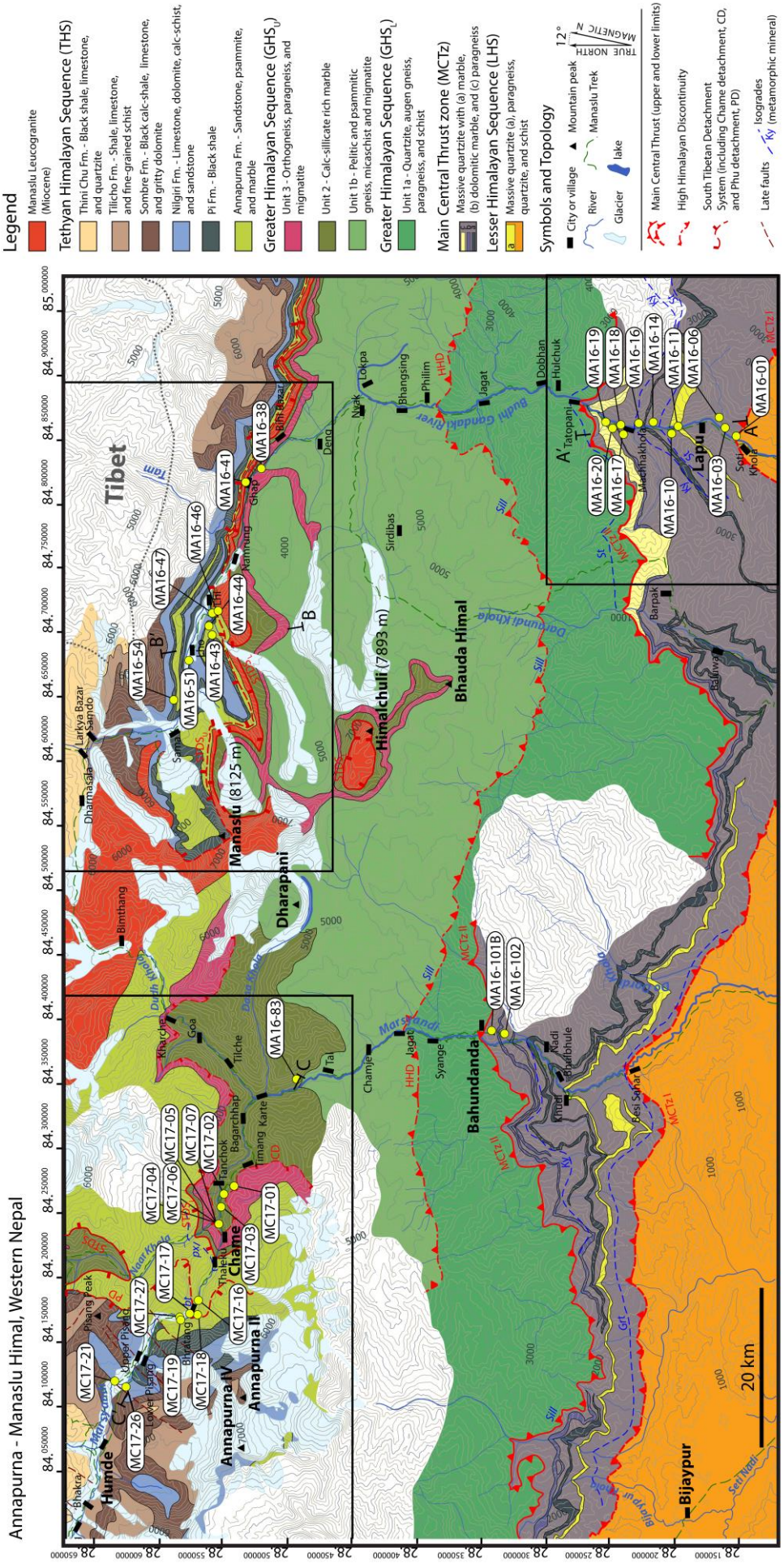

Figure 3. 1. *Geological sketch map of Manaslu area (modified after Colchen et al., 1986; Parsons et al., 2016b and Carosi et al., unpublished data). Analysed samples belong to the Budhi Gandaki valley (toward the east) and Marsyandi valley (toward the west). Study areas (black boxes) zoom are in* Fig. 3.2, Fig. 3.9, *and* Fig. 3.15.

In the study area, from bottom to top, the THS comprises the Cambrian-Ordovician Annapurna, Pi and Nilgiri Fm., the Silurian Sombre Fm., the Devonian Tilicho Fm. and the Permian-Carboniferous Thini Fm. (*Fig. 3.1*). At the base of the THS, the Annapurna Fm. and the Pi Fm., varying from marble, metapsammite, carbonate-bearing metarenite and black shale, are metamorphosed from the clinopyroxene-zone down to the biotite-zone (*Fig. 3.1*). A strong metamorphic field gradient, within 200 m, is documented, with a progressive attenuation of the metamorphic grade up to the Nilgiri Fm. and Sombre Fm. (e.g. Colchen et al., 1986; Schneider and Masch, 1993; Walters and Kohn, 2017). The main Himalayan shear zones occur in the study area (see Khanal and Robinson, 2013; Parsons et al., 2016b). Different definitions for the lower limit of the MCTz, and the STDS limits, are proposed (e.g. see Hodges et al., 1996, Searle and Godin, 2003; Parsons et al., 2016a, b; see Searle, 2010 for a review). Indeed, for the MCTz upper limit, or MCTz II (Chomrong Thrust), most authors agree on its location occurring in Tatopani (along the Budhi Gandaki valley) and Bahundanda towns (Marsyandi Valley) (Colchen et al., 1986; Schneider and Masch, 1993; Hodges et al., 1996; Searle and Godin, 2003; Larson and Godin, 2009; Larson et al., 2010; Searle, 2010; Parsons et al., 2016b; Walters and Kohn, 2017). The MCTz II is described as a sharp discontinuity that places the kyanite-zone gneisses over lower amphibolite facies rocks from ca. 22.5 Ma (Hodges et al., 1996; Searle, 2010). The MTCz lower limit, or MCTz I, is not placed in the Colchen et al. (1986) map. Hodges et al. (1996) and Searle et al. (2008) localized the MCTz I at almost 1 km of structural thickness below the Chomrong Thrust, based on strain gradients and metamorphic fabrics of the sheared rocks. However, Larson et al. (2010) and Parsons et al. (2016b) report the MTCz I limit at even lower structural levels, around Arughat Bazaar in the Budhi Gandaki valley, between the semipelite and pelite of the LHS (Kuncha Fm.) and the quartzite, semipelite and pelite of the GHS_L (still within the LHS according to Colchen et al., 1981, 1986; Searle and Godin, 2003). In this thesis, the MCTz I has been located near Soti Khola (*Fig. 3.1, Fig. 3.3a*) along the Budhi Gandaki valley and near Besi Sahar along the Marsyandi valley (*Fig. 3.1*), similarly to Khanal and Robinson (2013). Unit 1 of Colchen et al. (1986), Searle and Godin (2003) and Searle (2010) is divided into the GHS_L and the GHS_U through the HHD (*Fig. 3.1*). The HHD is defined by a hundred meters-thick top-to-the-south high-temperature -shear zone (close to the sillimanite-isograd), southward to Philim and around Jagat villages along the Budhi Gandaki and the Marsyandi valleys, respectively (Carosi et al., personal communication; *Fig. 3.1*). Unit 2 and Unit 3 are also included in GHS_U (*Fig. 3.1*).

Concerning the STDS, some important "unresolved" issues still persist. In the Marsyandi valley, within the Unit 2 and Unit 3 of the GHS_U, well exposed around Chame village, a >300-m-thick ductile shear zone, the Chame Detachment (Coleman, 1996; Coleman and Hodges, 1998; Searle and Godin, 2003) or Chame shear zone (Walters and Kohn, 2017) has been mapped. Object lineation, trending of ca. 100-110° toward the NW and plunging between 15-25°, in combination with ductile shear sense indicators, such as C-C'-S fabric, extensional shear bands, delta and sigma porphyroclasts and asymmetric folds, point out top-to-the-north/northwest sense of shear (Coleman, 1996). Since Coleman (1996), Coleman and Hodges (1998), and Searle and Godin (2003), the Chame Detachment has been interpreted as a ductile shear zone belonging to the STDS. Nonetheless, a critical issue concerns whether the shear zone is thrust- or normal-sense detachment, as few kinematic indicators seem to point to a shearing toward the south (Coleman, 1996). Over the years, the Chame shear zone has been interpreted as having a tectonic switch, with an early top-to-the-south shearing, followed by top-to-the-north/northwest normal shearing (Coleman, 1996). However, Walters and Kohn (2017) have recently reinterpreted this structure as an HT intra-GHS thrust (similar to the HHD), with a thrust-sense shearing occurring from ca. 30 Ma up to, at least, 17–16 Ma.

At higher structural levels, both in the Budhi Gandaki and in the Marsyandi valleys, further top-down-to-the-north/northwest ductile shearing occurs, involving the top of the GHS_U (Unit 2/Unit 3) and the THS (Annapurna Fm.) (*Fig. 3.1*). According to Walters and Kohn (2017), within the base of the Annapurna Fm., along the pyroxene-in isograd (see also Colchen et al., 1986 and Schneider and Masch, 1993), an STDS in *sensu stricto* occurs, coupling the GHS_U and the THS bottom (*Fig. 3.1*). The detachment continues toward the east, wrapping around the top of the Manaslu leucogranite (*Fig. 3.1*). According to Searle and Godin (2003) and Searle (2010), a major low-angle ductile shear zone, the Phu Detachment, occurs in the Marsyandi Valley at higher structural levels, within the biotite-bearing marbles of the Annapurna Fm. (THS). Searle and Godin (2003) identify the main STDS branch in the Phu Detachment (*Fig. 3.1*).

3.1. Sample description and results for the Main Central Thrust zone

Coupling field and microstructural and textural observations in the area, the MCTz is here defined as a ca. 10 km-thick top-to-the-south shear zone (*Fig. 3.1, Fig. 3.2, Fig. 3.3*), including a thick volume of the LHS unit in the staurolite/garnet zone, but located structurally upward with respect to Parsons et al. (2016b) map. At the mesoscale, a pervasive mylonitic foliation strikes of ca. N70-80 ° and dips 20-45° toward the N/NE (*Fig. 3.3a*, Colchen et al., 1986). This fabric is commonly related to the S2 foliation linked to the MCTz (Colchen et al., 1986; Searle et al., 2008; Larson et al., 2010). Quartz grains ribbons and mineral grain shape define a north-trending object lineation (L2) (*Fig. 3.3a*, see also Colchen et al., 1986; Larson et al., 2010; Parsons et al., 2016b). Within the LHS, at the MCTz I, bedding correlated to the S1 foliation, is folded (*Fig. 3.3a*, see also Colchen et al., 1986; Larson et al., 2010), with axial planes (A2) plunging of ca. 20° axes. Fabric analysis was carried out on thirteen out of eighteen field-oriented samples with an LHS-affinity according to Colchen et al. (1981, 1986) (*Table 3.1, Fig. 3.3a, b*). From lower to higher structural levels along the Budhi Gandaki valley, samples MA16-01, MA16-03 and MA16-06 belong to the Kuncha Fm. (Colchen et al., 1986) of the LHS. They consist of quartzite deformed in the garnet-zone (greenschist facies). Upward, samples MA16-10 and MA16-11 are massive quartzites, belonging to the greenschist facies rocks of the LHS (Ghandrung quartzites). MA16-14 is a quartz-rich paragneiss, belonging to the staurolite-zone (*Fig. 3.3a, b*) with an LHS "protholiths-affinity" according to Colchen et al. (1986).

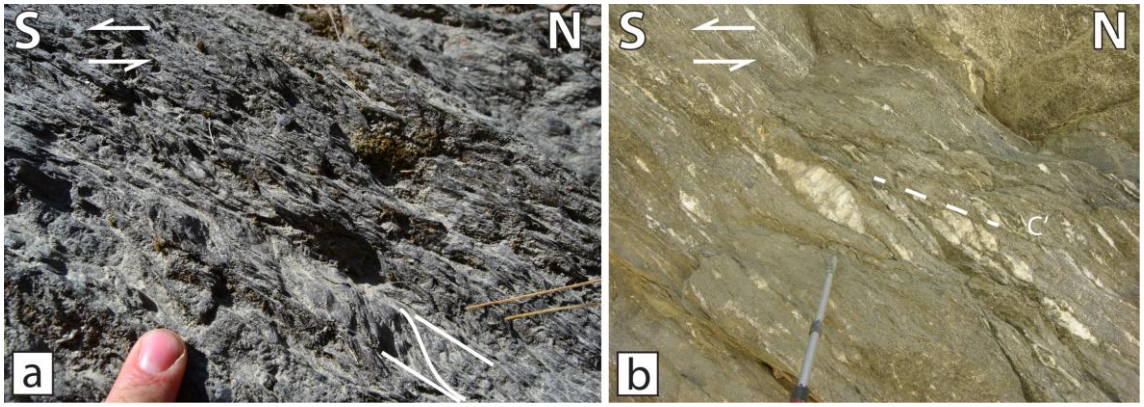

Figure 3. 2. *Photographs of MCTz outcrops in the Budhi Gandaki valley (credits: Montomoli, C., Carosi, R., Iaccarino, S., field expedition, A.A. 2016).* ***(a)*** *Micaschist showing S-C fabric consistent with a top-to-the-south sense of shear.* ***(b)*** *mylonitic phyllite with asymmetric clasts and S-C-C' fabric.*

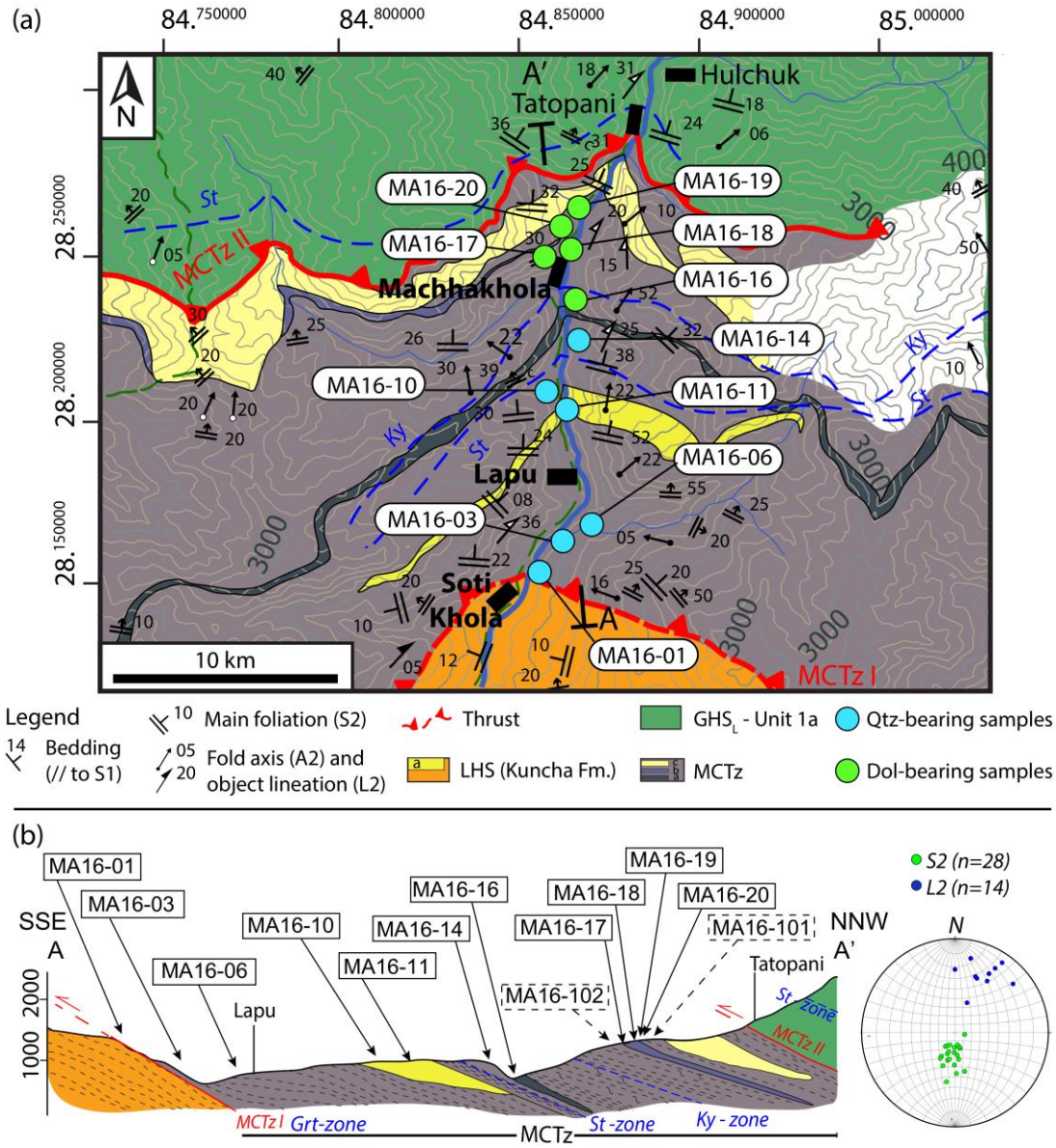

Figure 3. 3. (a) *Zoom of the geological sketch map of the lower Budhi Gandaki valley (see Fig. 3.1 for location and legend details).* ***(b)*** *Geological cross section of A-A' trace of Fig. 3.1, where the studied samples are projected (same vertical and horizontal scales). Samples MA16-101 and MA16-102 are projected from the Marsyandi valley. On the right, S2 and L2 are reported in the equal-angle lower hemisphere stereographic projection. Within the LHS, the a-horizon corresponds to the Ghandrung quartzite; whereas within the MCTz, the a-horizon corresponds to lower dolomitic marble, b-horizon to the upper dolomitic marble, and the c-horizon to the upper quartzites of Colchen et al. (1986). Abbreviations: Grt, garnet; Ky, kyanite; Sill, sillimanite; St, staurolite.*

Above, sample MA16-16 is a dolomite-bearing gneiss (lower limestone/dolostone of the LHS according to Colchen et al., 1986) in the kyanite-zone (*Fig. 3.2a, b*). Up-section, MA16-17, MA16-18, MA16-19, and MA16-20 are dolomite-bearing paragneiss and dolomitic marbles (upper limestone/ dolostone according to Colchen et al., 1986). From the Marsyandi valley toward the west (*Fig. 3.1*), samples MA16-102 and MA16-101 are amphibolite-facies massive quartzite and Grt-Tur-rich quartzite belonging to the kyanite zone. They represent the "upper quartzites" of the LHS of Colchen et al. (1986), or the massive quartzites of the GHS$_L$ of Parsons et al. (2016b).

Table 3.1. *Summary for the MCTz selected samples, referred to their unit and formation (lower Budhi Gandaki valley, see Fig. 3.2 for sample location). Samples are listed from bottom to top. Mineral assemblage, main features and related type of analysis are provided. Abbreviations: Ap – apatite; Bt – biotite; Cal – calcite; Chl – chlorite; Cpx – clinopyroxene; Dol – dolomite; Feld – feldspar; Grt – garnet; Kfs – K-feldspar; Mc – microcline; Mnz – monazite; Pl – plagioclase; Qtz – quartz; Wm – white mica; Rt – rutile; Tur – tourmaline; Zr – zircon; GBM – grain boundary migration; SGR – subgrain rotation recrystallization; Sb – oblique foliation; SPO – shape preferred orientation.*

Sample	Unit	Mineral Assemblage	Lithotype	Fabric and deformation m.	Analysis
MA16-01	MCTz (Kuncha Fm.)	Qtz+Pl/Kfs+Bt+Wm +Chl+Grt+Tur	Grt+Tur paragneiss	S-C fabric top-to-the-south; QTZ: SGR/GBM$_I$	◔
MA16-02	MCTz (Kuncha Fm.)	Qtz+Pl+Kfs+Wm+Bt +Chl+Grt+Tur	Grt+Tur paragneiss	S2+S1; asymmetric structures top-to-the-south; QTZ: SGR/GBM$_I$	○
MA16-03	MCTz (Kuncha Fm.)	Qtz+Pl+Kfs+Wm+ Grt+Tur+Mnz	Grt+Tur paragneiss	S-C fabric top-to-the-south; QTZ: SGR/GBM$_I$	◕
MA16-04	MCTz (Kuncha Fm.)	Qtz+Pl/Kfs+Wm+Bt +Chl+Tur+Mnz+Ap	Grt+Tur paragneiss	C-C'-S fabric top-to-the-south; QTZ: SGR	○
MA16-05	MCTz (Kuncha Fm.)	Qtz+Wm+Bt+Chl+ Tur+Zrn+Ap	Qtz-bearing micaschist	S2+S1 foliations	○
MA16-06	MCTz (Kuncha Fm.)	Qtz+Wm+Bt+Chl+ Zrn+Ap+Mnz	Qtz-bearing paragneiss	S-C fabric top-to-the-southwest; QTZ: SGR/GBM$_I$	◕
MA16-09	MCTz	Qtz+Kfs+Grt+Wm+ Bt+Tur+Chl	Grt+Tur micaschist	S2+S1; C-C'-S fabric top-to-the-south; QTZ: GBM$_I$	○
MA16-10	MCTz (massive quartzites)	Qtz+Kfs+Pl+Bt+Wm +Tur+Ap	Quartzite	S-C fabric top-to-the-south; QTZ: GBM$_I$; feld: plastic	◒
MA16-11	MCTZ (massive quartzites)	Qtz+Kfs+Wm+Zr+ Ap+Tur+Mnz	Quartzite	S2+ asymmetric structures; Qtz: GBM$_I$	◕
MA16-14	MCTZ (massive quartzites)	Qtz+Pl+Kfs+Wm+Bt +Mnz	Qtz-bearing paragneiss	S-C fabric top-to-the-southeast; QTZ: GBM$_I$; feld: plastic	◕
MA16-15	MCTZ (massive quartzites)	Dol+Qtz+Wm+Cpx	Marble	S2: SPO (Dol); Dol: GBM	○
MA16-16	MCTz (lower dolomitic marble)	Dol+Qtz+Wm+Bt+ Tur+Mnz	Dol-bearing impure marble	Quartz in dolomite matrix	◔
MA16-102	MCTz (massive quartzites)	Qtz+Pl+Kfs+Bt+Wm +Tur+Mnz+Ap	Tur-rich quartzite	S-C fabric top-to-the-south; QTZ: GBM$_I$ + annealing	◕
MA16-17	MCTz (upper dolomitic marble)	Dol+Qtz+Kfs+Bt+ Wm+Tur	Marble	S2+Sb: SPO (Dol); Dol: GBM	◓
MA16-18	MCTz (upper dolomitic marble)	Qtz+Dol+Kfs+Bt+ Wm+Tur	Dol-bearing impure marble	Quartz in dolomite matrix	○
MA16-19	MCTz (upper dolomitic marble)	Dol+Qtz+Kfs+Bt	Marble	S2+Sb: SPO (Dol); Dol: GBM	◓
MA16-101	MCTz (massive quartzites)	Qtz+Pl+Kfs+Bt+Wm +Grt+Mn+Ap+Tur	Grt- Tur- rich quartzite	S-C fabric top-to-the-south; QTZ: GBM$_I$; feld: plastic	◒
MA16-20	MCTz (upper dolomitic marble)	Dol+Qtz+Kfs+Bt+ Wm	Marble	S2: SPO (Dol+Cal); Dol: GBM	◔

Legend: ○ microstructural analysis; ◔ Texture analysis (XTG); ◒ Texture analysis (FA); ◐ Kinematic vorticity analysis

3.1.1. Microstructural analysis of the MCTz (Budhi Gandaki and Marsyandi valleys)

The main lithologies deformed by the MCTz are: Grt+Tur quartz-bearing paragneiss, quartzite, micaschist and dolomitic marbles (*Table 3.1*, *Fig. 3.4a-l*) belonging to both the LHS and GHS$_L$ concerning the "photolith" affinity. At the microscale, a pervasive S2 mylonitic foliation is the main structural feature in all samples. Very few relics of S1 foliation are present in the microlithons of S2 foliation, mainly within the LHS (*Table 3.1*). S2 is a spaced foliation characterized by a pervasive S-C fabric where C planes are marked by biotite shape preferred orientation (SPO) (see examples in *Fig. 3.4h, i, k, l*). All kinematic indicators, such as oblique foliation (*Fig. 3.4a, f*), snowball garnet, mineral fish (mica, plagioclase fish) and porphyroclasts with asymmetric strain shadow show a top-to-the-south shearing consistent with the MCTz flow.

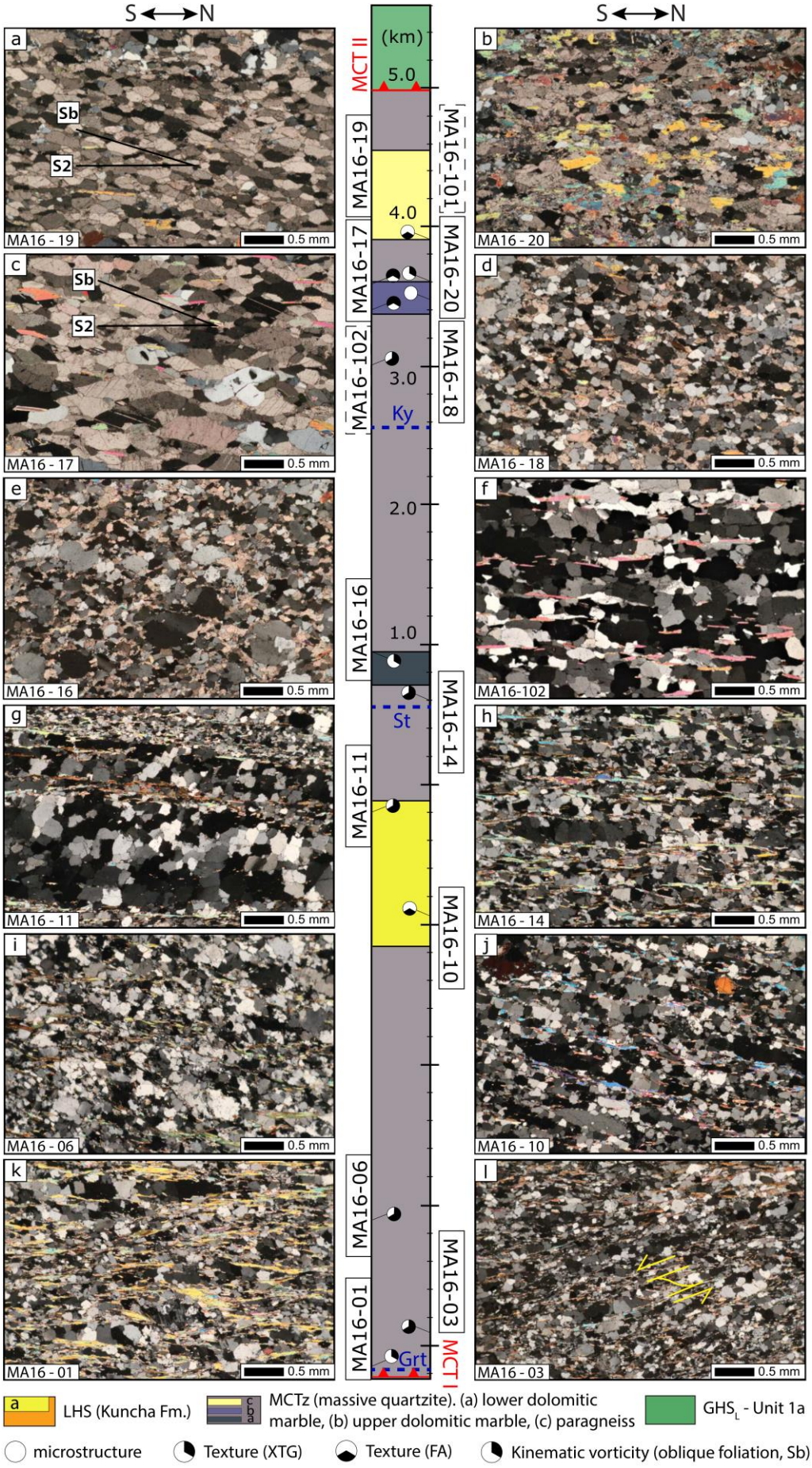

Figure 3. 4. *Optical micrographs of the samples selected to define the MCTz in the lower Budhi Gandaki valley. Sample location on the structural section is displayed by small circles (type of analysed are indicated by the symbology). Scale in the middle corresponds to vertical thickness in kilometers. See text for further details.*

Within a km-thick volume of quartz-rich paragneiss and quartzite, quartz is the most abundant mineralogical phase, with a modal amount over 20% in volume of each sample. Quartz is well interconnected and deformed, and so it represents the weak matrix (*Fig. 3.4f-l*) and/or the interconnected granoblastic layers (e.g. *Fig. 3.4g, j*) supporting the deformation (Handy, 1994). Feldspar, garnet, and kyanite grains behaved as mechanically strong clasts (Handy, 1994); plagioclase is deformed by mechanical twinning and plastic deformation. In the LHS-rocks, quartz displays intra-crystalline subgrains and slight bimodal distributions of grain sizes. Such microstructures indicate a plastic deformation caused by dynamic recrystallisation processes dominated by subgrain rotation (SGR) and grain boundary migration (GBM) recrystallization (*Fig. 3.4g-l*). Upward, along the MCTz, quartz grain size increases, and lobate and interconnected grain boundaries, undulose extinction and unimodal grain size distributions support GBM type I mechanisms (GBM_I) (*Fig. 3.4g, h, j*, Kruhl, 1996; Passchier and Trouw, 2005; Law, 2014). At the top of the section, in samples MA16-102 (*Fig. 3.4f*) and samples MA16-101 (LHS-protolith affinity), coarse-grained quartz crystals evolve with overpinning microstructures. In the upper and lower dolomitic marbles layers belonging to the LHS top, dolomite is the dominant mineralogical weak phase (e.g. *Fig. 3.4a-e*). Dolomite crystals are strongly recrystallized, with straight grain boundaries, unimodal grain size distribution and a shape preferred orientation defining south-directed oblique foliations (Sb) (*Fig. 3.4a, c*). Rare twins are recorded in dolomite (e.g. *Fig. 3.4c*). Dolomite microstructures show concomitant operation of GBM recrystallization and grain boundary sliding developed during the MCTz shearing (Leiss and Barber, 1999; Holyoke III et al., 2013; Wells et al., 2019). By adopting the oblique foliation-based method of Wallis (1995), in two dolomitic marbles (*Table 3.1, par. 2.2.2*), angles of 25°-22° ±2° correspond to sectional kinematic vorticity, Wn, between 0.64-0.81 (samples MA16-17 and MA16-19).

3.1.2. Texture analyses – MCTz (Budhi Gandaki and Marsyandi valleys)

Quartz and dolomite texture analyses were conducted on twelve field-oriented samples (*Table 3.1, Fig. 3.4*). Six quartz-bearing paragneiss and quartzite were selected for analyzing quartz [*c*]-axis orientation in different domains (by using the G60 crystal Fabric analyser). Furthermore, ten samples were investigated trough the X-ray Texture Goniometer to obtain the full quartz and dolomite fabric. Quartz and dolomite texture of most of the analyzed samples are shown in *Fig. 3.5*, *Fig. 3.6*, and *Fig. 3.7*, described from lower to higher structural levels. From bottom to top, quartz pole figures show well-defined textures, with almost orthorhombic (symmetric) patterns (*Fig. 3.5, Fig. 3.6, Fig. 3.7*). From ODF recalculation, quartz CPOs strength, expressed by the J-index (or texture index) of Bunge (1982), is relatively low within all samples using the XTG (*par. 2.2*), being of 1.10-1.29 (with the exclusion of sample MA16-102, J-index= 2.91). Low CPO intensity is also confirmed by the M-index of Skemer et al. (2005), being M=0.03 (a total random crystallographic orientation distribution is for M=0, see Skemer et al., 2005). Sample MA16-01 (Kuncha Fm., LHS, *Fig. 3.3, Fig. 3.4k*) has quartz [*c*]-axis maxima in the Y-direction of the strain ellipsoid (normal to the XZ plane) (*Fig. 3.6e*). This pattern is usually interpreted as the result of quartz intracrystalline deformation, accommodated in plane strain regime by the slip of prismatic {*m*}-planes $\{10\bar{1}0\}$ through vector direction parallel to the crystallographic quartz <*a*>-axes $<11\bar{2}0>$ (Schmid and Casey, 1986; see Passchier and Trouw, 2005; Toy et al., 2008 for reviews on lattice preferred orientation and slip systems development). Therefore, a contribution of $\{10\bar{1}0\}<11\bar{2}0>$ (prism <*a*> slip system) occurs (*Fig. 3.6e*).

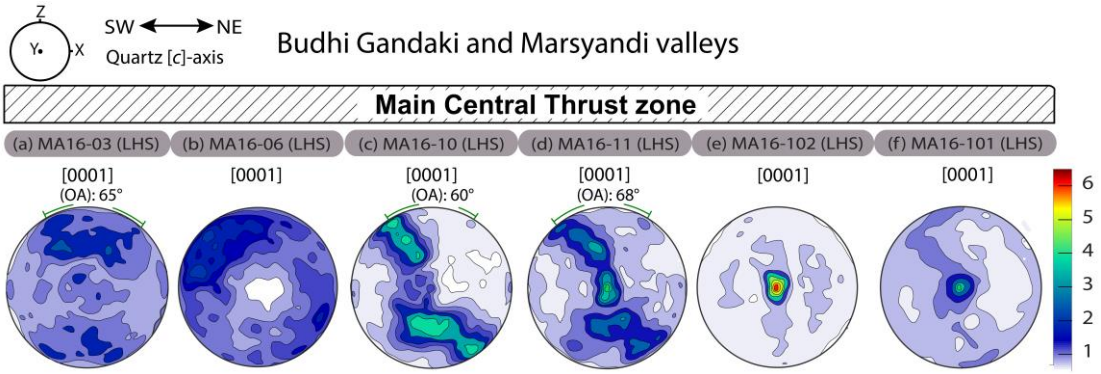

Figure 3. 5. *Quartz [c]-axis pole figures (equal area projection, lower hemisphere) of the analyzed samples deformed within the MCTz in the lower Budhi Gandaki and Marsyandi valleys (textures acquired through the G60 crystal fabric analyser, Georg-August University). Contours represent multiples of a uniform distribution. Samples are listed according to their structural levels (see* Fig. 3.4*). Pole figures view towards the west on projection plane, referred to the foliation pole (Z) and mineral lineation (X).*

Analysis through the XTG and the FA on sample MA16-03 (Kuncha Fm., LHS, *Fig. 3.4l*) provided different texture patterns (*Fig. 3.5a, Fig. 3.6d*), with quartz [*c*]-axis patterns from both processed pole figures showing strong maxima close to the Y-direction and the Z-direction of the finite strain ellipsoid (*Fig. 3.5a, Fig. 3.6d*). These maxima can be associated with the coupled activity of prism <*a*> slip system and the basal plane (0001) slip through the vector direction parallel to the <*a*>-*ax*es trend (Passchier and Trouw, 2005; Toy et al., 2008). Coupled activities of these slip systems, with slip direction parallel to the <*a*>-*ax*es trend, are consistent with crossed girdle type I pattern for the quartz [*c*]-axes in sample MA16-03 (Schmid and Casey, 1986; Kruhl, 1998; Toy et al., 2008; Faleiros et al., 2016). This pattern is consistent with the <*a*>-*ax*es pole figure (<11$\bar{2}$0>) and with the {*m*}- and {*r*}-planes pole figure (pole to {10$\bar{1}$0} and pole to {10$\bar{1}$1} planes), which show the strongest contribution of the rhomb <*a*> slip system. The Burger vector, defined by the strongest <*a*>-*ax*es maxima in <11$\bar{2}$0>, is subparallel to the lineation trend (*Fig. 3.6d*).

In sample MA16-06 (LHS, *Fig. 3.4i*), quartz texture has a slightly lower CPO (M=0.02), with asymmetric patterns. Quartz [*c*]-axis distributions acquired through both the XTG and the FA instruments (*Fig. 3.5b, Fig. 3.6c*) show strong maxima between the X- and Z-directions. Maxima trend is toward the south, supporting basal<*a*> slip (*Fig. 3.5b, Fig. 3.6c*). From the pole figures recalculated by the ODF (*Fig. 3.6c*), <*a*>-*ax*es maxima, with a couple in peripheric position, {*m*}-planes maxima and no rhombic strong maxima show the (0001)<11$\bar{2}$0> slip (basal<a> slip system). It is worth noting that [*c*]-axis maxima are very strongly southward rotated, as also <*a*>-*ax*es and {*m*}-planes maxima (close to the Z-direction, at almost 70° from the lineation trend). Upward, texture analysis with the G60 crystal Fabric analyzer and the XTG on the massive quartzites MA16-10 (*Fig. 3.5c*) and MA16-11 (*Fig. 3.5d; Fig. 3.6b*) show stronger quartz textures (M=0.08) and incomplete crossed girdle patterns, with auxiliary maxima close to the X-direction (*Fig. 3.5c*). Sinistral shear sense (geographically, top-to-the-south sense of shear) is indicated for both samples by the asymmetries of the [*c*]-axis fabric skeletons and by the strong leading edges. These patterns are confirmed for sample MA16-11 (*Fig. 3.5d; Fig. 3.6b*) by the peripheral <*a*>-*ax*es (in (<11$\bar{2}$0> pole figure) and {*m*}-planes (in {10$\bar{1}$0} pole figure) maxima, and by the strong rhombic maxima (poles to {10$\bar{1}$1}, or {*r*}-planes, and poles to {01$\bar{1}$1}, or {*z*}-planes).

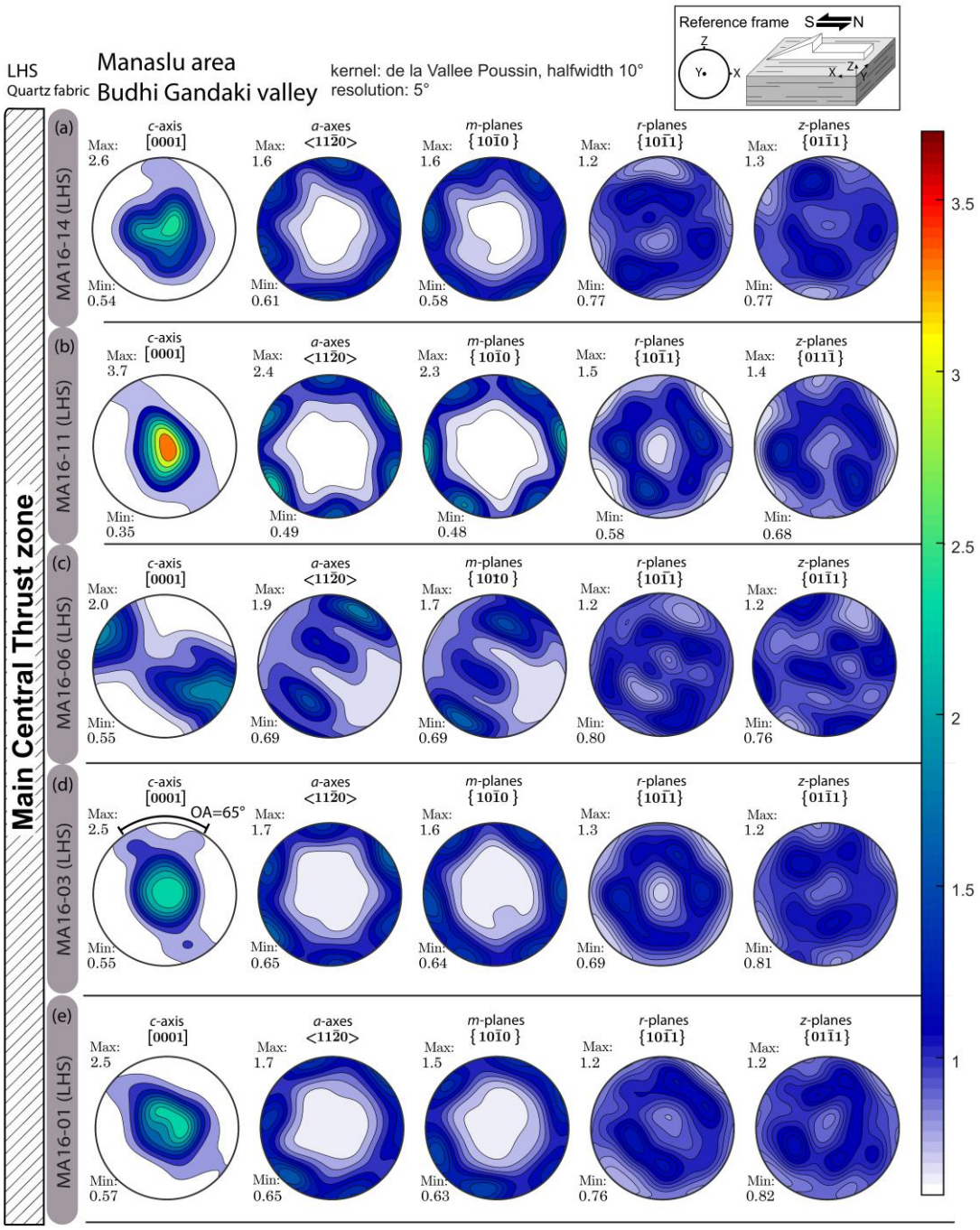

Figure 3. 6. *Quartz texture (from X-ray texture goniometer, XTG, analysis) displayed for the main crystallographic directions in pole figures (equal area projection, lower hemisphere). Contours represent multiples of a uniform distribution. Pole figures view towards the west on projection plane, referred to the foliation pole (Z) and mineral lineation (X). Samples from the LHS-protholith, are listed from the structural top to the bottom (see* Fig. 3.4 *for sample structural level).*

The compositionally and structurally heterogeneous quartz-bearing paragneiss MA16-14 (*Fig. 3.4h*) has no clear texture from the G60 crystal fabric microanalyzer. Nevertheless, full quartz texture, acquired by the XTG, indicate low CPO intensity (M=0.03) and Y-max pattern (*Fig. 3.6a*). At higher structural levels within the MCTz, pole figures of samples MA16-16, MA16-17, MA16-19, and MA16-20 (LHS-protolith affinity) show a well-developed dolomite texture (*Fig. 3.7a-e*) and a very low CPO intensity (M=0.01-0.03). The [*c*]-axis distributions define girdles normal to the shear direction, with strong peripheral maxima close to the Z-direction.

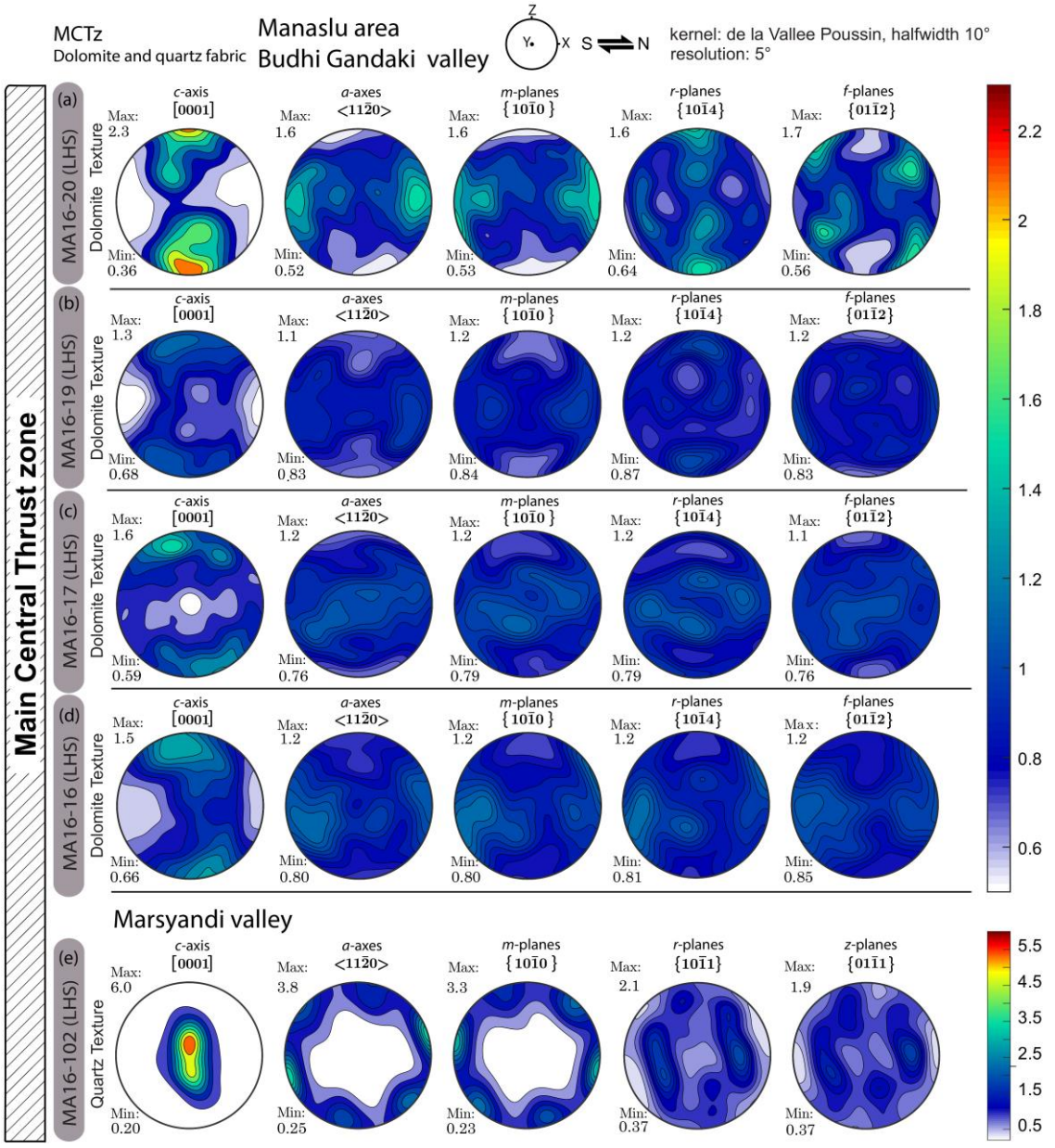

Figure 3.7. *Dolomite (a-d) and quartz (e) texture (XTG analysis) displayed for the main crystallographic directions (equal area projection, lower hemisphere). Contours represent multiples of a uniform distribution. Pole figures view towards the west on projection plane, referred to the foliation pole (Z) and mineral lineation (X). Samples are listed from top to bottom (see Fig. 3.3 for the structural level associated to each sample). Further details are in the main text.*

Subtle sinistral asymmetries indicate that dolomite textures developed during the top-to-the-south shearing of the MCTz in dislocation creep regime (Leiss and Barber, 1999; Delle Piane et al., 2008; Wells et al., 2019). In the uppermost sample, strong *r*- and *f*-maxima (on {10$\bar{1}$4} and {01$\bar{1}$2} pole figures, respectively) show the contribution of {*f*} slip.

Texture analysis on the Tur-rich quartzites MA16-102 (*Fig. 3.5f, Fig. 3.7c*) and MA16-101 (*Fig. 3.5g*) show well-developed and intense CPO (M=0.2). Single girdle [*c*]-axis distributions for both samples have sinistral asymmetry, consistent with the top-to-the-south shearing of the MCTz (see also Passchier and Trouw, 2005 and Law, 2014 for reviews). Strong [*c*]-axis maxima in the Y-direction (on the [0001] pole figure) support an important contribution of the prism<*a*> slip, shown by the full texture pattern of sample MA16-102 in *Fig. 3.7c*.

3.1.3. Temperature estimation – MCTz (Budhi Gandaki, Marsyandi valleys)

Deformation temperatures were estimated through the Faleiros et al. (2016) opening angle method (see also Krhul, 1998; Morgan and Law, 2004, *par. 2.2.1, Fig. 3.8a*). On [0001] quartz [*c*]-axis pole figure of sample MA16-03 (*Fig. 3.5a, Fig. 3.6d*), basal<*a*> maxima of the crossed girdle type I of the quartz [*c*]-axes defines an opening angle (OA), which is the angle measurable in the pole figures between the basal maxima (*Fig. 3.8b*). In sample MA16-03 (*Fig. 3.8b*), a small opening-angle of 60-65° (i.e. 63°) can be measured (Schmid and Casey, 1986; Kruhl, 1998; Toy et al., 2008; Faleiros et al., 2016, *Fig. 3.8b*). An opening angle of ca. 60-70° for the [*c*]-axis distribution on [0001] (60° for sample MA16-10 and 68° for sample MA16-11, *Fig. 3.8b*) corresponds to a deformation temperature of ~460-520 °C (*Fig. 3.8*).

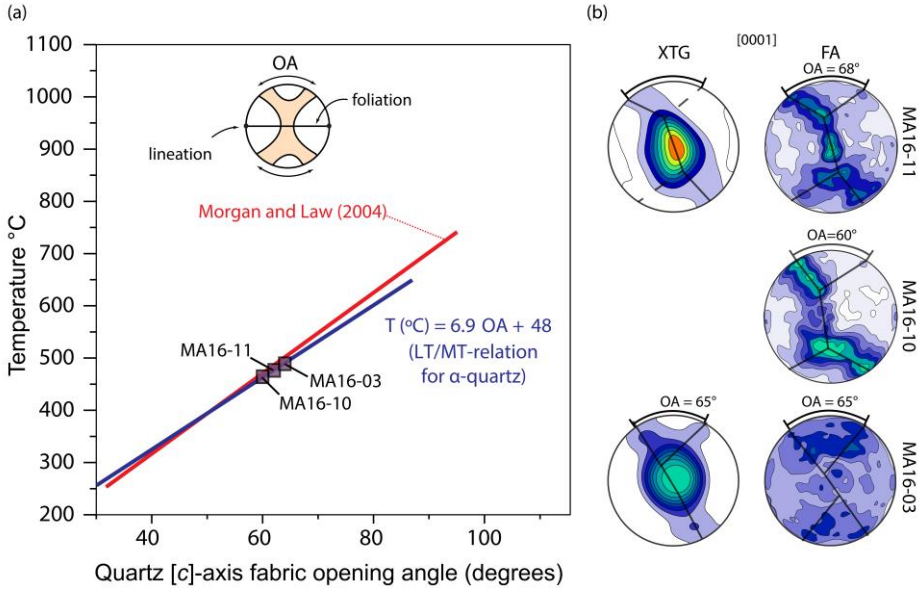

Figure 3.8. ***(a)*** *Quartz fabric opening-angle (OA)–temperature diagram, presenting the linear fits described by Morgan and Law (2004) and Faleiros et al., 2016. Purple squares correspond to the* ***(b)*** *quartz [c]-axis pole figures of samples investigated by the XTG, X-ray Texture Goniometer, and the FA, fabric analyzer (see Fig.3.5 and Fig. 3.6 for full fabric). Note that, even if fabric analysis from XTG and FA on MA16-03 provided different patterns, the automated script for the FA output and the manual detection for XTG output gave the same OA from [c]-axis maxima on the Z-direction.*

3.2. The South Tibetan Detachment System in the Budhi Gandaki and Marsyandi valleys

Microstructural analysis was carried out on samples from two N-S transects in the upper Budhi Gandaki valley and in the upper Marsyandi valley where, from lower to higher structural levels, the Chame Detachment (CD) and the STDS in *sensu stricto* occur.

The Chame Detachment in the Marsyandi valley affects the amphibolite facies rocks of the GHS_U, i.e. calc-silicate bearing marble and orthogneiss of the GHS II unit and migmatitic orthogneiss of the GHS III unit (*Table 3.2*), intruded by cm- to- m-thick leucocratic bodies (*Fig. 3.1, Fig. 3.9a, b*). The main foliation, corresponding to the S2 (e.g. Colchen et al., 1986; Walters and Kohn, 2017) dips toward the NW-SW and strikes toward N40° (*Fig. 3.9a*). Mineral lineation (defined by biotite and sillimanite or quartz) in the orthogneiss and in the deformed leucogranite (GHS III) gently plunges toward the W-NW (*Fig. 3.9a*, Coleman, 1996; Walters and Kohn, 2017). The main sense of shear, recorded through S-C-C' fabric (*Fig. 3.10a*) and feldspar sigma and delta porphyroclasts (*Fig. 3.10b*) at the outcrop scale, point a top-down-to-the-north/northwest shear.

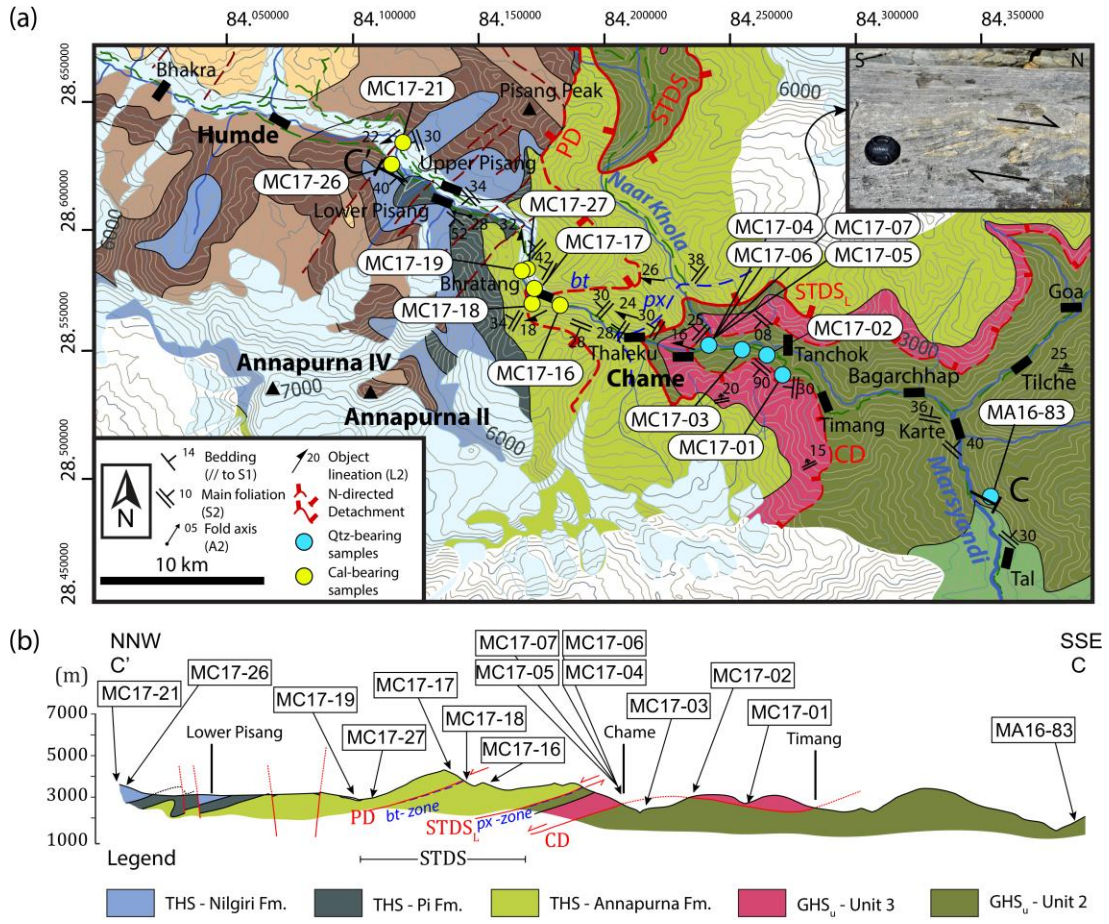

Figure 3. 9. (a) *Zoom of the geological sketch map of the upper Marsyandi valley (see Fig. 3.1). Example of S-C fabric.* ***(b)*** *Geological cross section of C-C' trace of Fig. 3.1 and study samples from the Chame Detachment and the STDS.*

At higher structural levels, the STDS in sensu stricto crops out in both valleys at the Annapurna Fm. (THS) base. The main foliation, S2, strikes parallel to the STDS, dipping toward the northwest, whereas object lineation L2 plunges toward the west-northwest. North-verging km-scale folds have south/southeast dipping axial planes (Searle, 2010, see also Parsons et al., 2016b). NE-SW striking normal faults, within the THS (*Fig. 3.9*), have been related to the late Miocene/Plio-Pleistocene extension linked to the Thakkhola graben toward the west (Hurtado et al., 2001).

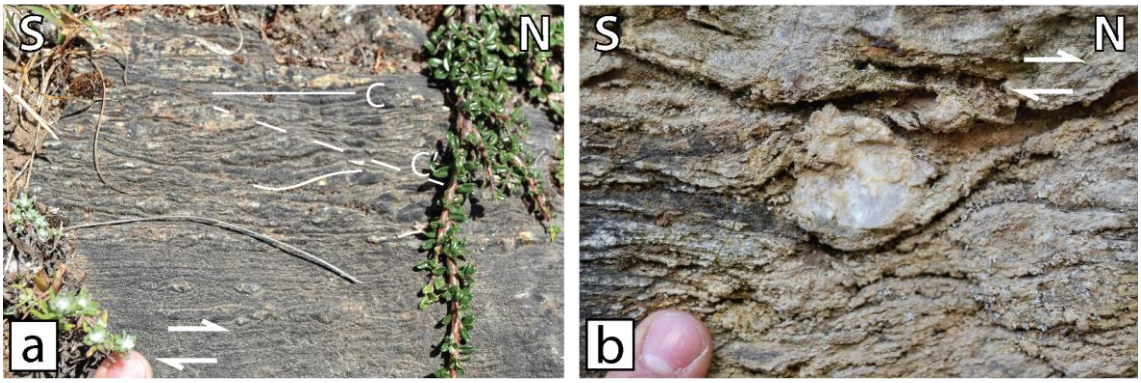

Figure 3. 10. *Photographs of Chame Detachment outcrops in the Marsyandi valley showing kinematic indicators coherent with a top-to-the-north shear (credits: Carosi, R., Iaccarino, S., Simonetti, M. field expedition, A.A. 2017).* ***(a)*** *Calc-mylonite with S-C-C' fabric sense of shear.* ***(b)*** *δ-type clast within calc-mylonite.*

***Table 3.2**. Summary for the STDS (included Phu Detachment, PD and the Chame Detachment (CD) samples (Budhi Gandaki and Marsyandi valleys). Abbreviations: Ap – apatite; Bt – biotite; Cal – calcite; Chl – chlorite; Dol – dolomite; Feld – feldspar; Grt – garnet; Kfs – K-feldspar; Mc – microcline; Mnz – monazite; Pl – plagioclase; Qtz – quartz; Wm – white mica; Rt – rutile; Spd – spodumene; Tur – tourmaline; Ttn – titanite; Zr – zircon; HHL – High Himalayan Leucogranite; BLG – bulging; GBM – grain boundary migration; GBS – grain boundary sliding; SGR – subgrain rotation recrystallization.*

	Sample	Formation	Mineral Assemblage	Lithotype	Fabric and deformation m.	Analysis
Budhi Gandaki valley (STDS)	MA16-54	THS (PI Fm. – Black shale)	Cal+Bt+Qtz	Marble	Cal: GBM + Twin Type II	◔
	MA16-51	THS (PI Fm. – Black shale)	Cal+Bt+Qtz	Marble	Cal: GBM + BLG + Twin Type II	◔
	MA16-44	THS (PI Fm. – Black shale)	Cal(+Dol)+Bt+Tur+Qtz+Pl+ Wm	Impure marble	S2 (Bt+Cal). Cal: GBM + Twin Type II	◔
	MA16-43	THS (Annapurna Fm.)	Cal+Qtz+Bt+Wm+Chl+feld+ Py	Impure marble	S2 (Bt+Cal). Cal: SGR/GBM + Twin Type II	◔
	MA16-47	THS (Annapurna Fm.)	Cal+Qtz+Bt+Tur+Pl+Spd+Kfs	Impure marble	Pervasive S2 (Bt). Cal: GBM + annealing	◕
	MA16-46	High Himalaya Leucogranite	Qtz+Pl+Mc+Tur+Bt+Spd+ Wm	Microgranite	S2 (Wm). Qtz: GBM/SGR + BLG. Pl: ductile deformation	◔
	MA16-41	High Himalaya Leucogranite	Qtz+Mc+Pl+Wm+Bt+Tur+Zr+ Ap+ Mnz	Tur-leucogranite	S2 (Bt). Qtz: GBM+BLG. Kfs graphic structure and myrmekite	◔
	MA16-38	GHS_U (Unit 3)	Qtz+fs+Bt+Wm+Ap	Augen orthogneiss	S2 (Bt). Qtz: GBM and brittle fracturing. Kfeld: myrmekites	◔
Marsyandi valley (PD)	MC17-21	THS (Nilgiri Fm.)	Cal+Bt+Wm	Marble	S2 (Cal SPO ± Bt ± Wm). Cal: GBM + BLG	◔
	MC17-26	THS (Nilgiri Fm.)	Cal+Dol+Qtz+Pl	Marble	S2 (Cal SPO ± Bt ± Wm). Cal: GBM + BLG	◔
	MC17-27	THS (Annapurna Fm.)	Cal+Qtz+Dol+Bt+Wm	Marble	S2 (Cal SPO ± Bt ± Wm). Cal: GBM + Twin type II	◕
	MC17-19	THS (Annapurna Fm.)	Cal+Dol+Qtz+Wm+Bt+Pl+Ttn	Marble	S2 (Cal SPO ± Bt ± Wm). Cal: GBM + Twin type II	◕
	MC17-17	THS (Annapurna Fm.)	Cal+Dol+Qtz+Bt+Zr+Ttn	Marble	S2 (Cal SPO ± Bt). Cal: GBM + Twin type II	◕
	MC17-18	THS (Annapurna Fm.)	Cal+Dol+Qtz+Bt+Wm+Ttn	Marble	S2 (Cal SPO ± Bt ± Wm). Cal: GBM + Twin type II	◔
	MC17-16	THS (Annapurna Fm.)	Cal+Dol+Qtz+Pl+Bt+Wm+Ttn +Zr	Impure marble	S2 (Bt+Cal SPO). Cal: GBM/GBS + Twin type II	◔
Marsyandi valley (CD)	MC17-07	GHS_U (HHL)	Qtz+Pl+Bt+Wm+Tur+Ap+Zr+ Py± Mnz	Tur-bearing leucogranite	S2 (Bt). Qtz: GBM/GBS	◕
	MC17-06	GHS_U (Unit 3)	Qtz+Pl+Bt+Wm+Tur+Zrn+ Ttn	Tur-bearing leucogranite	S2 (Bt + Wm). CS fabric top-to-the-N. Qtz: GBM II/GBS. Pl: tapered twins	◕
	MC17-05	GHS_U (Unit 3)	Qtz+Pl+Wm+Chl+py+Zr±Mnz +Ttn	Orthogneiss	S2 (Bt + Wm) ± CS fabric top-to-the-N. Qtz: GBM II. Pl: mechanic twins	◕
	MC17-04	GHS_U (Unit 3)	Qtz+Bt+Wm+Pl+Tur+Zr	Migmatitic orthogneiss	S2 (Bt + Sill). Qtz: GBM + annealing	◒
	MC17-02	GHS_U (Unit 3)	Qtz+Mc+Pl+Bt+Grt+Ap+Zr	Migmatitic orthogneiss	S2 (Bt). Qtz: GBM. Pl: myrmekite	◕
	MC17-01	GHS_U (Unit 3)	Qtz+Mc+Pl+Bt+Wm+Grt+Chl +Zr+ Mnz	Migmatitic orthogneiss	S2 (Bt + Wm). Qtz: GBM. Kfeld: myrmekites, pertites. Pl: mechanic twin	◕
	MC17-03	GHS_U (Unit 2)	Qtz+Bt+Tur+Hbl+Mc+Pl+Ttn	Bt-Hbl gneiss	S2 (Bt + Sill + Hbl). Qtz: GBM/GBS. feld: myrmekite	◒
	MA16-83	GHS_U (Unit 2)	Qtz+Cal+Pl+Mc+Cpx+Hbl+Bt +Scp+ Ttn+Mnz+Chl	Bt-Hbl gneiss	Qtz: GBM + annealing. Pl: tapering twinning and myrmekite.	◔

Legend: ◔ Texture analysis (XTG); ◒ Texture analysis (FA); ◐ Kinematic vorticity analysis; ◎ Paleopiezometry

3.2.1. Microstructural analysis of the Chame Detachment

From bottom to top, eight field-oriented samples belong to the Bt-Hbl gneiss (GHS_U, Unit 2), orthogneiss, migmatite (GHS_U, Unit 3) and to Tur-bearing leucogranite (e.g. MC17-06, MC17-07) intruding Unit 3 (*Table 3.2, Fig. 3.11a-h*). Bt-Hbl gneiss (GHS_U, Unit 2) have a main mineral assemblage of Qtz + Bt + Hbl + Mc + Pl + Ttn, with minor Cal ± Chl ± Scp (*Table 3.2*). Orthogneiss and migmatite (GHS_U, Unit 3) have a main mineral assemblage defined by Qtz + Mc + Pl + Bt + Wm ± Grt ± Ttn ± Chl (*Table 3.2*). Tur-bearing leucogranite, intruding Unit 3, has a mineral assemblage defined by Qtz + Pl + Bt + Wm + Tur + Zrn + Ttn (*Table 3.2*).

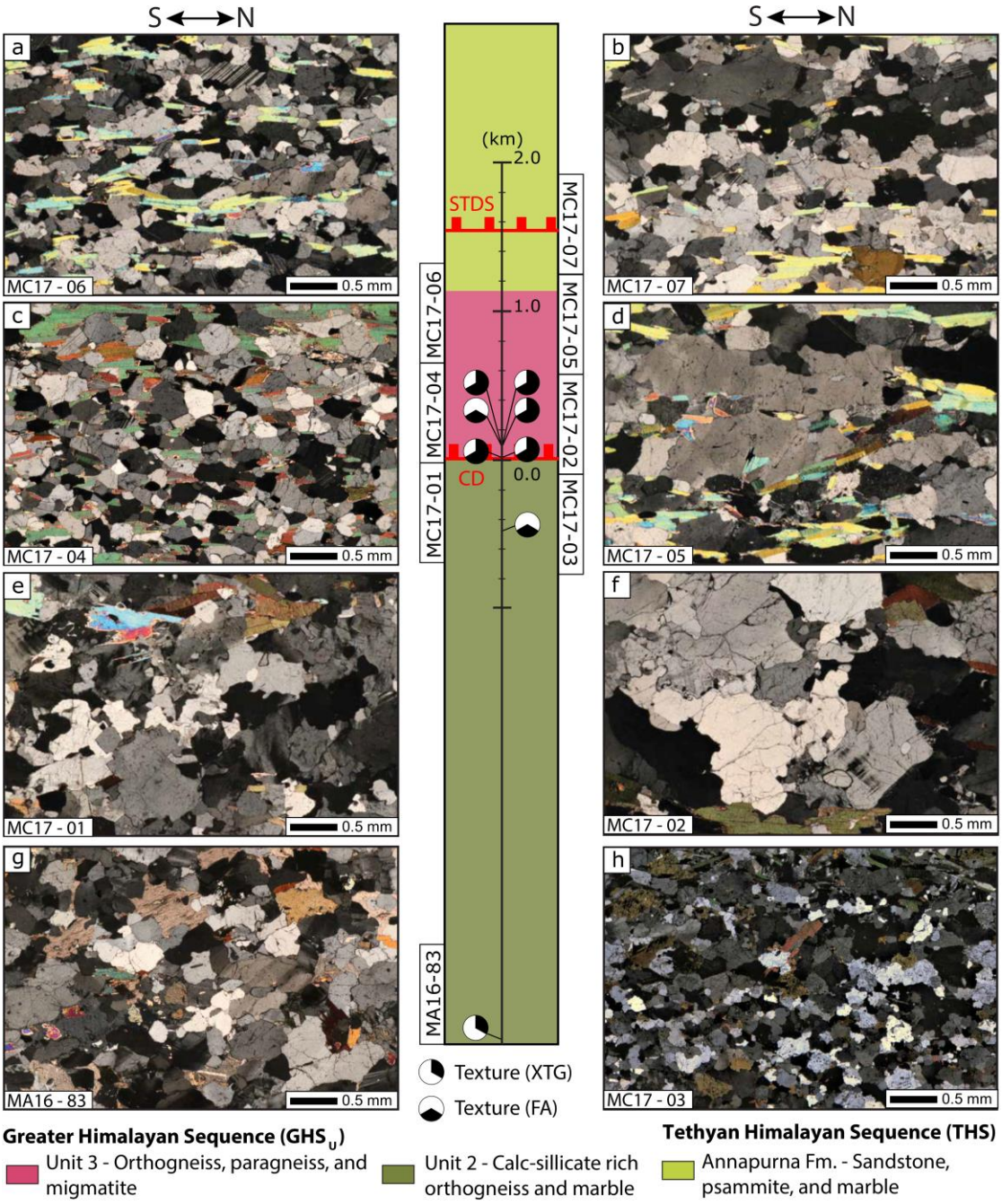

Figure 3. 11. *Optical micrographs of the samples selected to define the Chame Detachment in the upper Marsyandi valley. Samples are listed from top to bottom. Sample location on the structural section is displayed by dots. Scale in the middle corresponds to vertical thickness in kilometers. Texture (XTG) – samples analysed for quartz texture through an X-ray texture goniometer; Texture (FA) – samples analysed for quartz texture by a crystal-fabric microanalyser.*

Rough spaced parallel S2 foliation is marked by white mica (*Fig. 3.11a, b, d*) and biotite (*Fig. 3.11c, e, f*). Samples are only weakly foliated and, in the Bt-Hbl gneiss, calc-silicates are almost unoriented (*Fig. 3.11g, h*). At sample scale, few kinematic indicators occur, as S-C fabric (*Fig. 3.11d*) showing top-to-the-north sense of shear.
Quartz is plastically deformed, with lobate grain boundaries and deformation bands (*Fig. 3.11a-d, g-h*). Coupled with unimodal grain size distributions, microstructures indicate that quartz deformed in the GBM regime (*Fig. 3.11a- h, Table 3.2*). Plagioclase and microcline are plastically deformed, with mechanic and tapered twins, and undulose extinction (*Fig. 3.11a, b*). Myrmekite and pertite structures in feldspars occur (*Fig. 3.11e, f*).

3.2.2. Texture analysis of the Chame Detachment

Quartz texture analysis was carried out through both the G60+ automated crystal fabric analyzer (FA) (*Fig. 3.12a-g*) and the X-ray Texture Goniometer (XTG) (*Fig. 3.13a-f*). Quartz CPO intensity is quite low (M-index=0.01); however, all samples have well-defined textures. From bottom to top, the [*c*]-axis pole figure of sample MA16-83 (GHS II, *Fig. 3.11g*), investigated by the XTG (*Fig. 3.13f*), shows a type I crossed girdle pattern linked to the mixing of basal <*a*>, rhomb <*a*> and prism <*a*> slip (see Toy et al., 2008). The full texture is asymmetrically rotated. An opening angle of ca. 73° indicates deformation temperatures of ca. 550 °C (Faleiros et al., 2016).

At the GHS II/GHS III boundary, sample MC17-03 (*Fig. 3.11h*) was investigated through the crystal fabric analyzer (*Fig. 3.12a*). A weak CPO is defined by the peripheral distribution of the [*c*]-axis and by a maximum in the Y-direction.

Above, samples MC17-01 and MC17-02 (GHS III, *Fig. 3.11e, f*), close to Chame village, were studied with both analytical techniques (*Fig. 3.12b, c; Fig. 3.13d, e*). Well-developed quartz [*c*]-axis CPOs are consistent with type I crossed girdles (*Fig. 3.12b, c; Fig. 3.13d, e*). Asymmetric patterns are rotated toward the right, showing top-to-the-north non-coaxial deformation (*Fig. 3.12b, c; Fig. 3.13d, e*). A wide opening angle fabric (of 86.5° and 82.5°) indicates deformation temperatures of 620-645 °C.

Orthogneiss MC17-04 (*Fig. 3.11c*) was analyzed through the crystal fabric analyzer (*Fig. 3.12d*). Wide weak peripheral [*c*]-axis maxima, close to the X-direction, show type II crossed/cleft girdle pattern (Schmid and Casey, 1986; Xypolias et al., 2013). Maxima have dextral asymmetries, showing top-to-the-north shearing. A very-wide opening angle of 93.0° supports deformation temperatures of 685 °C (with the HT-relations of Faleiros et al., 2016, see *par. 2.2.1*).

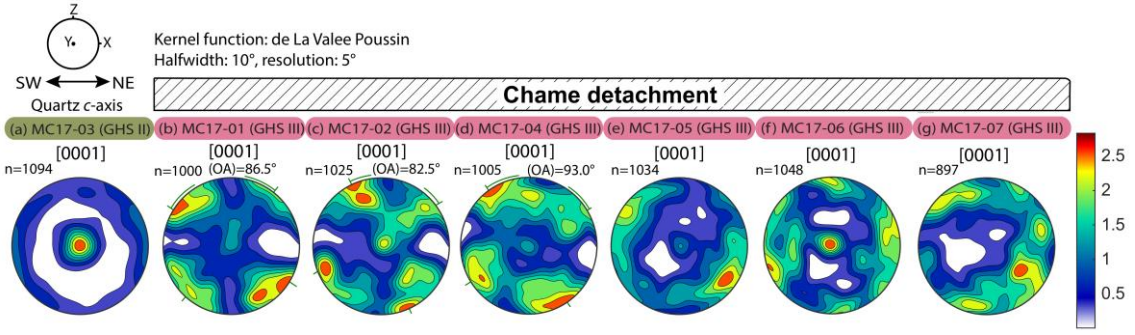

Figure 3. 12. *Quartz [c]-axis pole figures (equal area projection, lower hemisphere) from Chame Detachment in the upper Marsyandi valley (textures acquired through the G60 crystal fabric analyser). Contours represent multiples of a uniform distribution (equals to 1.0). Pole figures view towards the west on projection plane, referred to the foliation pole (Z) and mineral lineation (X). Samples are listed, from left to right, from lower to higher structural levels. OA is the opening angle; N is the number of measured crystals. The green label indicates GHS II-related protolith, pink labels to GHS III-related protolith, as in* Fig. 3.9.

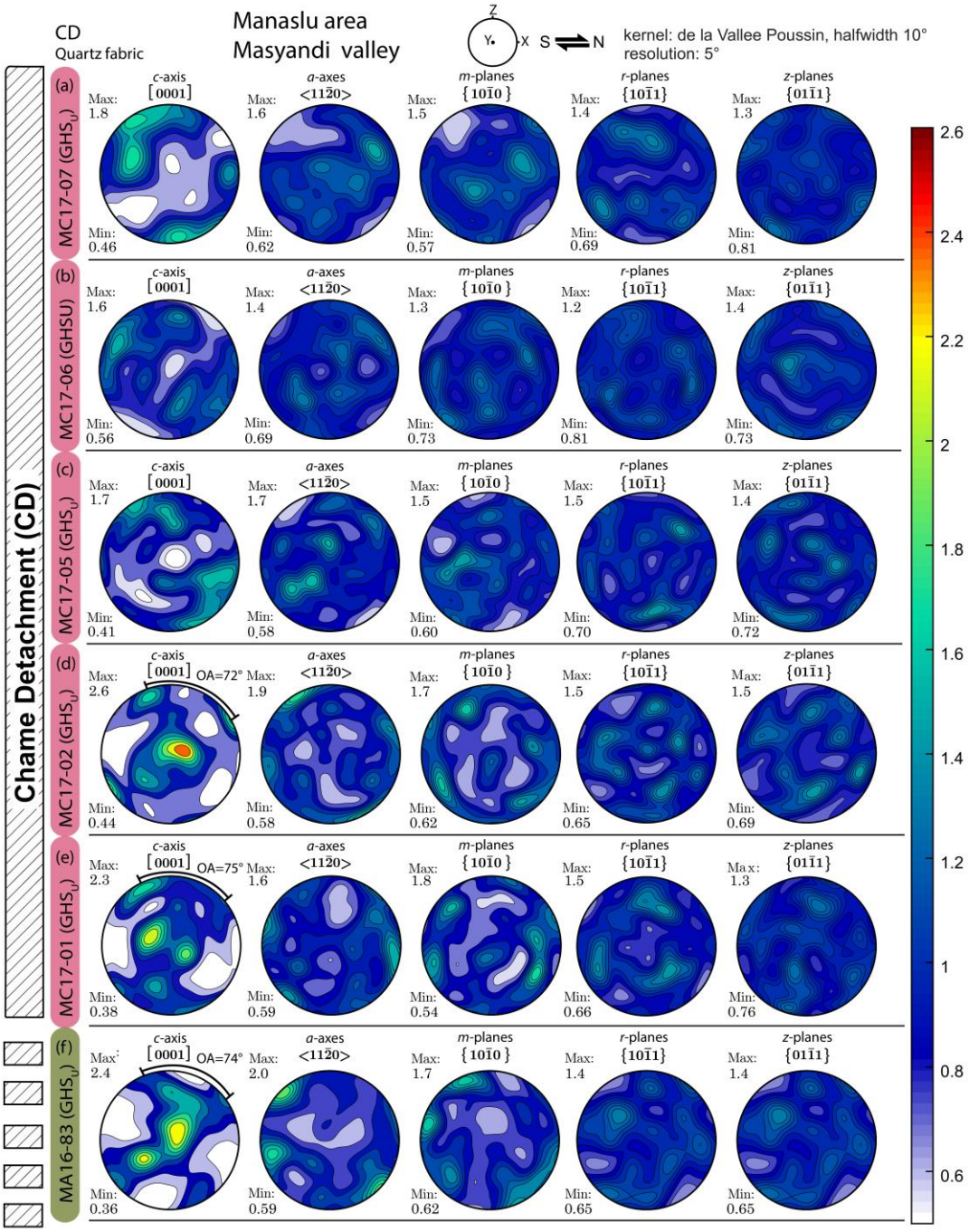

Figure 3. 13. *Quartz pole figures (XTG texture analysis) for the Chame Detachment, CD (equal area projection, lower hemisphere). Contours represent multiples of a uniform distribution. Pole figures view towards the west on projection plane. Samples are listed from top to bottom (see Fig. 3.9).*

Quartz textures in the Tur-bearing deformed granite (MC17-05, MC17-06, and MC17-07 *Fig. 3.11a, b,d*) were acquired by both the XTG and the FA (*Fig. 3.12e-g; Fig. 3.13a-c*). Comparing [*c*]- and <*a*>-*ax*es maxima (on [0001] and <11$\bar{2}$0> pole figures, respectively) with maxima on the prismatic {10$\bar{1}$0} and rhombic {10$\bar{1}$1}, {01$\bar{1}$1} planes, quartz textures are consistent with deformation through an HT-related prism<*c*> slip system (Mainprice et al., 1986). Texture sinistral asymmetry of [*c*]-axis maxima (close to the X-direction) shows top-to-the-north non-coaxial deformation (*Fig. 3.13a-c*). According to Mainprice et al. (1986), prism<*c*> slip typically occurs in quartz at temperatures above 650 °C.

3.2.3. Microstructural analysis of the STDS (Budhi Gandaki and Marsyandi valleys)

Microstructural analysis was performed on fifteen samples (eight samples from the upper Budhi Gandaki, seven samples from the upper Marsyandi, e.g. *Fig. 3.14a-d, Table 3.2*).

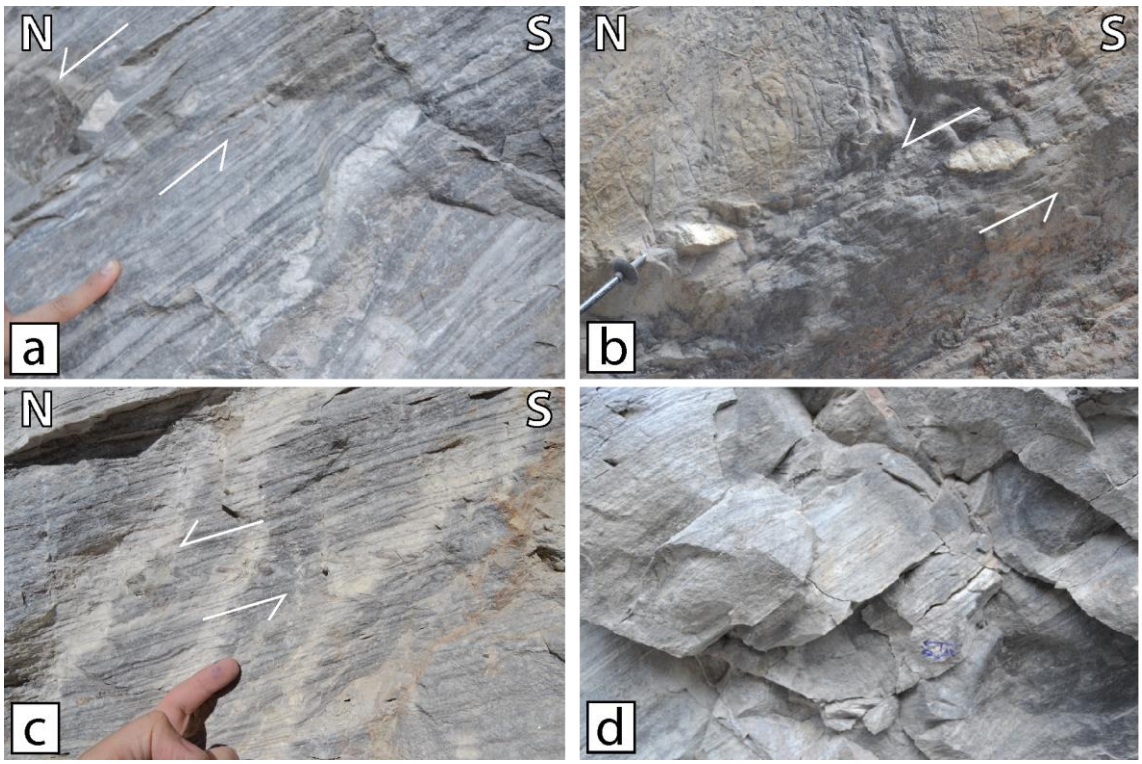

***Figure 3. 14**. Photographs of STDS outcrops in the Marsyandi valley (credits: Carosi, R., Iaccarino, S., Simonetti, M. field expedition, A.A. 2017). (**a**) Biotite marble (outcrop of MC17-19 sample), showing calcite asymmetric porphyroclasts consistent with a top-down-to-the-north sense of shear. (**b**) Asymmetric boudins in impure marbles, consistent with a top-down-to-the-north sense of shear. (**c**) Biotite marble (outcrop of MC17-17 sample), where asymmetric folds support the top-down-to-the-north sense of shear. (**d**) Biotite marble (outcrop of MC17-18 sample).*

UPPER BUDHI GANDAKI VALLEY

In the upper Budhi Gandaki, the study samples were (*Fig. 3.15 a, b*): calc-sillicate-bearing marble of the GHS II; migmatitic orthogneiss of GHS III; deformed Tur-bearing leucogranite of the HHL; biotite-marble from the Annapurna Fm. (THS); impure marble and black shale from the Pi Fm. (THS) (see *Fig. 3.16 a-h*); and the fine-grained marble of base of the Nilgiri Fm. (THS). At the microscale, samples show evidence of deformation and recrystallization in a ductile flow regime, whereas structures linked to fragile deformation (as fractures/veins, stylolites, etc.) lack. Within the GHS_U, the main mineral assemblage is defined by Qtz + Pl + Bt + Wm (*Table 3.2*). A weak rough S2 foliation is marked by biotite (*Fig. 3.16g*). Within the augen orthogneiss, MA16-38, quartz is the most abundant mineralogical phase (*Fig. 3.16g*); nevertheless, because of plagioclase and biotite crystals interpositions, few interconnected quartz aggregates occur. When crystals are quite interconnected, quartz has lobate grain boundaries, a unimodal distribution and undulose extinction. Feldspars have myrmekite structures (*Fig. 3.16g*). Two samples from the base and the top of the Manaslu intrusion (MA16-41 and MA16-46, respectively, *Fig. 3.16e, h*) have similar structures and amphibolite facies mineralogic composition, defined by Qtz + Pl + Mc + Tur + Bt + Wm (e.g. *Table 3.2*). A rough spaced S2 foliation is marked by medium-grained biotite and white micas (*Fig. 3.16e*).

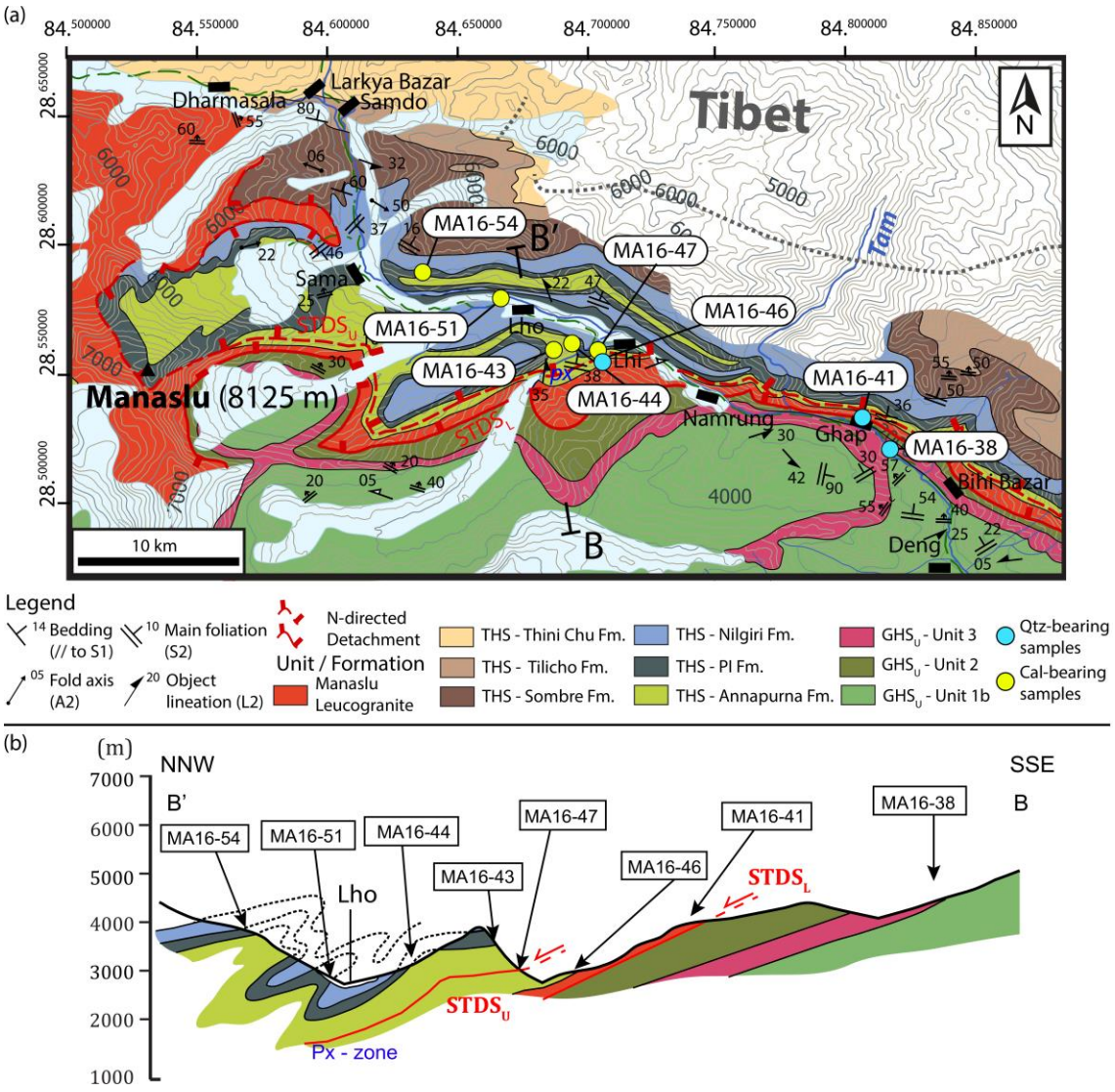

Figure 3. 15. (a) *Zoom of the geological sketch map of the upper Budhi Gandaki valley (see* Fig. 3.1 *for location).* ***(b)*** *Geological cross section of B-B' trace of* Fig. 3.1 *and study samples from the STDS.*

Quartz is quite interconnected, showing banded/undulose extinctions, small bulges and lobate grain boundaries. Plagioclase is plastically deformed and recrystallized with myrmekite structures (*Fig. 3.16e, h*). At higher structural levels, MA16-47 is a calc-silicate bearing impure marble of the Annapurna Fm. (THS) sampled close to the Manaslu pluton (*Fig. 3.15a*). A compositional alternation of carbonate-rich domains and very fine-grained quartz-feldspar domains is displayed (*Fig. 3.16f*). Within quartz-feldspar domains, a pervasive S2 foliation is marked by biotite, whereas in the carbonate-rich domain, calcite shape preferred orientation defines a dextral oblique foliation (*Fig. 3.16f*). Calcite is well-interconnected, has lobate grain boundaries, a unimodal grain size distribution and rare undulose extinction; moreover, undeformed type I and II twins (Burkhard, 1993; Ferrill et al., 2004) occur. Microstructures indicate that calcite was deformed plastically by grain boundary migration recrystallization and twinning (Schmid et al., 1987; Lafrance et al., 1994; Rutter, 1995; Barnhoorn et al., 2004; Rutter et al., 2007). Calcite dynamic recrystallization developed the oblique foliation, consistent with a top-to-the-north sense of shear. Minor clinopyroxene and tourmaline have skeletal shapes and are unoriented.

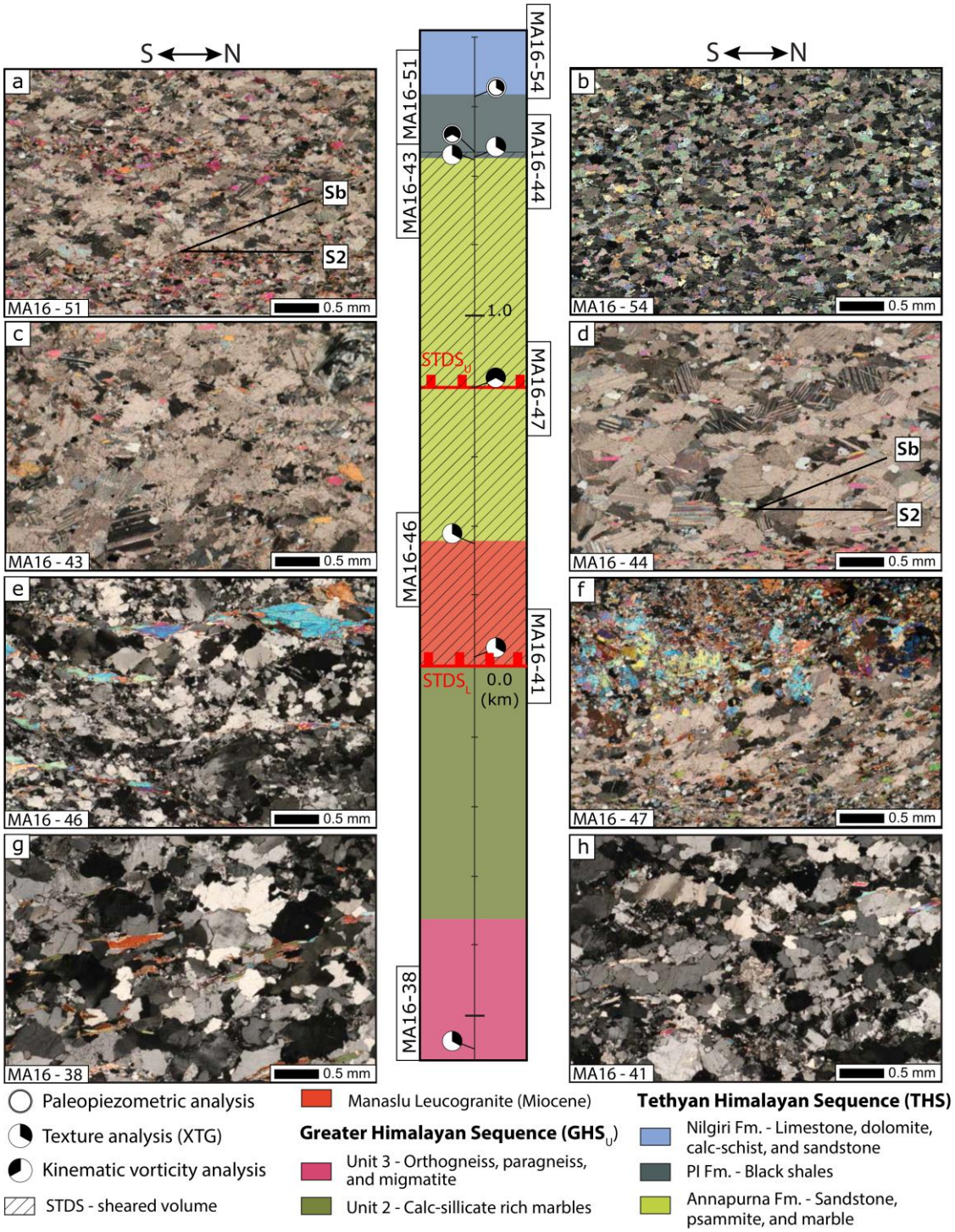

***Figure 3.16**. Optical micrographs of the orthogneiss, Tur-granite and marbles selected to define the STDS in the upper Budhi Gandaki valley. Samples are listed from top to bottom. Sample location on the structural section is displayed by the white dots. Scale in the middle corresponds to vertical thickness in kilometers. See text for further details.*

At much higher structural levels, samples MA16-43 and MA16-44 are greenschist facies impure marbles at the boundary between the Annapurna Fm. and the Pi Fm. belonging to the THS (*Fig. 3.15b*). Samples are constituted by Cal + Qtz + Bt + Wm + Pl + Chl (*Table 3.2*). The continuous foliation, S2, is marked by biotite and calcite (*Fig. 3.16c, d*). Calcite has a volumetric abundance over 95% of the total; moreover, crystals are well-interconnected with lobate grain boundaries,

have a unimodal grain size distribution and thick type II twins (*Fig. 3.16c, d*). Microstructures support the view that calcite suffered dynamic recrystallization in the GBM regime (*Table 3.2*). Moreover, this recrystallization developed the calcite shape preferred orientation that marks dextral oblique foliations.

The oblique foliation supports the idea that calcite deformed in a top-to-the-north non-coaxial regime. These microstructures can be recognized also for the uppermost samples, MA16-51 and MA16-54. Sample MA16-51 is a biotite- fine-grained marble (*Table 3.2*) defined by a simple mineral assemblage of Cal + Qtz + Bt. In this sample, calcite has a volumetric abundance over 98%, with a unimodal grain size distribution, lobate grain boundaries and type II twins. Calcite microstructures are still consistent with GBM dynamic recrystallization. Moreover, calcite displays a shape preferred orientation with long axis (calcite aspect ratio, AR=2) determining oblique foliations consistent with a top-to-the-north non-coaxial deformation. Quartz occurs in fine-grained rounded crystals (strong clast according to Handy, 1994) isolated in the carbonate weak matrix (*Fig. 3.16b*). At the top of the studied transect, MA16-54 (*Fig. 3.16a*) shows a calcite volumetric abundance over 75% of the total, with important portions where calcite has an abundance over 98%. However, calcite does not display shape preferred orientation and oblique foliations, and no kinematic indicators are present.

UPPER MARSYANDI VALLEY

Marble from the upper Marsyandi valley (*Fig. 3.17a-g*) shares very similar mineralogy and structures with the aforementioned Budhi Gandaki samples (*Table 3.2*). Five out of seven samples belong to different structural levels of the Annapurna Fm., whereas two uppermost samples (MC17-21 and MC17-26) are fine-grained marbles from the base of the Nilgiri Fm. (e.g. *Fig. 3.17a, b*). From bottom to top, MC17-16 is an impure marble defined by Cal + Dol + Qtz + Pl + Bt + Wm + Ttn (*Table 3.2*). Carbonate-rich domains are alternated with very fine-grained quartz-feldspar domains. A spaced foliation S2 is defined by the shape preferred orientation of biotite and calcite (*Fig. 3.17g*). Calcite has straight grain boundaries, a unimodal distribution and type II twins (*Fig. 3.17g*).

Above, samples MC17-17 and MC17-18 belong to the Annapurna Fm. core (*Fig. 3.9a*), close to the biotite-zone of Colchen et al. (1981, 1986), Schneider and Masch (1993), and Walters and Kohn (2017). Top-to-the-north kinematic indicators are represented by calcite grain oblique foliations. Interconnected calcite crystals have less than 1% of second-phase minerals (quartz and biotite). Calcite has lobate grain boundaries and a unimodal grain size distribution, indicating GBM dynamic recrystallization. Moreover, thick type II twins occur (*Fig. 3.17e, f*). In MC17-19 and MC17-27 (*Fig. 3.17c, d*), the mineral composition, calcite abundance and microstructures (as GBM in calcite and oblique foliations) are the same as described for the two lowermost samples (*Table 3.2*).

At the top, samples MC17-21 and MC17-26 are pure marbles from the Nilgiri Fm. (*Fig. 3.17a, b, Table 3.2*). Calcite has a very fine grain size; however, a grain shape preferred orientation defines the main S2 foliation. Rare twins are recorded in coarser grains (*Fig. 3.17a, b*).

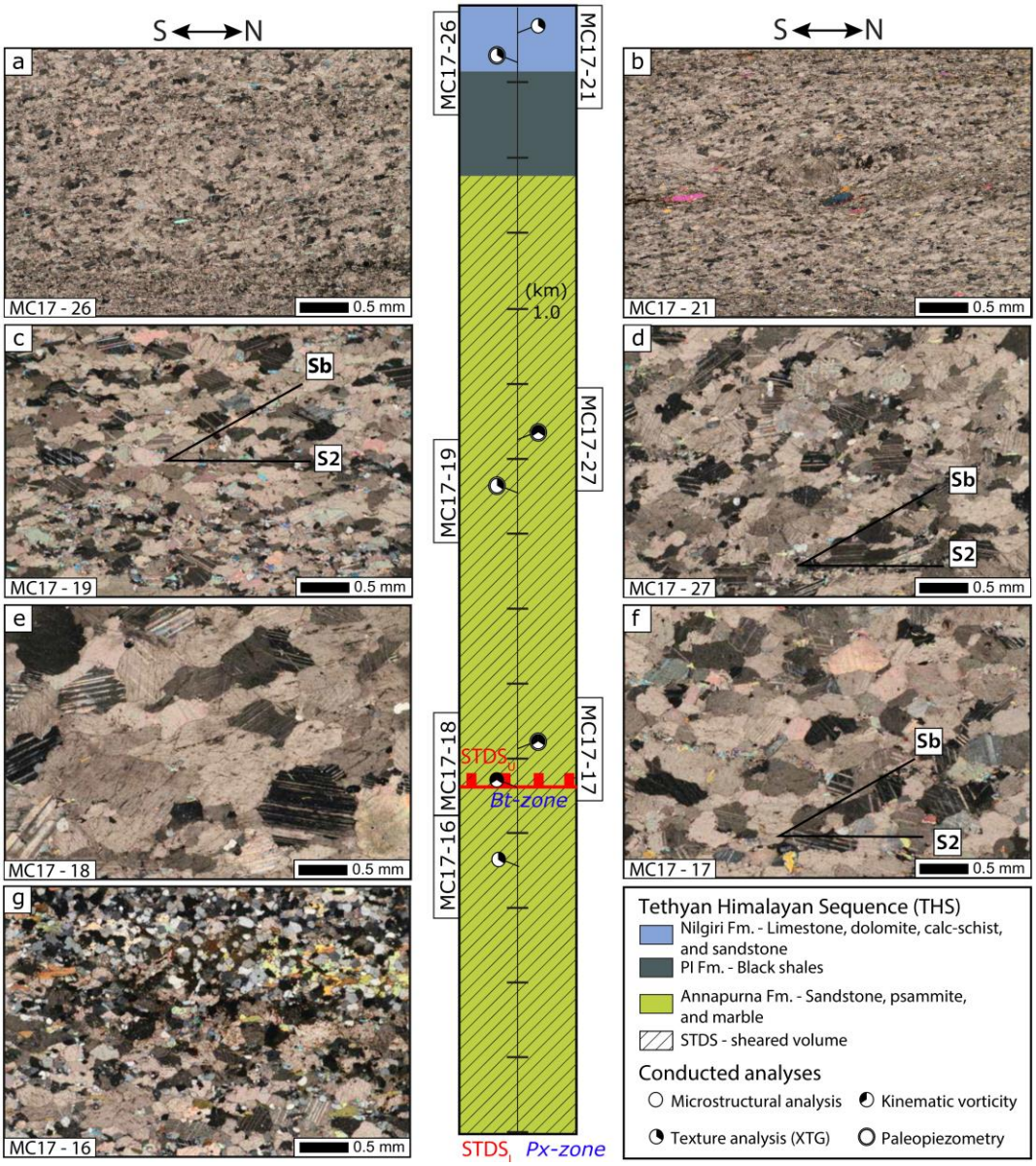

Figure 3. 17. *Optical micrographs of marbles selected to define the STDS in the upper Marsyandi valley. Samples are listed from top to bottom. Scale in the middle of the structural section corresponds to vertical thickness in kilometers. Sample location on the structural section is displayed by dots, following the legend on the bottom right. Kinematic indicators (as oblique foliations) support top-to-north shearing. See text for further details.*

3.2.4. Paleopiezometric analyses on marbles of the STDS

For six almost pure marbles from both valleys, stacked images of the full thin sections were used to distinguish subgrains and real grain boundaries of crystals through ImageJ software. Small portions of calcite grain size maps are reported in *Fig. 3.18*, and samples are listed from top to bottom (bigger areas of over 1000 clear and interconnected crystals per sample were analyzed for each sample; for an example of a full area, see *Fig. 2.2, par 2.1.1*). Grain size maps highlight that second-mineral phases (red particles in *Fig. 3.18*) are less than 2% of the analyzed area. The unimodal distribution of calcite in each sample is highlighted in *Fig. 3.18*, as well as lobate grain boundaries.

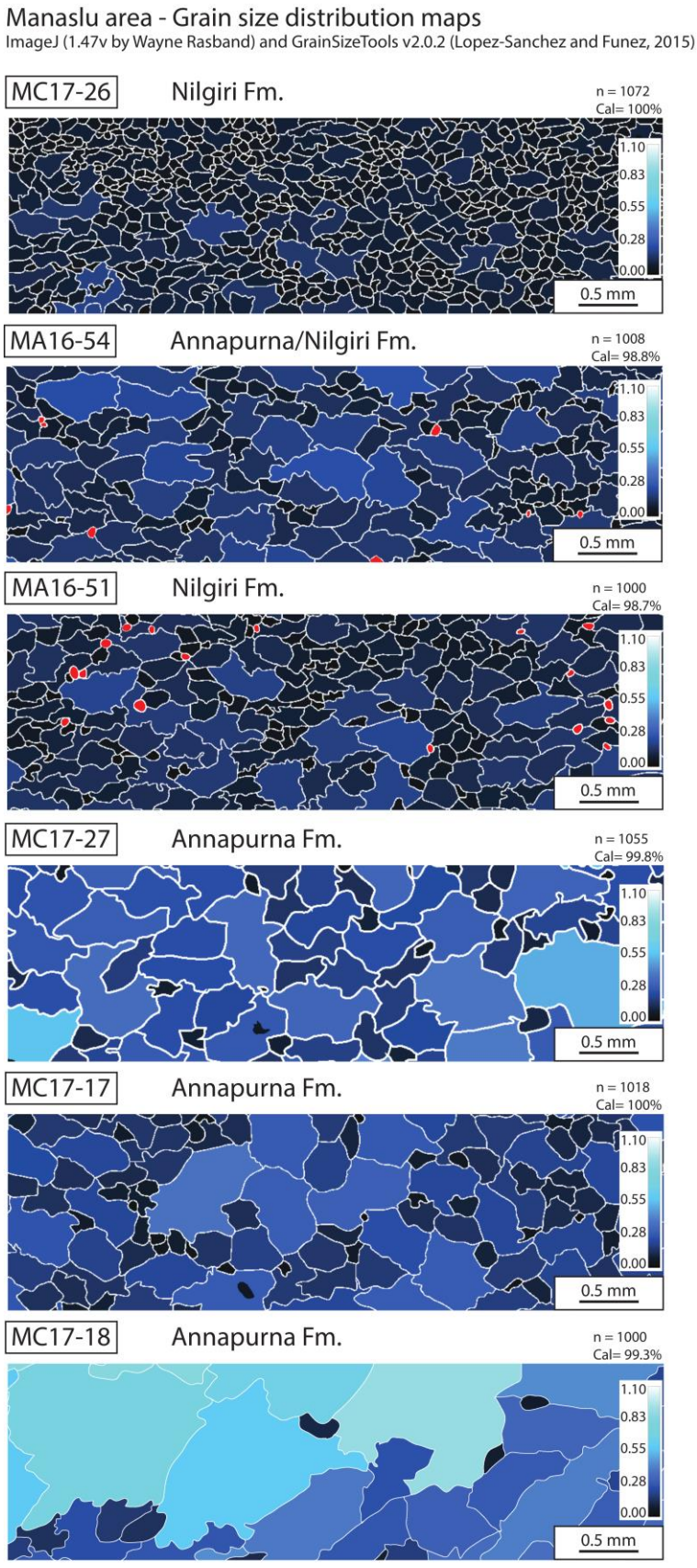

Figure 3. 18. *Small slices of the grain size distribution maps for marbles from the upper Budhi Gandaki and Marsyandi valleys. Maps were processed by ImageJ for areas of more than 1000 of calcite crystals in microlithon domains. Legend: n, number of analyzed interconnected crystals; Cal, calcite abundance (%) relative to all phase minerals within the analyzed areas. Vertical scalebar correspond to crystals equivalent radius. Samples are listed from top to bottom.*

***Table 3.3**. Results from grain size and e-twin analysis (see Fig. 3.9 and Fig. 3.15 for sample location). %Cal = abundance of calcite in the analyzed volume; n = number of analyzed interconnected crystals; Diff. stress = differential stress calculated from the mean grain size through the Barnhoorn et al. (2004), Rutter (1995), Rowe and Rutter (1990) and Rybacki et al. (2011) paleopiezometers; $\dot{\varepsilon}$ = strain rate after differential stress calculated for grain boundary mobility mechanisms through the Barnhoorn et al. (2004) equation for T=400°C and for twinning through Rybacki et al. (2011) equation for T=300°C.*

Sample	% Cal	n. analysed crystals	Mean Calcite grain size (µm)	Diff. stress Barnhoorn et al. (MPa)	Diff. stress Rutter (MPa)	$\dot{\varepsilon}$ (GBM) (s^{-1}) (T=400°C)	Mean twin density	Diff. stress Rowe and Rutter (MPa)	Diff. stress (twin) Rybacki et al. (MPa)	$\dot{\varepsilon}$ (twin) (s^{-1}) (T=300°C)
MC17-26	100.00	1072	410±140	11.3±1.0	12.7	2.79E-11	-	-	-	-
MA16-54	98.80	1008	620±160	7.8±1.5	8.8	1.29E-11	43.70	228.69	129±12	8.27E-13
MA16-51	98.70	1000	610±140	8.5±0.9	8.9	1.32E-11	46.63	233.50	133±12	1.2E-12
MC17-27	99.77	1055	800±550	7.2±0.6	7.0	7.97E-12	42.88	227.29	128±12	7.44E-13
MC17-17	100.00	1018	730±180	7.7±0.6	7.6	9.45E-12	53.17	243.26	142±13	2.64E-12
MC17-18	99.30	1000	960±320	6.8±1.7	6.0	5.66E-12	55.63	246.62	145±13	3.51E-12

Grain size decreases from the lower-located samples of the Annapurna Fm. to the structurally higher samples of the Nilgiri Fm (*Fig. 3.18*). Starting from grain size maps, grain size distribution was calculated (see *Table 3.3*). The mean grain size decreases up-section from 960 µm (sample MC17-18) to 410 µm (sample MC17-26, *Table 3.3*). Adopting the Barnhoorn et al. (2004) paleopiezometer, the measured mean grain sizes correspond to differential stress of 5-12 MPa (*Table 3.3, Fig. 3.19*). These values are in line with estimation of $\sigma_{(GBM)}$=6-13 MPa applying the Rutter (1995) piezometer. According to the Renner et al. (2002) equation, using an average deformation temperatures of 400 °C, as supported by Schneider and Marsh (1993) petrological estimates (440-370 °C), dynamic recrystallization of calcite on the STDS developed between 5.7 x 10^{-12} -2.8 x 10^{-11} s^{-1} (*Table 3.3*).

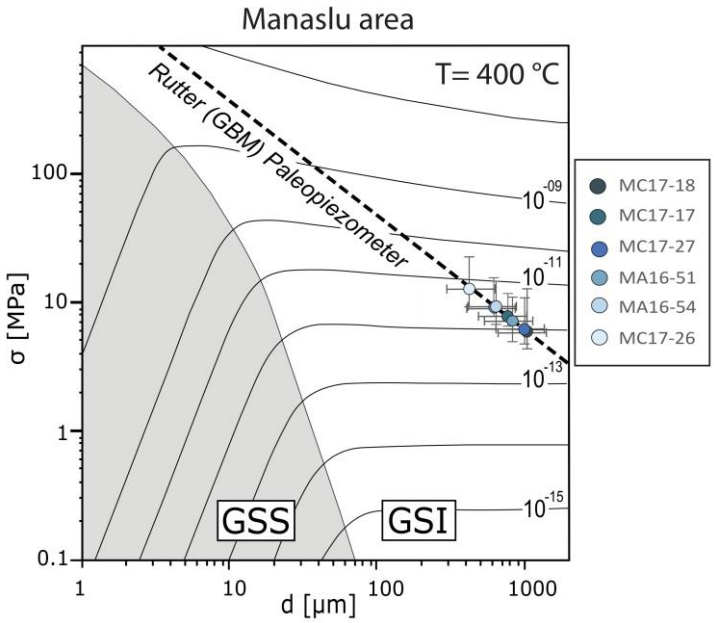

***Figure 3. 19.** Grain size vs. differential stress for calcite paleopiezometry (for T=400°C) (see Fig. 3.9 and Fig. 3.15 for sample structural positions.). The dashed line shows the calcite GBM-based paleopiezometer of Rutter (1995). The boundary between the grain size sensitive creep (GSS) field (Herwegh et al., 2003) and the flow laws of Renner et al. (2002) for grain size insensitive (GSI) regimes is given. Contours point to the strain rates. Differential stress after Barnhoorn et al. (2004) and Rutter (1995) fall in the same error bar, and on the Rutter (1995) regression line.*

Mechanical {*e*}-twins of type II in calcite, crosscutting the host grains have a thickness of ca. 2-5 µm and a mean twin density (D) of ca. 42.9-55.6 (normalized to 1 mm length) (*Table 3.3*). According to Rowe and Rutter (1990), these densities support differential stress of ca. 227-247 MPa, whereas exploiting the Rybacki et al. (2011) piezometer, the average differential stress is of $\sigma_{(TWINN)}$=130-145 MPa (*Table 3.3*). Assuming a deformation temperature of 300 °C for which twinning development dominates on dynamic recrystallization (e.g. Groshong, 1988, Ferrill et al., 2004), the exponential law of Rutter (1974) provides strain rates of 8.3 x 10^{-13} -3.5 x 10^{-12} s^{-1} (*Table 3.3*) adopting differential stress results from the Rybacki et al. (2011). Differential stress estimates, based on {*e*}-twins, differ considerably from the results obtained for the grain size distribution (one order of magnitude of difference). In-depth discussion about the meaning of such results is given in Chapter 7 (*par. 7.2.4*).

3.2.5. Texture analysis of the STDS (Budhi Gandaki and Marsyandi valleys)

Texture analysis was performed on the fifteen aforementioned samples with the aid of the XTG (eight samples from the upper Budhi Gandaki, *Fig. 3.20* and *Fig. 3.21*, and seven samples from the upper Marsyandi, *Fig. 3.22, Table 3.2*). Samples show compatible and similar textures (*Fig. 3.21, Fig. 3.22*), as described below.

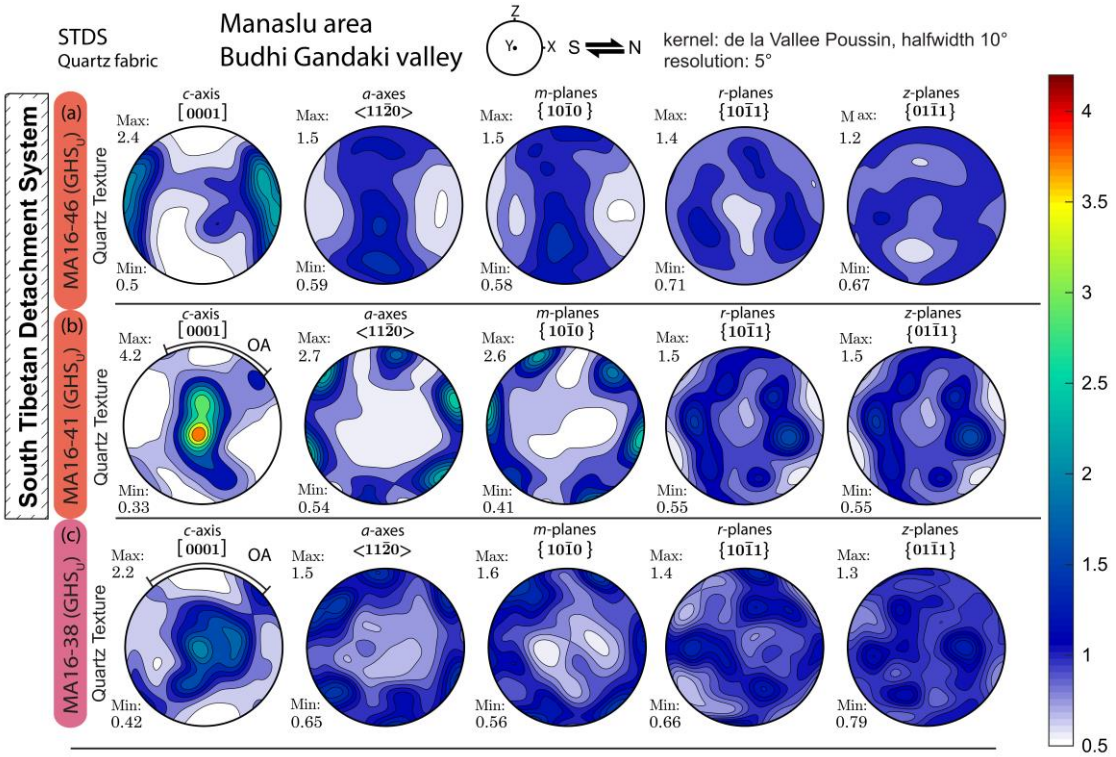

Figure 3. 20. *Quartz pole figures (equal area projection, lower hemisphere) in Budhi Gandaki valley displayed for the main crystallographic directions. Colour bar chart indicates multiples of uniform distribution (equals to 1.0) of CPO. Pole figures view towards the west on projection plane and refer as reference frame to the foliation pole (Z) and mineral lineation (X). Samples belong to the GHS_U and to Tur-granites of the HHL (*Fig. 3.16*). OA, fabric opening angle.*

UPPER BUDHI GANDAKI VALLEY

In the upper Budhi Gandaki, the augen orthogneiss MA16-38 (*Fig. 3.16g, Fig. 3.20c*) has a well-developed quartz texture with a low CPO intensity (M-Index=0.02). Quartz [*c*]-axes in [0001] pole figures are dispersed in rhombic maxima and on the Y-direction (prism<*a*> slip, see Toy et al., 2008), with further maxima close to the Z-direction (basal<*a*> maxima, see Toy et al., 2008)

(*Fig. 3.20c*). This pattern corresponds to a type II crossed girdle (see also Passchier and Trouw, 2005). Maxima on <11$\bar{2}$0> and {10$\bar{1}$0} are concentrated in peripheric position, supporting an important contribution of the prism<*a*> slip. On [0001] pole figure, basal<*a*> maxima determine a wide opening angle (*Fig. 3.20c*) of 85°, corresponding to deformation temperatures of ca. 635 °C (with calibration of Faleiros et al., 2016).

MA16-41 Tur-leucogranite (*Fig. 3.16h*) has a well-defined (*Fig. 3.20b*) and stronger CPO intensity (M-Index=0.05). A type I crossed girdle can be recognized by the [*c*]-axes distribution on [0001]. This pattern (*Fig. 3.20b*) is consistent with quartz plastic intracrystalline deformation in plane strain regime. The central axis of the type I crossed girdle has a dextral asymmetry (*Fig. 3.20b*). A wide opening angle of 87° corresponds to deformation temperatures of ca. 650 °C. At the top of the pluton, the Tur-bearing microgranite MA16-46 (*Fig. 3.16e*), intruded into the THS (*Fig. 3.15a, b*), has a weaker CPO (M=0.03). Nevertheless, a clear texture is displayed in all quartz pole figures (*Fig. 3.20a*). On [0001], quartz [*c*]-axes are focused in symmetric peripheric maxima on the X-direction, supporting intracrystalline deformation by prism<c> slip (see Toy et al., 2008). A couple of maxima in the Z-direction on the prismatic {10$\bar{1}$0} planes and further central maxima close to the Y-direction (*Fig. 3.20a*) can be interpreted as resulting from prismatic slip. The <*a*>-*ax*es maxima, oriented on the YZ-plane of the finite-strain ellipsoid, are only a minor component on the primitive circle (*Fig. 3.20a*). Therefore, quartz textures show prism<*c*> slip as the main slip system active in the dynamic recrystallization. According to Mainprice et al. (1986), prism<*c*> slip occurs in quartz at temperatures above 650 °C.

At higher structural levels, calcite and quartz textures were investigated in pure and impure marbles (examples in *Fig. 3.21a-g*). Calcite textures show similar patterns for all samples, with subtle sinistral asymmetries indicating a non-coaxial flow (e.g. *Fig. 3.21b, d-f*). A low CPO intensity is recorded for all samples (M-index=0.01-0.03). On [0001] pole figures, calcite [*c*]-axes define strong peripheric maxima close to the Z-direction, with auxiliary maxima defining a central girdle (*Fig. 3.21a, b, d-f*). From bottom to top, sample MA16-47 (*Fig. 3.16f*) has strong maxima on <11$\bar{2}$0> close to the Y direction (*Fig. 3.21f*). Moreover, {*f*}-planes on {01$\bar{1}$2} define strong maxima on the Y-direction and close to the X-direction. This texture pattern shows intracrystalline {*f*} slip which, according to De Bresser and Spiers (1997), typically occurs at deformation between 500-800 °C. The {*e*}-planes, on {01$\bar{1}$8}, define strong maxima similar to the [*c*]-axes pattern, with slightly sinistral asymmetries (*Fig. 3.21f*). Sinistral asymmetries on both [0001] and {01$\bar{1}$8} pole figures in sample MA16-47 indicate a plastic deformation in calcite occurred by {*e*}-twinning in non-coaxial deformation (*Fig. 3.21f*). Therefore, for sample MA16-47, calcite CPO supports intracrystalline {*f*} slip and {*e*}-twinning. It is noteworthy that {*e*}-planes on {01$\bar{1}$8} define strong maxima, similar to the [*c*]-axes pattern, in all samples.

In samples at higher structural levels, MA16-43 (*Fig. 3.21e*), MA16-44 (*Fig. 3.21d*), and MA16-51 (*Fig. 3.21b*) from the Annapurna and Pi Fm.s (*Fig. 3.16a, c, d*), <*a*>-*ax*es on <11$\bar{2}$0> are focused in a girdle parallel to the foliation strike. In these two samples, textures show a dominance of {*e*}-twinning as a deformation mechanism recorded by calcite, with only minor intracrystalline slip. In sample MA16-54 (*Fig. 3.21a*) at the top (Pi Fm. top), <*a*>-*ax*es on <11$\bar{2}$0> are focused in a couple of maxima on the X-direction, parallel to the lineation trend. In such sample, {*r*}-planes {10$\bar{1}$4} define well-developed peripheric maxima close to the Z-direction. These patterns show strong intracrystalline deformation by {*r*} slip (see also De Bresser and Spiers, 1993, 1997; Barber et al., 2007). According to De Bresser and Spiers (1993), {*r*} slip can occur in a wide deformation temperature range, between 300-800°C. Therefore, for sample MA16-54, calcite CPO supports intracrystalline {*r*} slip and {*e*}-twinning.

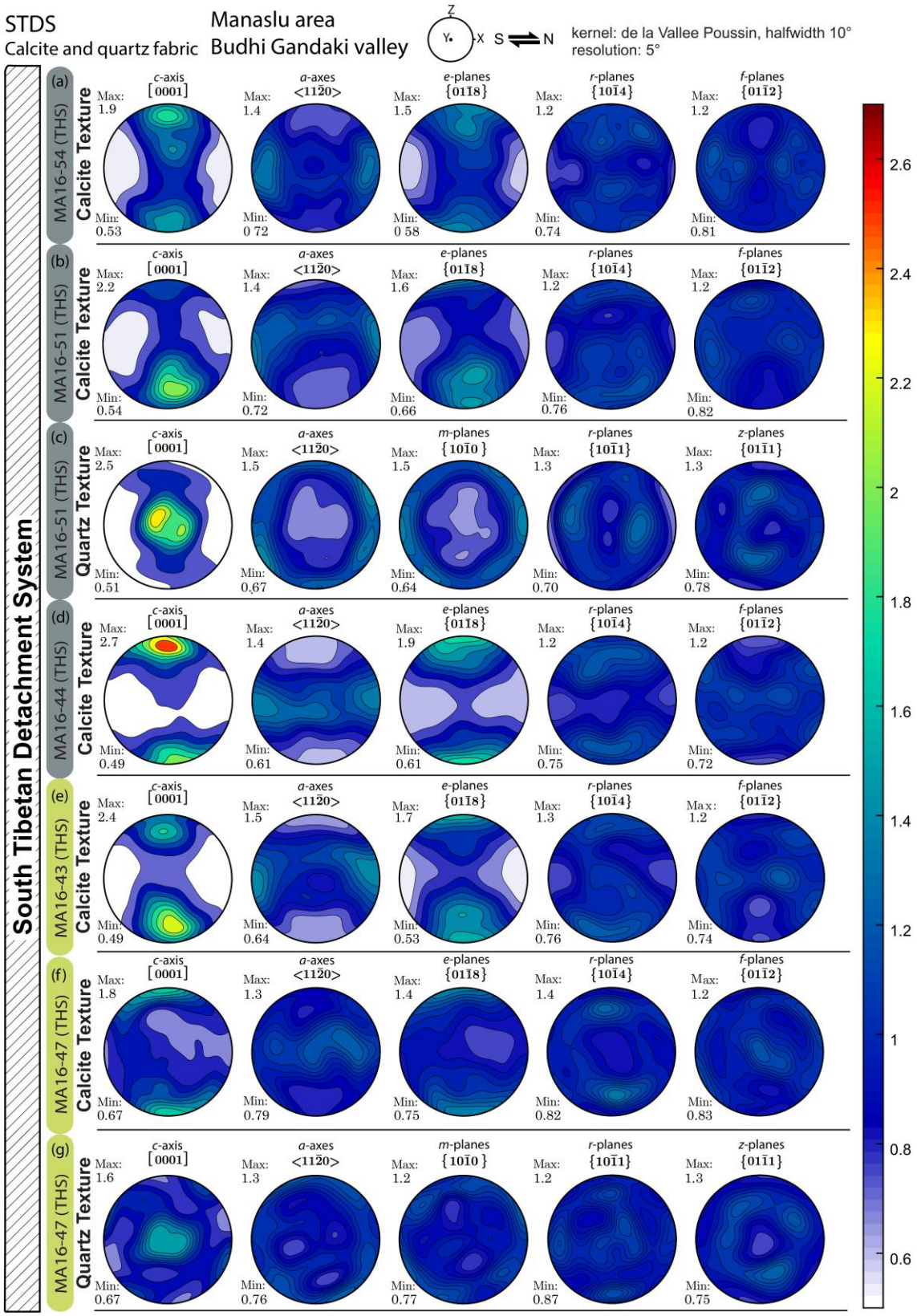

Figure 3. 21. *Calcite and quartz textures (equal area projection, lower hemisphere, XTG analysis) along the Budhi Gandaki valley, displayed for the main crystallographic directions. Each row corresponds to a sample (on the left side the mineral texture is reported for each sample, i.e. calcite texture or quartz texture). Samples belong to the THS, from the Annapurna Fm. up to the Pi Fm. Samples are listed from top to bottom (Fig. 3.16). Colour bar chart indicates multiples of uniform distribution (equals to 1.0) of CPO. All pole figures view towards the west on projection plane and refer as reference frame to the foliation pole (Z) and mineral lineation (X). See text for further details.*

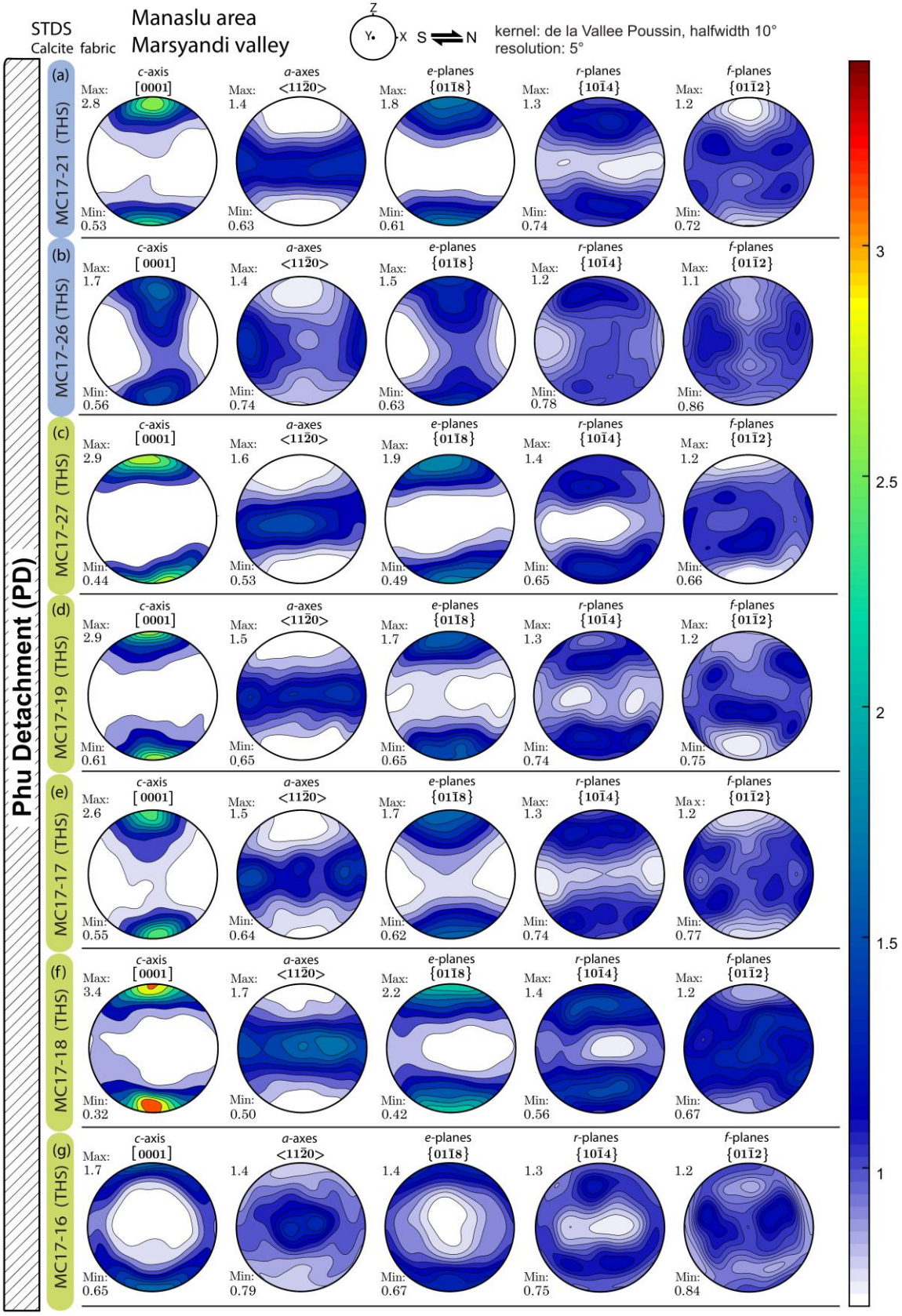

Figure 3. 22. *Calcite textures (equal area projection, lower hemisphere, XTG analysis) along the Marsyandi valley. Samples belong to the THS, from the Annapurna Fm. up to the Nilgiri Fm. Samples are listed from top to bottom (Fig. 3.17). Colour bar chart indicates multiples of uniform distribution (equals to 1.0) of CPO. All pole figures view towards the west on projection plane and refer as reference frame to the foliation pole (Z) and mineral lineation (X).*

Quartz textures were also acquired through the XTG. However, only the uppermost MA16-51 and the lowermost MA16-47 had enough interconnected quartz in quartz-rich layers to be analyzed. Quartz textures in *Fig. 3.21c* show weak but clear CPO. On [0001], the [*c*]-axes pattern defines a Type I crossed girdle, with a slightly dextral asymmetric central axis (*Fig. 3.21c*). This asymmetry is confirmed by the stronger couple of <*a*>-*ax*is maxima on <11$\bar{2}$0>, close to the X-direction. Quartz texture of sample MA16-51 therefore indicates intracrystalline deformation consistent with a top-to-the-north non-coaxial flow. Sample MA16-47 has a less clear CPO (*Fig. 3.21g*). However, a main central Y-maxima can be recognized on [0001] pole figure. Coupling quartz and calcite textures, it can be inferred that the asymmetry in the calcite [*c*]-axis maxima developed from {*e*}-twinning during a top-to-the-north non-coaxial flow.

UPPER MARSYANDI VALLEY

From the Marsyandi valley, calcite textures in marbles (*Fig. 3.22a-g*) are quite similar to those described for the Budhi Gandaki valley. Calcite has a weak CPO intensity (M-index=0.01-0.05) but well-defined maxima. On [0001], [*c*]-axes define strong and slightly asymmetric maxima (sinistral asymmetry) close to the Z-direction, with further maxima on the Y-direction forming a central girdle (from bottom to top, samples MC17-17, MC17-26 and MC17-21; *Fig. 3.22a, b, e*). From bottom to top, five samples from the Annapurna Fm. (MC17-16, MC17-18, MC17-17, MC17-19, and MC17-27), on <11$\bar{2}$0>, <*a*>-*ax*is maxima define central girdles parallel to the XY-plane (*Fig. 3.22c-g*). On {01$\bar{1}$8}, the poles to the {*e*}-planes show similar strong pattern, supporting {*e*}-twinning development in a top-to-the-north non-coaxial deformation. Maxima on {10$\bar{1}$4} (or {*r*}-planes) and {01$\bar{1}$2} (or {*f*}-planes) define small circles (see also Barner et al., 2007). These patterns are consistent with the coexistence of {*e*}-twinning and intracrystalline deformation developed in a top-to-the-north non-coaxial flow. Similar, but symmetric patterns are otherwise recorded in the uppermost two samples from the Nilgiri Fm. (*Fig. 3.22a, b*). In sample MC17-26, however, <*a*>-*ax*es on <11$\bar{2}$0> are focused in a couple of maxima on the X-direction, parallel to the lineation trend. In such samples, {*r*}-planes on {10$\bar{1}$4} and {*f*}-planes on {01$\bar{1}$2} define well-developed peripheral maxima close to the Z- and X-direction, respectively (*Fig. 3.22b*). This texture indicates strong intracrystalline deformation by {*r*} and {*f*} slip, typically occurring between 300-800°C (De Bresser and Spiers, 1993, 1997).

3.2.6. Kinematic of the flow of the STDS$_U$ and finite strain analysis

Sectional vorticity number (Wn) and mean kinematic vorticity (Wm) were estimated in six samples (two samples from the Budhi Gandaki and four samples from the Marsyandi valleys) applying both the Wenk et al. (1987) texture-based method and the Wallis (1995) oblique foliation-based method. Both methods were applied adopting the same reference frame (main foliation, Sp). This widely adopted (e.g. Spanos et al., 2015; see Sarkarinejad and Heibati, 2017 for a review) simplification is supported by the fact that the STDS was a mature shear zone, with a long-lasting history where the main foliation is close to the parallelism with the shear zone boundaries (Fossen, 2010).

From bottom to top, the Wallis (1995) method was applied on samples MC17-18, MC17-17, MC17-27, and MA16-51 (see *Table 3.4*) where calcite oblique foliation (Sb) is present (*Fig. 3.16b, d; Fig. 3.17c, d, f*). Measuring the δ angle between the Sb and the mylonitic foliation, S2 (only ca. 20 oblique foliations for each sample), this angle ranges between ca. 38-41° (*Table 3.4*). According to Wallis (1995), the corresponding mean kinematic vorticity value (Wm) is between 0.97-0.99 (*Table 3.4*).

Table 3.4. *Results from kinematic vorticity analyses after applying the Wenk et al. (1987) method and the Wallis (1995) method. Angles ω° and δ° are the angles of asymmetry of the [c]-axes pattern, and the angle between the oblique foliation (Sb) and the main foliation (S2), respectively. Wn is the sectional vorticity number. ND – non-detected.*

		Wallis, 1995		*Wenk et al., 1987*		
Budhi Gandaki	*δ°*	*Wn*	*simple shear%*	*ω°*	*simple shear%*	*Wn*
MA16-51	38	0.97	84	8	29	0.44
MA16-47	*ND*	*ND*	*ND*	5	20	0.31
Marsyandi	δ	Wn	simple shear%	ω°	simple shear%	Wn
MC17-27	40	0.98	87	10	34	0.51
MC17-19	*ND*	*ND*	*ND*	8	28	0.43
MC17-17	40	0.98	87	7	26	0.4
MC17-18	41	0.99	91	*ND*	*ND*	*ND*

From bottom to top, the Wenk et al. (1987) method was applied in samples MA16-47, MC17-17, MC17-19, MC17-27, and MA16-51 (*Table 3.4*), where asymmetric calcite textures support twinning and intracrystalline slip. In the study samples, the angles of asymmetry (*Table 3.4*) vary from 5-10°, indicating a pure-shear dominated flow during {*e*}-twinning development. Simple shear contribution is of ca. 20-35% (*Table 3.4*). In a monocline plane strain deformation (as supported also by quartz textures, e.g. *Fig. 3.21c*), these percentages correspond to sectional vorticity number (Wn) of 0.30 to 0.50 (*Table 3.4, Fig. 3.23*). These estimates, based on the influence of {*e*}-twins, differ considerably from the vorticity results obtained with the Wallis (1995) method, which is based on the shape preferred orientation of crystals developed for grain boundary mobility mechanisms. Further discussions are given in Chapter 7 (*par. 7.2.5*).

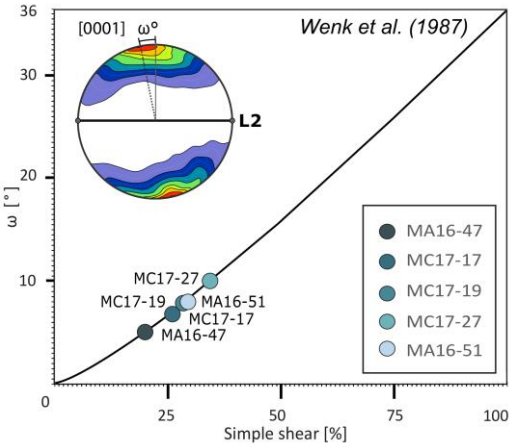

Figure 3. 23. *Simple shear estimates based on the Wenk et al. (1987) method. Samples are marbles from the Budhi Gandaki and Marsyandi valleys. Simple shear% vs ω° of calcite [c]-axis maxima asymmetry is shown.*

Finite-strain analysis was carried out on six oriented impure marbles (*Fig. 3.24*), using the center-to-center method (Fry, 1979) on thin sections approximating the XZ plane of finite strain ellipsoid (*par. 2.1.2*). Calcite crystals were selected as strain markers (ca. 150-210 centroids for each sample). Since calcite is dynamically recrystallized, crystals centroids do not only depend on the strain amount, but they record only a part of the finite deformation. Therefore, the adopted method provides a minimal estimate of the finite strain. The calculated finite-strain equivalent ellipse ratio (R_{XZ}) is of ca. 1.9-2.4 (*Fig. 3.24*). Finite-strain ratios R_{XZ} (*Fig. 3.24*) and kinematic vorticity estimations (*Fig. 3.24*) were used to derive the shortening with the Wallis et al. (1993) equation (*par. 2.2.2*). Adopting the mean kinematic vorticity (Wm) estimated through the Wallis (1995) oblique foliation-based method, the "maximum" shortening, S, ranges between 0.91-0.96 (*Table 3.5*), corresponding to perpendicular shortening of 4-9%. Using the sectional kinematic vorticity (Wn) estimated starting from Wenk et al. (1987) simple shear estimates, the "maximum" shortening ranges between 0.74-0.79 (*Table 3.5*), corresponding to perpendicular shortening of 21-26%. As these results depend on the different vorticity estimates obtained with the Wallis (1995) and the Wenk et al. (1987) methods, further discussions are given in Chapter 7 (*par. 7.2.5*).

***Table 3.5**. Shortening (S) estimation adopting the finite-strain ratio, Rxz, from Fry (1979) and Waldron and Wallace (2007) analysis (see Fig. 3.24) for Wallis et al. (1993) equation. Kinematic vorticity analyses after applying the method of Wallis (1995) and of Wenk et al. (1987) were used. Wm is the mean kinematic vorticity to be used for shortening estimates. For kinematic vorticity estimates after Wenk et al. (1987), Wm=Wn (sectional vorticity number) was assumed. ND – non-detected.*

		After Wallis, 1995		*After Wenk et al., 1987*	
Budhi Gandaki	*Rxz*	*Wm*	*S*	*ca. Wn*	*S*
MA16-51	2.18	0.97	0.91	0.44	0.70
Marsyandi	*Rxz*	*Wm*	*S*	*ca. Wn*	*S*
MC17-27	2.00	0.98	0.93	0.51	0.74
MC17-17	1.87	0.98	0.94	0.4	0.75
MC17-18	1.88	0.99	0.96	*ND*	*ND*

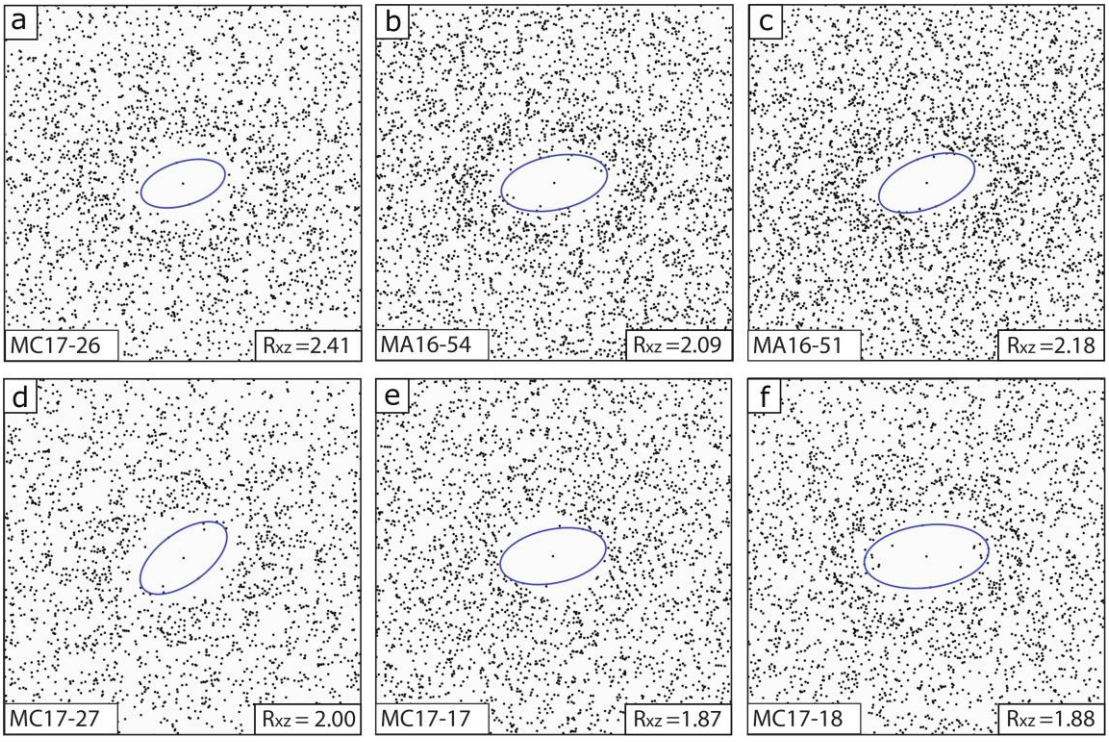

***Figure 3. 24.** Results of the finite strain analysis (Fry plots) for selected samples from the upper Budhi Gandaki and the Marsyandi valleys (for the starting original images, see par. 2.1.2 for example). Low-density areas, highlighted in blue, are defined through the exponential edge detection method (EED) of Waldron and Wallace (2007).*

3.3. Summary of data on the Manaslu area

- Microstructural analyses have been conducted on eighteen samples from the MCTz from two nearly N-S oriented valleys. Paragneiss in the garnet-zone, included at the MCTz base, passes up-section to dolomite-bearing gneiss and dolomitic marbles up to amphibolite-facies massive quartzite in the kyanite-zone at the shear zone top. Within the thick mylonitic zone, a top-to-the-south transport direction has been documented in literature and confirmed my microstructures. A dominant foliation, corresponding in literature to the S2 foliation, occurs, whereas an older S1 foliation is only preserved within the LHS, at the base of the shear zone.

- Quartz, dolomite, and feldspar microstructures and textures have been investigated on thirteen samples combining two different texture analyser (X-ray Texture goniometry and crystal-fabric microanalyzer). Low CPO intensities (J-index, M-index) are recorded. Textures and microstructures (e.g. CS-fabric, oblique foliations, etc) show sinistral asymmetries, consistent with the non-coaxial flow.
- The "orientation of oblique grain shape fabrics" method BY Wallis (1995) has been applied on dolomitic marbles at the MCTz top, providing data for a general shear flow defined by a pure shear component of 40-56%.
- The Faleiros et al. (2016) fabric opening angle method and quartz, dolomite and feldspars microstructures, dolomite textures, and the metamorphic mineral assemblage support an up-section temperature increase from 460 °C to 600 °C from LHS-affinity rocks to GHS_L-affinity rocks.

- Microstructural analyses have been conducted on twenty three samples from the STDS from two nearly N-S oriented valleys. Along the Budhi Gandaki valley (eastern valley), the ductile STDS has been defined by a lower limit, $STDS_L$, between the GHS_U and the THS, and an upper limit, $STDS_U$, within the THS. The $STDS_L$ and the $STDS_U$ include a km-thick ductile mylonitic zone where few kinematic indicators are recognizable. In the Marsyandi valley, on the west, a further branch, the Chame Detachment, occurs at lower structural levels, wholly within the GHS_U. The STDS in *sensu strictu* in the Marsyandi valley broadly corresponds to the $STDS_L$ in the Budhi Gandaki valley; whereas the Phu Detachment in the Marsyandi valley prosecutes into the $STDS_U$ eastward. Only a dominant foliation, corresponding in literature to the S2 foliation, occurs.
- The Chame Detachment has been investigated for quartz microstructures and textures on eight Tur-bearing leucogranite, orthogneiss, migmatitic orthogneiss and Bt-Hbl gneiss though the X-ray Texture goniometry and the crystal-fabric microanalyzer. Kinematic indicators at the outcrop- to the microscale support a top-to-the-north sense of shear. Combining the Faleiros et al. (2016) fabric opening angle methods with quartz and feldspars microstructures, and the metamorphic mineral assemblage, supports high deformation temperatures of 620-685 °C occurring during top-to-the-north normal-sense of shearing. Toward the south, out of the shear zone, quartz type I crossed girdle supports a different temperature of of ca. 550 °C.
- Fifteen samples from the STDS have been studied, providing comparable results for calcite microstructures and calcite and quartz textures (X-ray Texture goniometry). Texture and microstructures indicate that calcite in the THS marbles deformed by grain boundary mobility and twinning under a top-to-the-north non-coaxial flow at reasonable temperatures of ca. 400-450 °C.
- Calcite grain size decreases up-section, supporting differential stress of 7-11 MPa under strain rates of 10^{-12}-10^{-11} s^{-1}. Calcite twins support differential stress of ca. 130-150 MPa under strain rates of 10^{-13}-10^{-12} s^{-1} for temperatures of 300-350 °C.
- Simple shear contribution based on "orientation of oblique grain shape fabrics" method support a simple-shear dominated flow with 84-91% of simple shear, whereas the texture-based method (influenced by twinning) supports a general shear flow with 20-34% simple shear. These estimates, coupled with finite strain analysis on calcite, support a maximum perpendicular shortening of 21-26%.

4. Kali Gandaki valley

The Kali Gandaki valley in the Mustang-Myagdi region (Western Nepal) is the deepest gorge comparing the altitude of the river and the highest peaks on either side, i.e. the Mt. Dhaulagiri (8167m high), to the west, and the peaks of Mt. Annapurna (8091m) to the east. Particularly, the Kali Gandaki valley cuts the Himalayas with a N-S trend, normal to the main structural directions (Colchen et al., 1986; Vannay and Hodges, 1996; Godin, 2003; Carosi et al., 2014), offering a natural cross section of the belt. The upper part of the valley exposes the crystalline rocks of the GHS_U and the nearly continuous sequence of the THS (Colchen et al., 1980; Carosi et al., 2014, Parsons et al., 2016b; *Fig. 4.1*). The GHS_U consists of a N-dipping 300 m-thick sequence of garnet-tourmaline augen gneiss and foliated leucogranite (Unit III of Searle and Godin, 2003), abundant calcsilicate and marbles (Unit II), small lenses of kyanite-or- sillimanite bearing metapelite (*Fig. 4.1a*). This volume is affected by the contractional top-to-the-south Kalopani shear zone (KSZ) (*Fig. 4.1a, b*), originally regarded as an out-of-sequence thrust (Vannay and Hodges, 1996) and recently interpreted as an older, in sequence contractional ductile shear zone (Carosi et al., 2016). At higher structural levels, the 1500 m-thick Annapurna Detachment, AD, is the local segment of the STDS (Brown and Nazarchuk, 1993; Vannay and Hodges, 1996; Godin et al., 1999a; Godin, 2003; Searle, 2010). Within the Annapurna Detachment (AD), the main lithologies involved are calc-silicate-rich marbles, white marbles and impure marbles of both the GHS_U and THS (*Fig. 4.2, Fig. 4.3 a-j*).

At the top of the GHS_U, the Larjung Fm. is a 200 m-thick sequence of calc-silicate-bearing marble (*Fig. 4.3 g-j*) (Coleman, 1996; Hodges et al., 1996; Brown and Nazarchuk, 1993; Vannay and Hodges, 1996; Godin et al., 1999a; Searle, 2010). The coarse-grained marbles of the Larjung Fm. have a mineral assemblage of Cal+Qtz+Bt+Ms+K-feld (*Fig. 4.3 g-j*, *Table 4.1*), where minor Cpx+Grt+Ves, Cpx+Scp, and Hbl±Grt point out an amphibolite facies (Vannay and Hodges, 1996). Above the GHS_U, the base of the THS comprises the highly deformed Sanctuary Fm. (Pêcher, 1978), consisting of Proterozoic/Cambrian black schist, sandstone and limestone at the core of large anticlinal fold nappe in the Annapurna Fm. (*Fig. 4.1a, b*). The Annapurna Fm. is composed by 1000-1300 m of Cambrian coarse-grained marbles and impure metalimestone (*Fig. 4.3b-f*), with calcareous psammitic and pelitic schist and interbedded phyllite (Hodges et al., 1996; Vannay and Hodges, 1996; Godin et al., 1999a, 2001; Godin, 2003; Searle, 2010). A mineral assemblage of Cal+Qtz+Ms+Bt±Ep±Chl defines a biotite-zone in the greenschist-facies (*Fig. 4.3b-f*, *Table 4.1*). Upward, the Nilgiri Fm. consists of Ordovician massive bedded micritic limestone (Bordet et al., 1971) with a main mineral assemblage of Cal+Qtz+Ms (*Fig. 4.3a*, *Table 4.1*). The Nilgiri Fm. grades to the north into 400 m of pink dolomitic sandstone and quartzites (the North Face quartzites of Bodenhausen et al., 1964). The Palaeozoic sequence continues with the thick Silurian-Devonian Sombre Fm., comprehensive of black shales, limestones, and arenaceous sandstones, capped by the Permian-Carboniferous Tilicho Lake Fm. and Thini Chu Fm. (*Fig. 4.1a*). Above, a continuous Mesozoic-to-Cenozoic succession defines the upper non metamorphic part of the THS (Bordet et al., 1971; Colchen et al., 1980; Gradstein et al., 1992; Neupane et al., 2020).

Two main deformation events are recorded by fabrics within both the GHS_U and the THS: the D1 phase, related to the collisional stage, and the D2 phase, linked to the exhumation under HT/MP-LP conditions (Coleman, 1996; Hodges et al., 1996; Vannay and Hodges, 1996; Godin et al., 1999a). The D2 phase is responsible for the movement of the Annapurna Detachment, and for the development of NE-verging folds in the THS (*Fig. 4.1 a, b; Fig. 2a-c*).

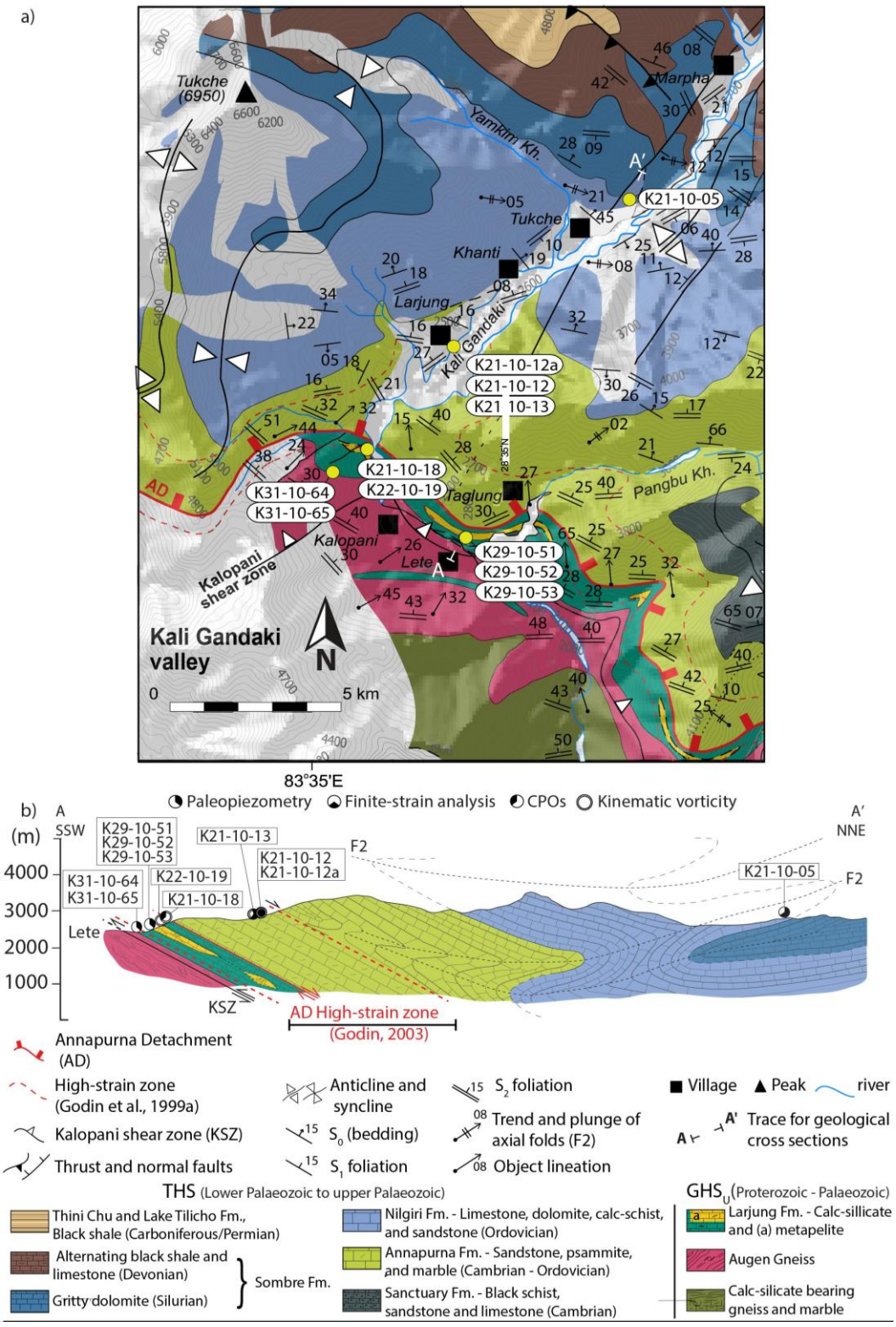

Figure 4. 1. (a) *Upper Kali Gandaki valley geological sketch map (after Godin, 2003) showing the location of study samples.* ***(b)*** *S-N geological cross section from Lete to Tukche villages (A-A' trace in a) where study samples are projected. Legend is in accordance with Godin (2003) geological map and deformation phase definition.*

Due to the differences in rheology, variations in deformation styles are recorded at different structural levels for both the D1 and the D2 stages from the GHS_U to the THS (for a review, see Godin, 2003; Carosi et al., 2014; Parsons et al., 2016a, b). Northern to the Annapurna Detachment, within the low-to-non metamorphic THS, southwest-verging isoclinal folds F1 occurs, re-folded by the dominant F2 NE-verging mega-folds (*Fig. 4.1a*, *Fig. 4.2c*, Colchen et al., 1986; Vannay and Hodges, 1996; Searle, 2010; Parsons et al., 2016b; see Godin, 2003 for review).

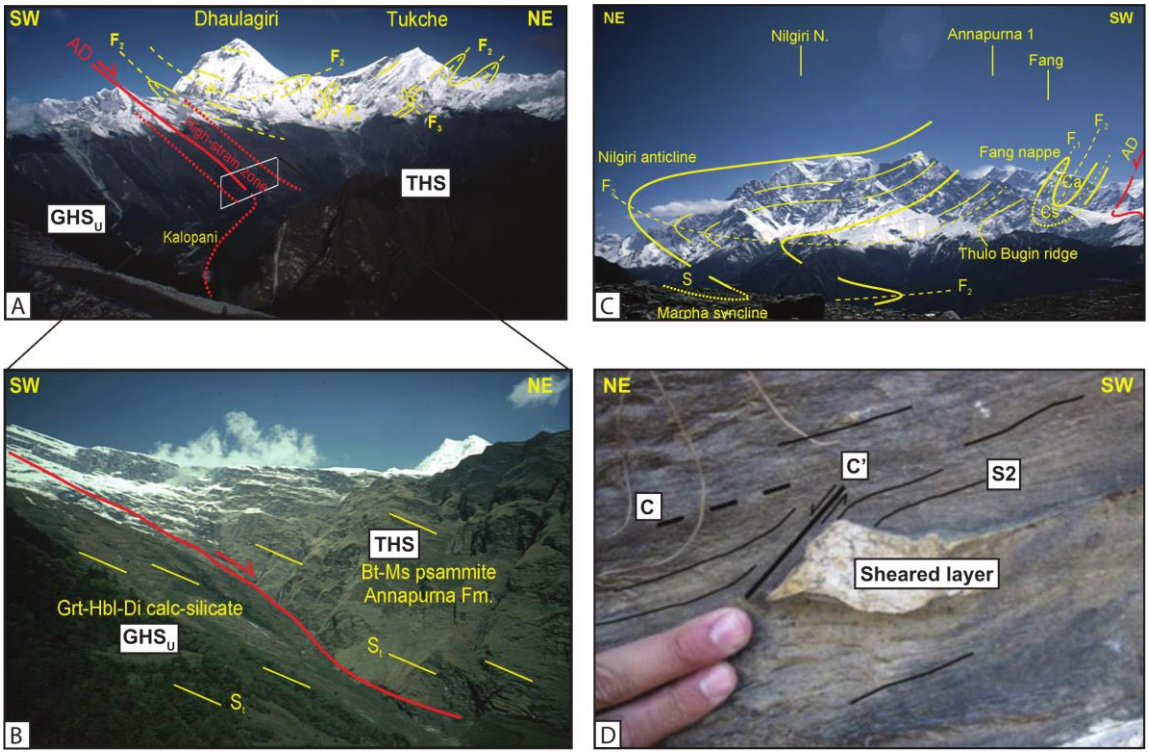

*Figure 4. 2. Panorama images and outcrop photo of the Annapurna Detachment (AD) in the Kali Gandaki valley (after Carosi et al., 2014). (**a**) Panorama from Thulo Bugin, where NE-verging F2 folds and minor F3 folds are highlighted in the THS rocks. The Annapurna detachment high-strain zone follows Godin (2003) definition. (**b**) Zoom of the panorama from the white box in (a), showing the Annapurna Detachment. (**c**) View east to Nilgiri anticline, showing the SW-verging F1 fold of the Fang nappe in the Sanctuary Fm. (barely observable in Fig. 4.1a) and the NE-verging Nilgiri anticline (F2). (**d**) Example of top-down-to-the-northeast shear band in a leucogranitic dyke affecting the metapelite of the Larjung Formation (GHS_U).*

4.1. Sample description and results for the Annapurna Detachment

In this thesis, a collection of over ten samples belonging to the GHS_U and the THS was studied (*Table 4.1).* Samples are projected into the cross section in *Fig. 4.1b*, covering a N-S transect almost between Lete and Tukche towns. In the study area, the high-strain zone of the Annapurna Detachment (AD) affects the amphibolite-facies Larjung Fm. (GHS_U), at the base (e.g. *Fig. 4.2b, d*), and the greenschist facies, biotite-muscovite psammite and marbles of the Annapurna Fm. (THS) at the top (Godin et al., 1999a, *Fig. 4.1a, Fig. 4.2a-c*).

Samples show microstructures related to ductile inter- and intracrystalline deformation (D2 structures), and to post-kinematic brittle deformation (including fractures, veins, and fluid inclusions trails at a high angle to the main foliation). A pervasive foliation S2 strikes almost parallel to the shear zone trend, transposing the D1 structures (Godin, 2003; Parsons et al., 2016a). Micas and calcite show a shape preferred orientation (calcite aspect ratios range between ca. 2–2.5), determining a continuous foliation parallel to the detachment zone (*Fig. 4.3b-j*; Parsons et al., 2016a). This fabric developed from the Larjung Fm. (GHS_U) to the Annapurna Fm. (THS) without clear break (Colchen et al., 1986; Vannay and Hodges, 1996; Godin et al., 1999a; Carosi et al., 2014).

The studied samples have interconnected calcite crystals, which are almost 65-75% of the bulk volume in the Larjung Fm. (GHS) and 65-80% in the Annapurna Fm. (THS) (*Table 4.2*). The important volumetric abundance of carbonates and their interconnection indicate that calcite is the weak phase that can accommodate the deformation (Handy, 1994).

***Table 4.1**. Studied samples formations, mineral assemblage, main features and related analysis. Abbreviations: Bt – biotite; Cal – calcite; Chl – chlorite; Dol – dolomite; Feld – feldspar; Qtz – quartz; Wm – white mica; Rt – rutile; GBM – grain boundary migration; SGR – subgrain rotation recrystallization; SPO – shape preferred orientation.*

Sample	Formation	Mineral Assemblage	Calcite deformation	Analysis	Fabric
K21-10-05	Sombre	Cal+Qtz+Wm	pressure solution	◔	Isotropic coarse-grained
K21-10-12A	Annapurna	Cal+Dol+Qtz+Wm+Bt±Chl	SGR + twinning	●	Continuous foliation (S2), SPO
K21-10-12	Annapurna	Cal+Dol+Qtz+Wm±Rt	GBM + twinning	●	Continuous foliation (S2), SPO
K21-10-13	Annapurna	Cal+Dol+Qtz+Wm+Bt±Chl	GBM + twinning	◔	Continuous foliation (S2), SPO
K21-10-18	Annapurna	Cal+Dol+Qtz+feld±Bt±Wm±Chl	GBM + twinning	◕	Continuous foliation (S2), SPO
K22-10-19	Annapurna	Cal+Dol+Qtz+Bt+Wm	GBM + twinning	●	Continuous foliation (S2)
K29-10-51	Larjung	Cal Dol+Qtz+Bt	GBM + twinning	◔	Continuous foliation (S2)
K29-10-52	Larjung	Cal+Dol+Qtz+Bt	GBM + twinning	●	Continuous foliation (S2)
K29-10-53	Larjung	Cal+Dol+Qtz+Bt	GBM + twinning	◔	Continuous foliation (S2)
K31-10-64	Larjung	Cal+Dol+Qtz+Bt	GBM + twinning	◕	Continuous foliation (S2), SPO
K31-10-65	Larjung	Cal+Dol+Qtz+Bt	GBM + annealing	◕	Continuous foliation (S2), SPO

Legend: ○ microstructural analysis; ◔ paleopiezometry; ◒ Finite-strain analysis; ◕ Texture analysis.

Lobate grain boundaries (*Fig. 4.3, Fig. 4.4*), undulose extinction, and a unimodal distribution of clasts are the calcite main microstructures. A shape preferred orientation of calcite grains is parallel to the S2 foliation (*Fig. 4.3b, c, d, e, i*). Calcite microstructures in samples are typical of intracrystalline deformation and dynamic recrystallization (see Schmid et al., 1987 for a first review). At the base of the Annapurna Detachment, calcite grain size distribution is unimodal (*Fig. 4.4*). Microstructures and grain size distributions support grain boundary migration recrystallization (GBM) at the base. At the top, calcite grain size becomes slightly bimodal (e.g. K21-10-12a), with new grains and sub-grains, and rare calcite ribbons and porphyroclasts (*Fig. 4.3b*). Microstructures and grain size distribution of sample K21-10-12a support subgrain rotation recrystallization (SGR) as deformation mechanism at the top of the studied transect (Schmid et al., 1987; Rutter, 1995; Barnhoorn et al., 2004; Rogowitz et al., 2014; Platt and De Bresser, 2017).

Calcite mean grain size varies from bottom to top (*Fig. 4.4*), with equivalent diameters from 770 µm, in the Larjung Fm. (GHS), to 390 µm in the Annapurna Fm. (THS) (*Table 4.2*).

Single sets of fine twins (Burkhard, 1993; Ferrill et al., 2004) are developed in calcite host grains (*Fig. 4.3*). At low structural levels, within the Larjung Fm. (GHS_U), calcite grain boundaries are straight (*Fig. 4.3j*), defining a polygonal structure. Polygonal structure in calcite supports local annealing or extremely low strain rates (see also Vannay and Hodges, 1996).

Within small asymmetric lens-shaped quartz aggregates, crystals are incipiently deformed (e.g. samples K21-10-12a, THS, and K21-10-18, GHS_U) whereas, out of the aggregates (e.g. *Fig. 4.3*), quartz occurs in rare rounded single clasts (Handy, 1994; Herwegh and Berger, 2004; Holyoke III and Tullis, 2006).

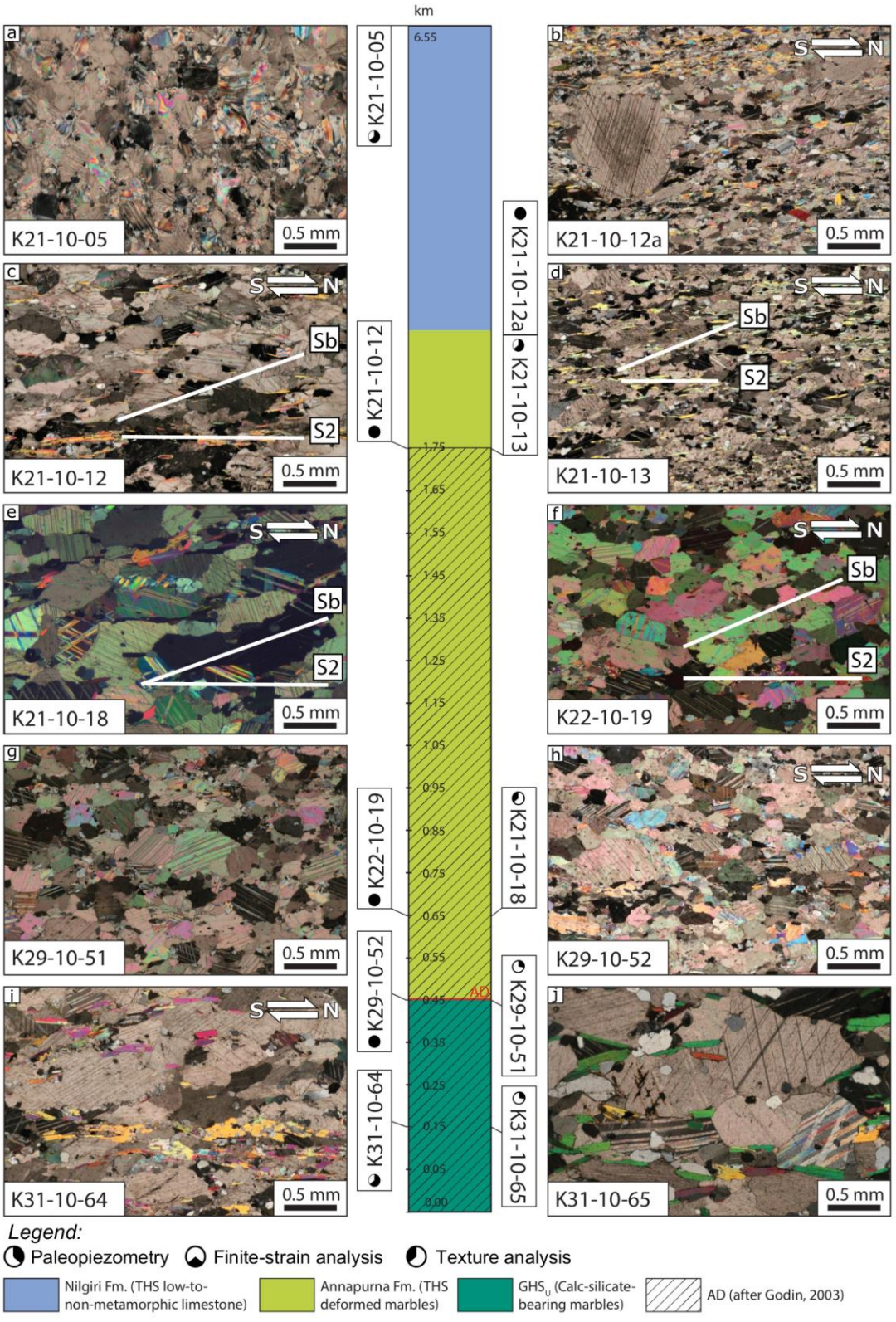

Figure 4. 3. *Microphotos of representative samples (see Fig. 4.1 for sample location).* ***(a)*** *Coarse-grained limestone (Nilgiri Fm., THS).* ***(b)*** *Impure marble (Annapurna Fm., THS) at the upper limit of the Annapurna Detachment (AD). A coarse twinned calcite porphyroclast is surrounded by new calcite grains.* ***(c)*** *Impure marble (Annapurna Fm.). Oblique foliation (Sb) points a top-to-north shearing. Type II {e}-twins crosscut the host grains.* ***(d)*** *Impure marble (Annapurna Fm.); Sb indicates top-to-north shearing.* ***(e)*** *Marble, (Annapurna Fm.); calcite has straight grain boundaries.* ***(f)*** *Coarse marble (Annapurna Fm.).* ***(g)*** *Coarse-grained white marble (Larjung Fm.).* ***(h)*** *Coarse-grained amphibolite facies impure marble (Larjung Fm).* ***(i)*** *Coarse-grained marbles (Larjung Fm.) at the base of the AD.* ***(j)*** *Coarse-grained marbles (Larjung Fm.). Calcite has straight grain boundaries.*

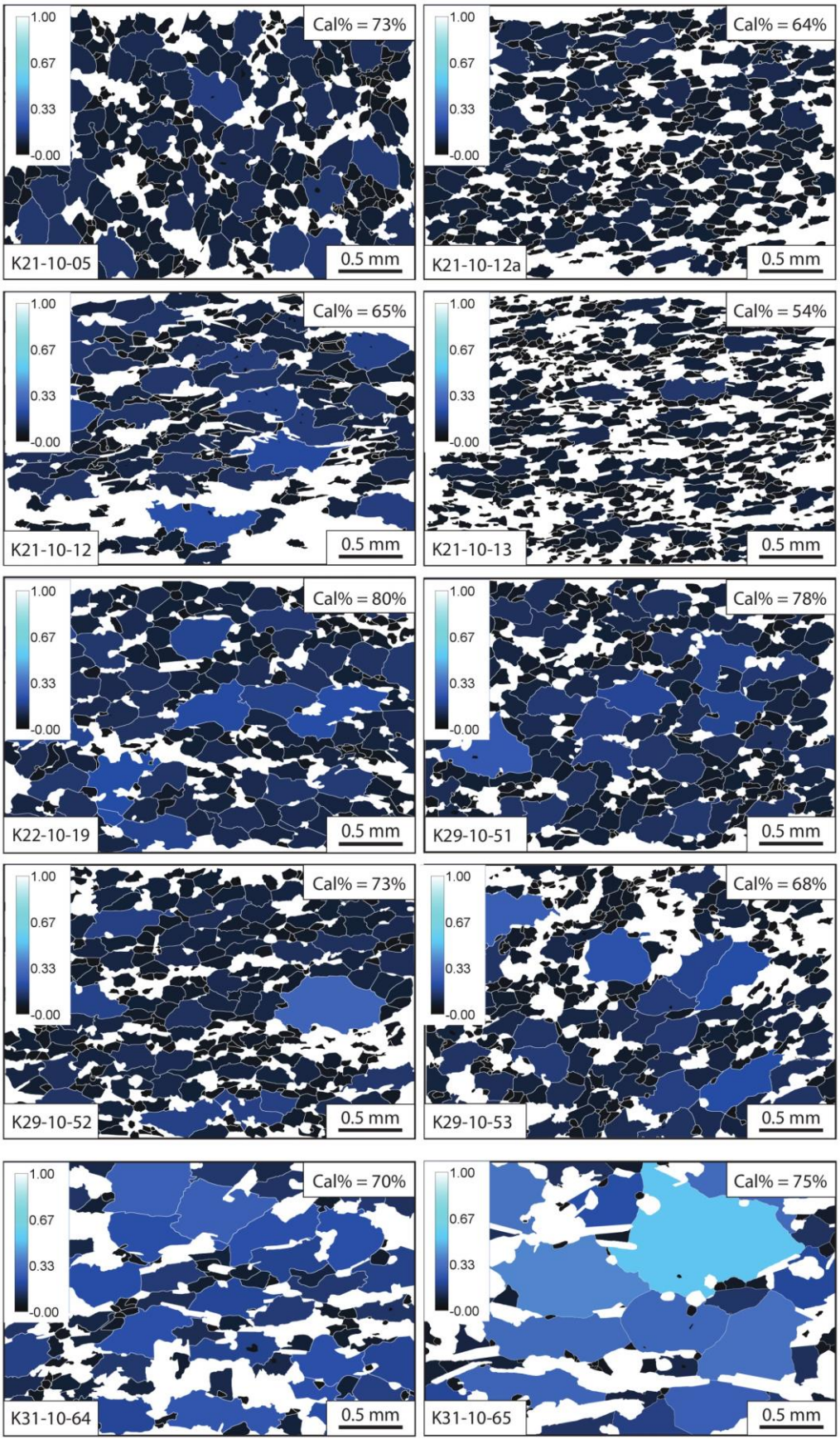

Figure 4. 4. *Grain size distribution maps of analysed sample. Cal% is the measured 2D abundance of calcite in each sample. The vertical scalebar on the left of each map correspond to the equivalent radius of each grain. See Fig. 4.3 for sample location.*

Table 4.2. *Differential stress and strain rate estimations through grain size and twin analyses. %Cal = abundance of calcite in sample; AR = aspect ratio; RMS= root mean square calcite crystal equivalent diameter; Diff. stress = differential stress (σ) calculated from the RMS by the Barnhoorn et al. (2004) paleopiezometers. ε̇(GBM) = strain rate from dynamic recrystallization mechanisms (Renner et al., 2002). Diff. stress (twin) = differential stress based on the twin density from Rowe and Rutter (1990) and Rybacki et al. (2011) paleopiezometers. ε̇(twin) = strain rate from Rybacki et al. (2011).*

Sample	% Cal	AR	RMS (μm)	Diff. stress (GBM) (MPa)	ε̇ (s^{-1}) (T=400°C)	Mean twin density	Diff. stress (twin) Rowe and Rutter (MPa)	Diff. stress (twin) Rybacki (MPa)	ε̇ (twin) (s^{-1}) T=300°C
K21-10-12A (THS)	64	2.24	250±30	13.7±4.8	3.1E-11	-	-	-	-
K21-10-12 (THS)	65	2.45	390±180	10.2±3.6	1.7E-11	47.92	236	135±6	1.41E-12
K22-10-19 (THS)	80	1.98	530±170	8.3±2.9	1.1E-11	67.47	261	160±7	1.26E-11
K29-10-51 (GHS)	78	1.96	490±160	8.7±3.1	1.2E-11	-	-	-	-
K29-10-52 (GHS)	73	2.13	440±140	9.4±3.3	1.4E-11	76.51	270	171±8	3.29E-11
K31-10-64 (GHS)	70	2.48	710±150	6.8±2.4	7.3E-12	48.98	237	136±6	1.54E-12
K31-10-65 (GHS)	75	2.41	770±200	6.5±2.3	7.4E-12	-	-	-	-

4.2. Paleopiezometric analysis of the Annapurna Detachment

Second-mineral phase (white "holes" in *Fig. 4.4*) affects the grain size in several samples (e.g. placing as an obstacle to the mechanisms of dislocation climb and growing competitively, see Herwegh and Berger, 2004). For this reason, only six out of ten marbles (from *Fig. 4.4*), where calcite recrystallized by GBM (70-80% of calcite abundance), were selected (*Table 4.2*) for paleo piezometric investigations. Adopting the Rutter (1995) paleopiezometer for GBM mechanisms, the measured mean grain sizes correspond to differential stress of $\sigma_{(GBM)}$=7-13 MPa (*Fig. 4.5*). Similar differential stress can be estimated for the sample at the top of the detachment zone (K21-10-12a), adopting the SGR-based paleopiezometer of Rutter (1995), that provides $\sigma_{(SGR)}$=6 ± 1 MPa. Adopting Barnhoorn et al. (2004) piezometer for all samples, the values are σ=8-17 MPa (*Table 4.2; Fig. 4.5*). According to the Renner et al. (2002) equation, by assuming deformation temperatures in the THS of 400 °C, dynamic recrystallization of calcite developed between 10^{-12} - 10^{-11} s^{-1} (*Table 4.2*).

Mechanical {*e*}-twins of type II in calcite, crosscutting the host grains have a thickness of ca. 3 μm and a mean twin density (D) of ca. 47.9-49.0 (normalized to 1 mm length) (*Table 4.2*). According to Rowe and Rutter (1990), these densities support differential stress of ca. 235-270 MPa, whereas exploiting the Rybacki et al. (2011) piezometer, the differential stress $\sigma_{(TWINN)}$=135-170 MPa (*Table 4.2*). Assuming a deformation temperature of 300 °C for twinning development, the exponential law of Rutter (1974) supports strain rates in the order of 1.4 x 10^{-12} -3.3 x 10^{-11} s^{-1} (adopting results from the Rybacki et al., 2011, *Table 4.2*). As in the case of the Manaslu area, differential stress estimates, based on {*e*}-twins, differ considerably from the results obtained for the grain size distribution (one order of magnitude of difference). In-depth discussion about the meaning of such results is given in Chapter 7 (*par. 7.2.4*).

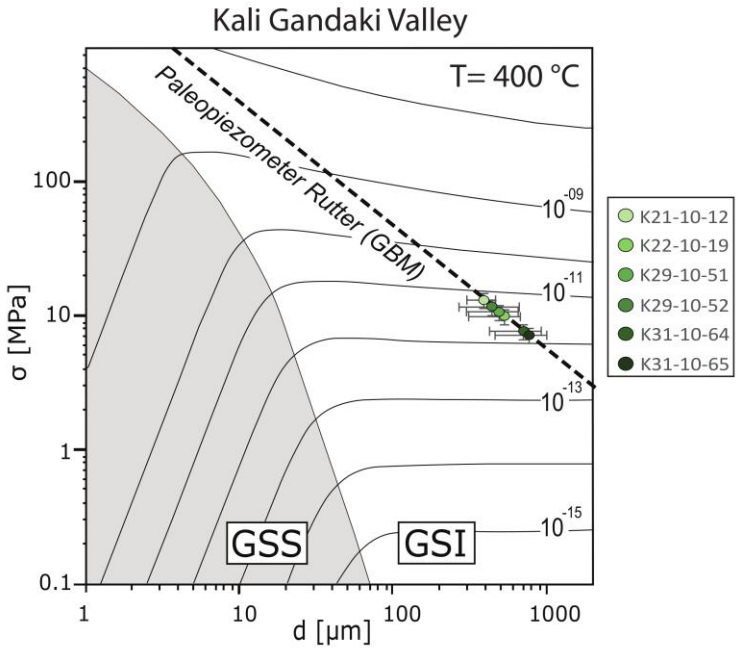

Figure 4. 5. *Grain-size- vs. differential-stress diagram for calcite (simplified for T=400 °C for all samples). The dashed line corresponds to the calcite GBM-based paleopiezometer of Rutter (1995). The boundary between the grain size sensitive creep (GSS) field (Herwegh et al., 2003) and the flow laws of Renner et al. (2002) for grain size insensitive (GSI) regimes is given. Contours correspond to the strain rates. Applying the flow law of Rutter (1995) and Barnhoorn et al. (2004), the differential stress is of the order of 10 MPa (see text for more details).*

4.3. Calcite and quartz texture along the Annapurna Detachment

Calcite and quartz texture analyses were performed on five impure marbles (from top to bottom, K21-10-12a, K21-10-12, K21-10-18, K22-10-19, and K29-10-52, see *Table 4.1, Fig. 4.6a-h*) through the X-Ray Texture Goniometer (XTG), using the macroscopic foliation as reference frame. Within samples, the analyzed calcite grains are well-interconnected and is significatively abundant (*Fig. 4.3*). Of these five samples, three impure marbles from the Annapurna Fm. (THS) were selected for further texture analysis on quartz. In these samples, quartz occurs as isolated grains within calcite-rick sheared domains. All calcite and quartz textures investigated are reported in pole figures in *Fig. 4.6*. Obtained pole figures support the presence of calcite and quartz (*Fig. 4.6b, e, h*) textures in the Kali Gandaki valley, with low CPOs intensities of J-index=1.09-1.39 and M-index=0.02-0.04 for calcite. Quartz CPOs are also low, with J-index of 1.16 and M-indexes of 0.01 (almost close to a total random crystallographic orientations' distribution, see Skemer et al., 2005).

With the exclusion of the uppermost sample K21-10-12a (*Fig. 4.6a*), calcite pole figures are quite similar from lower to higher structural levels. Calcite [*c*]-axes pole figures support weak but well-defined broad asymmetric maxima in the Z-direction (almost normal to the foliation) with an auxiliary central girdle (normal to the X-direction). In sample K21-10-12 (*Fig. 4.6c*), [*c*]-axis maxima are distributed in broad orthorhombic maxima in the Z-direction; moreover, auxiliary central girdle has a dextral asymmetry. The <*a*>-axes are distributed in a girdle parallel to the XY-direction, supporting no-evidences for strong rhomb<*a*> slip, coherently with the $r(10\bar{1}4)$ small circle distribution (*Fig. 4.6c*). Moreover, the poles to the {*e*}-planes define two couples of strong maxima on the Z-direction, supporting that {*e*}-twinning developed in calcite close to a pure shear flow (Wenk et al., 1987).

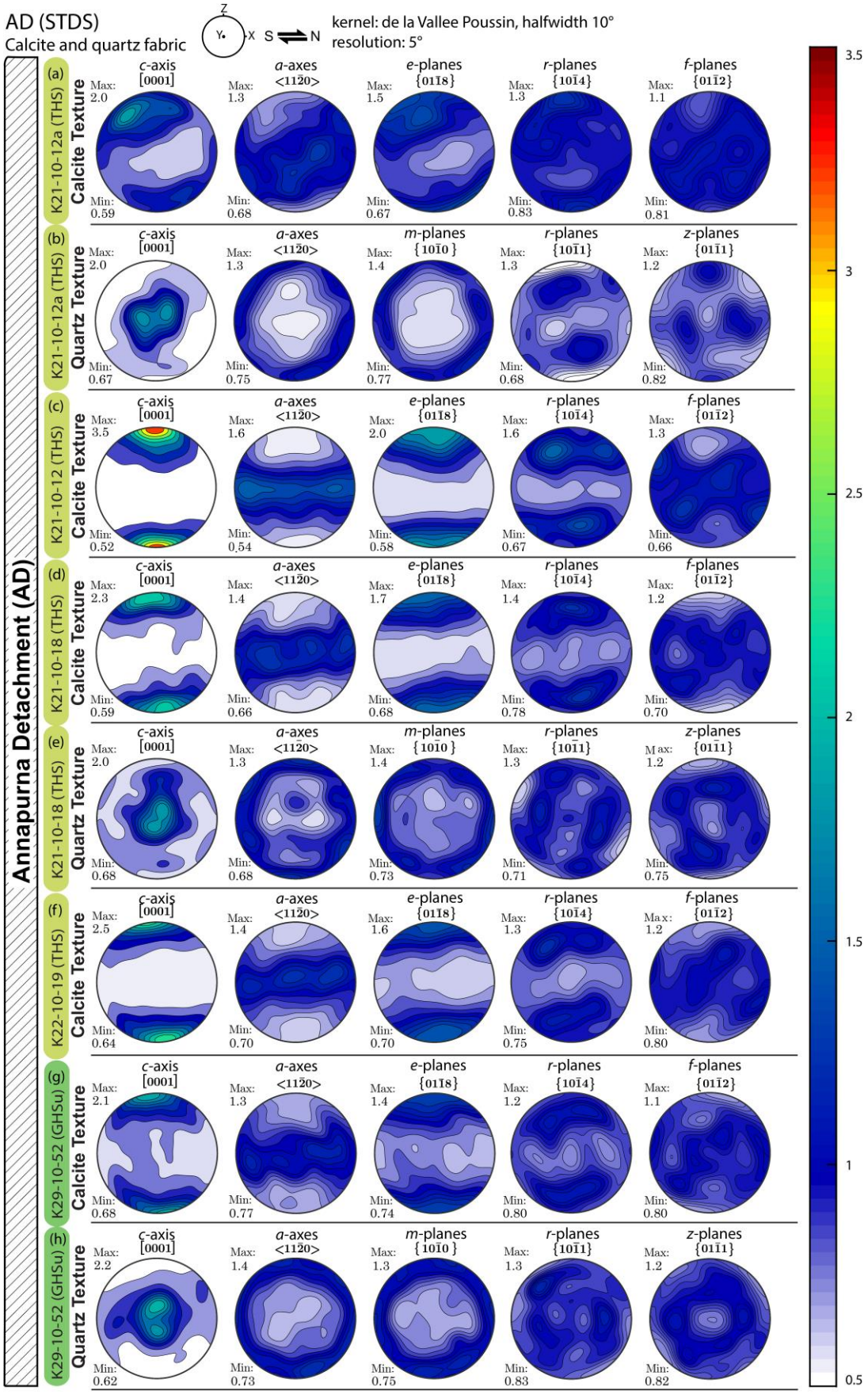

Figure 4. 6. *Calcite and quartz pole figures (equal area projection, lower hemisphere). Each row shows calcite or quartz texture for one sample (on the left side, the type of mineral texture is reported). Specimens are listed from top to bottom along the structural profile (see Fig. 4.3). Colour bar chart indicates multiples of uniform distribution (equals to 1.0) of CPO. All pole figures view towards the west on projection plane and refer as reference frame to the foliation pole (Z) and mineral lineation (X).*

In samples K21-10-18, K22-10-19, and K29-10-52 (*Fig. 4.6d, f, g*), [*c*]-axis maxima and <*a*>-*ax*es girdles, poles to {11$\bar{2}$0}, have an anticlockwise asymmetry (toward the south), indicating that the deformation occurred in a non-coaxial flow (Wenk et al., 1987). From bottom to top, along the AD profile, textures asymmetries decrease (*Fig. 4.6c, d, f, g*) supporting a heterogeneous deformation (Kern and Wenk, 1983; Wenk et al., 1987). Moreover, strong {*e*}-planes {01$\bar{1}$8} pole maxima (with a subsidiary central girdle) have strong anticlockwise asymmetry, pointing toward the south (*Fig. 4.6d, f, g*). This indicates that the non-coaxial deformation recorded had a top-down-to-the-north sense of shear, as {*e*}-twinning determines a specular rotation on the {*e*}-plane of the host crystal in general shear flows (Kern and Wenk, 1983; Schmid et al., 1987; Wenk et al., 1987; Ratschbacher et al., 1991; Erskine et al., 1993; Leiss et al., 1999; Leiss and Molli, 2003; Lacombe, 2010). Poles to the rhombic planes {10$\bar{1}$4} and {01$\bar{1}$2} are consistent with weak small circles distributions (*Fig. 4.6d, f, g*), supporting minor intracrystalline deformation (Schmid et al., 1987). In the uppermost sample (K21-10-12a), calcite [*c*]-axes pole figures support weak and poorly-defined CPO, with peripheral girdle and minor asymmetric maxima close to the Z-direction (*Fig. 4.a*). Such asymmetry is consistent with the asymmetric distribution of the <*a*>-*ax*es and the poles to the rhombic planes and {*e*}-planes.

Quartz textures were investigated along both XZ and YZ planes, to analyze a larger fraction of sample and to more accurately recalculate the ODF since this mineral is concentrated only in discrete layers embedded within calcite rich-matrix. Although quartz is not representative for the kinematic flow conditions and is affected by the strong partitioning of the deformation, textures are weak but defined (*Fig. 4.6b, e, h*). Quartz [*c*]-axes pole figure patters (*Fig. 4.6b, e, h*) correspond to asymmetric and incomplete Type I crossed girdle (Schmid and Casey, 1986). This asymmetric pattern is coherent with a north-directed flow (see also Passchier and Trouw, 2005). Dominant prism <*a*> slip and minor mix of basal <*a*>, and rhomb <*a*> slip systems supported maxima of <*a*>-*ax*es and {*m*}-planes, as well as the pole to the rhombic {*r*}-planes and {*z*}-planes. For the uppermost sample, K21-10-12, quartz [*c*]-axis maxima (*Fig. 4.6b*), synthetic to the Annapurna Detachment shearing, indicate that in calcite (*Fig. 4.6a*) the central auxiliary girdle, northward rotated, is a relic of intracrystalline deformation developed during the non-coaxial flow. Therefore, orthorhombic [*c*]-axis and {*e*}-planes maxima support that calcite was reoriented by {*e*}-twinning in a coaxial flow. The other quartz textures (*Fig. 4.6e, h*) confirm the calcite-textures interpretation for samples K21-10-18 and K29-10-52, developed by intracrystalline slip and twinning during the non-coaxial flow of the AD. Moreover, pole figures (*Fig. 4.6e, h*) support that quartz intracrystalline deformation was accommodated during the AD ductile activity, at "typical" deformation temperatures (according with to the mixed <a> slip observed in quartz), in the THS, between 400-500 °C (Mainprice et al., 1986; Schmid and Casey, 1986).

4.4. Finite strain analysis and kinematic of the flow of the Annapurna Detachment

Finite-strain analysis was carried out on six oriented impure marbles (*Table 4.3*), using the centre-to-centre method (Fry, 1979) on thin sections approximating the XZ plane of finite strain ellipsoid. About 100-225 calcite crystals for each sample were measured (vacancy corrected for the exponential edge detection method, EED, of Waldron and Wallace, 2007). Recrystallized calcite crystals (selected strain markers, 220-350 centroids), have an almost homogeneous grain size distribution (*par. 4.1*) without clusters.

Since calcite is dynamically recrystallized, crystals centroids do not only depend on the strain amount, but also on the differential stress. Therefore, the adopted method provides a minimal estimate of the finite strain. The calculated finite-strain equivalent ellipse ratio (R_{XZ}) subtle increases down-section within the Annapurna Detachment vertical profile, varying from 1.24 to 1.58 (*Table 4.3, Fig. 4.7*).

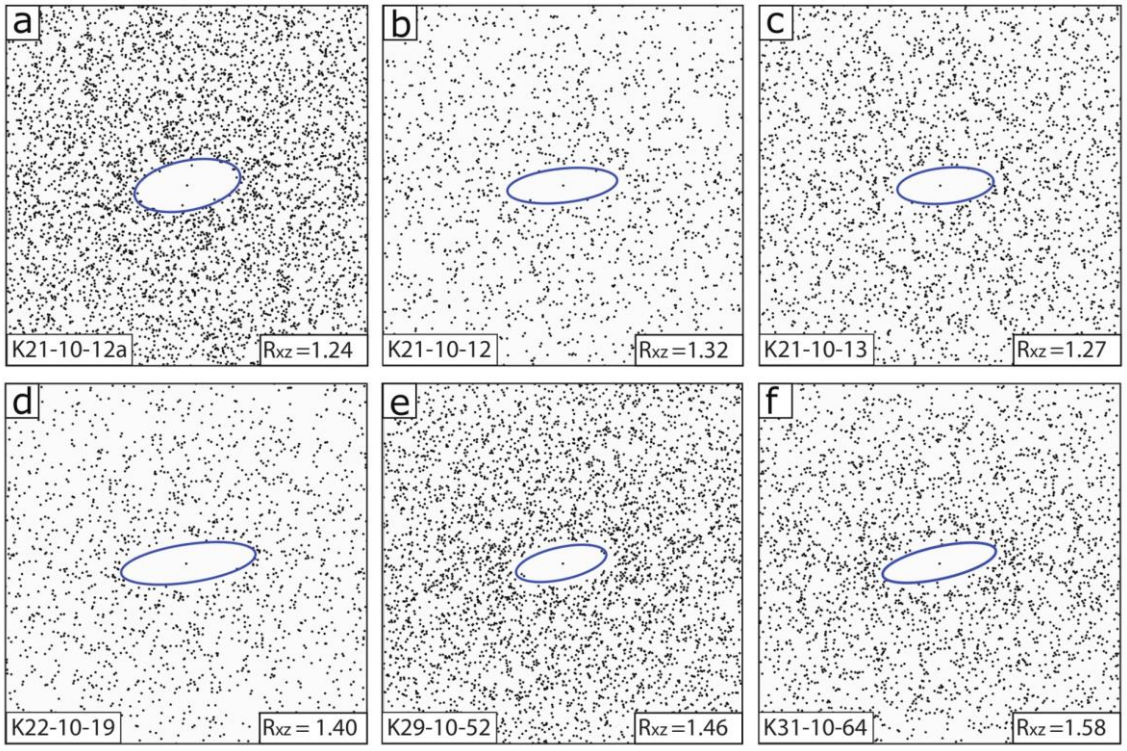

Figure 4. 7. *Results of the finite strain analysis (Fry plots) for selected samples. Low-density areas are defined through the exponential edge detection method (EED) of Waldron and Wallace (2007).*

Sectional vorticity number (Wn) and mean kinematic vorticity (Wm) were estimated in four samples through both Wenk et al. (1987) texture-based method, and Wallis (1995) oblique foliation-based method. Both methods were applied adopting the same reference frame (main foliation, S2). As the Annapurna Detachment is a mature shear zone, the main foliation is almost parallel with the shear zone boundaries.

Wallis (1995) method was applied on samples (K21-10-12, K21-10-13, K22-10-19, and K29-10-52) where oblique foliations (Sb) were recorded (e.g. *Fig. 4.3*). Measuring the δ angle between the Sb and the main foliation S2 (for only ca. 10 oblique foliations in each sample, e.g. *Fig. 4.3*), angles decrease up-section from ca. 26 to 20° (*Table 4.3*). According to Wallis (1995), the corresponding mean kinematic vorticity values (Wm) range between 0.79-0.64 from bottom to top (*Table 4.3*).

Wenk et al. (1987) method was applied in three samples (K21-10-18, K22-10-19, K29-10-59) as calcite textures were monocline and deformed by twinning and intracrystalline slip. In the study samples, the angle progressively decreases up-section (*Table 4.3, Fig. 4.8*), from ca. 15 to 10°, supporting a pure-shear dominated flow with a contribution from ca. 50% to ca. 30% of simple shear (*Table 4.3*).

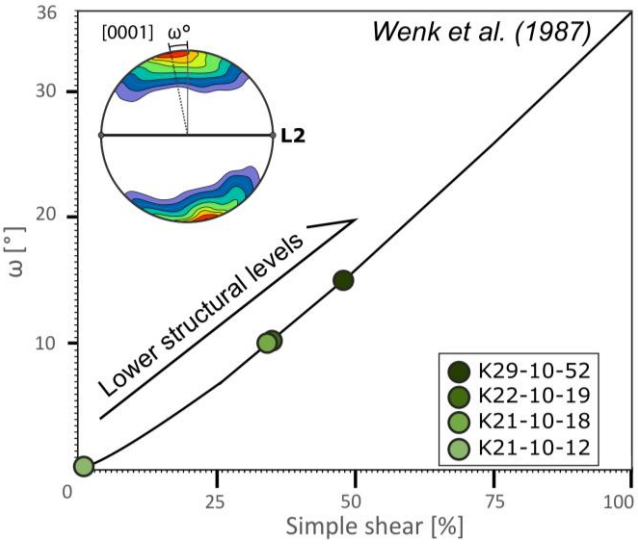

Figure 4. 8. *Simple shear estimates based on the Wenk et al. (1987) method. An increase of the simple shear contribution occurs from higher to lower structural levels along the vertical profile of the AD.*

Assuming monocline plane strain deformation (supported by quartz textures, *Fig. 4.6e, h*), the simple shear percentages correspond to sectional vorticity numbers (Wn) of 0.71 to 0.45 from bottom to top (*Table 4.3*). As for the case of the Manaslu area, kinematic vorticity estimates vary considerably for the two methods applied and an in-depth discussion is provided in Chapter 7 (*par. 7.2.5*).

Finite-strain ratios R_{XZ} (*Fig. 4.7*) and kinematic vorticity estimations (*Fig. 4.8*) have been combined to derive the shortening perpendicular to the shear zone though the Wallis et al. (1993) equation (*par. 2.2.2*). Adopting the mean kinematic vorticity (Wm) estimated through Wallis (1995) method, the "maximum" shortening ranges between 0.89-0.92 (*Table 4.3*), corresponding to perpendicular shortening of 8-11%. Using the sectional kinematic vorticity (Wn) estimated through Wallis (1995) method, the "maximum" shortening ranges between 86-87% (*Table 4.3*), corresponding to perpendicular shortening of 13-14%.

Table 4.3*. Results from finite-strain and simple shear analyses. Rxz = Axial ratios from the ellipse voids (Waldron and Wallace, 2007); δ°= angle between the main foliation (Sp) and the oblique foliation (Sb); Wm = mean vorticity number (after Wallis, 1995); S = shortening; ω° = angle between the main <c> axes orientation and the plane normal to the foliation; Wn = sectional vorticity number obtained from the Wenk et al. (1987) method. ND – non detected.*

Sample	Rxz	δ° (Sb angle)	simple shear %	Wm (Wallis, 1995)	S (Rxz, Sb)	ω° [*c*]-axis	simple shear %	Wn (Wenk et al., 1987)	S
K21-10-12A	1.242	*ND*	*ND*	*ND*	*ND*	*ND*	*ND*	*ND*	*ND*
K21-10-12	1.322	20	41	0.64	0.92	*ND*	*ND*	*ND*	*ND*
K21-10-13	1.270	23	46	0.72	0.91	*ND*	*ND*	*ND*	*ND*
K22-10-18	*ND*	*ND*	*ND*	*ND*	*ND*	10	30	0.45	0.86
K22-10-19	1.403	25	49	0.77	0.90	10	30	0.45	0.86
K29-10-52	1.463	26	50	0.79	0.89	15	50	0.71	0.87

4.5. Summary of data on the Kali Gandaki valley

- Eleven samples have been studied along a N-S transect from the Annapurna Detachment (AD), the local segment of the ductile South Tibetan Detachment System. Calcite microstructures and calcite and quartz textures (studied through an X-ray Texture goniometry) have been characterized on mylonitic marbles. The metamorphic mineral assemblage supports an up-section temperature decrease from the GHS_U to the THS.
- Texture and microstructures indicate that calcite in the GHS_U and THS marbles deformed by grain boundary mobility (grain boundary migration and subgrain rotation recrystallization mechanisms from bottom to top) and by twinning under a top-to-the-north non-coaxial flow at reasonable temperatures from 550-400 °C (from the GHS_U to the THS).
- Calcite grain size decreases up-section, supporting differential stress of 6-14 MPa under strain rates of 10^{-11}-10^{-10} s^{-1} for temperatures of 400-450 °C. Calcite twins support differential stress of ca. 135-170 MPa under similar strain rates for temperatures of 300-350 °C.
- An almost constant general shear flow (30-50% of simple shear) has been obtained adopting the “orientation of oblique grain shape fabrics” and the texture-based method (influenced by twinning). These estimates, coupled with finite strain analysis on calcite, support a perpendicular shortening of 13-14%.

5. Lower Dolpo Region

The Dolpo area is the largest and least accessible district of Nepal (Karnali Pradesh province, Western Nepal), with an extension of about 8,000 km^2 divided into two regions: the Lower and the Upper Dolpo. The Lower Dolpo (*Fig. 5.1*) is a key area for studying the Himalayan shear zones, since the MCTz and the STDS crop out at in a few kms, and are spectacularly exposed in the arid and deep nearly NS-trending valleys (*Fig. 5.1*). During this work, a collection of over twenty field-oriented samples belonging to the LHS, the GHS, and the THS, from an almost N-S transect between Kangmara La and Dunai village (*Fig. 5.1*) (Frank and Fuchs, 1970; Fuchs, 1977; Carosi et al., 2002, 2007; DeCelles et al., 2020) have been studied. Study samples from the LHS are greenschist facies phyllite, quartzite, garnet-bearing micaschist and kyanite-bearing quartzite (Frank and Fuchs, 1970; DeCelles et al., 2001; Robinson et al., 2006; Carosi et al., 2007) deformed by the MCTz activity (*Fig. 5.2, Fig. 5.3*). The GHS_L is made up of greenschist to amphibolite facies paragneiss, quartzite, and quartz-bearing mica schist, varying up-section from the garnet-zone, up to the kyanite-zone (*Fig. 5.3*, Carosi et al., 2007). The GHS_U, at higher structural levels, consists of amphibolite-facies migmatite and orthogneiss, which pass upward to a thick sequence of amphibolite-facies calcsilicate-rich gneiss and white marbles (Fuchs et al., 1988; Carosi et al., 2002, 2007, 2019). Above, the THS metamorphic series consists of greenschist crystalline limestones, which pass progressively up-section to non-metamorphic marine sediments (Frank and Fuchs, 1970; Fuchs, 1977; Carosi et al., 2007). Of the main deformation phases, SW-verging isoclinal folds (F1) related to the D1 phase are preserved from the mega to the microscale only within the low- to non-metamorphic sequence of the THS, well above the STDS upper limit (Carosi et al., 2002, 2007, 2010). Structures regionally associated to the D2 phase are represented by the MCTz, the HHD and the STDS, characterized by huge sheared volumes even if the detailed definition of their upper and lower limits are not always clear.

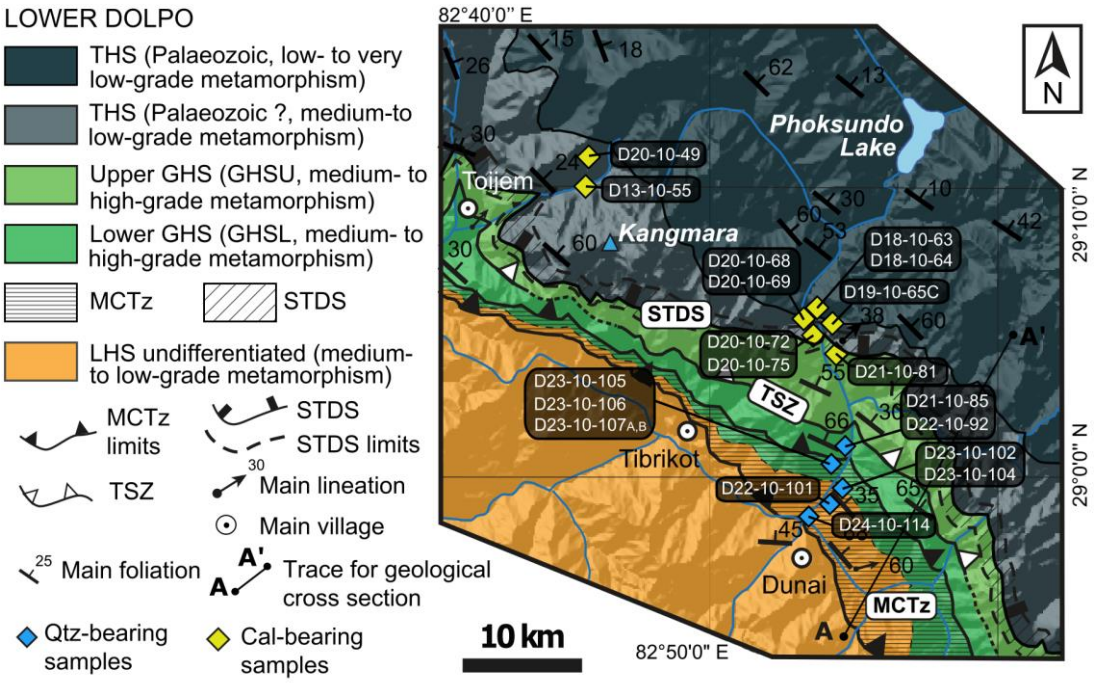

Figure 5. 1. *Geological sketch map of Lower Dolpo region (modified after Carosi et al., 2018). The blue pointers correspond to the samples used to define and localize the MCTz, whereas the orange diamonds correspond to the samples used to define the STDS.*

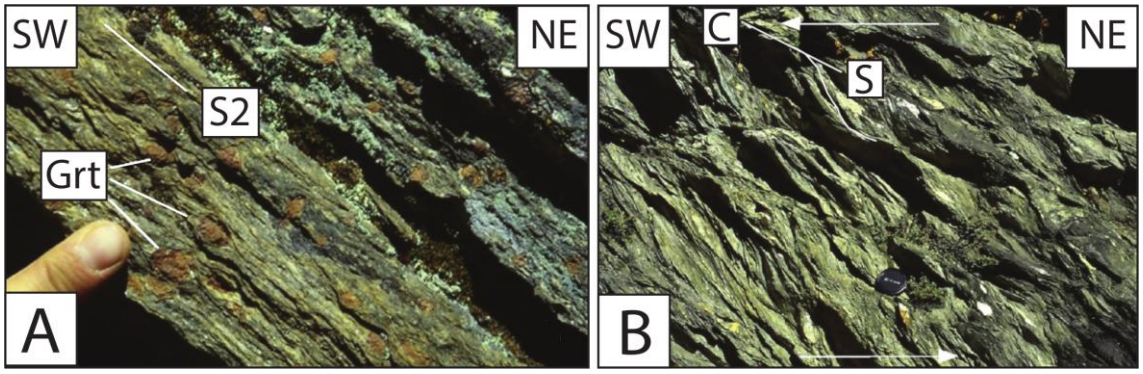

Figure 5. 2. *Outcrop photoes from the Main Central Thrust zone in the Lower Dolpo (Carosi et al., 2007). (**a**) Garnet-bearing micaschists in the LHS. (**b**) phyllites in the Main Central Thrust zone base.*

The MCTz crops out with a variable thickness of 1–5 km (*Fig. 5.3*), involving the upper part of the LHS and the basal portion of the GHS_L. At the microscale, the S1 foliation is poorly recorded and mainly transposed by the dominant and pervasive S2 foliation, being recognizable only in the microlithons of the spaced S2 foliation and/or as an internal foliation within inter-tectonic porphyroblasts (after Passchier and Trouw, 2005). The S2 foliation, marked by muscovite and biotite, strikes parallel to the MCTz boundaries varying up-section from a spaced to a continuous foliation. In some samples, the S2 completely transposes the previous S1 foliation (*Fig. 5.4*). The HHD, between the GHS_L and the GHS_U, is represented by the Toijem Shear Zone (TSZ), a 40–50 m- high-temperature intra-GHS discontinuity (*Fig. 5.1, Fig.5.3*) (Carosi et al., 2010, 2018, 2019). Both the MCTz and the HHD show kinematic indicators coherent with the top-to-the-southwest sense of shear (Carosi et al., 2010, 2018, 2019). The STDS cropping out in the Lower Dolpo (*Fig. 5.1, Fig.5.3*), couples the calcsilicates-bearing marbles of the GHS_U and the low-grade marbles of the THS, with a structural thickness of 1-2 km (Carosi et al., 2002, 2007, 2013). Kinematic indicators at the mesoscale support the top-down-to-the-east/northeast sense of shear (Carosi et al., 2002). In the Upper Dolpo Region, ca. 50 km westward to the study area, the lower limit of ductile activity of the STDS is constrained at 23–25 Ma by zircon and monazite U-(Th)-Pb dating of the undeformed Bura Buri leucogranite, intruding both GHS and THS (*Fig. I*), and crosscutting the STDS (Bertoldi et al., 2011; Carosi et al., 2013). Above the upper limit of the STDS, the D2 resulted in northeast-verging, tight, km-scale folds in the THS (Carosi et al., 2002, 2007). These structures are associated to a spaced crenulation cleavage, S2, parallel to the STDS boundaries, deforming the older foliation S1. In some cases, the S1 can be observed in thin sections within microlithon domains (*Table 5.1*).

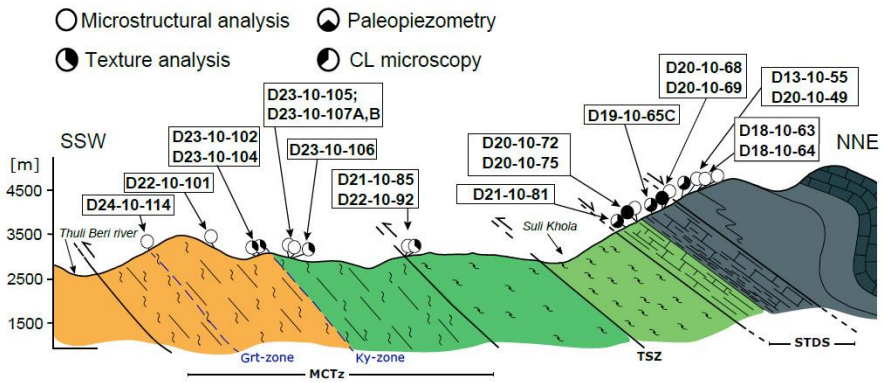

Figure 5. 3. *Geological cross section of A-A' trace of Fig. 5.1 (modified after Carosi et al., 2007) and study samples. TSZ: Toijem Shear Zone, local segment of the HHD.*

5.1. Sample description and results for the Main Central Thrust zone

Fabric analysis was carried out on ten field-oriented samples from the MCTz from both LHS- and GHS_L- protolith affinity rocks, belonging to different structural levels (*Fig. 5.1, Fig. 5.3*, *Table 5.1*).

Table 5.1. *Compilation of main features of study samples and related type of analyses. Abbreviations: fol. – foliation; Bt – biotite; Cal – calcite; Chl – chlorite; Cpx – clinopyroxene; Dol – dolomite; felds – feldspar; Grt – garnet; Kfs – K-feldspar; Ky – kyanite; Pl – plagioclase; Qtz – quartz; Sil – sillimanite; Wm – white mica; GBM – grain boundary migration; SGR – subgrain rotation recrystallization; SPO – shape preferred orientation.*

	Sample	Lithology	Mineral Assemblage	Deformation mechanisms	Analysis	Fabric
THS	D18-10-63	impure marble	Cal+Qtz+Bt+Wm	Quartz: pressure solution Calcite: rare Twin Type I	◕	S1 (continuous fol. Wm) + S2 (crenulation fol., Wm)
	D18-10-64	carbonate-rich metapelite	Qtz+Cal+Ab+Wm +Bt	Quartz: annealing Calcite: annealing	○	S2 (continuous fol., Wm)
	D20-10-49	carbonate-rich metapelite	Cal+Qtz+Ab+Wm +Bt±Ilm±Ap	Pressure solution	○	S1 (continuous fol., Wm) + S2 (spaced fol., Wm)
	D13-10-55	carbonate-rich metapelite	Qtz+Cal+Wm+Bt+ Chl	Quartz: pressure solution Calcite: Twin Type I	○	S1 (continuous fol., Wm) + S2 (spaced fol., Wm)
STDS	D20-10-68	carbonate-rich metapelite	Cal+Qtz+Kfs±Wm ±Bt±Chl	Quartz: annealing Calcite: annealing+Twin	◕	S2 (continuous fol., SPO Cal)
	D20-10-69	impure marble	Cal+Qtz+Pl+Kfs+ Wm+Bt	Calcite: GBM + Twin Type II	○	S2 (continuous fol., SPO Cal)
	D19-10-65	impure marble	Cal+Qtz±Bt±Wm± Chl	Calcite: GBM + Twin Type II	◕	S2 (continuous fol., SPO Cal)
	D20-10-72	Calc-silicate-bearing impure marble	Qtz+Cal+Dol+ bt±Cpx	Calcite: GBM + Twin Type II	○	S2 (continuous fol., SPO Cal)
GHS_U	D20-10-75	Calc-silicate-bearing impure marble	Cal+Dol+Wo+Bt± Qtz±Cpx	Calcite: GBM + Twin Type II	◕	S2 (continuous fol., SPO Cal)
	D21-10-81	Calc-silicate-bearing impure marble	Cal+Pl+Qtz+Bt+ Wm±Kfs±Cpx±Chl	Calcite: GBM + annealing + Twin Type II	◕	S2 (continuous fol., SPO Cal)

	Sample	Lithology	Mineral Assemblage			Fabric
GHS_L	D21-10-85	Ky-paragneiss (mylonite)	Qtz+Kfs+Pl+Bt+ Wm+ky	Quartz: GBM II; feldspars: ductile HT deformation	◔	S2 (spaced fol. by Wm)
	D22-10-92	Ky-paragneiss (mylonite)	Qtz+Kfs+Pl+Ky± Wm±Bt	Quartz: GBM II; feldspars: ductile HT deformation	○	S2 (spaced fol. by Bt)
	D23_10-107B	Ky+Grt paragneiss (mylonite)	Qtz+felds+Grt+ Ky+ Wm+Bt	Quartz: GBM I/GBM II	○	S2 (spaced fol. by Bt)
	D23-10-107A	Ky+Grt paragneiss (mylonite)	Qtz+felds+Ky+ Grt±Bt	Quartz: GBM I/GBM II	○	S2 (spaced fol. by Bt)
MCTz	D23-10-106	Ky+Grt paragneiss (mylonite)	Qtz+felds+Ky+ Wm+Bt+Grt±Chl	Quartz: GBM I	◔	S2 (spaced fol. by Bt)
	D23-10-105	paragneiss	Qtz+felds+Wm	Quartz: GBM I	○	S2 (spaced fol. by Wm+Bt)
	D23-10-104	quartzite	Qtz+Wm+Bt	Quartz: GBM I	◔	S2 (continuous fol. by Bt)
	D23-10-102	quartzite	Qtz+Bt±Pl	Quartz: GBM I	◔	S2 (continuous fol. by Bt)
LHS	D22-10-101	Grt-paragneiss (mylonite)	Qtz+felds+Ky+Bt +Wm±Grt	Quartz: GBM/SGR	○	S2 (spaced fol. by Bt)
	D24-10-114	Grt-paragneiss (mylonite)	Qtz+felds+Grt+ Bt+Wm±Chl	Quartz: GBM/SGR	○	S1 (continuous fol., Wm) + S2 (spaced fol. by Bt)

○ microstructural analysis; ◔ texture analysis; ◒ paleopiezometry

5.1.1. Structural analysis of the MCTz

As aforementioned, the exact definition of the MCTz limits is not strictly recognizable at the mesoscale. However, within the MCTz, both LHS- and GHS_L- protolith affinity samples are sheared. They are represented by highly (compositionally/structurally) heterogeneous quartzite, quartz-rich paragneiss, and garnet-bearing mica schist (*Fig. 5.4a-h*).

In samples, top-to-the-south sense of shear is confirmed by S-C-C' fabrics, snowball garnet, mineral fish (mica, garnet, plagioclase, and kyanite fish), and porphyroclasts with asymmetric strain shadow (*Fig. 5.4c, d, g, h*). From bottom to top, the S-C fabrics are marked by syn-kinematic recrystallization of white mica and biotite while, at low structural level, within the LHS, the C' bands are defined by chlorite and opaque minerals (*Fig. 5.4g*).

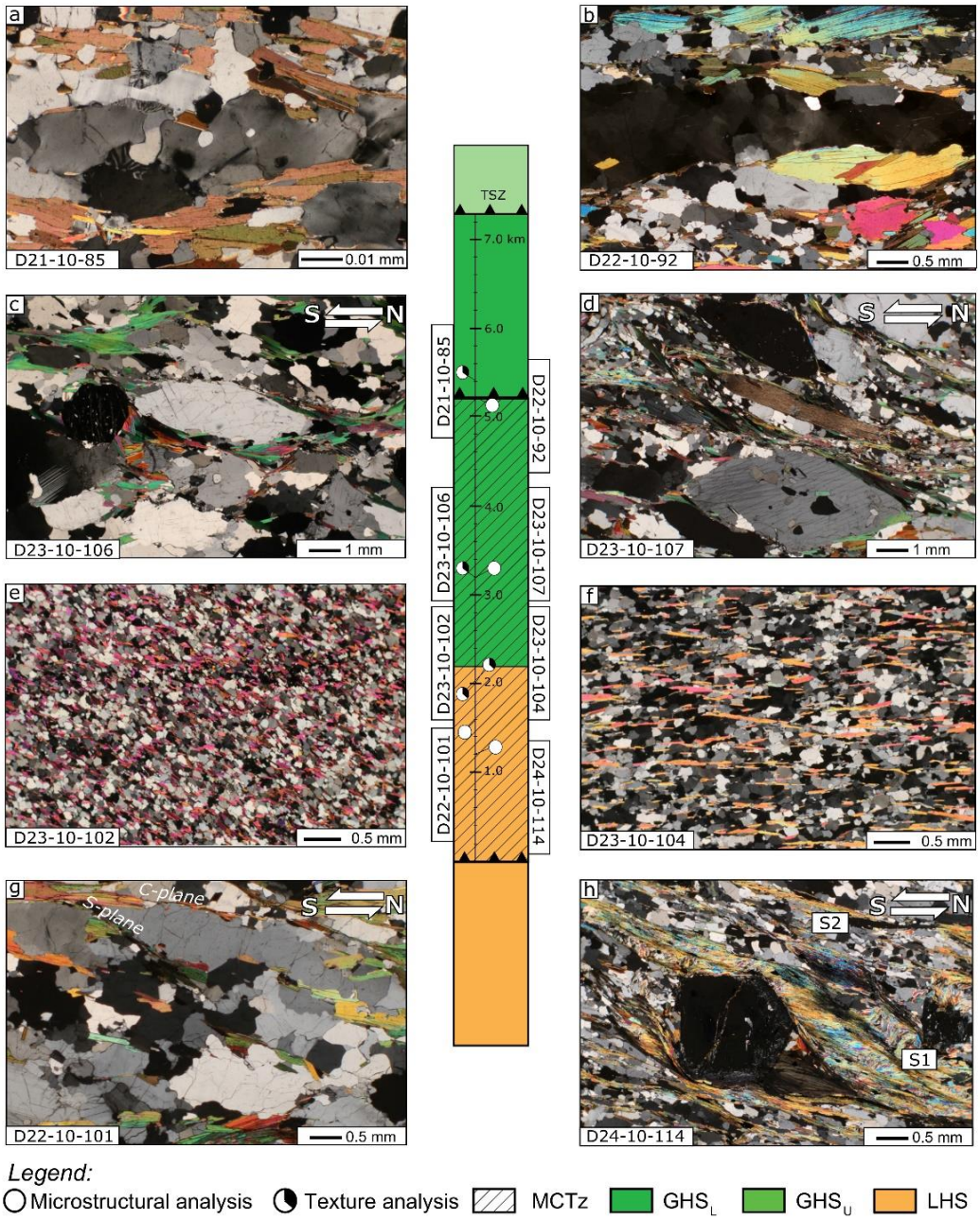

Figure 5. 4. *Optical microphotos of the selected samples along the MCTz (and main analyses performed).* ***(a)*** *GHS$_L$ mica schist, with HT-related myrmekite in feldspar.* ***(b)*** *GHS$_L$ mica schist with chessboard subgrain microstructures in quartz (GBM type II).* ***(c)*** *GHS$_L$ garnet-bearing paragneiss, with MT-related microstructures of GBM type I in quartz.* ***(d)*** *GHS$_L$ kyanite-bearing paragneiss, with S-C fabric and kyanite, plagioclase, and garnet fishes, coherent with a top-to-south sense of shear.* ***(e)*** *LHS mica-bearing quartzite.* ***(f)*** *LHS mica-bearing quartzite.* ***(g)*** *LHS paragneiss with GBM type I in quartz and S-C fabric (top-to-south sense of shear).* ***(h)*** *LHS garnet-bearing schist with a spaced foliation S2 and relics of crenulated S1 foliation. The coarse-grained garnet in the middle is replaced by chlorite along the grain boundaries. The small garnet grain on the right is an inter-tectonic porphyroblast.*

Within the study samples, quartz is the most abundant mineralogical phase, with a mode always exceeding 20% in volume of the sample. Therefore, quartz can be interpreted as the weak matrix/interconnected granoblastic layers, supporting the deformation (Handy, 1994). Feldspar, garnet, and kyanite grains, *vice versa*, behaved mostly as mechanically strong clasts (Handy, 1994), although, in the uppermost structural levels, feldspars are deformed by mechanical twinning and myrmekitic recrystallization (*Fig. 5.4a*).
Intra-crystalline subgrains and slight bimodal distributions of quartz grain sizes indicate a plastic deformation occurred by dynamic recrystallization processes dominated by subgrain rotation (SGR) and grain boundary migration (GBM) recrystallization at lower structural levels. Up-section, quartz fabric evolves with lobate and interconnected grain boundaries, undulose extinction, and unimodal grain size distributions. Quartz microstructures can be reconducted to GBM type I mechanisms (GBM_I) (*Fig. 5.4f*, Kruhl, 1996; Passchier and Trouw, 2005; Law, 2014). Up-section, chessboard microstructures in quartz support GBM type II (GBM_{II}) mechanisms of dynamic recrystallization (Kruhl, 1996; Passchier and Trouw, 2005; Law, 2014; *Fig. 5.4b*).

5.1.2. Quartz texture analysis of the MCTz

Three homogeneous quartz-rich tectonites from different structural levels (D23-10-102; D23-10-104; and D21-10-85) were selected for studying the quartz CPO patterns (*Fig. 5.5a-d*) through the X-Ray Texture Goniometer (XTG), using the foliation as reference frame (e.g. see *Fig. 5.5* for biotite texture as reference frame). Data from one more sample (D23-10-106), analysed by a Neutron Texture Goniometer SKAT (ND) at the IBR-2 reactors in Dubna, Russia, were processed through MTex Toolbox (*Fig. 5.5b*). This sample, a heterogeneous garnet and kyanite-bearing paragneiss, was analysed with this apparatus since quartz has a grain size too coarse for the XTG; therefore, not statistical representative for the full quartz texture (Fazio et al., 2017).

Results of the texture analyses support the presence of quartz textures, with asymmetric [*c*]-axis and <*a*>-*ax*es patterns. Sinistral asymmetries are coherent with a top-to-the-south non-coaxial flow, highlighting that quartz CPO developed during the MCTz ductile activity for the three lower samples (D23-10-102; D23-10-104; D23-10-106). *Vice versa*, an almost symmetric geometry is recorded in the structurally highest-located sample D21-10-85. Quartz CPO intensity, expressed by the J-index (Bunge, 1982), ranges between 1.13-1.64, corresponding to low M-index of Skemer et al. (2005) of 0.01-0.07. The uppermost structurally located sample, D21-10-85, however, has much lower CPO intensity, close to a total random distribution, with values of M-index of Skemer et al. (2005) of 0.005. Within the MCTz, from lower to higher structural levels, quartz textures vary according to the described microstructures. In the homogeneous quartzite D23-10-102, which is the structurally lowest-located sample (*Table 5.1, Fig. 5.4e*), quartz [*c*]-axes pole figure (*Fig. 5.5d*) points to an incomplete crossed girdle pattern. This pattern can be the result of $\{10\bar{1}1\}<11\bar{2}0>$ (rhomb <*a*> slip system) and minor $\{10\bar{1}0\}<11\bar{2}0>$ (prism <*a*> slip system, Schmid and Casey, 1986). Quartz [*c*]-axes pole figure is coherent with the <*a*>-*ax*es pole figure $<11\bar{2}0>$ and with the {*m*}-planes $\{10\bar{1}0\}$ pole figure. On $<11\bar{2}0>$, <*a*>-*ax*es maxima support the strongest contribution of the rhomb <*a*> slip system, with a Burger vector subparallel to the lineation trend (*Fig. 5.5d*). According to Mainprice et al. (1986) and Schmid and Casey (1986), this type of quartz texture develops at deformation temperature of ~400–500 °C.

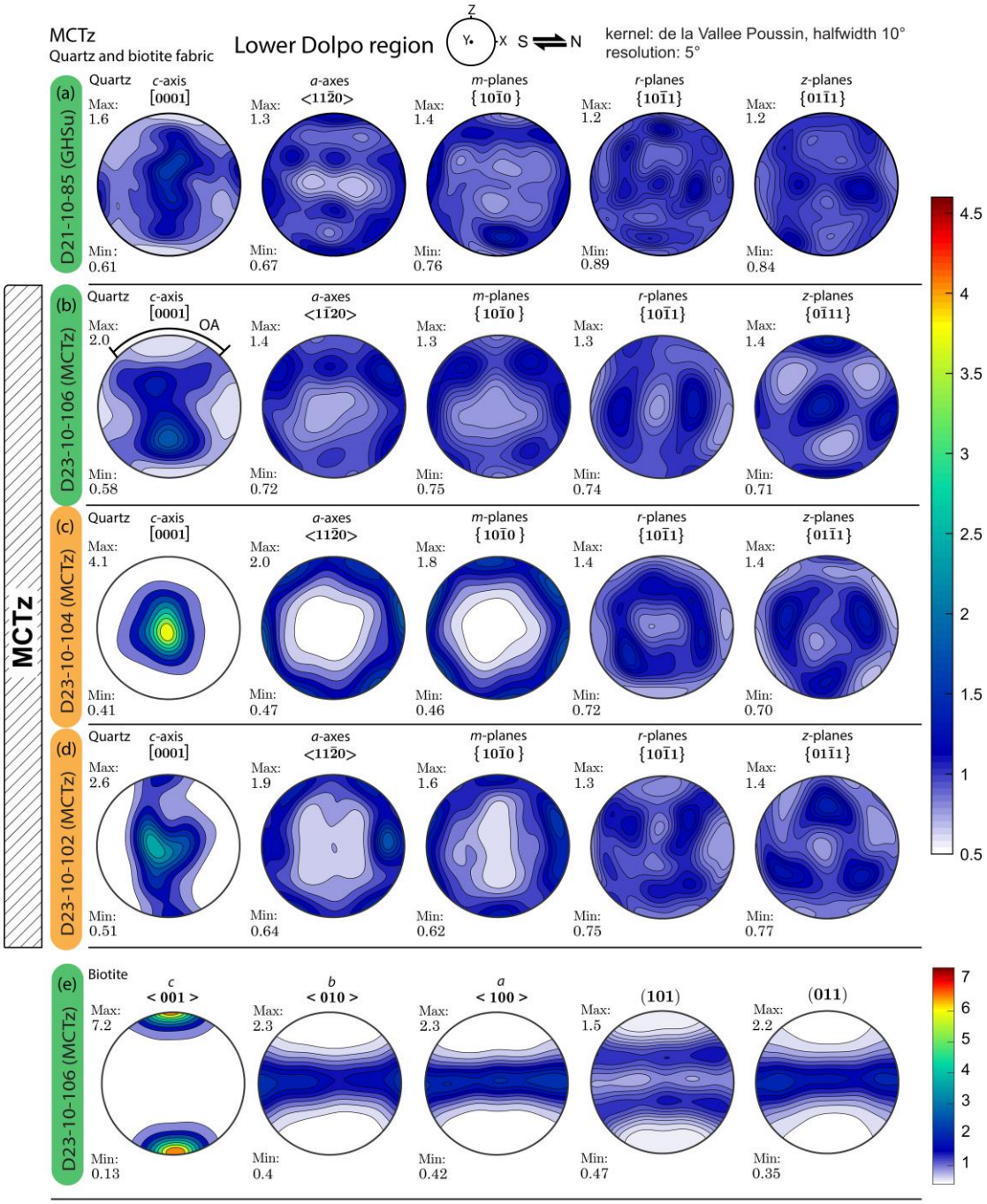

Figure 5. 5. *Quartz and biotite pole figures, equal area lower hemisphere stereographic projection. All pole figures view towards the west on projection plane and refer as to the foliation (Z) and mineral lineation (X). Colour bar chart indicates multiples of uniform distribution (equals to 1.0) of CPO.* ***(a)*** *Low CPO of quartz with HT-related pattern in the GHS_L above the upper limit of the MCTz.* ***(b)*** *Quartz [c]-axis and a-axis maxima support the top-to-south non-coaxial flow of the MCTz through crossed-girdle pattern GHS_L in the MCTz,* ***(c)*** *the Y-max pattern at the top of the LHS and (**d**) the incomplete crossed-girdle in the LHS. (**e**) Biotite texture as reference frame for foliation (sample D23-10-106).*

Upward, in the quartzite D23-10-104, with an LHS-protolith affinity (*Table 5.1, Fig. 5.4f*), the quartz [*c*]-axes pattern evolves to a Y-max pattern ([*c*]-axes maximum centered in the Y-direction of the finite strain axes). Y-max pattern on [0001] supports that quartz deformed plastically and recrystallized close to plane strain regime by prism <*a*> slip system (Schmid and Casey, 1986; Stipp et al., 2002; Passchier and Trouw, 2005; Toy et al., 2008; Law, 2014). The prism <*a*> slip is testified also by the three peripheral couples of maxima <*a*>-*ax*es and {*m*}-planes pole figure, in which Burger vector is subparallel to the lineation trend (*Fig. 5.5c*). According to Mainprice et al.

(1986) and Schmid and Casey (1986), quartz [*c*]-axes Y-axis point maxima develop for deformation temperature between 500–600 °C. Northward, along the MCTz, in sample D23-10-106 belonging to the base of the GHS_L (*Fig. 5.4c*), the quartz [*c*]-axes pole figure patter (*Fig. 5.5b*) corresponds to a complete Type I crossed girdle (Schmid and Casey, 1986), coherent with a plane strain regime (see also Passchier and Trouw, 2005). Dominant prism <*a*> slip and minor mix of basal <*a*>, and rhomb <*a*> slip systems supported maxima of <*a*>-*ax*es and {*m*}-planes, as well as the pole to the rhomb {*r*}-planes and {*z*}-planes. The complete Type I crossed girdle on [0001] defines a wide opening-angle of ~95° that, according to Faleiros et al. (2016) corresponds to deformation temperature of 695 °C. The uppermost analyzed kyanite-bearing paragneiss D21-10-85, belonging to the GHS_L (*Fig. 5.4*), has weak [*c*]-axis maxima broadly spread in a girdle in the YZ-direction (*Fig. 5.5a*), with a couple of further maxima in the X-direction (parallel to the lineation). The single strong maxima of ca. 2.4 is probably related to a single coarse grain. This pattern supports the development of prism <*a*> and rhomb <*a*> slip systems (Mainprice et al., 1986; Schmid and Casey, 1986; Toy et al., 2008). Maxima on the $<11\bar{2}0>$ and $\{10\bar{1}0\}$ are not clear enough to relate the [*c*]-axis maxima in the X-direction to the prism <*c*> slip system. However, by coupling the chessboard subgrains and to the slightly synthetic orientation of the [*c*]-axis maxima, it is possible to infer the activity of the $\{10\bar{1}0\}<0001>$ slip system, supporting a deformation temperatures above 650 °C (Kruhl, 1996).

5.2. Sample description and results for the South Tibetan Detachment System

Fabric analysis was carried out on ten field-oriented samples, both with GHS_U- and THS protolith affinity, belonging to different structural levels (*Fig. 5.6*, *Fig. 5.7*, *Table 5.1*).

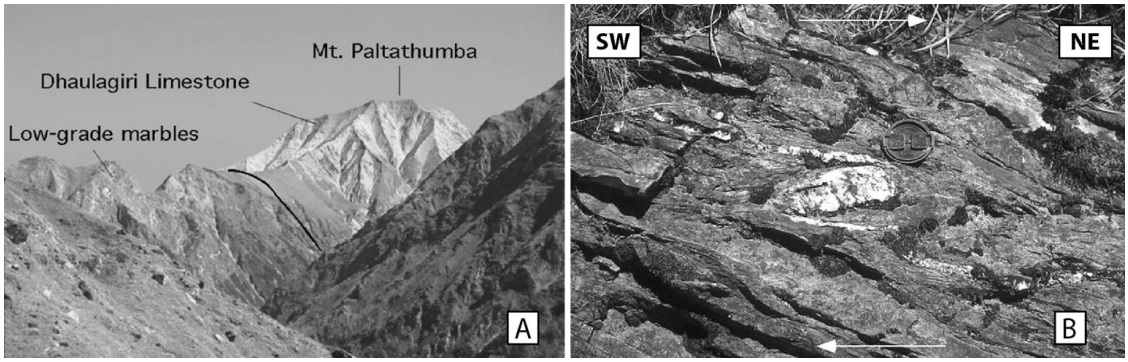

***Figure 5.6**. (**a**) Low-grade marbles of the THS at the STDS top in the Lower Dolpo (Carosi et al., 2007). (**b**) Rotated leucogranite dike (δ-type) in marbles at the THS base in the Lower Dolpo, indicating a top-to-the-northeast sense of shear (Carosi et al., 2002).*

5.2.1. Structural analysis of the STDS

In the Lower Dolpo Region, the STDS involves calcsilicate-bearing marbles of the GHS_U and impure marbles and carbonate-bearing metapelites of the THS (*Fig. 5.7*, *Table 5.1*). Very little kinematic indicators are present. Moreover, apparent similar lithology of the THS and the GHS_U makes difficult tracing the STDS at the mesoscale (see Carosi et al., 2002).

At the microscale, samples record two foliations: a continuous crenulated S1 foliation, occurring only at high structural levels in the low-metamorphic rocks of the THS (*Fig. 5.5a*), and a dominant S2 foliation (*Fig. 5.7b, c*), striking parallel to the STDS trend (*Fig. 5.7d-h*). The S2 foliation varies up-section from a continuous and pervasive foliation to a discrete and parallel spaced foliation (Passchier and Trouw, 2005) in the low-metamorphic samples of the THS (*Fig. 5.7a*).

At the base of the STDS, within the GHS_U, the continuous S2 foliation is marked by a grain shape preferred orientation (SPO) of calcite, biotite, white mica and calc-silicates (e.g. wollastonite, *Fig. 5.7g*), whereas up-section, within the THS, foliation is marked by biotite and calcite (± white micas). Therefore, from lower to higher structural levels along the STDS, a gradient of metamorphism occurs with a progressive upward decrease of temperature, from the amphibolite facies of the GHS_U-rocks down to the low-greenschist facies of the THS.

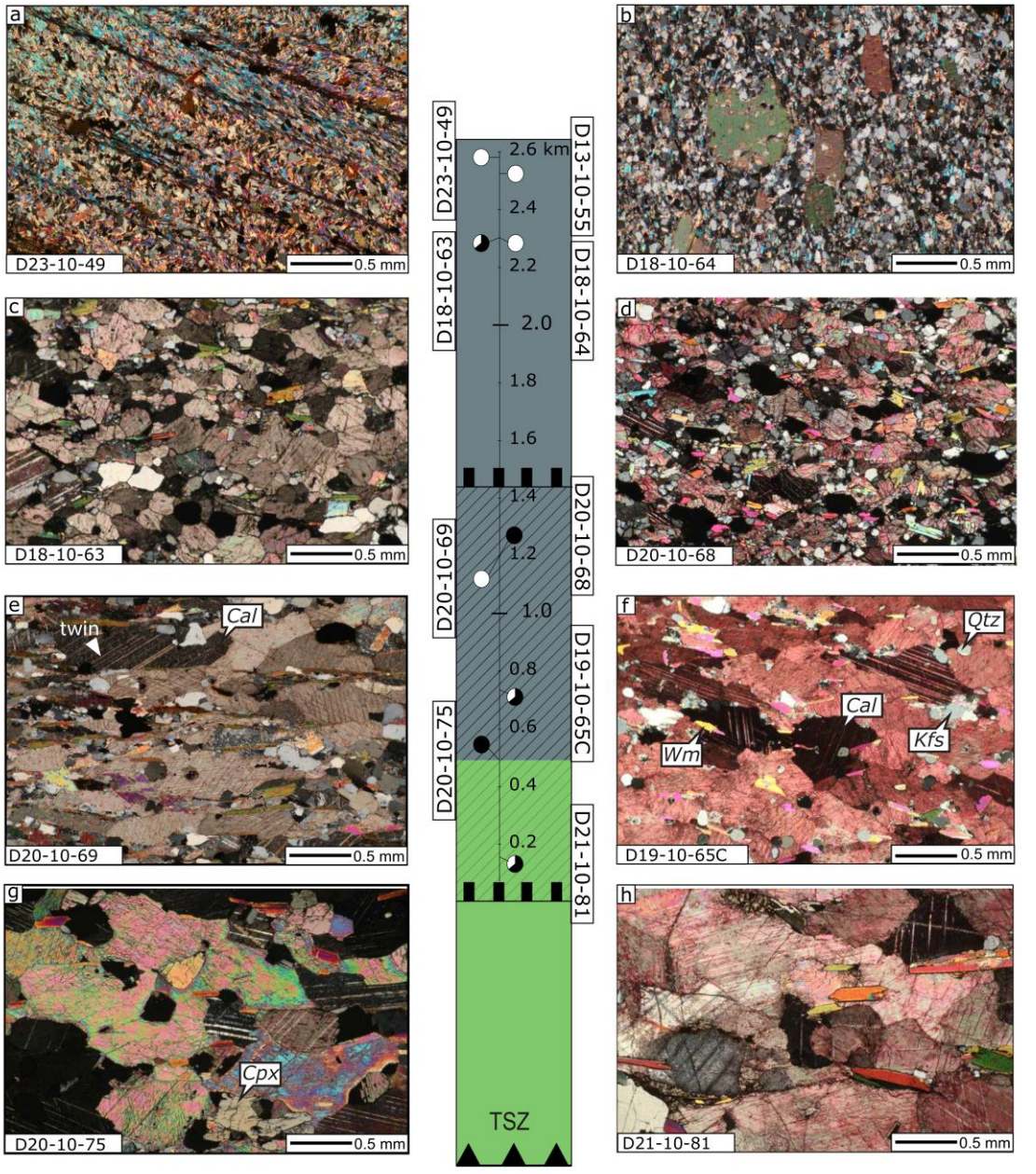

Figure 5. 7. *Optical micrographs of some key samples selected to define the STDS ductile shear zone in the Lower Dolpo (see Fig. 5.1, Fig. 5.3). The uppermost carbonate-bearing metapelite* ***(a)*** *and metapsammite* ***(b)*** *are low-grade THS greenschist-facies rocks above the upper limit of the STDS, where post-kinematic mm-size biotite overprint the S1 and S2 foliations.* ***(c)*** *Slightly deformed impure marble (THS).* ***(d)*** *Carbonate-bearing metapelite from the THS, in which calcite is deformed by twinning (sample stained with alizarine to highlight the rare dolomite).* ***(e-f)*** *THS impure marbles strongly deformed; calcite defines the S2 foliation being deformed by GBM mechanisms and twining (D19-10-65C was stained with alizarine to highlight the very rare dolomite). Quartz is isolated as strong clast in the calcite weak matrix.* ***(g)*** *Calc-silicate-bearing impure marble from the top of the GHS_U, in which the calcite weak matrix is deformed by GBM (defining the S2 foliation) and twinning.* ***(h)*** *Calc-silicate-bearing impure marble from the GHS_U, with straight calcite grain boundaries (sample stained with alizarine to highlight dolomite).*

From the upper structural levels of the STDS, up to almost 1 km above it in the THS (see *Fig. 5.3*; Carosi et al., 2007), undeformed randomly oriented mm-size static brown and white micas develop with a poikilitic structure, with isotropic quartz inclusions (*Fig. 5.7a, b*). Minor evidences for brittle deformation occur.

Calcite is an important volumetric phase (always above 50% of the total volume, *Fig. 5.8*), enveloping rounded strong porphyroclasts of quartz and (twinned) dolomite. This amount and distribution of crystals support that calcite is the weak matrix that can accommodate the deformation (e.g. see definitions of Handy, 1994, and works of Herwegh and Berger, 2004; Holyoke III and Tullis, 2006). Consequently, as in the case of quartz-bearing lithologies along the MCTz, it is possible to compare the calcite structures at the microscale from sample to sample within the STDS. In the structurally lowermost sample D21-10-81 (GHS_U, *Fig. 5.7h*), calcite has a coarse grain size, with a SPO (aspect ratio, AR=2.20) parallel to the STDS trend.

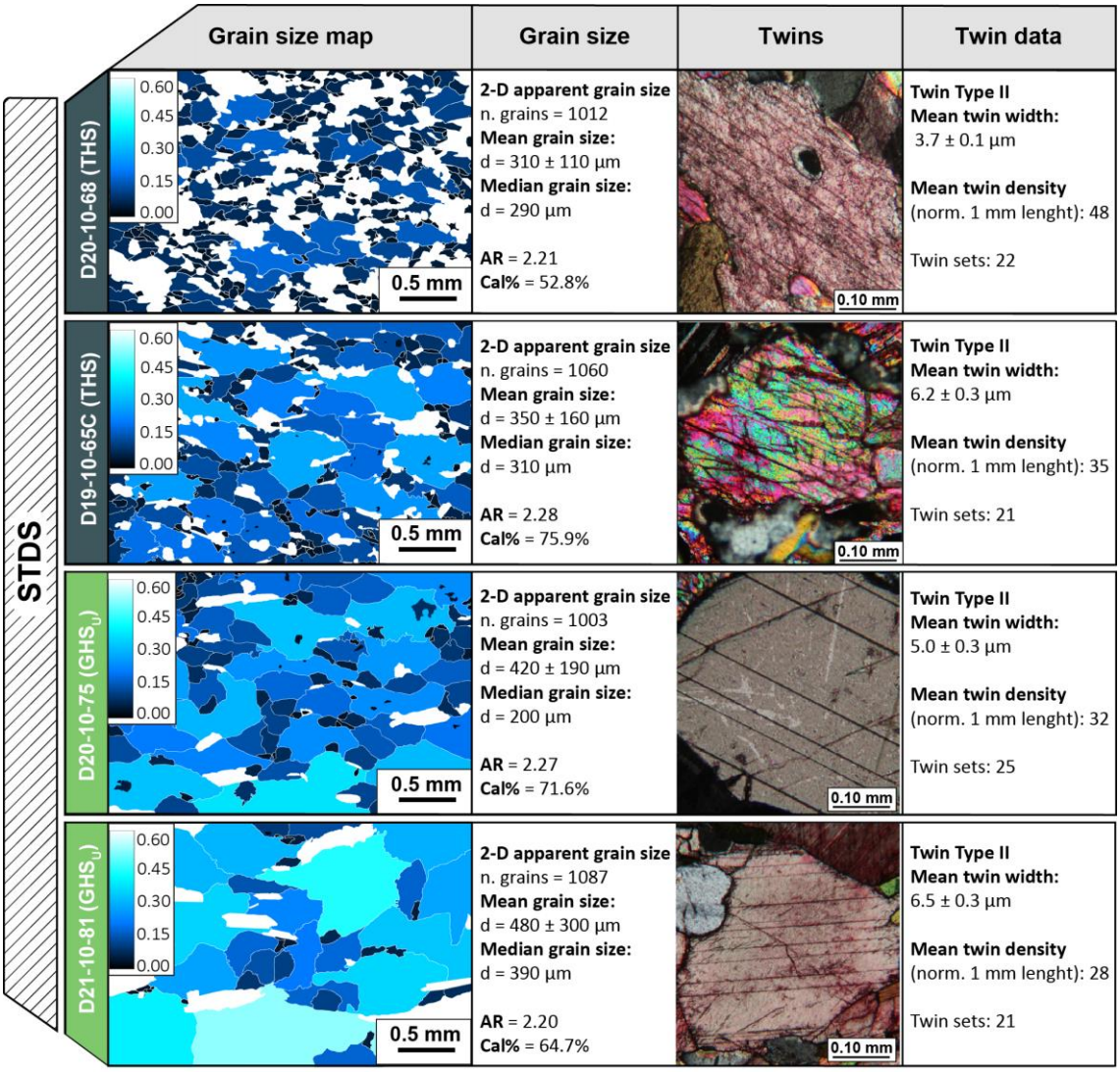

Figure 5. 8. *Calcite microstructures of selected samples from the STDS. In columns on the first column, small parts of grain maps are presented for each sample (for each sample, bigger areas with over 1000 crystals have been analysed). Samples are listed from higher to lower structural levels. Upper left colour-coded calibration bar indicates the equivalent radius of grains. The second column summarizes the grain size distribution data (Cal% is the calcite volumetric abundance with respect to the bulk compositions; RMS is the root-mean-square for the grain size derived from the equivalent area of each grain). The third column shows optical micrographs of twinned calcite. Samples are the same as in the first column. The fourth column provides the detected twin types.*

Moreover, straight grain boundaries and a lack of undulose extinction occur, and only rare twins can be recognized in the coarser grains. These microstructures support that calcite suffered annealing processes or fast recovery (Leiss et al., 1999; Barnhoorn et al., 2005) after dynamic recrystallization processes linked to the STDS shearing (Vannay and Hodges, 1996). Up-section, calcite SPO (AR=2.2–2.3), undulose extinction and lobate grain boundaries (*Fig. 5.7d-g*) indicate a plastic deformation occurred during the ductile shearing of the STDS. Type II {*e*}-twins (Burkhard, 1993; Ferrill et al., 2004) in calcite highlight a further ductile crystal plastic deformation mechanism (*Fig. 5.7d-g*).

Compiling grain size maps (e.g. *Fig. 5.8*, done with ImageJ software) and recalculating the grain size distribution (with GrainSizeTools v2.0.2, analyzing over 1000 crystals per samples), results indicate calcite unimodal distributions in all samples (*Fig. 5.9a-c*). Unimodal distributions and microstructures support that, during the S2 development, calcite deformed plastically by GBM dynamic recrystallization processes (Schmid et al., 1987; Lafrance et al., 1994; Rutter et al., 1995; 2007). Moreover, grain size distribution decreases up-section, from equivalent diameters of ca. 420 µm to 310 µm (*Fig. 5.9d*). The mean {*e*}-twin densities, D (Rowe and Rutter, 1990), vary up-section (*Fig. 5.9e*), increasing from 28% up to 48%.

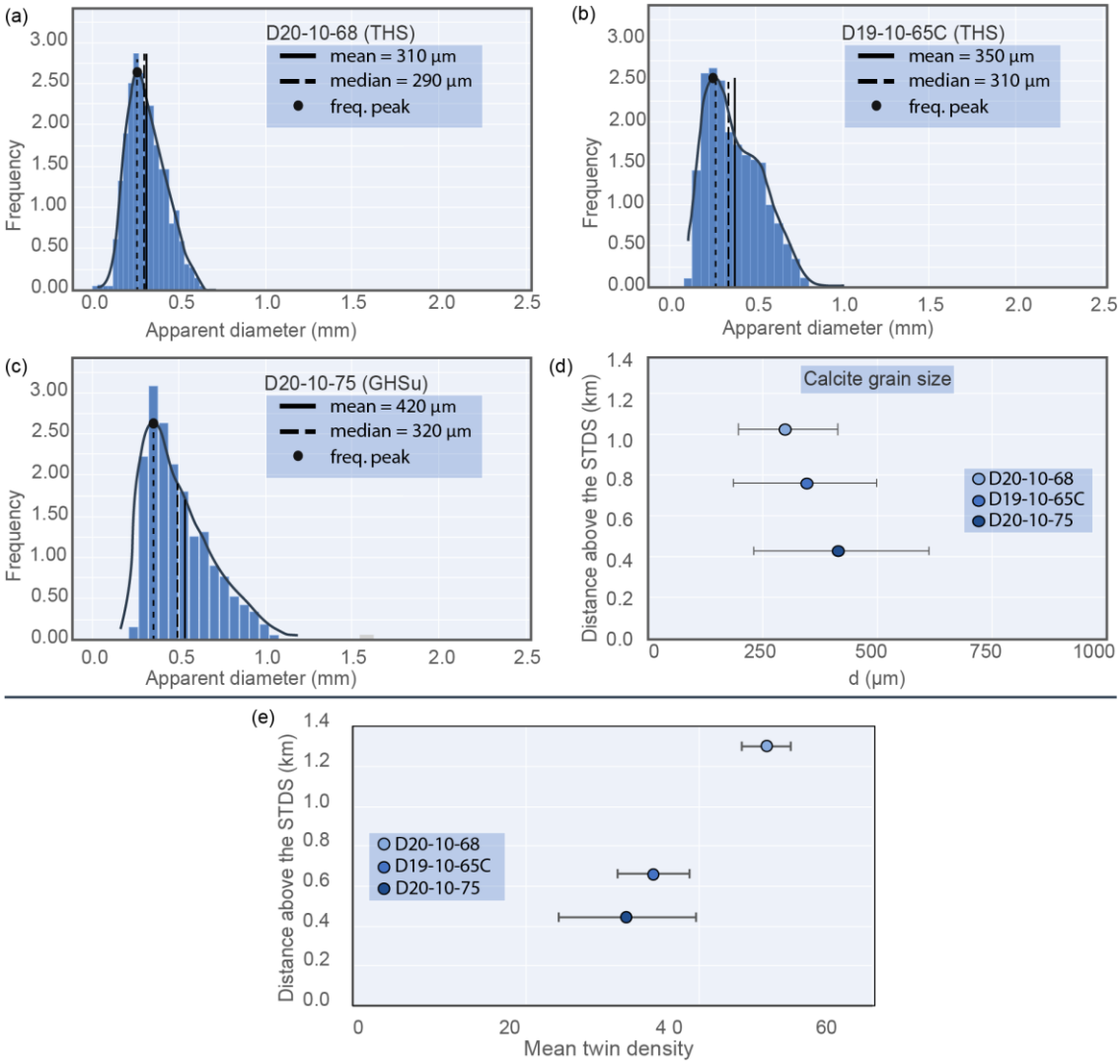

Figure 5. 9. *(**a-c**) Calcite grain size distribution istogram of the impure marbles selected for the STDS in the Lower Dolpo (samples are listed from higher to lower structural levels). (**d**) Grain size distribution (d, diameter) increases down-section from the THS to the GHS$_U$. (**e**) Graph of {e}-twin density (normalized to 1 mm) vs structural distance from the STDS base to the top. Th {e}-twin density decreases down-section from the THS to the GHS$_U$.*

5.2.2. Paleopiezometric analysis of the STDS

For the GBM dynamic recrystallization, the Rutter (1995) paleopiezometer provides differential stress of 13-16 MPa (*Fig. 5.10*). Compatible results of 9-12 MPa are provided by Barnhoorn et al. (2004) paleopiezometer (*Fig. 5.10, Table 5.2*). Adopting this range of differential stress values, the corresponding strain rates are of ca. 2.2-1.2 x 10^{-11} s^{-1} calculated for a temperature of 400 °C (Renner et al., 2002).

Table 5. 2. *Paleostress results (see Fig. 5.1, Fig. 5.3 for sample location). Diff. stress = differential stress calculated from the RMS by the Barnhoorn et al. (2004) and Rybacki et al. (2011) paleopiezometers. ε̇, strain rate calculated from differential stress estimates provided using the Barnhoorn et al. (2004) and Rybacki et al. (2011) piezometer.*

Sample	Unit	Mean grain size (μm)	Diff. stress (GBM) Rutter, 1995	Diff. stress Barnhoorn et al., 2004	ε̇ (GBM) (400 °C) (s^{-1})	Mean twin density	Diff. stress Rybacki et al., 2011	ε̇ (Twin) (350 °C) (s^{-1})
D20-10-68	THS	310±110	16±6	11.5±0.3	2.1 x 10^{-11}	48	135±6	9.5 x 10^{-11}
D19-10-65C	THS	350±160	15±8	10.6±1.0	1.8 x 10^{-11}	35	115±5	1.7 x 10^{-11}
D20-10-75	GHS_U	420±190	13±6	9.4±0.9	1.4 x 10^{-11}	32	110±5	1.1 x 10^{-11}

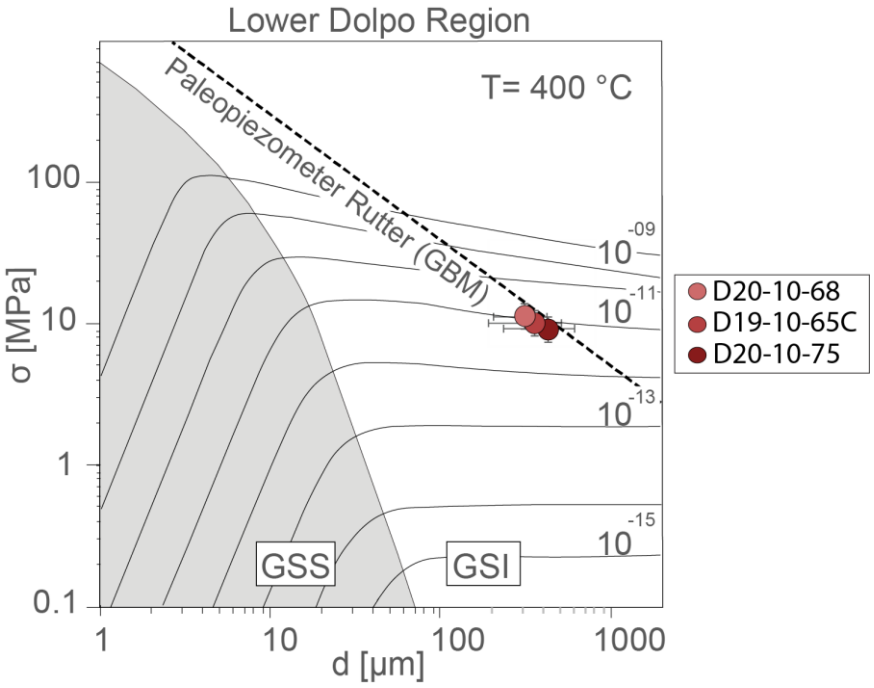

Figure 5. 10. *Grain size vs. differential stress for calcite paleopiezometry (for T=400 °C). The dashed line corresponds to the calcite GBM-based paleopiezometer of Rutter (1995). The boundary between the grain size sensitive creep (GSS) field (Herwegh et al., 2003) and the flow laws of Renner et al. (2002) for grain size insensitive (GSI) regimes is given. Contours are recalculated strain rates. Samples differential stress recalculated through Barnhoorn et al. (2004) piezometer almost fall into Rutter (1995) line.*

In the case of {*e*}-twins, the Rowe and Rutter (1990) piezometer supports higher differential stress values, of 195–235 ± 40 MPa, whereas the Rybacki et al. (2011) piezometer returns values of 110–135 ±6 MPa (*Table 5.2*). By adopting the differential stress results from Rowe and Rutter (1990) piezometer for temperatures of 350 °C, the corresponding strain rates (through Rutter, 1974 equation) are in the order of 10^{-11} s^{-1}, as well as adopting results from the Rybacki et al. (2011) flow law for the same temperature (*Table 5.2*).

5.2.3. Calcite and quartz texture analysis of the STDS

In order to acquire calcite crystallographic orientations, five representative specimens were selected from the GHS_U to the THS (*Table 5.1*) in which the analyzed grains were well-interconnected and significatively abundant. Moreover, three impure marbles from the THS were also selected for texture analysis on quartz (*Table 5.1*), where this mineral occurs as isolated clast in deformed domains. All calcite and quartz textures are reported as pole figures in *Fig. 5.11a-h*. As summarized in *Fig. 5.11*, results support the presence of calcite textures in the Lower Dolpo, with low CPOs intensities, indicated the J-index (1.05-1.15) and by the M-index (0.01-0.02) for samples D20-10-75, D19-10-65C, D20-10-68, that strongly decreases in the lowest sample D21-10-81 and in the uppermost less deformed sample, D18-10-63 (M-Indexes of 0.006-0.008). Comparing calcite and quartz maxima, further information can be achieved.

Starting from the calcite pole figures, textures recorded by the XTG vary from the base to the top of the sampling. The lowermost sample, belonging to the GHS_U (D21-10-81, see *Fig. 5.6h*), with a very little CPO intensity, is defined by broad maxima coherent with orthorhombic geometries for all the analyzed crystallographic elements (*Fig. 5.11h*). In samples D20-10-75, D19-10-65C and D20-10-68 (*Fig. 5.11a, c, e, g*) calcite [*c*]-axes pole figures (poles to the basal plane) support weak, but well-defined broad asymmetric maxima in the Z-direction (almost normal to the foliation). The [*c*]-axis maxima and *<a>-ax*es girdles, poles to $\{11\bar{2}0\}$, have a counterclockwise asymmetry (toward the south), supporting a deformation occurred in a non-coaxial flow. Traced from bottom to top, textures asymmetries decrease (*Fig. 5.11a, c, e, g*) supporting a heterogeneous deformation (Kern and Wenk, 1983; Wenk et al., 1987). Moreover, strong {*e*}-planes $\{01\bar{1}8\}$ pole maxima (with a subsidiary central girdle) are strongly rotated toward the south (*Fig. 5.11a, c, e, g*). As {*e*}-twinning determines a specular rotation on a {*e*}-plane of the host crystal in general shear flows (Schmid et al., 1987), calcite textures indicate ductile deformation with top-down-to-the-north non-coaxial flow.

The structurally uppermost sample, D18-10-63 (*Fig. 5.6c, Fig. 5.11a*), besides not having a strong CPO, has very large and poorly defined maxima on [0001], consistent with a girdle distribution hardly comparable with the distribution of the {*e*}-planes poles maxima (*Fig. 5.11a*). Pole to the rhombic planes *r*$(10\bar{1}4)$ and *f*$(01\bar{1}2)$ are consistent with weak small circles distributions (*Fig. 5.11a*), supporting minor intracrystalline deformation (Schmid et al., 1987). The symmetric geometry and the low intensity of the CPO allow assuming that sample was not deformed by non-coaxial flow.

Less information can be obtained from the quartz pole figures (*Fig. 5.11b, d, f*), as (according to microstructures) it is not representative of the flow conditions. However, in all analyzed impure marbles, texture measurements on both XZ and YZ planes of the finite strain ellipsoid allowed to recognize the occurrence of rhomb*<a>* slip in a top-to-the-north sense of shear (*Fig. 5.11b, d, f*). In samples, subsidiary [*c*]-axis maxima close to X-direction does not support deformation accommodated by prism*<c>* slip, since there are not records for that on the prismatic {*m*}-planes $(10\bar{1}0)$ (*Fig. 5.11d*). Quartz textures confirm the calcite-textures interpretation, supporting "typical" deformation temperatures (according with mixed *<a>* slip) in the THS between 400-500 °C (Mainprice et al., 1986; Schmid and Casey, 1986).

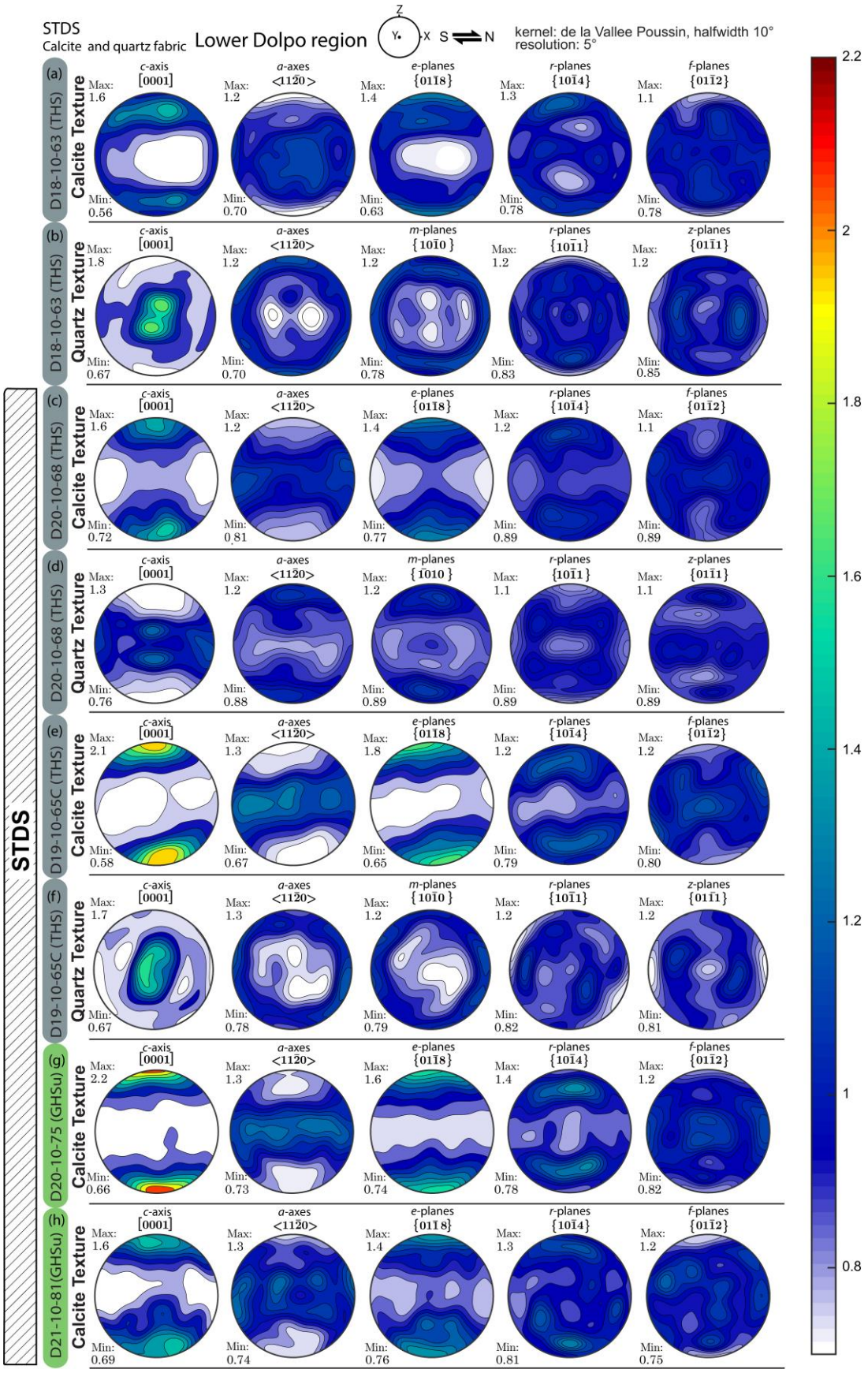

Figure 5. 11. *Compilation of the main calcite (**a,c,e,g,h**) and quartz (**b,d,f**) pole figures (equal area projection, lower hemisphere) for the STDS ductile shear zone. Each row shows calcite or quartz texture for each sample (on the left side, the investigated mineral phase is reported). Specimens are listed from top to bottom along the structural profile (see Fig. 5.7). Colour bar chart indicates multiples of uniform distribution (equals to 1.0) of CPO. All pole figures view towards the west on projection plane and refer as reference frame to the foliation pole (Z) and mineral lineation (X).*

5.2.4. Simple shear and pure shear contributions in the STDS

Texture analyzes support that three samples are suitable for Wenk et al. (1987) texture-based method kinematic vorticity analysis. Traced up-section, samples are: D21-10-81, D20-10-75, D19-10-65C, and D20-10-68 (*Table 5.1*). Measured ω angles vary from ca. 15° to 5° supporting a deformation occurred under general shear, with simple shear contributions of 50-20% (*Fig. 5.12*) supporting an heterogeneous general shear flow.

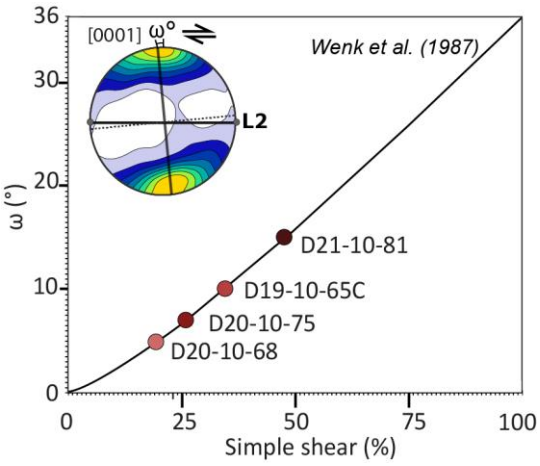

Figure 5. 12. *Simple shear estimation through the Wenk et al. (1987) method for calcite in marble. The asymmetry angle ω° (foliation/[c]-axis maximum) is related to the simple shear contribution*

5.3. Summary of data on the Lower Dolpo Region

- Ten samples with LHS- and GHS_L-protolith affinity have been studied from the MCTz. Paragneiss in the garnet-zone, at the MCTz base, passes up-section to quartzites and amphibolite-facies kyanite-bearing paragneiss, within a thick mylonitic showing a top-to-the-south transport direction. A dominant foliation, corresponding in literature to the S2 foliation, occurs, whereas a S1 foliation is preserved in low-strain areas (e.g. strain shadow of porphyroblast) at the base of the shear zone.
- Quartz texture has been investigated combining two different texture analyser (X-ray Texture goniometry and neutron diffractometry). Low CPO intensities (J-index, M-index) are recorded. Textures and microstructures (e.g. CS-fabric, oblique foliations, etc) show sinistral asymmetries, consistent with the non-coaxial flow showed at the outcrop-scale.
- Combining the Faleiros et al. (2016) fabric opening angle method with quartz and feldspars microstructures supports an up-section temperature increase from ~400 °C up to >700 °C, in agreement with the distribution of Barrovian index-minerals.

- Ten samples have been studied from the South Tibetan Detachment System (STDS). Only the S2 foliation occurs within the STDS, while crenulated S1 foliation occurs within the THS above the mylonitic zone. Within the STDS, the metamorphic mineral assemblage supports an up-section temperature decrease from the GHS_U to the THS, from amphibolite (calc-silicate bearing marble) to greenschist facies (biotite-bearing marble and metapelite).
- Calcite microstructures and calcite and quartz textures (by X-ray Texture goniometry) have been characterized. Texture and microstructures indicate that calcite in the GHS_U and THS marbles deformed by grain boundary migration recrystallization and twinning under a top-to-the-north non-coaxial flow from reasonable temperatures of 600 °C to 400 °C (decreasing up-section from the GHS_U to the THS).
- Calcite grain size in the THS decreases up-section, supporting differential stress of 8-12 MPa under strain rates of 10^{-11} s^{-1} for temperatures of 400 °C. Calcite twins support differential stress of ca. 105-135 MPa under strain rates (10^{-12}-10^{-11} s^{-1}) for temperatures of 300-350 °C.
- A general shear flow (50-20% of simple shear) has been obtained adopting the texture-based method of Wenk et al. (1987).

6. Microchemistry and ^{40}Ar–^{39}Ar geochronology on the Tethyan Himalaya Sequence

6.1. Sample description and mineral chemistry

Three samples from the Lower Dolpo area (D20-10-69; D20-10-49; and D18-10-64, *Fig. 5.1*) were selected for chemical and geochronological investigations (*Table 6.1, Table 6.2, Table 6.3, Fig. 6.1*). In particular, as reported in the geological sections in *Fig. 6.2a, b*, these samples are structurally close to the samples analyzed for the calcite and quartz textures in the previous chapter (*Fig. 5.1b*).

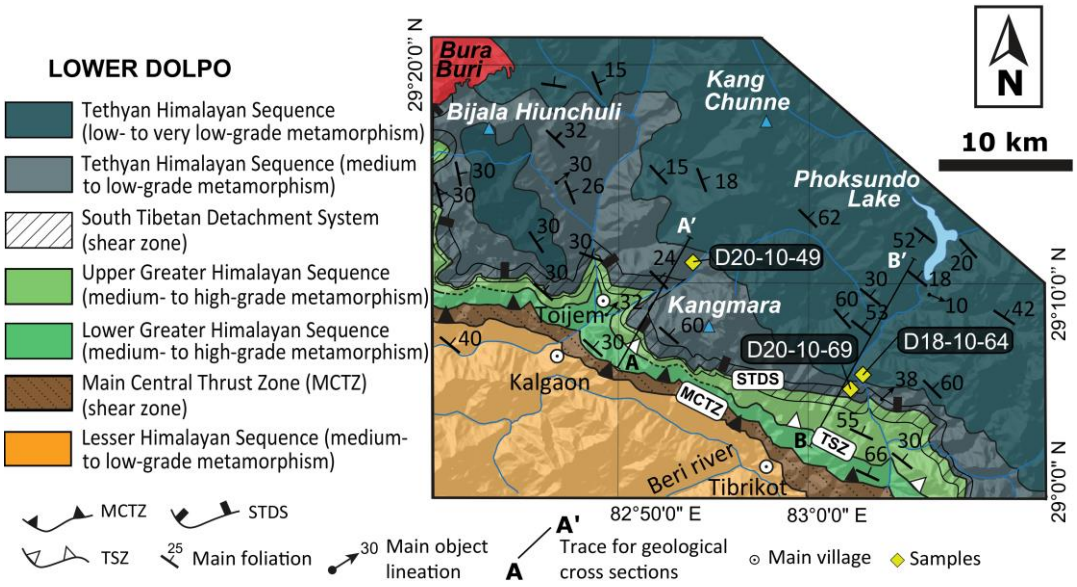

Figure 6. 1. *Geological sketch of the Lower Dolpo Region for the study samples (after Carosi et al., 2018).*

Table 6. 1. *Samples selected for mineral chemistry and ^{40}Ar – ^{39}Ar laserprobe analyses. MCal, calcite; Qtz, quartz; Pl, plagioclase; Kfs, K-feldspar; Wm, white mica; Bt, biotite; Phl, phlogopite; Ab, albite; Ilm, ilmenite; Ap, apatite.*

Sample	Lithology	Mineral assemblage	Fabric/Event	Deformation mechanisms/ recrystallization	analyses
D20-10-69	impure marble (STDS)	Cal+Qtz+Pl+Kfs+Wm+Phl	S2 (Phl)	Cal: GBM + annealing + Twin Type II Wm: poikiloblastic structure	EMP; ^{40}Ar–^{39}Ar step-heating analysis (Phl)
D20-10-49	carbonate-bearing metapelite (THS)	Qtz+Cal+Ab+Wm+Bt±Ilm±Ap	S1 (Wm) + S2 (Wm) + M3 (Bt)	Cal: Type I twin Bt: poikiloblastic Wm: decussate	EMP; ^{40}Ar–^{39}Ar *in-situ* analysis (Wm-S1, Wm-S2; Bt)
D18-10-64	carbonate-bearing metapsammite (THS)	Qtz+Cal+Ab+Wm+Bt±Ilm± Zrn	M3 (Bt)	Bt: poikiloblastic Wm: decussate	EMP; ^{40}Ar–^{39}Ar step-heating analysis (Bt)

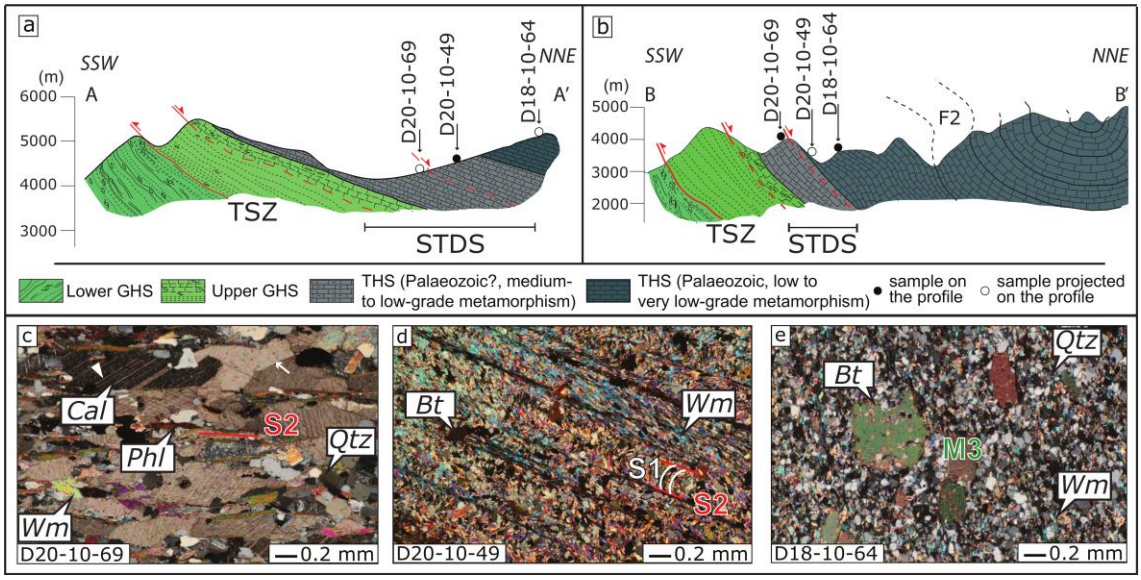

Figure 6. 2. (a) *Geological cross section (B-B' traces, see Fig. 5.1) crossing the area from where sample D20-10-49 was sampled (D20-10-69 and D18-10-64 are projected through the foliation trend).* ***(b)*** *Geological cross section (trace C-C' in Fig. 5.1) and location of D20-10-69 and D18-10-64 samples (sample D20-10-49 projected).* ***(c)*** *Micro photo under polarized nicols of the impure marble D20-10-69, with brown mica (phlogopite) and calcite marking the main foliation (S2) striking parallel to the STDS boundaries.* ***(d)*** *Sample D20-10-49, a carbonate-bearing metapelite, with a main spaced foliation (S2) and relicts of S1 continuous foliation in the microlithons. A post-kinematic biotite (M3) overprints both foliations. White micas show partially decussate shapes and homogenous high birefringence, with no evidences of internal strain, supporting static recrystallization.* ***(e)*** *Poikiloblastic post-kinematic dark mica (biotite) crystals in the upper-located carbonate-bearing metapsammite. Mineral abbreviation: Bt, biotite; Cal, calcite; Phl, phlogopite; Qtz, quartz; Wm, white mica.*

Samples were carefully selected as representative of the main structures recorded at different structural levels, as following (traced up-section):

- D20-10-69: strongly foliated impure marble deformed under greenschist facies (see *Table 6.1* for the mineral assemblage), in which the continuous foliation, defined by brown and white micas and calcite, strikes parallel to the STDS. Calcite constitutes the weak matrix according to Handy (1994), with a volumetric abundance over 75% of interconnected crystals, with respect to the bulk composition. Calcite is deformed by GBM dynamic recrystallization and twinning (*Fig. 6.2c*, see Schmid et al., 1987; Lafrance et al., 1994; Rutter, 1995; Platt and De Bresser, 2017); nevertheless, straight grain boundaries indicate static annealing processes. Brown and white micas are apparently (re)crystallized during the S2 foliation development; however, white micas have a poikilitic structure with quartz and feldspars inclusions (*Fig. 6.3a, b*).
According to the chemical classification in Deer et al. (1962), dark micas are homogeneous phlogopite (*Table 6.3, Fig. 6.4a, b*), with constant titanium (*Fig. 6.4a*) and potassium (*Fig. 6.4b*) contents. Potassium content close to 1 a.p.f.u. (0.95-1.00 a.p.f.u.) indicates a lack of interlayer chlorite. According to Capedri et al. (2004) chemical composition classification, white micas are phengitic muscovite (*Fig. 6.4e*) with low paragonitic contents (*Fig 6.4f*). Minor compositional variations in Si and Al are neglectable with respect to the analytical uncertainty, ranging from 3.10–3.17 atom per formula unit (a.p.f.u.) and 2.48–2.61 a.p.f.u., respectively (*Table 6.3*).

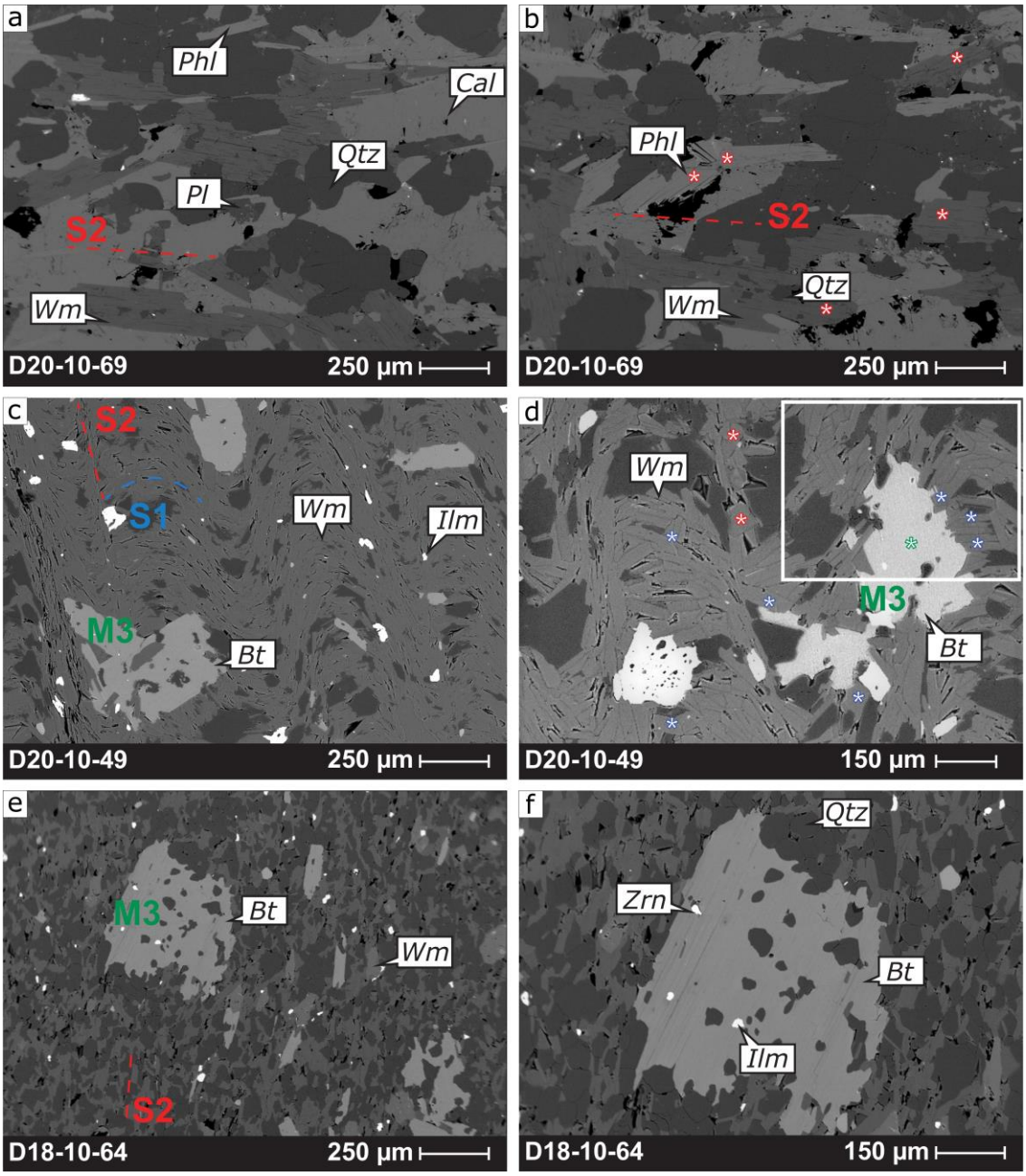

Figure 6. 3. *Backscattered electron (BSE) images of study samples (listed from bottom to top). Small coloured stars indicate crystals with cryptic or clear evidences of static recrystallization.* ***(a)*** *Dark mica (phlogopite) slightly elongated on the S2 foliation (sample D20-10-69).* ***(b)*** *Red stars point out phlogopite and white mica crystals sub-parallel to the S2 foliation (crystals laths are at high angle to each other). Poikiloblastic structure of white mica shows quartz inclusion.* ***(c)*** *Poikiloblastic unoriented biotite porphyroblast overprinting both the S1 and S2 foliations, marked by white mica (sample D20-10-49); see also ilmenite, crystals.* ***(d)*** *Key area of sample D20-10-49; in the white box, white micas show partially decussate shapes within the S1 domains (e.g. see light blue stars).* ***(e)*** *Coarse-grained biotite crystals in sample D18-10-64.* ***(f)*** *Zoom of the biotite poikiloblastic structure of figure (e), with quartz, ilmenite, and zircon inclusions (sample D18-10-64). Wm, white mica; Bt, dark mica; Qtz, quartz; Ilm, ilmenite; Zrn, zircon.*

- D20-10-49: This sample belongs to the Palaeozoic greenschist facies rocks of the THS exposed in a northwestern valley close to the main studied N-S transect (*Fig. 5.2, Fig. 6.2a, b*). The lack of top-down-to-the-north/northeast kinematic indicators, as in the structurally close sample D18-10-63 previously described, and the shift to a spaced and less pervasive S2 foliation, with a

crenulated S1 foliation recorded (*Fig. 6.2d*), indicate that the sample is located above the upper limit of the STDS as sample D18-10-63 (for structural position, see also *Fig. 5.5c* in Chapter 5). Sample D20-10-49 is a low-grade carbonate-bearing meta-arenaceous rock (see *Table 6.1* for the mineral assemblage), in which both quartz and calcite are poorly deformed, being enveloped in lower-competence materials defined by the white micas on the S1 and S2 foliations (Jiang, 1994a, b; Jiang and Williams, 1999; Bhandari and Jiang, 2021). In both S1 and S2 foliations, white micas have decussate shapes and homogenous birefringence from core to rim (*Fig. 6.3d*), with no evidences of internal strain (related to folding), indicating a mimetic recrystallization (*Fig. 6.3d*). Coarse-grained mm-size static and poikilitic brown micas overprint both S1 and S2 foliations, with randomly spread quartz inclusions (*Fig. 6.3c, d*, see also Carosi et al., 2007).
According to Deer et al. (1962), brawn micas are annitic biotites, with no appreciable intragrain compositional variations. The constant potassium content close to 1a.p.f.u. (0.96-1.01 a.p.f.u.) indicates a lack of interlayer chlorite (*Fig. 6.4b*). Titanium contents vary from 0.17-0.20, with neglectable differences (*Fig. 6.4a*).
According to Capedri et al. (2004), white micas are homogeneous phengitic muscovite (*Fig. 6.4e*), with low paragonitic contents (*Fig. 6.4f*). No appreciable variations of Si, Al, Na and XMg occur in white micas on the S1 and the S2 foliations with respect to analytical sensitivity (*Fig. 6.4g, h*). The highest contents of Si (e.g. 3.25 a.p.f.u.) and XMg number (0.48), coupled with lowest Al contents (e.g. 2.34 a.p.f.u.) in micas on the S1 foliation are very similar to the lower Si contents (e.g. 3.14 a.p.f.u.) and xMg number (0.37), coupled with the higher Al contents (e.g. 2.47 a.p.f.u.) in phengitic muscovite on the S2 planes (*Table 6.3*). No Ti and other major element contents variability occur, with neglectable differences of 0.05 a.p.f.u. for the Ti.

- D18-10-64: Sampled near D18-10-63 sample (at almost 1 km of structural highness above D20-10-69, *Fig. 6.2a, b*), shares some characteristics as the low metamorphic facies (low greenschist facies), the lack of kinematic indicators consistent with the ductile deformation of the STDS, and the presence of a slightly S2 foliation. Sample D18-10-64 is a carbonate-bearing metapsammite (see *Table 6.1* for the mineral assemblage) in which millimeter-size brown micas porphyroblasts crosscut all structures (*Fig. 6.2e, Fig. 6.3e, f*). A poikilitic structure in brown micas, with only isotropic distributed quartz inclusions, is observed in the basal sections (001).
Coarse-grained brown micas are annitic biotite (*Fig. 6.4a*, Deer et al., 1962), with potassium contents ranging from 0.87-1.02 a.p.f.u. (*Fig. 6.4b, d, Table 6.3*). These values are a bit lower than expected stoichiometric content for biotite; however, they are consistent with essentially unaltered biotite and in line with several estimations in the Himalayan metamorphic rocks (Vannay and Hodges, 1996; Montomoli et al., 2013; Warren et al., 2014; Parsons et al., 2016a). Titanium contents vary from 0.10-0.20 a.p.f.u. (*Fig. 6.4a*), with no significant internal zoning, from core to rim, or systematic variations from different crystals (*Fig. 6.4c*). Fine-grained isotropic white micas (*Fig. 6.2*) are homogeneous phengitic muscovite (*Fig. 6.4e*) according to Capedri et al. (2004) chemical classification, with low paragonitic contents (*Fig. 6.4f*). There are no major compositional variations in Si and Al contents (*Fig. 6.4e*), ranging respectively from 3.20–3.29 a.p.f.u. and 2.25–2.38 a.p.f.u (*Table 6.3*).

Table 6. 2. *Representative electron microprobe analyses of biotite (wt% oxides) and atoms per formula unit (a.p.f.u.) recalculated based on 11 oxygens (b.d.l. = below detection limit). Full chemical dataset is given in appendix, see* Table A.1., Table A.2, *and* Table A.3.

	Sample								
	D20-10-69			**D20-10-49**			**D18-10-64**		
wt%	***rim***	***core***	***rim***	***S1***	***S2***	***S2***	***isotrope distribution***		
SiO_2	45.60	45.51	45.73	46.40	47.41	46.07	48.51	48.69	47.37
TiO_2	0.71	0.97	0.91	0.99	0.77	1.11	0.80	0.57	0.94
Al_2O_3	31.81	31.44	32.15	28.81	29.24	29.36	29.01	28.72	28.90
$FeO_{(tot)}$	1.45	1.52	1.31	4.11	3.96	3.94	3.07	2.99	2.99
MnO	0.02	*b.d.l.*	0.02	*b.d.l.*	0.01	0.00	*b.d.l.*	*b.d.l.*	*b.d.l.*
MgO	2.31	2.31	1.93	1.78	1.89	1.63	2.22	2.28	2.04
CaO	0.12	*b.d.l.*	0.04	0.03	0.07	0.00	0.02	*b.d.l.*	*b.d.l.*
Na_2O	0.30	0.32	0.30	0.25	0.33	0.20	0.24	0.23	0.20
K_2O	11.35	11.27	11.24	10.95	10.81	11.14	11.20	11.19	11.24
BaO	0.29	0.24	0.45	0.34	0.38	0.30	0.28	0.30	0.25
F	*b.d.l.*	*b.d.l.*	0.08	0.08	0.17	*b.d.l.*	0.15	0.14	0.01
Cl	*b.d.l.*	0.01	*b.d.l.*	*b.d.l.*	*b.d.l.*	*b.d.l.*	*b.d.l.*	*b.d.l.*	*b.d.l.*
H_2O	4.39	4.36	4.35	4.28	4.31	4.32	4.37	4.36	4.36
Total	98.68	97.94	98.51	98.02	99.36	98.07	99.85	99.46	98.32
a.p.f.u.									
Si	3.116	3.128	3.125	3.220	3.236	3.194	3.278	3.300	3.255
Al_T	0.884	0.872	0.875	0.780	0.764	0.806	0.722	0.700	0.745
Al_O	1.677	1.674	1.714	1.576	1.589	1.594	1.589	1.595	1.596
Ti	0.037	0.050	0.047	0.052	0.040	0.058	0.041	0.029	0.048
Fe	0.083	0.087	0.075	0.239	0.226	0.229	0.173	0.170	0.172
Mn	0.001	*b.d.l.*	0.001	*b.d.l.*	0.001	*b.d.l.*	*b.d.l.*	*b.d.l.*	*b.d.l.*
Mg	0.235	0.237	0.197	0.184	0.192	0.168	0.223	0.230	0.210
Ca	0.009	*b.d.l.*	0.003	0.002	0.005	*b.d.l.*	0.001	*b.d.l.*	*b.d.l.*
Ba	0.008	0.007	0.012	0.010	0.010	0.008	0.007	0.008	0.007
Na	0.043	0.043	0.039	0.034	0.044	0.027	0.032	0.030	0.027
K	0.989	0.988	0.980	0.969	0.942	0.985	0.966	0.967	0.985
F	*b.d.l.*	*b.d.l.*	0.017	0.017	0.037	*b.d.l.*	0.032	0.031	0.002
Cl	*b.d.l.*	0.001	*b.d.l.*	*b.d.l.*	0.001	*b.d.l.*	*b.d.l.*	*b.d.l.*	*b.d.l.*
H	2.000	1.999	1.983	1.983	1.962	2.000	1.968	1.969	1.997
sum_oct.	2.050	2.049	2.033	2.050	2.048	2.048	2.026	2.024	2.026
Mg/(Mg+Fe)	0.739	0.731	0.725	0.436	0.459	0.424	0.563	0.576	0.549
Na/(Na+K)	0.039	0.041	0.039	0.033	0.045	0.027	0.032	0.030	0.027

Table 6. 3. *Representative electron microprobe analyses of white micas (wt% oxides) and atoms per formula unit (a.p.f.u.) recalculated based on 11 oxygens (b.d.l. = below detection limit). Full chemical dataset is given in appendix; see* Table A.4, Table A.5, *and* Table A.6.

	Sample								
	D20-10-69			**D20-10-49**			**D18-10-64**		
wt%	***rim***	***core***	***rim***	***rim***	***core***	***rim***	***rim***	***core***	***rim***
SiO_2	37.80	38.11	37.54	35.27	35.60	35.25	34.98	35.37	34.98
TiO_2	2.04	2.15	2.18	3.20	3.42	3.03	3.32	3.30	3.37
Al_2O_3	17.45	17.29	17.30	15.94	15.83	16.00	15.21	15.31	15.50
$FeO_{(tot)}$	11.85	11.70	11.85	21.57	21.24	21.57	22.01	22.15	21.94
MnO	*b.d.l.*	*b.d.l.*	0.05	0.02	*b.d.l.*	*b.d.l.*	0.04	0.05	0.03
MgO	15.04	15.32	15.35	9.28	9.06	9.23	8.58	8.76	8.41
CaO	0.15	0.03	0.01	*b.d.l.*	*b.d.l.*	0.03	0.13	*b.d.l.*	*b.d.l.*
Na_2O	0.10	0.09	0.06	0.09	0.04	0.06	0.08	0.05	0.05
K_2O	10.24	10.27	10.37	9.88	9.88	10.00	9.68	10.04	10.01
BaO	0.12	0.06	0.07	0.22	0.22	0.17	0.17	0.15	0.19
F	0.30	0.45	0.43	0.33	0.33	0.38	0.23	0.32	0.26
Cl	0.02	0.02	0.02	*b.d.l.*	*b.d.l.*	*b.d.l.*	*b.d.l.*	0.01	*b.d.l.*
H_2O	3.90	3.85	3.84	3.71	3.72	3.68	3.70	3.69	3.69
Total	99.01	99.32	99.06	99.52	99.31	99.40	98.14	99.19	98.43
a.p.f.u.									
Si	2.794	2.807	2.781	2.734	2.758	2.737	2.757	2.761	2.752
Al_T	1.206	1.193	1.219	1.266	1.242	1.263	1.243	1.239	1.249
Al_O	0.304	0.308	0.292	0.190	0.203	0.201	0.197	0.194	0.199
Ti	0.123	0.119	0.121	0.187	0.199	0.177	0.171	0.170	0.188
Fe	0.732	0.721	0.734	1.398	1.376	1.400	1.451	1.446	1.443
Mn	0.001	*b.d.l.*	0.003	0.001	*b.d.l.*	*b.d.l.*	0.003	0.003	0.002
Mg	1.686	1.682	1.695	1.073	1.046	1.069	1.009	1.019	0.986
Ca	*b.d.l.*	0.003	0.001	*b.d.l.*	*b.d.l.*	0.002	0.011	*b.d.l.*	*b.d.l.*
Na	0.011	0.013	0.008	0.013	0.005	0.009	0.013	0.008	0.008
K	0.947	0.965	0.978	0.978	0.976	0.991	0.974	0.100	1.005
Ba	0.003	0.002	0.002	0.007	0.007	0.005	0.005	0.005	0.006
F	0.114	0.104	0.100	0.082	0.080	0.093	0.056	0.078	0.064
Cl	0.003	0.003	0.003	*b.d.l.*	*b.d.l.*	0.003	*b.d.l.*	0.001	*b.d.l.*
H	1.884	1.894	1.898	1.918	1.920	1.907	1.944	1.922	1.935
Mg/(Mg+Fe)	0.697	0.700	0.698	0.434	0.432	0.433	0.410	0.413	0.406

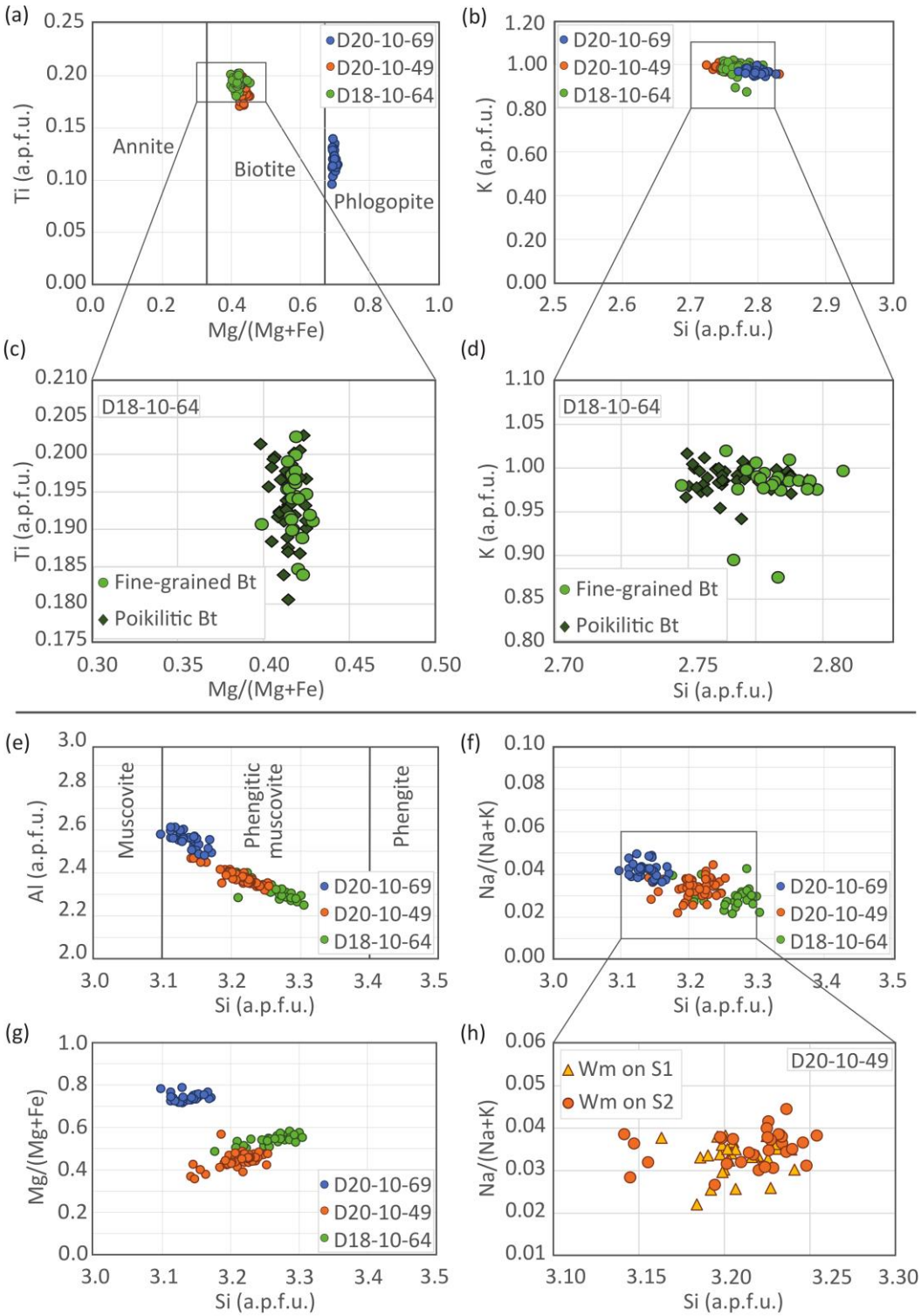

Figure 6. 4. *Chemical variation of mica for the analysed samples from the electron microprobe analyses (a.p.f.u. recalculated per O=11).* ***(a)*** *Discrimination diagram for Mg/(Mg+Fe) in biotites (after Deer et al., 1962) plotted against titanium content.* ***(b)*** *Biotite chemical compositions point out K content close to 1 (a.p.f.u.).* ***(c)*** *Zoom of the discrimination diagram for Mg/(Mg+Fe) in biotite from sample D18-10-64, where fine-grained crystals and coarse grained porphyroblasts are plotted.* ***(d)*** *Zoom of the discrimination diagram for K content in biotite from sample D18-10-64 indicates no chemical variations from fine-grained crystals to coarse grained porphyroblasts.* ***(e)*** *Discrimination diagram for white micas (after Capedri et al., 2004).* ***(f)*** *Na/(Na+K) values indicate low paragonitic contents in white mica.* ***(g)*** *White mica chemical variations for Mg/(Mg+Fe).* ***(h)*** *Zoom of the white mica discrimination diagram for Na/(Na+K), where the two populations of micas on the S1 and S2 foliations are plotted (sample D20-10-49). White micas chemical composition overlaps, and no systematic variation in the celadonite composition occur.*

6.2. Geothermometry and geobarometry on micas

The Ti content of biotite in graphitic aluminous pelites, in system containing a Ti-bearing phase (ilmenite o rutile), can be used for a qualitative temperature estimation applying the Ti-in-biotite geothermometer of Henry et al. (2005). Basically, the geothermometer is based that Ti contents in biotite, equilibrated in the range of 400-600 MPa, are sensitive to the temperature of formation (Henry et al., 2005). Among the study samples, D20-10-49 and D18-10-64 (containing ilmenite, *Table 6.1, 6,2; Fig. 6.3*) are suitable for the Ti-in-biotite geothermometer, which provides medium-to-high temperatures of 500-545 °C and 520-550 °C for sample D20-10-49 and D18-10-64, respectively.

Si contents of white mica in the simplified chemical system K_2O-MgO-Al_2O_3-SiO_2-H_2O (KMASH) can be used for a qualitative and comparative pressure estimates applying the Massonne and Szpurka (1997) geobarometer. Basically, the content of silica in phengite coexisting with quartz, K-feldspar, phlogopite and H_2O is a function of the pressure occurring during the white mica recrystallization. For samples D20-10-49 and D18-10-64, the silica content ranges (3.15-3.20 a.p.f.u. and 3.20-3.25 a.p.f.u., respectively, *Fig. 6.4e-g*) provided a semi-quantitative pressure value around 0.5-0.6 GPa (0.5±0.1 GPa for sample D20-10-49, and 0.6±0.1 GPa for sample D18-10-64), assuming a temperature range of 500-550 °C according to the Ti-in-biotite geothermometer estimates (Henry et al., 2005). Such pressure estimates are translated into a depth of 15-18 km by assuming a crustal density of 2,700 kg/m^3 (see Bucher and Grapes, 2011).

6.3. ^{40}Ar–^{39}Ar laser analyses

^{40}Ar–^{39}Ar laser analyses were performed in step-heating on mica separates on samples D20-10-69 and D18-10-64 (*Fig. 6.5 a-d*), and *in-situ* on a rock chip drilled from sample D20-10-49 (*Fig. 6.6 a-d*). Full isotope database is provided in Appendix (see *Table A.7, Table A.8*, and *Table A.9*).

<u>D20-10-69 (phlogopite oriented on the S2 foliation):</u>

For sample D20-10-69, it was possible separating only phlogopite crystals on the S2 foliation, as white micas have feldspar inclusion (*Fig. 6.3b*), which can contaminate the ^{40}Ar ages. Step-heating analysis on phlogopite provided a discordant age profile, with an overall saddle shape (*Fig. 6.5a*). Nevertheless, ten consecutive steps, which represent about 85% of the total $^{39}Ar_K$ released, provided concordant ages unsolvable within analytical uncertainties (Mean Squared Weighted Deviate MSWD=0.78), coherent with an error-weighted mean age of 13.85±0.08 Ma (*Fig. 6.5a*). At low and high temperatures, few discordant steps are characterized by high Ca/K ratios (*Fig. 6.5a*), supporting a contamination by mineral impurities (e.g. calcite) at such steps. The three-isotope correlation plot in *Fig. 6.5c* ($^{36}Ar/^{40}Ar$ versus $^{39}Ar/^{40}Ar$), or isochron plot, yield an apparent intercept age of 13.83±0.11 Ma.

<u>D20-10-49 (Phengitic muscovite on the S1 and S2 foliations, post-kinematic biotite):</u>

For sample D20-10-49, it was possible investigating on a rock chip (*Fig. 6.6a*) the three microstructural sites: (1) phengitic muscovite on the S1 crenulated planes; (2) phengitic muscovite on the S2 foliation; (3) overprinting static biotite, or M3 (*Fig. 6.6b*). However, twenty-seven *in-situ* analyses provided homogeneous isotopic composition for phengitic muscovite aligned along on both the S1 and the S2 foliations, corresponding to Ar ages of ca. 12.3-13.5 Ma (*Fig. 6.6c, d*; see *Fig. 6.6d* for spot location). Results are listed in the *Appendix* section (*Table*

A.9). Thirteen out of sixteen analyses on phengitic muscovite on the S1 foliation yielded an error-weighted mean age of 12.60±0.11 Ma (Mean Squared Weighted Deviate, MSWD=1.47), unsolvable within analytical uncertainties with the mean age of 12.56±0.16 Ma (MSWD=1.74) obtained for the phengitic muscovite on the S2 foliation (ten out of eleven analyses, *Appendix, Table A.9*). These ages are in line with six *in-situ* analyses on biotite, providing homogeneous isotopic composition within analytical uncertainties (MSWD=1.59), and a mean age of 12.57±0.19 Ma (*Fig. 6.6e, f*).

D18-10-64 (static biotite):

Excluding the first two steps, which are characterized by a very low radiogenic Ar content, step-heating analysis on annitic biotite provided a discordant age spectrum, with an overall sigmoidal-shaped profile raging from ca. 10.4 to ca. 15.6 Ma in age (*Fig. 6.5b, Appendix, Table A.8*). Six steps out of thirteen analyses provided a narrow interval of 11.7–11.0 Ma at intermediate temperatures. As for sample D20-10-69, low and high temperature show few rdiscordant steps, likely due to contamination from calcite as supported by concomitant higher Ca/K ratios (*Fig. 6.5b*). The three-isotope correlation plot in *Fig. 6.5d* ($^{36}Ar/^{40}Ar$ versus $^{39}Ar/^{40}Ar$) for these five steps supports a well-defined negative correlation MSWD of 0.88. The apparent intercept age is of 10.61±0.21 Ma, coherent with a $^{40}Ar/^{36}Ar$ initial ratio of 471.38±55.12 (*Fig. 6.4d*). The comparison of the discordant age spectrum, the isochron plot, and the compositional homogeneity from the microscopic scale to the isotope-scale indicate parentless ^{40}Ar hosted in the biotite crystal lattice or/and the presence of fluid inclusions within quartz entrapped in the poikilitic structure of biotite.

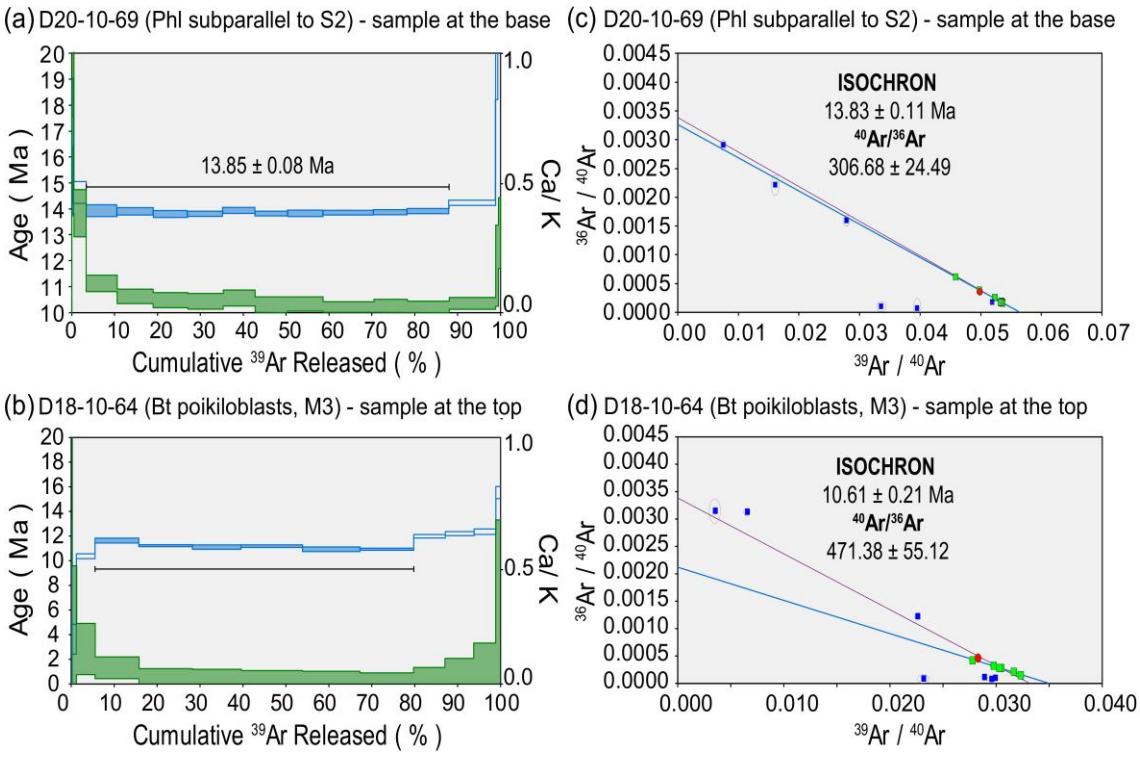

Figure 6. 5. (a, b) *^{40}Ar–^{39}Ar age spectra of dark micas of sample D18-10-64 (structurally highest sample) and D20-10-69 (structurally lowest sample).* ***(c, d)*** *Isochron diagrams (three-isotope correlation diagrams) for step-heating data of samples D18-10-64 and D20-10-69.*

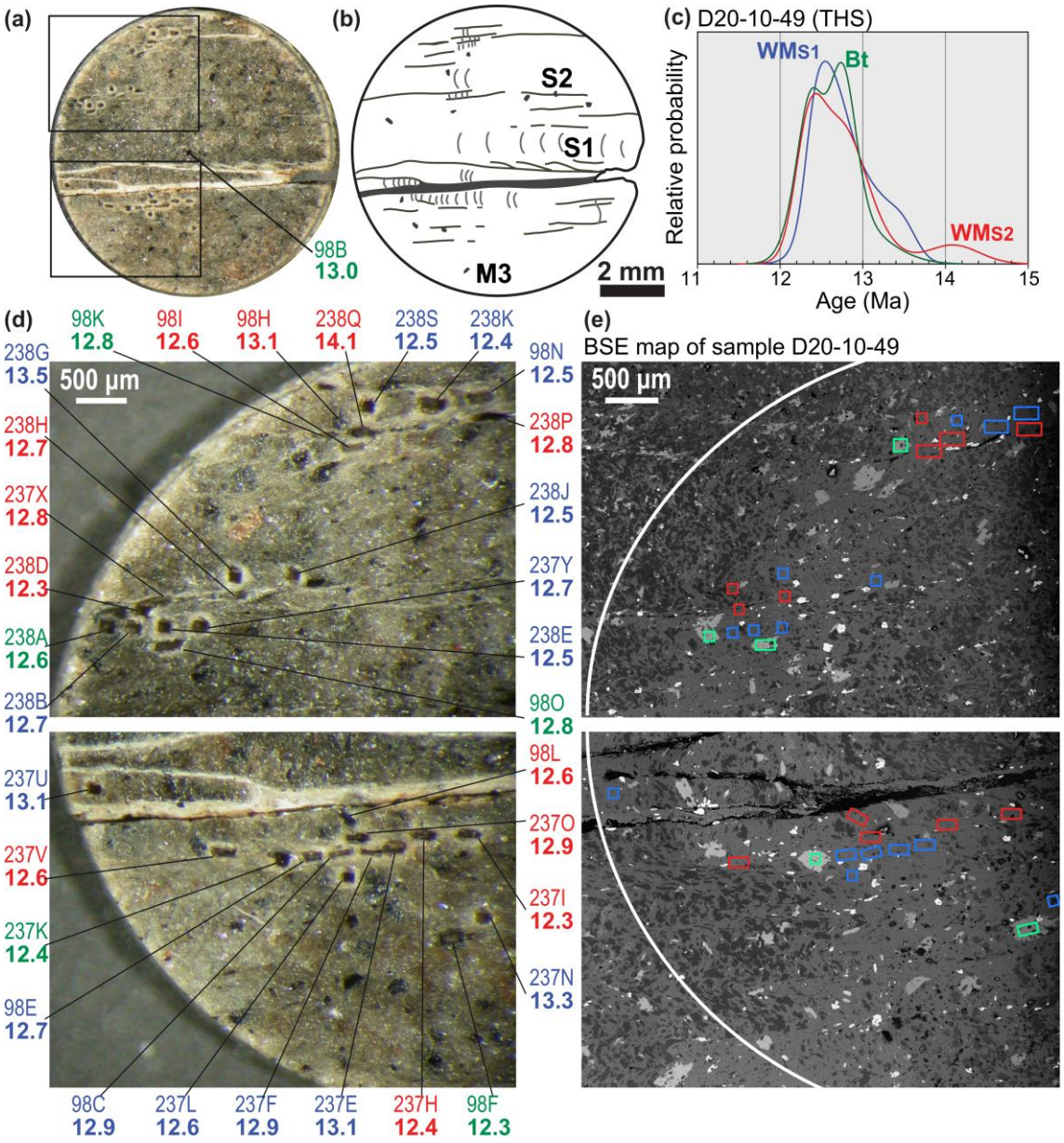

Figure 6. 6. (a) *Drilled rock chip showing one of the spot analyses of biotite porphyroblast.* ***(b)*** *Line drawing of (a) showing the structural interpretation.* ***(c)*** *Cumulative probability plot of ^{40}Ar–^{39}Ar ages from white micas aligned along the S1 (blue line) and on the S2 (red line) foliations, and for the porphyroblastic static biotite (green line).* ***(d)*** *Close up of* ***(a)*** *showing the investigated areas by the ^{40}Ar–^{39}Ar laserprobe and the distribution of Ar ages.* ***(e)*** *BSE-photomosaic of the drilled rock chip showing the corresponding investigated areas through coloured boxes. Blue boxes correspond to white micas on S1 domains; red boxes to white micas on S2 cleavages, and green boxes correspond to poikilitic biotite crosscutting S1 and S2 domains.*

6.4. Summary of geochronological data

- Two superposed tectonic foliations (S1 and S2) and a late static mica growth (M3) have been described in the Tethyan Himalaya Sequence (THS). Microstructural analysis shows cryptic evidence of mimetic static recrystallization for white micas aligned along both the S1 and S2 foliations, and for S2 biotite (at lower structural levels, at the STDS top), together with the development of poikiloblastic biotite (at higher structural levels).

- Compositional analyses highlighted little variation in the investigated micas, supportive for at least partial chemical re-equilibration of micas. Geothermobarometry on white mica and biotite supports crystallization temperatures of 500-550 °C at pressure around 0.5-0.6 GPa (corresponding to ca. 15-18 km in depth).
- ^{40}Ar–^{39}Ar laser step-heating and *in-situ* data of micas from different structural levels and from different microstructural positions (aligned along the S1 and S2 foliations, or M3 poikiloblasts) yielded an up-section age variation from ~14 to ~11 Ma. It is important to note that where microstructures were analysed separately by the ^{40}Ar–^{39}Ar *in-situ* technique, data from both the S1 and S2 foliations and from the static biotite (M3) gave indistinguishable ages at ~12.6 Ma.

7. Discussion

7.1. Discussion of data for the Main Central Thrust zone

Defining the MCTz location and rheological behaviour overtime are fundamental for understanding the Himalayan evolution. Over the last years, and the MCTz limits have been defined following different criteria such as: the lithological contrast, the mineral-in isograd, age constrains or strain gradient (Searle et al., 2008). In this Ph.D. thesis, the MCTz was investigated in two key areas of the central Himalaya (Western Nepal), which are located around the Manaslu range and the Lower Dolpo region (*Fig. 1*). These areas are more than 200 km apart but show common features. The main lithologies from the LHS and the GHS_L are quartzite, quartz-bearing paragneiss, mica schist (Manaslu area and Lower Dolpo region), and dolomite-bearing marble (Manaslu area).

In the Manaslu area, the lower limit of the MCTz (MCTz I) was placed on the basis of microstructural evidences – e.g. when CS-fabric indicates a top-to-the-south sense of shear (*Fig. 3.4i, k, l*), and as texture analysis supports clear asymmetric quartz CPO (*Fig. 3.6e*). The MCTz I, therefore, occurs close to the garnet-zone (e.g. sample MA16-01, *Fig. 3.1*), comparable with the MCTz lower limit in the Lower Dolpo region based on the same approach (e.g. sample D24-10-114 showing CS-fabric, *Fig. 5.4h*, close to the garnet-zone, *Fig. 5.3*). In both areas, the S1 foliation is poorly recorded, and is only preserved in low-strain areas within the LHS, at the base of the shear zone (*Fig. 5.4h*) or preserved as internal foliation in Barrovian minerals (e.g. garnet). S2 foliation strikes toward the NE (*Fig. 3.3a, Fig. 5.1*), defining the C-planes of S-C fabric within the shear zone. Despite minor compositional variations from area to area, metamorphic facies and vertical zoning occur. Garnet-zone metamorphic facies (greenschist facies) in the LHS passes up-section to the kyanite zone (amphibolite facies) in the GHS_L (*Fig. 3.3b, Fig. 5.2*). With the exception of dolomite-bearing marble in the Budhi Gandaki valley of Manaslu area, quartz is the most abundant mineralogical phase. In (almost) all samples, it represents the ductile and weak deformed matrix, in which second-phase minerals (e.g. feldspar, garnet) are included as "strong clast" (Handy, 1994). Although rocks show heterogeneous composition (*Fig. 3.4, Fig. 5.4, Table 3.1, Table 5.1*), it is possible to identify significant and large portions in which quartz is closely interconnected (especially in the Manaslu area). Therefore, it is possible to compare the lithologies for the deformation mechanisms of quartz both within the same area, for different structural levels, and from area to area, on a regional scale (Fossen, 2010).

In both the Manaslu and the Lower Dolpo areas, from lower to higher structural levels, quartz microstructures show a transition from the subgrain rotation recrystallization/grain boundary migration (SGR/GBM) regime in the LHS-affinity rocks, to GBM type I up to GBM type II in the GHS_L (*Fig. 3.4, Fig. 5.4, Table 3.1, Table 5.1*). The use of microstructures as a geothermometer is a rather delicate subject. After the work of Stipp et al. (2002) on the eastern Tonale fault zone, quartz crystal plastic deformation was used to infer a wide temperature range from 250 to 700 °C in natural rocks. These temperature ranges have been used in an absolute way, although the Stipp et al. (2002) work did not provide a real geothermometer (see also Law, 2014 for a review of quartz geothermometers). Quartz microstructures can derive from different amount of strain rates, temperature, fluid circulations, etc. (Law, 2014). With the big assumption that samples deformed within the same shear zone have similar fluids contents and strain intensity, the transition from SGR to GBM regime can reflect a vertical progressive increase of temperature-

strain rate ratio. Assuming comparable strain rates along strike, the transition can reflect an up-section temperature increase (as in the case of Stipp et al., 2002).

7.1.1. Texture development in quartz and dolomite-bearing mylonites

Quartz texture analyses were carried out with different apparatus (X-ray Texture goniometer, XTG, and G60 crystal fabric microanalyzer, FA). X-ray texture goniometry allowed analysis of full textures of crystals (quartz, dolomite, calcite, and mica). Moreover, it allowed to calculate the orientation distribution function (ODF) for selected mineral phases. However, X-ray texture goniometry only allows to select the areas to be analysed, and a minor control over analyzed crystals is possible. Especially for heterogeneous quartz-bearing paragneiss, X-ray texture goniometry also analyzed isolated quartz crystals, enveloped between mica- and feldspars-rich layers (see also Fazio et al., 2017). Such crystals are subjected to flow partitioning (see Kilian et al., 2011). Laboratory experiments on synthetic quartz aggregates proved an important control of micas on the development (inhibition) of quartz texture, as 15% of micas enhances pressure solution processes during foliation development (Tullis and Wenk, 1994). Therefore, micas-enveloped quartz crystals are not significative and fully representative of the flow conditions. The main risk of blind texture analyses is then that of producing low defined texture and low CPO (see also Fazio et al., 2017). The G60 crystal fabric microanalyzer allowed manual selection of areas to be analyzed. Therefore, it was possible to select portions of hundreds of interconnected crystals to refine texture analyses. With this apparatus, only quartz [*c*]-axis orientations were obtained. Using a non-fully automated apparatus, operators risk influencing the results according to their own experiences (see also Fazio et al., 2017). Nevertheless, both analytical methods provided consistent and complementary results for all studied samples (*Fig. 3.5, Fig. 3.6, Fig. 3.7, Fig. 5.5*). Comparing results from XTG and FA output made it possible to obtain bulk texture information, without operator bias, and detailed information for quartz [*c*]-axes, on selected areas. Samples from different study areas share the main results:

- Low CPO intensities (J-index, M-index);
- Texture development (and sinistral asymmetry of the [*c*]-axis maxima);
- Systematic variations throughout MCTz vertical profiles of texture patterns.

CPO INTENSITY:

As emphasized by Skemer et al. (2005) and Skemer and Karato (2007), the main problem concerning J-index is that it is sensitive to the number of grains, so it can be applied only if thousands of crystals are measured. However, as pointed out by Schaeben (2007), J-index should be a more robust method for quantifying CPO strength, taking into account the original ODF dataset (while the M-index is a partial measure, taking into account the difference between uniform and measured misorientation angles; see also Mainprice et al., 2015). However, for the X-ray texture analyses conducted, both indices are ideal, since thousands of crystals were measured for each sample. In the Manaslu area, J-index ranges between 1.10-1.29, with the exclusion of the more homogeneous sample MA16-102 (J-index= 2.91). In Lower Dolpo region, J-index (Bunge, 1982; Schaeben et al., 2007) varies from 1.13-1.64. The M-index points to low CPO intensities for both areas, as well as the J-index, ranging from 0.01-0.08 in the Manaslu area (up to 0.2 for sample MA16-102) and from 0.01-0.07 in the Lower Dolpo region. Therefore, the CPO strength of the heterogeneous quartz-bearing samples is consistent in both areas. Fabric strength was spatially correlated with high strain zones, to define the MCTz limits (e.g. Hunter

et al., 2016, 2018; Larson et al., 2017; Starnes et al., 2020). However, weak CPO does not necessarily correspond to low temperatures and/or strain magnitudes, as micas can trigger (or enhance) deformation mechanisms that are more efficient than dislocation creep (e.g. pressure solution-solution transfer, grain boundary sliding, see Olgaard, 1990; Handy, 1994; Hippertt, 1994; Tullis and Wenk, 1994; Herwegh and Berger, 2004; Song and Ree, 2007; Hunter et al., 2016). The distribution of the inhibiting phase plays a fundamental role in this, perhaps even more than abundance (Graziani et al., 2020). In the Manaslu and Lower Dolpo areas, weak quartz CPO can be attributed to the highly compositional and structural heterogeneity of polymineralic rocks (*Table 3.1, Table 5.1*). CPO strength cannot therefore be used alone to define the limits of the shear zone in the heterogeneous samples studied in the Manaslu and Lower Dolpo areas. With the exception of samples MA16-16 (*Fig. 3.4e*) and MA16-20 (*Fig. 3.4b*), low dolomite CPO in dolomite-bearing marbles (J-index=1.05-1.40; M-index=0.01-0.03) can rather be attributed to grain boundary sliding deformation mechanisms (Leiss and Barber, 1999; Holyoke III et al., 2013; Wells et al., 2019), as dolomite shows straight grain boundaries (*Fig. 3.4a, c*).

TEXTURE DEVELOPMENT AND ASYMMETRIES

Within the two sampling areas (Manaslu valleys and Lower Dolpo Region), most of texture patterns show a sinistral top-to-the-south asymmetry of the [*c*]-axis maxima (*Fig. 3.5, Fig. 3.6, Fig. 3.7, Fig. 5.5*). Both quartz and dolomite texture asymmetries develop synthetically to the shear sense (Lister, 1977; Lister and Hobbs, 1980; Wallis, 1992, 1995; Leiss and Barber, 1999, Lacombe, 2010 with references). With the common assumption that the internal reference frame of oriented samples approximates the geographical's one, quartz and dolomite texture asymmetries indicate a top-to-the-south non-coaxial flow. This is consistent with the independent kinematic indicators at the microscale (e.g. CS-fabric, oblique foliation, mineral fish, asymmetric strain shadow) supporting that the MCTz non coaxial flow is the driving force behind quartz and dolomite texture development.

In the Manaslu area, the upper limit of the MCTz can be placed at the transition from sinistral asymmetric quartz and dolomite texture patterns of lowermost samples (*Fig. 3.5, Fig. 3.6, Fig. 3.7*) to the symmetric pattern of dolomite texture in sample MA16-20 (*Fig. 3.7a*). Similarly, in the Lower Dolpo quartz symmetric maxima in [0001] pole figure (*Fig. 5.5a*) of the uppermost sample D21-10-85 allowed constraining the upper limit of the MCTz. This transition from asymmetric to symmetric textures is quite progressive. The strong compositional heterogeneity of the samples, however, does not allow the use of texture asymmetries to quantify flow kinematic vorticity. As pointed out by Kilian et al. (2011) and Bhandari and Jiang (2021), when significant flow partitioning occurs (as in the case of S-C fabrics and S-planes isolating quartz aggregates), it is not possible to quantify the kinematic vorticity through the quartz [*c*]-axis fabrics. This means that the angle of asymmetry could be not strictly significative of high or low kinematic vorticity in the case of significant flow partitioning. However, as in the studied samples quartz [*c*]-axis fabrics asymmetry is consistent with micro-scale kinematic indicators, and its CPO is low but well-defined, it is possible to relate it to the non-coaxial flow of the MCTz, and to use the asymmetry in a semi-quantitative way.

VARIATION OF TEXTURE PATTERNS ALONG THE MCTZ

Representative samples, with LHS-protolith affinity, from the Manaslu area, have [*c*]-axis orientations supporting, from bottom to top, Z-point maxima pattern, crossed girdle Type I

pattern and Y-point maxima pattern (*Fig. 3.5a-e, Fig. 3.6a-e*). Z-point maxima patterns have originally been interpreted as the basal<*a*> slip result (Baëta and Ashbee, 1969; Mainprice et al., 1986; Schmid and Casey, 1986; Krhul, 1998; Morgan and Law, 2004). However, it has been proved that {π}<*a*> (or {10$\bar{1}$2}<11$\bar{2}$0> slip), {*z*}<*a*> (or {01$\bar{1}$1}<11$\bar{2}$0> slip) can be more efficient slip systems for Z-point maxima development (Morales et al., 2011, 2014). Comparing, for each sample, all pole figures, [*c*]-axis patterns are, in principle, interpreted as the results of intracrystalline deformation, with mixed <*a*>slip. Dominant prism<*a*> slip occurs at higher structural levels (Mainprice et al., 1986; Schmid and Casey, 1986). The same pattern is observed for the Lower Dolpo region (*Fig. 5.5c, d*), where [*c*]-axis patterns evolve up-section from incomplete crossed girdle to point maxima-in-Y geometry. At higher structural levels, quartz textures support single girdle patterns at the top of the LHS in the Manaslu area (*Fig. 3.5f, g, Fig. 3.7a*). In the Lower Dolpo, quartz textures from quartz-bearing GHS_L-samples, at the interface with the LHS, evolve from type I crossed girdle (*Fig. 5.5b*) to single girdle immediately above the MCTz upper limit (*Fig. 5.5a*). These patterns are compatible from both areas. Moreover, they can be interpreted as the results of mixed <*a*> slip, defining a wide opening angle (ca. 95 ° in sample D23-10-106). Auxiliary maxima on the X-direction can be attributed to prism<*c*> slip in the uppermost sample D21-10-85 (*Fig. 5.5a*, see Kruhl, 1996).

Pioneering works have linked slip system activation to the overcoming of their critical resolved shear stress at certain thermal conditions (Blumenfeld et al., 1986; Mainprice et al., 1986; Schmid and Casey, 1986; Kruhl, 1996). Accordingly, in both areas, recognized slip systems show a temperature variation consistent with an up-section increase. Basal<*a*> up to mixed<*a*> slip systems would correspond to 400–500 °C (Mainprice et al., 1986; Schmid and Casey, 1986) for the upper LHS. The occurrence of a wide opening angle in crossed girdle and single girdle patterns are typically associated with higher temperature conditions, above 500 °C (see also Passchier and Trouw, 2005 for a concise review). Progressively higher deformation temperatures, of above 650 °C, can be supported by prism<*c*> slip in the uppermost sample, D21-10-85 immediately above the MCTz upper limit (*Fig. 5.5a; Fig. 7.1, Fig. 7.2*). Regarding the empirical geothermometer based on the opening angle of the quartz fabric skeleton, the small opening angle (60-68°) on [0001] of samples MA16-03, MA16-10, and MA16-11 at the base of the MCTz (*Fig. 3.6b, d*) supports deformation temperatures of ca. 460-520 °C in the Manaslu area (using the calibrations of Faleiros et al., 2016). The wide opening angle (95°) on [0001] in sample D23-10-106 (*Fig. 5.5b*), provides deformation temperatures of ca. 695 °C at higher structural levels, toward the MCTz top (*Fig. 7.2*).
Dolomite textures confirm this temperature increase in the Manaslu area (*Fig. 3.7b-e*), where peripheral maxima close to the X-direction on <11$\bar{2}$0> and {*r*}- and {*f*}-maxima girdle geometry support the contribution of {*f*}-slip within the dolomite-bearing marble at the top of the MCTz (*Fig. 7.1, Fig. 7.2*). According to Barber et al. (1981), {*f*}-slip develops in dolomite at temperatures well-above 550 °C. Interpreted dolomite slip systems are compatible with inferred dolomite microstructures. Rare twins (*Fig. 3.4a, c*), straight grain boundaries, unimodal grain size and oblique foliation development were interpreted as resulting from intracrystalline deformation (consistent with {*f*} and/or {*r*} slip) and {*f*} twinning, see Leiss and Barber, 1999; Holyoke III et al., 2013; Wells et al., 2019). Therefore, microstructures and textures are consistent with concomitant operation of GBM recrystallization and twinning at temperatures above 550 °C.

7.1.2. MCTz temperature gradient

Fabric analyses point to a heterogenous deformation of the MCTz. However, whether they indicate a temperature gradient (from T=400/500 °C to T~700 °C up-section) or a strain/strain rate gradient, etc., is not directly inferable based on texture data only. A brief compilation of texture pattern interpretation for the two studied areas is reported in *Fig. 7.1* and *Fig. 7.2*.

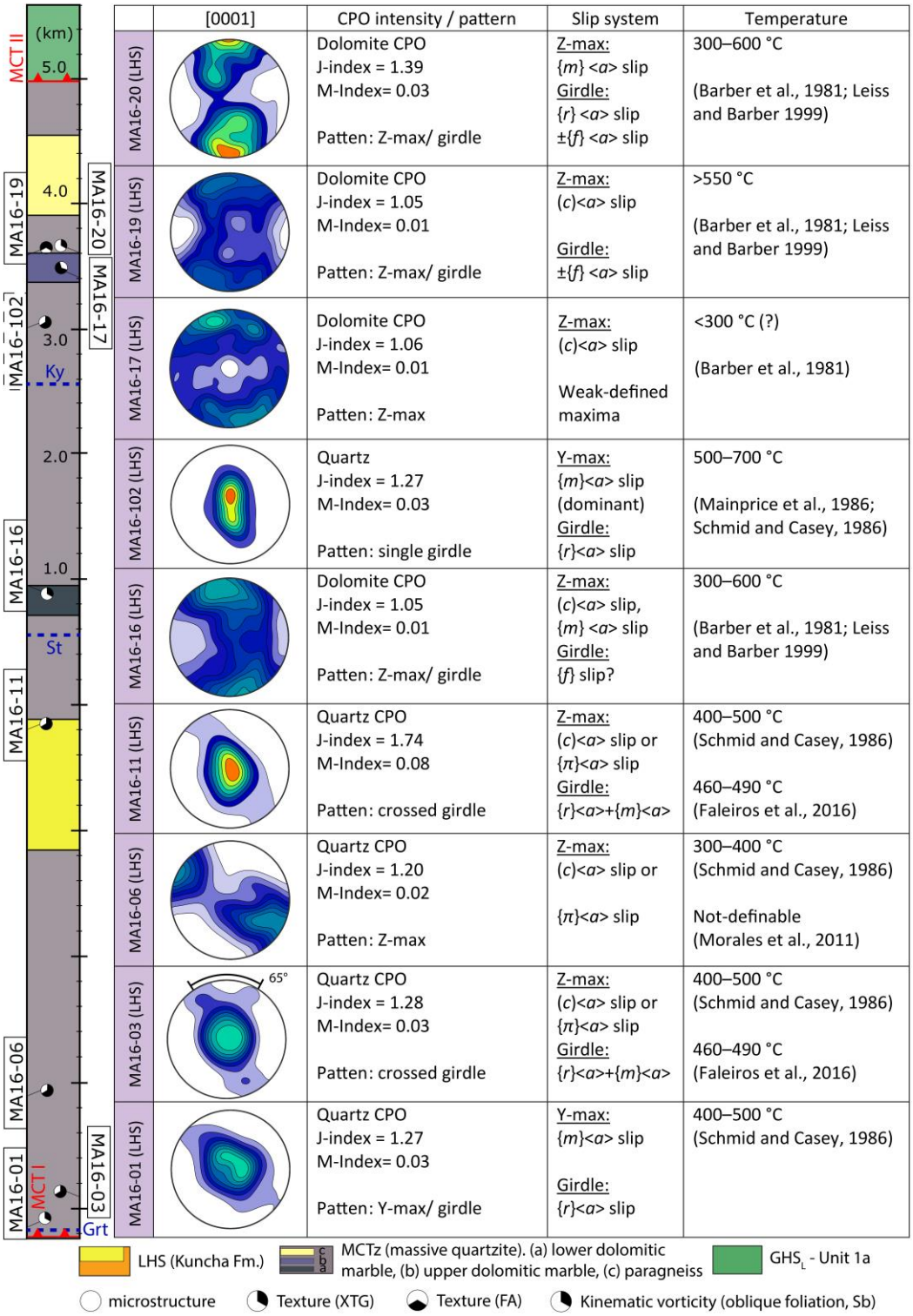

Figure 7. 1. *List of the main quartz and dolomite texture features and interpretations from the Manaslu area (X-ray texture goniometry). Pole figures are equal area lower hemisphere projection, and view towards the west on projection plane. Contours are multiples of uniform distribution (equals to 1.0) of CPO. Samples are listed from higher to lower structural levels, as reported on the left-side structural section (see Fig.3.5 and Fig. 3.7).*

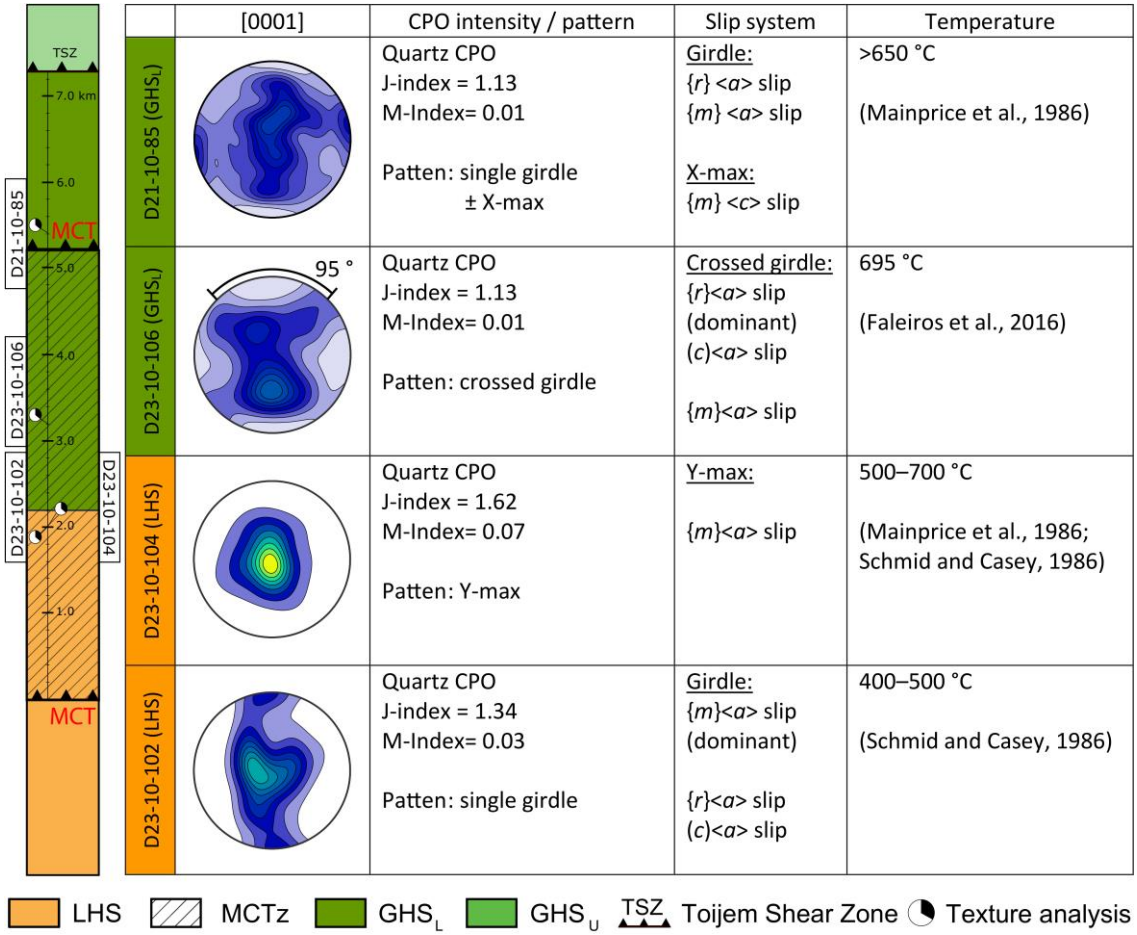

Figure 7. 2. *List of the main quartz texture features and interpretations from the Lower Dolpo region. Samples are listed from higher to lower structural levels as reported on the left-side structural section.*

As microstructures, slip system activations also depend on strain rate, water fugacity (Blacic, 1975; Okudaira et al., 1998), and strain intensity (Lister and Hobbs, 1980; Kilian and Heilbronner, 2017). Moreover, concerning the empirical thermometer of Faleiros et al. (2016) based on quartz texture, it is necessary to assume that the opening angle is provided by the basal<a> slip, which cannot be verified by the reported texture of this thesis. Z-point maxima can be also related to {π}<*a*> slip for high strains (Morales et al., 2011). An increasing temperature trend may not be the cause of such paterns, requiring further external constraints. Metamorphism zoning and upward variation of the index minerals (from garnet to kyanite zones) in both studied areas allow identification of an up-section trend of increasing metamorphic temperatures. Therefore, it is important to focus on the coherence of "slip system attributed temperatures", opening angle-based geothermometer (Faleiros et al., 2016), and external geothermometers (e.g. metamorphic data). Dwelling on the metamorphic zonation, the greenschist facies recorded by the LHS is usually an MP/LT metamorphic facies, with a temperature upper "limit" of ca. 500 °C. Amphibolite facies (recorded by the Ky-zone in the GHS$_L$) is consistent with MP/MT-HT conditions, with temperatures between 500-700 °C (Philpotts, 1990). The metamorphic zonation is therefore in accordance with the temperature trend inferred by the quartz slip systems. Textures can therefore better define the MCTz temperature gradient, particularly where index-minerals or mineral phases useful for geothermometry are lacking in the rock. As reported in *par. 7.1.4*, these data are in line with several observation in the Himalaya.

7.1.3. MCTz non-coaxial flow

In the Manaslu area, the application of vorticity of flow gauge, based on the oblique foliations (Wallis, 1995) in dolomite (*Fig. 3.4a, c*), provides sectional kinematic vorticity values (Wn) ranging between 0.64-0.81. Assuming a plane and monocline deformation, it is possible to convert the obtained values into percentage of simple shear. Equal contribution of pure and simple shear to the kinematic flow corresponds to Wm = 0.71 (see Law et al., 2004, Xypolias, 2010). Therefore, dolomite oblique foliations indicate a general shear flow, in which simple and pure shear give almost the same contribution (*Fig. 7.3*).

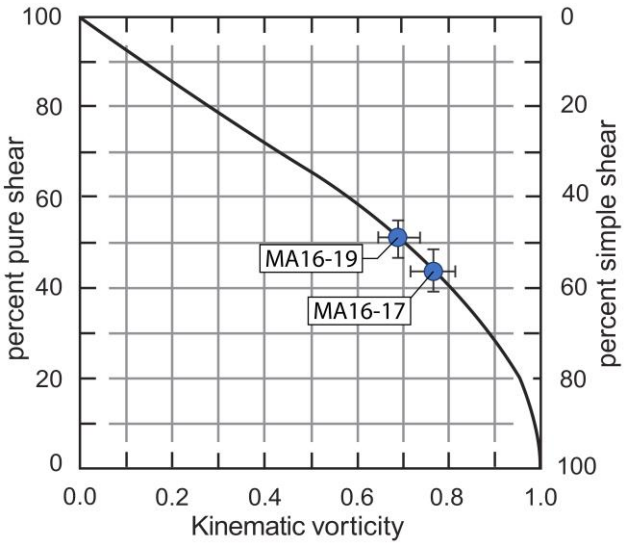

Figure 7. 3. *Adapted Law et al. (2004) graph for kinematic vorticity estimates obtained in this thesis for the Budhi Gandaki valley. Relationship between kinematic vorticity and relative components of pure and simple shear for instantaneous 2D flow is given. Results support a general shear flow (upward lower kinematic vorticity estimates)*

These estimations rely on the simplification that the main foliation (S2) is close to being parallel to the MCTz boundaries, which needs more explanation. In large-scale shear zones it is usually possible to identify a strain gradient. Mylonitic foliations (XY plane of the finite strain ellipsoid) during progressive deformation tend to rotate toward the shear plane (see Xypolias, 2010 for a review). Mylonitic foliation is therefore close to parallelism with the shear plane at the shear zone core (at high strain), and at a high angle to the shear zone boundaries (Ramsay, 1980, see Fossen and Cavalcante, 2017 for a review). Thus, estimated values should be taken in principle as semi-quantitative results, and therefore considered to represent a minimum estimation of the kinematic vorticity of the MCTz, as the shear plane is not defined. However, two main factors must be taken into account: (*i*) an almost parallelism within the core of a shear zone is assumed if it has a high enough strain to parallelize the foliation; (*ii*) as a shear zone matures, the foliation is typically rotated more and more to parallelize itself at the external boundaries (see also Passchier and Trouw, 2005). Regional-scale considerations are helpful for solving these questions. Shortening estimates for the MCTz range between 105 to 157 km in central Himalaya (West/Central Nepal, see Schelling and Arita, 1991; Schelling, 1992; Kohn et al., 2004; Khanal and Robinson, 2013; Robinson and Martin, 2014), with minimum displacement of 52-53 km in Arunachal Himal (Ningthoujam et al., 2015) and Bhutan (Long et al., 2011), eastern Himalaya, and maximum displacement of 259 km in Kumaun-Garhwal India (Srivastava and Mitra, 1994)

of western Himalaya (see also Parsons et al., 2020). In the Budhi Gandaki valley of central Himalaya, Khanal and Robinson (2013) estimated a shortening of 116 km for the MCTz. Nevertheless, the MCTz thickness in the study areas is (now) of ca. 5-10 km. This is a prime reason why the MCTz has been widely considered as a mature high-strain zone, developing mylonitic foliation with the same constant orientation for tens of kms. Given the little variation in foliation orientation, it can be assumed that (1) the strain is sufficient to parallelize the foliation to the shear plane, or that (2) there are no strain variations that can be solved in the study areas (therefore, the angle between foliation and shear plane is constant). Oblique foliation analysis provided semi-quantitative kinematic vorticity estimates for the Manaslu area.

In the Lower Dolpo region, kinematic vorticity quantification was not possible to achieve, as strong compositional heterogeneities, structural layering and S-C fabric isolate quartz aggregates (e.g. within the S-planes), indicating flow and strain partitioning. Therefore, quartz texture asymmetries were not exploitable for kinematic vorticity quantification (Bhandari and Jiang, 2021; Jiang, 1994a, b; Jiang and Williams, 1999, Kilian et al., 2011).

7.1.4. Integrating MCTz results on a regional scale

Along the Himalaya, the MCTz is defined by a composite structure (Searle et al., 2008). For instance, in NW India (western Himalaya), an upper shear zone (locally named Vaikrita Thrust) and a more external shear zone toward the south (Munsiari Thrust) have been recognized (Searle et al., 2008; Iaccarino et al., 2020; Montemagni et al., 2020). A careful look at the dataset in literature suggests that the up-section deformation temperature increase occurs within the MCTz in all the different Himalayan areas. A brief compilation of deformation temperatures for the MCTz profile, from western to eastern Himalaya (based on independent geothermometers), is reported (*Fig. 7.4*). Examples of temperature estimates in central Himalaya are from Iaccarino et al. (2017a) and Frassi (2015) in Western Nepal; Yakymchuk and Godin (2012) in the close Karnali valley (Fig. 1, ca. 100-150 km to the NW of the Lower Dolpo), and from Larson et al. (2010) and Parsons et al. (2016a) for the the Manaslu area.

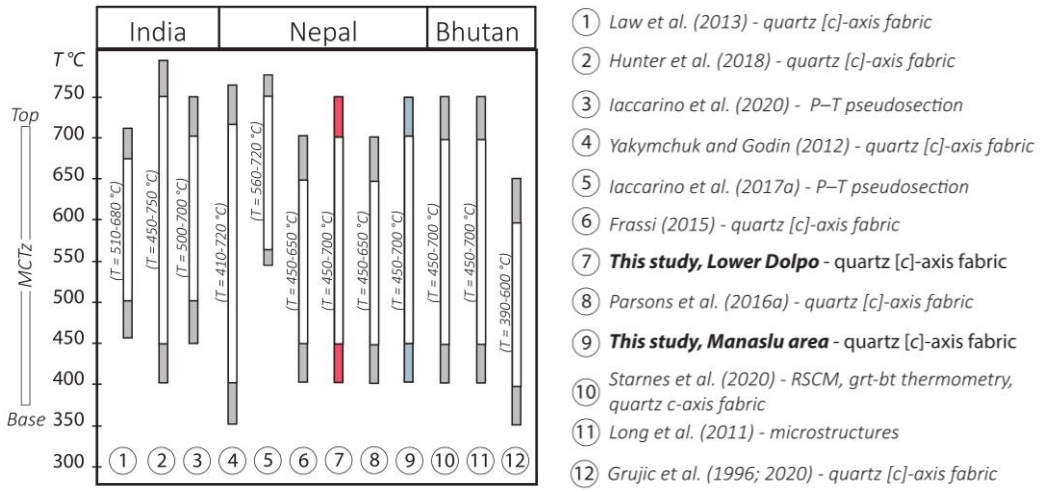

Figure 7. 4. *Selected publication showing temperature profiles across the MCTz in different areas along the Himalaya. White rectangles correspond to temperature ranges, from bottom to top of the shear zone, estimated by authors. In grey, expected associated errors based on analytical methods used (in red for the Lower Dolpo estimates and in light blue for the Manaslu area estimates of this thesis).*

The temperature trend also occurs in western Himalaya, where deformation temperatures from 510 °C to 640 °C from the MCTz base up at ~ 1 km of structural thickness above have been described (i.e. the Sutlej valley and the Shimla Klippe of NW India, see Law et al., 2013; Garhwal of NW India, see Hunter et al., 2018; Iaccarino et al., 2020). Consistently, it has been reported in Bhutan, eastern Himalaya, with estimated temperatures from 500 °C to 670 °C from the garnet to the kyanite zones (Grujic et al., 1996, 2020; Long et al., 2011; Starnes et al., 2020). This path has been used in the different tectonic models for describing the Himalayan exhumation story (*Fig. 1.4*, see *par. 1.1*). In accordance with the thrust kinematic of the MCTz, the higher temperatures recorded at the roof of the shear zone indicate rocks exhumed from deeper structural levels, whereas the lower deformation at the base, towards the south, indicate that exhumation started from shallower structural levels. Recently, in NW India, Montemagni et al. (2020) showed how the deformation ages of the MCTz decrease towards the south from its northern deeper branch (Vaikrita Thrust) to the southern shallower branch (Munsiari Thrust). In combination with kinematic investigations, Montemagni et al. (2020) and Kanyan et al. (2021) proposed that the MCTz migrated from deeper to shallower levels, where deformation temperature was higher, to shallower structural levels toward the south (in line with the general "in-sequence shearing" model of Montomoli et al., 2015), with a temporal lowering of the simple shear component. This supports a "decelerating-strain path" overtime (see also Grasemann et al., 1999). Indeed, in NW India, the highest simple shear contributions of Wm=0.90-0.95 (coupling the rigid-grain orientation method and the oblique recrystallized grain/quartz [*c*]-axis fabric) are associated to deformation temperatures of 510-610°C at the MCTz top (Law et al., 2013), whereas Wm=0.49-0.58 have been provided for the MCT base, toward the south, through the rigid grain net method (Montemagni et al., 2020).

In this Ph.D. thesis, kinematic investigations are based on dolomite oblique foliations at the MCTz top, developed for temperatures of 550-600°C, in agreement with {f} slip/twinning in dolomite (Barber et al., 1981). The obtained kinematic vorticity values (Wn=0.64-0.81) are in good agreement with Larson et al. (2010) mean kinematic vorticity estimates, at the MCTz top along the Budhi Gandaki and Daraudi valleys (Wm=0.72-0.87), found through the rigid grain net method. For instance, the highest values of Wm=0.72-0.87 have been suggested for the top of the MCTz (Chomrong Thrust, at structural levels comparable to MA16-19 sample, *Fig. 3.3, Fig. 7.3*), whereas lower kinematic vorticity estimates of Wm=0.50-0.73 have been reported for the MCTz core (Larson et al., 2010). These values are in line with published mean kinematic vorticity of Larson and Godin (2009) closely westward to the Manaslu area (Wm= 0.49-0.80) and with estimates of 0.66-0.77 in the Lower Dolpo (rigid porphyroclast method, Carosi et al., 2007), consistent with Wm=0.63-0.77 proposed in Eastern Nepal (Jessup et al., 2006). For instance, Carosi et al. (2007) interpreted their results as a minimum estimation, according to Law et al. (2004). A similar interpretation can be applied for the oblique-foliation results of this thesis, since the MCTz shear plane was not strictly detected. Combing the literature dataset for Western-Eastern Nepal with the results obtained in the present study (Wn=0.64-0.81), a "decelerating strain-path" can be therefore proposed also for the central Himalaya. Investigating syn-kinematic metamorphic minerals, microstructures and textures provided data on the MCTz which are comparable to the regional scale. A thermal field gradient from T=400-500 °C to T ~ 700 °C from bottom to top of the MCTz, occurred with higher simple shear component (Wn=0.64-0.81) at deeper structural levels, at the shear zone top.

7.2. Discussion of data for the South Tibetan Detachment System

7.2.1. Chame shear zone (Masryandi valley)

From the Manaslu area, a small suite of seven samples was studied from near Chame town, where the Chame Detachment/shear zone has been mapped (see Coleman, 1996; Coleman and Hodges, 1998; Searle and Godin, 2003). Since contradictory kinematic indicators are present at the outcrop scale and different kinematics has been inferred by previous authors (Coleman, 1996; Walters and Kohn, 2017, see *par. 3*), microstructure and texture analyses were carried out on the samples belonging to Unit 2 and Unit 3 of the GHS_U (*Table 3.2*). Moreover, two deformed Tur-bearing granites, intruding Unit 3, were also analyzed (*Table 3.2*).

Microstructure analysis from sheared rocks Unit 2 and Unit 3 rocks highlights the development of a mylonitic foliation, forming the C-planes of CS fabric (e.g. *Fig. 3.11d*). A top-to-the-northwest is supported by this kinematic indicator. Texture analyses conducted with different apparatus support the presence of asymmetric quartz CPO within Unit 2 and Unit 3 samples (*Fig. 3.12b-e; Fig. 3.13c-e*). Quartz textures (crossed girdle patterns on [0001], *Fig. 3.12b-d* and X-max pattern on [0001], *Fig. 3.12e*) can be interpreted in principle as resulting from intracrystalline deformation by mixed <*a*>-slip and prism<*c*> (Schmid and Casey, 1986; see Toy et al., 2008 for a review). Opening angle thermometry (with the calibration of Faleiros et al., 2016) on three samples (MC17-01; MC17-02; MC17-04) from Unit 3 supports quartz texture development at T=620-685 °C. Moreover, prism<*c*> slip in sample MC17-05 indicate texture development at T>650 °C (Mainprice et al., 1986). As mentioned above for MCTz (*par. 7.1.2*), there are still critical issues regarding the empirical opening-angle thermometer of Faleiros et al. (2016), as it is not always possible to recognize whether maxima on the Z-direction (of the strain ellipsoid) depend on basal<*a*> or π<*a*> slip (Morales et al., 2011). Nevertheless, precisely because it is an empirical equation based on natural samples, it can be proposed that the Faleiros et al. (2016) equation takes into account the cases in which the fabric opening-angle is given by basal and rhombic slips. Furthermore, as regards the use of the slip systems as geothermometers, prism<*c*> is the only one for which, to date, the range of temperatures proposed by Mainprice et al. (1986) still seems to be valid. Therefore, X-max on [0001] in sample MC17-05 (*Fig. 3.12e, Fig. 3.13c*) and further <*a*> and {*m*} maxima would confirm that quartz textures developed at T>650 °C. Texture analyses on the two Tur-bearing granites (in which a rough foliation was present) are very poorly defined through the crystal fabric analyzer (*Fig. 3.12f,g*). Indeed, quartz textures seem to be better defined through X-ray texture goniometry, where X-max on [0001] and girdle distributions on {*a*}- and {*m*}-planes, with {*m*} maxima on the Z-direction, support prism<*c*> slip. Textures that are not well-developed may be due to the strong layering and mineral composition heterogeneity. Moreover prism<*c*> slip may be concomitant with melting processes in granites (as occurs at T>650 °C, Mainprice et al., 1986). It is noteworthy that sample MC17-05, close to the Tur-bearing granites, shares similar textures (*Fig. 3.13a-c*), but also that crossed girdle textures from more distant samples support the same temperature range.

As introduced in *par. 3.*, some open questions remain as it is not easy to identify whether the Chame shear zone is a thrust- or normal-sense discontinuity or when it reached a detachment kinematic (Coleman, 1996; Searle, 2010). In their recent work, Walters and Kohn (2017) interpreted the Chame shear zone as an intra-GHS thrust-sense discontinuity for two main reasons: (*i*) two temperature gradients and cooling paths were recognized for the footwall and

the hanging wall rocks; (*ii*) a repetition of Unit 2 occurs (see also *Fig. 3.9a,b*). For the first point, through independent geothermometers (Zr-in-titanite, Hbl–Pl thermometry, Plagioclase–scapolite and garnet–biotite thermometry), Walters and Kohn (2017) report an inverted temperature gradient within the hanging wall rocks with simultaneous heating of the footwall. They coupled geothermometers and thermochronology to infer a shallow cooling path for the hanging wall rocks, and a steep cooling path for the footwall (Walters and Kohn, 2017). Moreover, peak Zr-in-titanite temperatures would have occurred at 760–850 °C, and the inverted temperature path would have lasted, in the hanging wall, from 30 Ma up to 16-17 Ma (U-Pb dating on titanite, Walters and Kohn, 2017). However, the studied samples support asymmetric quartz textures (*Fig. 3.12, Fig. 3.13*), consistent with the CS-fabric at the microscale (*Fig. 3.11d*) and at the mesoscale (*Fig. 3.9a*). pointing to a top-to-the-northwest sense of shear. As the described asymmetric patterns developed at temperatures of 620-685 °C (from Faleoiros et al., 2016 fabric opening-angle, and prism<*c*> thermometry), it is possible that the Chame shear zone experienced normal shearing when it was still at temperatures slightly below 700 °C. Moreover, it is possible assuming that normal shearing was already active during Tur-bearing intrusion. Concerning the Unit 2 repetition (*ii*), in the light of their results, Walters and Kohn (2017) suggest that it is the result of 1.3 km-thick zone of imbrication or localized strain associated with thrust tectonics. However, they also report that, as a second hypothesis, it may not be a tectonic repetition, and that the orthogneiss may derive from different intrusions. This is the preferred interpretation adopted in this thesis. Therefore, the Chame Detachment is here linked to a lower, ductile branch of the STDS occurring in the Masryandi valley (Manaslu area), wholly within the upper part of the GHS_U. This interpretation is also in agreement with the data of Hodges et al. (1996) and Searle (2010).

7.2.2. Discussion of data for the STDS *in sensu stricto*

The STDS was studied in four key valleys in Western Nepal occurring, from east to west, in the Manaslu area (upper Budhi Gandaki and Marsyandi valleys), Mustang-Myagdi region (Kali Gandaki valley) and Lower Dolpo region. Samples have been selected from a solid sampling to be as representative as possible of the entire STDS structure in the study areas, i.e., representing the lithologies exposed from the footwall to the hanging wall of the shear zone. Along the study transects, several common features are present:

- A thick (1-2 km) volume of sheared rocks, with few top-to-the-north kinematic indicators, involves calcsilicate-bearing gneiss and marble in the GHS_U and (impure) marble in the THS (see also Schneider and Masch, 1993; Carosi et al., 2002; Godin, 2003).
- The boundary between the GHS_U and the THS is not sharp and not even well recognizable at the mesoscale. However, the GHS_U is plastically deformed in the amphibolite facies (calcsilicates occur in marbles in all studied areas), whereas the THS is plastically deformed under greenschist facies. Samples do not show evident brittle deformation structures linked to the STDS. Metamorphic-related temperatures have a rapid up-section decrease (Colchen et al., 1981, 1986; Carosi et al., 2002; Godin, 2003; Searle and Godin, 2003; Searle, 2010; see also Law et al., 2011 in the Everest area toward the east). An isograde condensation within 200 m occurs from the pyroxene-zone to the biotite-zone in the Marsyandi valley (Colchen et al., 1986; Walters and Kohn, 2017).

- The main foliation recorded at the outcrop and microscopic scale is S2 foliation, while S1 foliation is preserved at higher structural levels, within the THS. The S2 foliation (marked by SPO of micas, calcsilicate and calcite) is parallel to the boundaries of the mylonitic zones (e.g. Searle, 2010). The S2 is more and more penetrative from higher to lower structural levels, supporting increasing strain (Carosi et al., 2007).
- In all studied areas, kinematic indicators are recognizable in sheared marble at the microscale, as slightly developed CS-fabric, asymmetric porphyroclast (*Fig. 4.3b*), and oblique foliation (*Fig. 3.16b, d; Fig. 3.17c, d, f; Fig. 4.3c-f*).
- In each sheared marble, calcite constituites the weak matrix (up-to over the 98% of the bulk volume) accommodating the deformation. Calcite has unimodal grain size distribution and lobate grain boundaries, which can be interpreted as due to GBM dynamic recrystallization. Straight calcite grain boundaries in some samples occur, indicating a local annealing process. However, annealing lowered the CPO intensity without strong influences on grain size and texture. Calcite grain size increases systematically down-section (*Fig. 3.18*; *Fig. 4.4*; *Fig. 5.6*).
- Calcite grain boundary mobility results in oblique foliations during the non-coaxial flow of the STDS in a genereral shear/simple shear-dominated flow.
- On an equal structural level, calcite and quartz textures are similar from area to area (*Fig. 3.21, Fig. 3.22, Fig. 4.6, Fig. 5.11*). Calcite twinning developed during the non-coaxial flow of the STDS as supported by calcite and quartz texture.
- Calcite grain size correspond to differential stress values of ca. 5-14 MPa in all studied marbles (5-13 MPa in the pure marbles from the Manaslu area, *Table 3.3, Fig. 3.19*; 6-14 MPa in marbles from the Kali Gandaki valley, *Table 4.2, Fig. 4.d*; 6-12 Ma in the impure marbles from the Lower Dolpo region, *Fig. 5.10, Table 5.2*) according to Rutter (1995) and Barnhoorn et al. (2004) paleopiezometers. Assuming temperatures of ca. 400-450 °C, differential stress (connected to grain size) developed under strain rates of ca. 10^{-11}–10^{-12} s^{-1} (*Fig. 3.19; Fig. 4.d*; *Fig. 5.10,* see the summary in *Table 7.1*).
- Calcite grains show type II {*e*}-twin microstructures, also recorded by texture (Burkhard, 1993; Ferrill et al., 2004, *par. 7.3.1*). Calcite paleopiezometers based on twin density (in samples where twinning contribution is strong, *par. 7.3.1*) support differential stress of ca. 100-170 MPa (130-150 MPa in the Manaslu area, *Table 3.3*; 130-170 MPa in the Kali Gandaki valley, *Table 4.2*; 105-135 MPa in the Lower Dolpo region, *Table 5.2*, see *Table 7.1*) according to Rybacki et al. (2011) piezometer. Strain rates values for twinning paleostress results are of ca. 10^{-12} s^{-1} for temperatures of ca. 300 °C (see *Table 7.1*).
- Calcite twinning developed during the non-coaxial flow of the STDS.

The coherence of all these features in marbles and impure marbles collected in the different valleys (comparing similar structural levels) indicates that the described fatures and deformation paths are not simply due to local factors. As samples are representative of the main lithotypes from bottom to top of the shear zone and calcite constitutes the weak matrix accommodating the deformation, samples and their features can be considered representative for the STDS flow in this part of the belt, where carbonate-bearing rocks are the dominant lithology. However, this does not imply that local variability in flow components cannot occur within this thick (compositionally) heterogeneous and long-lasting shear zone, as shown below (e.g. *par. 7.2*).

7.2.3. Texture interpretation for the STDS *in sensu stricto*

As for the MCTz, texture analyses carried out on the impure marbles of the GHS_U and the THS show low CPO values for both calcite and quartz. As for *par. 7.1*, the low CPO was interpreted as due to structural anisotropies and second-phase minerals distribution (see also Tullis and Wenk, 1994). However, it is possibly determined by minor annealing processes within the GHS_U marbles, as supported by straight grain boundaries microstructures (*Fig. 4.3j; Fig. 5.5h*), and/or the activity of multiple slip systems and twin planes (as supported by texture analysis). As noted by Rutter (1974), Barnhoorn et al. (2005) and Herwegh et al. (2008), annealing processes can considerably attenuate calcite CPO intensity without obliterating its fabric.

In all studied areas, calcite has well-defined textures (*Fig. 7.5*), with [*c*]-axis asymmetries, with respect to the mylonitic foliation, more evident at the GHS_U/THS interface. As for the MCTz, the lack of texture and microstructure asymmetries was used to localize the upper limit of the STDS ductile shear zone in all studied areas.

Comparing calcite and quartz textures, and calcite abundance and distribution, it is possible to infer that, in all selected samples, calcite was the weak mineralogical phase that accommodated the deformation. Calcite textures have strong maxima on the Z-direction and minor girdles parallel to the YZ-plane of the strain ellipsoid (*Fig. 3.21; Fig. 3.22; Fig. 4.6; Fig. 5.11; Fig. 7.5*).

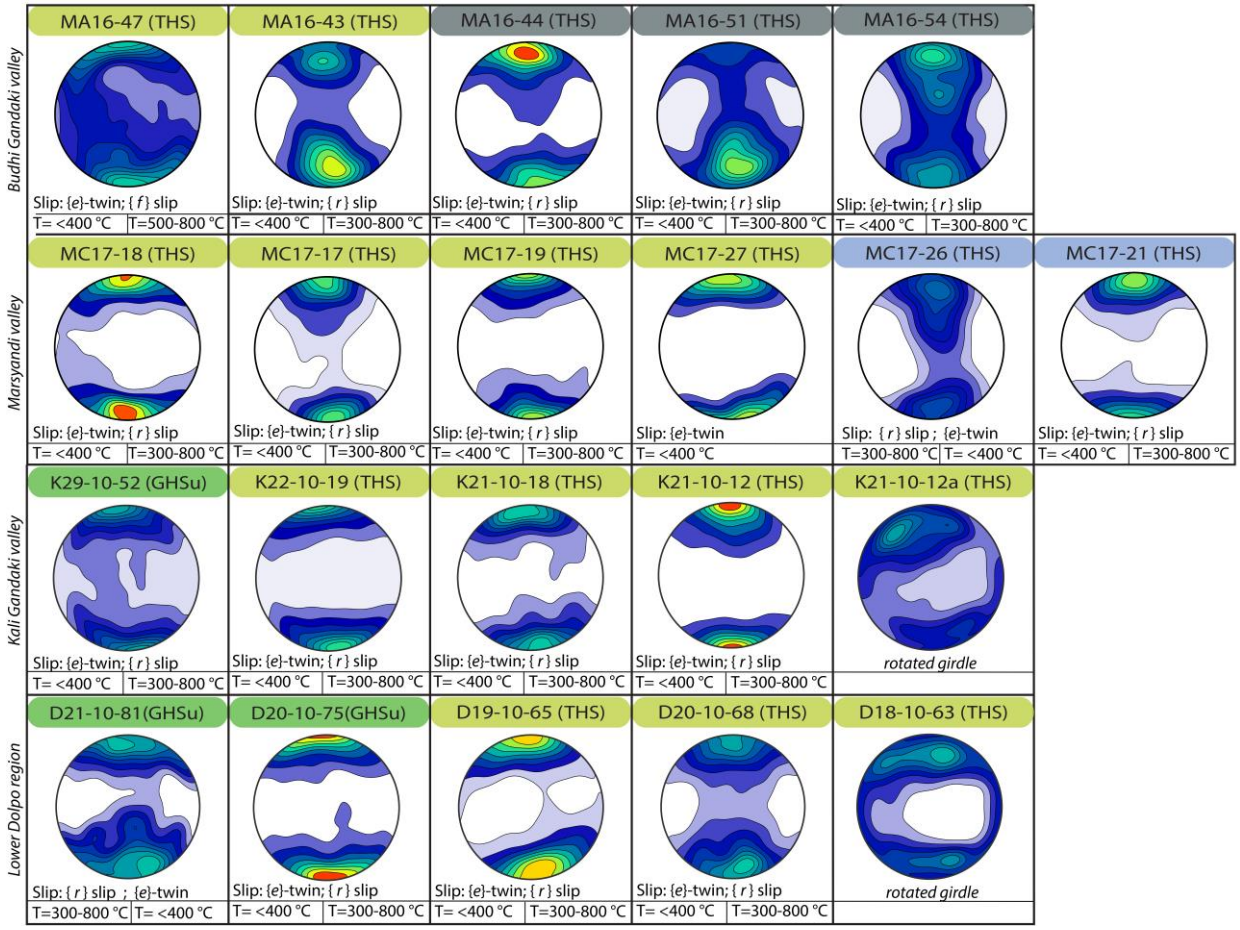

Figure 7. 5. *Calcite texture interpretation for almost all analyzed samples. Temperature estimations are based on Schimid et al. (1987), De Bresser and Spiers (1993, 1997), Ferrill et al. (2004) and Barber et al. (2007) works. All calcite asymmetric textures support {e}-twinning and top-to-north sense of shear. For GHS-affinity samples, intracrystalline slip is also an important mechanism; whereas for THS-affinity samples, intracrystalline slip is almost minor (excluding the fine-grained marble MC17-26). See* Fig. 3.21, Fig. 3.22, Fig. 4.6, *and* Fig. 5.11 *for further details.*

Comparing the whole dataset of calcite (*Fig. 7.5*) and quartz pole figures, particularly in the case of the same sample with both textural data, calcite asymmetric texture patterns can be interpreted as resulting from intracrystalline slip and twinning on the {*e*}-planes. Calcite sinistral asymmetry of [0001] maxima can be interpreted as due to twinning occurring in a dextral (top-to-the-north) non-coaxial flow (Schmid et al., 1987; Wenk et al., 1987). Under non-coaxial flow, {*e*}-twinning in calcite causes a rotation of the [*c*]-axis by 52° along the plane normal to the shear plane, with an opposite direction to the shear sense (the [*c*]-axis orientation of the host crystal is symmetrical to the normal to the {*e*}-plane, see Wenk et al., 1987; Lacombe, 2010; Tripathy and Saha, 2015). Therefore, both antithetic asymmetric patterns of calcite and synthetic asymmetric quartz textures (where it was possible to analyze) support the top-to-the-north sense of shear of the STDS. Only few samples escape this interpretation. In samples MA16-43 and MA16-47, at the GHS_U/Annapurna Fm. interface in the upper Budhi Gandaki valley (*Fig. 3.21e, f*), <*a*>-axis and {*r*}-planes define a couple of maxima on the X-direction, and on the Z-direction, respectively. This supports a stronger contribution of {*r*}-slip, as {*r*}-slip totally replace twinning at HT (with a transition starting from ca. 400 ° C, see Schmid et al., 1987; De Bresser and Spiers, 1993, 1997). This is consistent with amphibolite metamorphic assemblage of the sample. In the structurally higher located samples from the top of the Pi Fm. in the upper Budhi Gandaki valley (samples MA16-51, MA16-54, *Fig. 3.21a, b*) and the Nilgiri Fm. base in the Masyandi valley (samples MC17-26, MC17-21; *Fig. 3.22a, b*), a similar texture pattern occurs. In this case, however, a stronger contribution of {*r*}-slip can be linked to the calcite grain size rather than to deformation temperatures, as grain boundaries are a serious obstacle to twin propagation, so that twins can compete with intracrystalline slip only in coarse-grained crystals (Schmid et al., 1987). Moreover, a good example can be provided by sample MA16-51 (*Fig. 3.21b*), as it shows an almost symmetric [*c*]-axis orientation besides having asymmetric (and antithetic) {*e*}-maxima. This symmetric [*c*]-axis pattern, where microstructure shows that calcite define oblique foliations (*Fig. 3.16b*), can be interpreted as due to the stronger contribution of the {*r*}-slip, which orients the [c]-axis synthetically to the shear sense (Schmid et al., 1987). At the top of the structural section in the Budhi Gandaki and Marsyandi valleys, in samples MA16-54, MC17-26, and MC17-21, no kinematic indicators are highlighted from microstructure (*Fig. 3.16a, Fig. 3.17a, b*) to texture analysis (*Fig. 3.21a, Fig. 3.19a, b, Fig. 7.5*). The STDS upper limit in the Budhi Gandaki valley is therefore placed at the Pi fm. base, above sample MA16-51 and below sample MA16-54, while in the Marsyandi, around samples MC17-19 and MC17-27.

7.2.4. Paleostress conditions along the STDS

For the paleostress estimations based on dynamic recrystallization mechanisms, the Rutter (1995) and Barnhoorn et al. (2004) paleopiezometers are reliable methods in pure marbles, as recently validated by Platt and De Bresser (2017). In fact, these methods are widely used (Rutter et al., 2007; Rogowitz et al., 2014; Negrini et al., 2018) comparing with pioneering paleo piezometers by Schmid et al. (1980). A main issue related to both methods is the presence of second-mineral phases, like micas, that usually cause finer grain size during dynamic recrystallization processes (Herwegh and Berger, 2004; Ebert et al., 2008). This can be valid for the Lower Dolpo region and the Kali Gandaki valley, where calcite, with a volume abundance of less than 90%, is often interrupted by micas. Nevertheless, pure marbles from the Manaslu area have an amount of second-mineral phase less than 2% in the analysed large areas; where calcite

has a unimodal grain size (*Fig. 3.18*). Therefore, the studied suite from the Manaslu area provides a "nearly" ideal natural example of marbles suitable for paleostress estimations for dislocation creep deformation. Differential stress estimates of ca. 5-13 MPa (*Fig. 7.6, Table 7.1*) are reliable indicators of the differential stress associated with a GBM regime.

Concerning the two flow laws (Rowe and Rutter, 1990, and Rybacki et al., 2011, 2013) used for twinning characterization, it is worthy to note that the {*e*}-twins development requires at least 2-12 MPa of differential stress (Jamieson and Spang, 1976; Wenk et al., 1987; Burkhard, 1993; Lacombe and Laurent, 1996; Ferrill, 1998). Therefore, they can really develop together with GBM mechanisms in a natural shear zone. Among three different piezometers proposed by Rowe and Rutter (1990) after experimental works, the one used in this thesis (twin density) is based on the assumption that twin incidence is a function of applied stress, giving a neglectable role to deformation temperatures. More recently, Rybacki et al. (2011, 2013), based on the same assumption, provided a reviewed twin-density piezometer designed for natural conditions.

Table 7. 1. *Paleostress results for all analyzed marbles, differential stress for dynamic recrystallization (after Barnhoorn et al., 2004 piezometer) and twinning (after Rybacki et al., 2011 piezometer For strain rate calculation, a simplification is proposed for the deformation temperature estimates recorded within the structural section as equal to that assumed for the THS (T_{GBM} = 400 ° C, T_{twin} = 300 ° C). Note that, therefore, the GHS, deemed to be hotter than the THS, recorded strain rates higher than those estimated for the STDS hanging wall. Note also that sample MC17-26 (from the Marsyandi valley in the Manaslu area) and D20-10-63 (from the Lower Dolpo) belong to the THS above the STDS hanging wall; therefore, the estimated differential stress reflects the general deformation associated to the D2 phase rather than the deformation linked to the STDS.*

Manaslu valleys	Diff. stress (grain size, MPa)	$\dot{\varepsilon}$ (s^{-1}) (T=400°C	Diff. stress (twin, MPa)	$\dot{\varepsilon}$ (s^{-1}) (T=300°C)
MC17-26 (THS)	11.3±1.0	2.8E-11	ND	ND
MA16-54 (THS)	7.8±1.5	1.3E-11	129±12	8.27E-13
MA16-51 (THS)	8.5±0.9	1.3E-11	133±12	1.2E-12
MC17-27 *(THS)*	7.2±0.6	7.9E-12	128±12	7.44E-13
MC17-17 *(THS)*	7.7±0.6	9.5E-12	142±13	2.64E-12
MC17-18 *(THS)*	6.8±1.7	5.7E-12	145±13	3.51E-12
Kali Gandaki valley	Diff. stress (grain size, MPa)	$\dot{\varepsilon}$ (s^{-1}) (T=400°C)	Diff. stress (twin, MPa)	$\dot{\varepsilon}$ (s^{-1}) (T=300°C)
K21-10-12A *(THS)*	13.7±4.8	3.1E-11	ND	ND
K21-10-12 *(THS)*	10.2±3.6	1.7E-11	135±6	1.4E-12
K22-10-19 *(THS)*	8.3±2.9	1.1E-11	160±7	1.3E-11
K29-10-51 *(GHS)*	8.7±3.1	1.2E-11	ND	ND
K29-10-52 *(GHS)*	9.4±3.3	1.4E-11	171±8	3.3E-11
K31-10-64 *(GHS)*	6.8±2.4	7.3E-12	136±6	1.5E-12
K31-10-65 *(GHS)*	6.5±2.3	7.4E-12	ND	ND
Lower Dolpo region	Diff. stress (grain size, MPa)	$\dot{\varepsilon}$ (s^{-1}) (T=400°C)	Diff. stress (twin, MPa)	$\dot{\varepsilon}$ (s^{-1}) (T=300°C)
D20-10-63 *(THS)*	11.5±2.4	2.2E-11	ND	ND
D20-10-68 *(THS)*	9.8±4.2	1.6E-11	134.97	6.2E-11
D19-10-65C *(THS)*	8.6±4.7	1.2E-11	115.08	7.8E-12
D20-10-75 *(GHS)*	8.7±4.3	1.2E-11	109.85	4.3E-12

A main limiting factor of the Rowe and Rutter (1990) and Rybacki et al. (2011) piezometers is the assumption that grain size has no influence on twin development, although the greater the grain size, the easier is twins development (Casey et al., 1978; Spiers, 1982; Spiers and Rutter, 1984; Schmid et al., 1987; Rutter et al., 2007). Nevertheless, for marbles with a significant grain size (falling within the grain size insensitive field), the grain size should have a minimum (if any) effect in inhibiting twin development, and twin densities are normalized for the grain size. As also pointed out by Rybacki et al. (2013) and Brandstätter et al. (2017), for natural samples, the Rowe and Rutter (1990) method is limited as it is calibrated for a temperature range of 400-800 °C in which, however, dislocation glide dominates on the twinning mechanism. Therefore, the ca. 200 MPa estimation in this thesis, derived from the Rowe and Rutter (1990) method, may be an overestimation, but differential stress of 105-170 MPa through the Rybacki et al. (2011, 2013) twin-density method should be quite accurate (*Table 7.1*). Even considering that second-phase minerals affected twinning development, calcite grain size based paleopiezometers and twin-density based piezometers provided two different results. It is therefore reasonable to infer that calcite grain size development and twinning reflect different stages of deformation, where grain boundary mobility and twinning have different relative contribution. It is noteworthy that strain rate estimates are constant for both deformation mechanisms and differential stress records (ca. 10^{-11}–10^{-12} s^{-1}, see *Table 7.1*). This result strengthens the hypothesis that calcite twinning and grain size developed during the non-coaxial deformation of the STDS. Different differential stress values for GBM and twinning are interpreted as photographs of two different stages in the progressive evolution of the STDS.

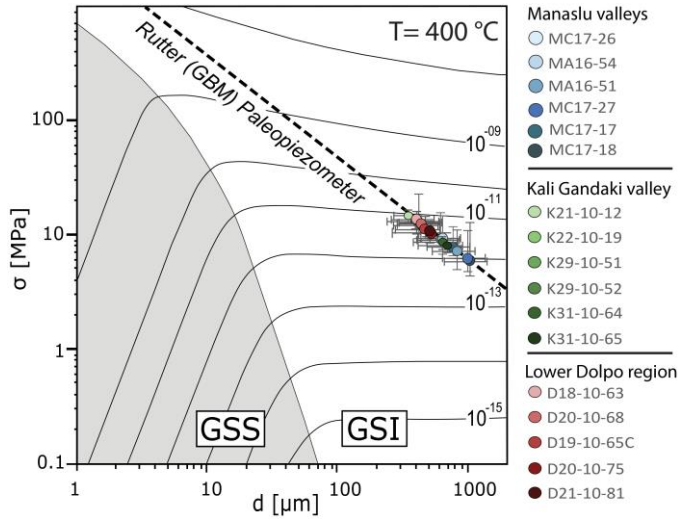

Figure 7. 6. *Deformation-mechanism map for all studied marbles affected by the STDS. The dashed line corresponds to the calcite GBM-based paleopiezometer of Rutter (1995). The boundary between the grain size sensitive creep (GSS) field (Herwegh et al., 2003) and the flow laws of Renner et al. (2002) for grain size insensitive (GSI) regimes is given. Contours correspond to the strain rates for an average of T=400 °C (see Fig. 7.5). Differential stress after Barnhoorn et al. (2004) fall in the same error bar, on Rutter (1995) regression line (dashed line). In the left legend, samples are listed from top to bottom. Note that all samples fall into the magnitude order of 10 MPa.*

7.2.5. Kinematic vorticity and shortening variations for STDS shearing

Kinematic vorticity estimates through independent methods are provided for all the study areas (*Table 7.2*). A main advantage of coupling the Wallis (1995) oblique foliation method and the Wenk et al. (1987) texture-based method is that both require the same reference frame, which is the shear plane. As discussed in *par. 7.1.3*, the shear plane can be approximated by the mylonitic foliation, as the S2 foliation is almost parallel to the shear zone boundaries. This

assumption is also usually adopted in other tectonic settings where mylonitic foliation is pervasive, supporting high-strain conditions (Spanos et al., 2015; Sarkarinejad and Heibati, 2017). Advantages and limitations of the Wallis (1995) oblique foliation method are discussed in *par. 7.1.3*. Concerning the texture-based method of the Wenk et al. (1987), more issues are:

(i) Calcite tends to rebalance itself even at low-to-very low temperature conditions (Schmid et al., 1987; Ratschbacher et al., 1991; Burkhard, 1993; Kurz and Neubauer, 1996; Kurz et al., 2000; Smith et al., 2013; Bauer et al., 2018), even if calcite intracrystalline deformation at temperatures below 150 °C are poorly constrained;

(ii) Intracrystalline slip systems and twinning reorient the calcite [*c*]-axis in the opposite way (Bestmann et al., 2000), determining the broad maxima on [0001] pole figures;

(iii) Second-phase minerals may influence twinning and the kinematic vorticity recorded by calcite (see also Jiang, 1994b, Bhandari and Jiang, 2021 for quartz deformation).

The first two limitations are attenuated as only samples where {*e*}-planes and the [*c*]-axes maxima compatible with a stronger contribution of twinning over intracrystalline slip were selected (see also Schmid et al., 1987). Therefore, it may be assumed that calcite rebalance at low temperature conditions (<300 °C) after the STDS shearing end was neglectable (*i*) and that {*e*}-twins determined the main texture (*ii*). Concerning the third limitation, it is not possible to completely eliminate the problem of second-phase minerals for studied samples from the Lower Dolpo and Kali Gandaki valley (*iii*). However, samples from the Manaslu are pure marble, and provided compatible results. Evidence of strong flow partitioning in the studied samples is lacking. Therefore, it is possible to consider the results obtained in this work in a semi-quantitative way for the STDS kinematic flow. Comparing results for the study areas, some distinctions have to be made (*Table 7.2*).

Table 7. 2 *Kinematic vorticity results for all study areas using the Wallis (1995) method for oblique foliation (Sb) and the Wenk et al. (1987) method for calcite asymmetric [c]-axis fabric induced by twinning and intracrystalline slip. Shortening perpendicular to the flow plane, calculated using the Wallis et al. (1993) method, is provided.*

Area	Finite Strain	*Sb-method*			*[c]-axis method*		
	Rxz	*simple shear %*	*Wm*	*Shortening %*	*simple shear %*	*Wn*	*Shortening %*
Budhi Gandaki							
MA16-51	2.18	84	0.97	9	29	0.44	30
MA16-47	*ND*	*ND*	*ND*	*ND*	20	0.31	*ND*
Marsyandi							
MC17-27	2.00	87	0.98	7	34	0.51	26
MC17-19	*ND*	*ND*	*ND*	*ND*	28	0.43	*ND*
MC17-17	1.87	87	0.98	6	28	0.4	25
MC17-18	1.88	91	0.99	4	26	0.4	*ND*
Kali Gandaki							
K21-10-12A	1.24	*ND*	*ND*	*ND*	*ND*	*ND*	*ND*
K21-10-12	1.32	44	0.64	8	*ND*	*ND*	*ND*
K21-10-13	1.27	51	0.72	9	*ND*	*ND*	*ND*
K22-10-18	*ND*	*ND*	*ND*	*ND*	30	0.45	*ND*
K22-10-19	1.40	56	0.77	10	30	0.45	14
K29-10-52	1.46	58	0.79	11	50	0.71	13
Lower Dolpo							
D20-10-68	*ND*	*ND*	*ND*	*ND*	20	0.31	*ND*
D19-10-65C	*ND*	*ND*	*ND*	*ND*	35	0.52	*ND*
D20-10-75	*ND*	*ND*	*ND*	*ND*	26	0.40	*ND*
D21-10-81	*ND*	*ND*	*ND*	*ND*	50	0.71	*ND*

MANASLU AREA AND LOWER DOLPO REGION

Kinematic vorticity estimates are quite different for the two adopted methods. The Wallis (1995) oblique foliation method (with angle δ°=38-41°) supports high kinematic vorticity values of Wm=0.97-0.99, corresponding to a simple shear dominated flow (84-91% of simple shear, *Table 3.4, Table 7.2, Fig. 7.7*). *Vice versa*, kinematic vorticity estimates from the Wenk et al. (1987) method, (with ω°=5-10°), supports simple shear contributions of 20-35% (Wn=0.31-0.51) and a general shear flow with a very strong contribution of pure shear (*Table 3.4, Table 7.2, Fig. 7.7*). Even if no clear trends are recognizable, the higher kinematic vorticity is recorded at lower structural levels, toward the GHS.

For the Lower Dolpo region, no oblique foliations were recognized. However, low kinematic vorticity estimates were again obtained with the Wenk et al. (1987) method (*Fig. 7.7*). Also, in the lower Dolpo measured ω angles (5-10°) support a general shear flow, with low simple shear contributions of 20-35% (*par. 5.2.4, Table 7.2*) consistent with results from the Manaslu area. Moreover, with this method in both areas, simple shear contribution increases down-section.

KALI GANDAKI VALLEY

Marbles involved by the Annapurna Detachment (STDS) have nearly constant kinematic vorticity values (*Table 4.3*) without any clear trend. However, stronger simple shear contributions are recognized in lower structural levels. The Wallis (1995) oblique foliation method, (with δ°=20-26°) supports kinematic vorticity values of Wm=0.64-0.79, corresponding to a sub-simple shear flow (41-50% of simple shear, *Table 3.4, Table 7.2*). Consistently, kinematic vorticity estimates from the Wenk et al. (1987) method, with ω° of [*c*]-axis maxima asymmetry of 10-15°, supports simple shear contributions of 30-50% (Wn=0.45-0.71) and a general shear flow (*Table 3.4, Table 7.2*). Despite these two methods having their own limitations, both indicate that the STDS flow conditions in the Kali Gandaki valley are different from the other two study areas (see *Fig. 7.7*).

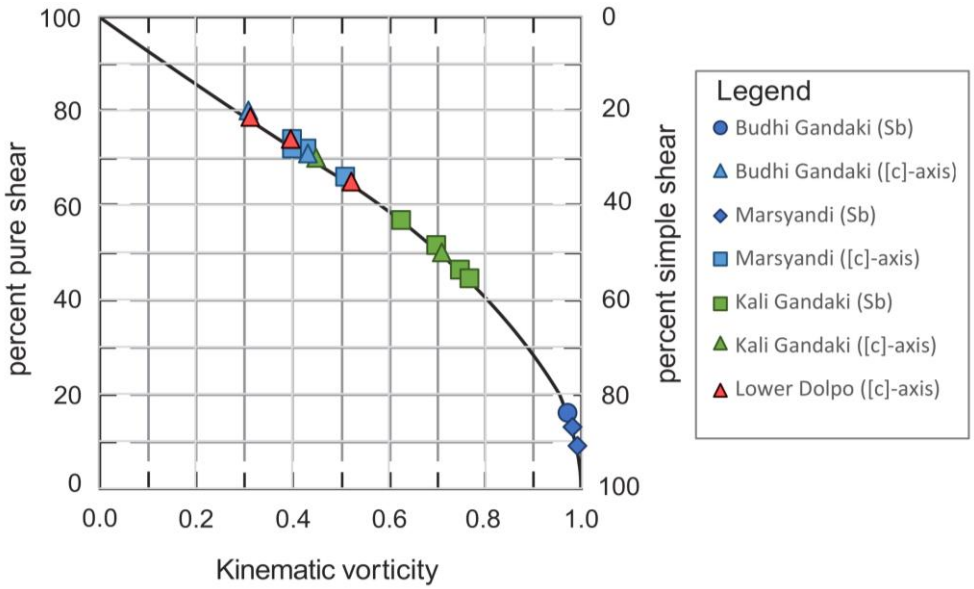

Figure 7. 7. *Adapted Law et al. (2004) graph for kinematic vorticity estimates obtained in this thesis for all studied areas. Relationship between kinematic vorticity and relative components of pure and simple shear for instantaneous 2D flow is given. Note that twin-based kinematic vorticity estimates (through the Wenk et al., 1987 method) support a general shear flow, with strong pure shear components in the Manaslu and Lower Dolpo areas. Oblique foliation-based kinematic vorticity estimates provide relative higher simple shear contribution in the Manaslu and Kali Gandaki valleys. See* Table 7.2 *and text for details.*

DATA DISCUSSION

For the Kali Gandaki valley, the short ranges of variation of kinematic vorticity through independent methods indicate that both oblique foliation and twinning recorded the same geometry of flow throughout the Annapurna Detachment (30-50% of simple shear, *Fig. 7.7*). As reviewed by Xypolias (2010), vorticity estimates obtained from the oblique foliation method record a late small increment of ductile deformation. In contrast, according to Wenk et al. (1987), twinning can record the vorticity of a larger segment of the deformation history and slightly underestimate the simple shear component (due to the aforementioned limiting factors). The consistency in the estimates obtained from both methods can imply that (*i*) twinning and grain boundary mobility in calcite developed as alternating processes during the same interval of ductile deformation at LT-conditions (e.g. Schmid et al., 1987, Wenk et al., 1987), or that (*ii*) twinning and dynamic recrystallization processes were not contemporaneous but both developed for the same steady state flow (e.g. see Spanos et al., 2015). As reported in the previous *par. 7.2.4*, temperature and paleo stress conditions significatively changed from the GBM-regime to the twinning regime, so that oblique foliation and twinning developed in two different steps of the same progressive evolution of the shear zone (*Table 7.1*). Therefore, within the Annapurna Detachment, the strain rate and the kinematic vorticity remain constant during the whole deformation history of the shear zone (*ii*), even if the other parameters changed. Alternatively, this can imply that twinning started developing together with oblique foliation, re-orienting calcite [*c*]-axes against the sense of shear. Twin incidence in crystals increased over time, up to the final investigated pattern, as deformation temperature decreased and higher differential stress conditions were induced by constant strain rates.

Concerning the Manaslu area (and the Lower Dolpo region), results show a more complicated history. Kinematic vorticity estimates using oblique grain-shape fabrics provide indications for a simple shear-dominated flow (Wm=0.97–0.99), which is consistent with estimates from the Everest area, far to the east, obtained through three independent methods (porphyroclast distribution method of Wallis et al., 1993; porphyroclast hyperbolic distribution method of Simpson and De Paor, 1997; and quartz [*c*]-axis fabric and strain ratio method of Wallis, 1992, 1995) by Law et al. (2004) (Wm = 0.67–0.98). Similar values (Wm = 0.74–0.91) were found also in the sheared limestone and marble of the THS by Jessup et al. (2006) through the Wallis (1995) method. Nevertheless, kinematic vorticity estimates using the texture-based method indicate a pure shear-dominated flow (Wn=0.31–0.51) during twinning development both in the Manaslu area and in the Lower Dolpo region. This possibly implies that (*i*) the Wenk et al. (1987) method drastically underestimated the kinematic of the flow in the studied samples of both areas or, alternatively, (*ii*) the STDS experienced a complex evolution history, with a lowering of the kinematic vorticity over time.

The first implication could be due to the aforementioned method limiting factors. However, despite possibly having some influence on the Lower Dolpo samples, it seems that selected marbles from the Manaslu area are very suitable for the kinematic vorticity estimations through the Wenk et al. (1987) method. Therefore, there is a real great difference in the recorded flow. It is worthy of note that in the Kali Gandaki valley, values of Wn = 0.45–0.71 using the Wenk et al. (1987) method partially overlap with Wn of 0.31–0.51 for the Lower Dolpo region and the Manaslu area. This indicates that, in the last two areas, only the top-to-the-north sense of shear and strain rates stayed constant.

The heterogeneity of the vorticity within the structural sections and from area to area can be due to a lithological control, such as the variable volumetric aboundance of micas and second-phase minerals. Alternatively, it can be explained by a heterogeneity of the kinematic flow within the huge deformed volume. The flow component variability can be related to an internal geometrical and kinematic complexity of the multi-branch thick crustal-scale shear zone.
Shortening estimates were achieved through the Wallis et al. (1993) equation by combining finite strain analyses (Fry, 1979; Waldron and Wallace, 2007) and kinematic vorticity estimates (Wenk et al., 1987; Wallis, 1995). Finite strain analyses on the Manaslu area and the Kali Gandaki valleys provided a minimum strain estimate, as the available strain markers (calcite crystals) are recrystallized. Therefore, shortening results also represent minimum estimates, especially if combined with the oblique foliation-based kinematic vorticity estimates (5-11% in both areas, *Table 3.5, Table 4.3*). According to paleopiezometric estimates (*par. 7.3.2*), calcite twins only developed after the end of calcite dynamic recrystallization. Therefore, it can be assumed that the analyzed calcite crystals are a more suitable finite-strain marker when compared with twining-based Wn estimations (Wenk et al., 1987 method). Combining the finite strain estimates with Wn data, the obtained shortening ranges between 25-30% in the Manaslu area (*Table 3.5*) and 13-14% in the Kali Gandaki valley (*Table 4.3, Table7.2*).

7.3. Implication for STDS evolution

As suggested by Schmid et al. (1987), twinning deformation in calcite can occur in alternation with GBM mechanisms, as twinning mechanisms involve the entire host crystal, up to its grain boundaries (inhibiting GBM). Moreover, twinning commonly develops under lower temperature conditions than those of GBM regime (Schmid et al., 1987; Kennedy and White, 2001), and/or at higher differential stress (Rutter, 1995; De Bresser and Spiers, 1997; Rutter et al., 2007). Fabric analyses show that both the GBM mechanisms, responsible for the calcite oblique foliation, and twinning developed during the non-coaxial ductile deformation of the STDS. GBM is synchronous to the blastesis of metamorphic index minerals (e.g. calc-silicates in the GHS_U marbles), supporting the view that the dynamic recrystallization developed at temperatures between 450-650/700 °C traced down-section (Vannay and Hodges, 1996). Moreover, it should be stressed how the Type II {*e*}-twin, frequently observed in the study samples overprinting GBM, usually develops at temperatures below 300-400 °C (Schmid et al., 1987; Rutter, 1995; De Bresser and Spiers, 1997; Kennedy and White, 2001; Ferrill et al., 2004). Paleostress analyses based on calcite, point out that the two deformation mechanisms (GBM and twins) developed under very dissimilar differential stress conditions, ≤10 MPa during GBM processes, and of one order of magnitude higher during twinning along {*e*}-planes (maily 100-150 MPa after Ribacki et al., 2011, 2013; >200 MPa after Rowe and Rutter, 1990). GBM and twinning did not develop together, but at different temperature and differential stress conditions, during the STDS activity at nearly same strain rates values (10^{-12}–10^{-11} s^{-1}).
Linking together, all these considerations make it possible to define two different progressive stages of STDS ductile shearing. In line with the typical schematic strength profile of crustal rocks (Ranalli and Murphy, 1987; Kohlstedt et al., 1995, see *Fig. 7.8*), defined for constant strain rate, as in the study case, a transition from deformation/flow at deeper to shallower crustal levels can be recognized. GBM recrystallization occurred during an early stage of STDS shearing, referred to as $D2_{early}$, at lower structural levels, where rocks were hotter (450-650 °C) and plastically deformed at lower differential stress conditions (5-15 MPa). Twinning occurred later,

during a late stage of shearing, referred to as $D2_{late}$, at higher structural levels and lower temperature conditions (ca. 300 °C) and at different rheological conditions, characterized by higher differential stress values (100-170 MPa). In the Manaslu area (and in the Lower Dolpo), grain size and twin width increase down-section, indicating that both deformation mechanisms developed in down-section progressively warmer rocks. It supports a lowering of strain/temperature ratio for twinning development. Kinematic vorticity data in the Manaslu area and in the Lower Dolpo also support the view that the flow conditions (degree of coaxiallity of the flow) varied over time during the progressive evolution of the STDS (*par. 7.3.2*). A simple shear-dominated flow evolved into a general shear flow over time. If so, it is possible to infer that the STDS is a shear zone that experienced a decelerating strain path (Simpson and De Paor, 1993; Grasemann et al., 1999). Interestingly, a similar strain path has also been suggested for the MCTz (Grasemann et al., 1999). In the Kali Gandaki valley, twin density increases down-section, showing increasing strain/temperature ratio (Ferrill et al., 2004; Lacombe, 2010). Moreover, no significant variation kinematic vorticity is present from the $D2_{early}$ to the $D2_{late}$. This supports the view that the Annapurna Detachment, the local segment of the STDS, had minor variation in the Kali Gandaki valley during progressive shallowing. The down-section kinematic vorticity increases may correspond to a strain gradient (down-section strain increase) or to a kinematic gradient.

7.3.1. Integrating STDS results on a regional scale

The proposed $D2_{early}$ temperature trend is comparable with the findings of Long et al. (2019), who suggest a field gradient of ~160–260 °C/km in western Bhutan. Similarly, Antolín et al. (2013), Parsons et al. (2016a), and Soucy La Roche et al. (2018a, b) have proposed deformation temperatures of 500 to 400 °C within the STDS, traced from the GHS_U up in to the THS, in the central and western Nepal Himalaya. In eastern Nepal (Everest-Rongbuk area), higher temperatures ($T \geq 650$ °C) are proposed for the GHS_U rocks (Law et al., 2004, 2011; Cottle et al., 2011; Corthouts et al., 2016; Waters et al., 2019). However, regardless of the exact temperature values reported in the literature, which will depend on the positions of individual samples analyzed in the thick shear zone, as well as other local factors, it is important to emphasize that a significantly steep thermal field gradient occurs along the STDS. Recently, several authors have investigated the calcite crystal fabrics of marbles deformed within the STDS in the central Himalaya (e.g. Corthouts et al., 2016; Parsons et al., 2016a; Larson et al., 2020). From calcite texture analyses, Parsons et al. (2016a) suggested that ductile flow in the GHS_U occurred in calcite via {c}<a> slip and {f} slip, indicating HT-MT deformation conditions similar to those reported in this thesis. In all the presented studied areas of this thesis, $D2_{early}$ deformation stage recorded differential stress of 5–15 MPa. This range matches with proposed stress estimates for ductile flow along the STDS in other parts of the Himalaya. In the Mt. Everest region, further to the west, Law et al. (2011) suggested 10–15 MPa of differential stress at the base of the ductile STDS using the grain size-based quartz piezometer of Stipp and Tullis (2003), increasing to 25–35 MPa beneath the detachment. These values have recently been confirmed by Waters et al. (2019), who suggested 12 MPa as an average differential stress for the STDS base. In the same area, Corthouts et al. (2016) proposed stresses of 29–38 MPa using the same flow law. Slight differences in the literature data are probably due to the use of different lithotypes (strain partitioning and strain memory change in different lithotypes) and structural height of individual samples within the STDS, together with varying strain paths and circulating grain boundary

fluids, etc. Nevertheless, these previously published paleostress estimates for the STDS are remarkably similar to our estimates based on carbonate-bearing rocks and highlight the low differential stress conditions under which main ductile shearing on the STDS occurred. Non-coaxial flow in the STDS, consistent with the defined $D2_{early}$ deformation stage of this thesis, has been documented along the Himalaya (*see par. 7.3.3*). Westward to the Lower Dolpo Region, in the Upper Karnali valley (NW Nepal), Nagy et al. (2015) reported consistent vorticity estimates. Also, several work in the Everest Himalaya (e.g. Law et al., 2004, Jessup et al., 2006) report a simple shear dominated dominated flow. Microstructures associated with $D2_{late}$ deformation stage in this thesis indicate differential stress of 105-170 MPa at temperatures below 350 °C in the three areas investigated here. It is noteworthy that this stress range is similar to the paleostress values derived by Corthouts et al. (2016) above the upper brittle strand of the STDS in the Mt. Everest Region, where they suggest differential stresses of 126 MPa applying the grain size-based Rutter (1995) method.

7.3.2. Progressive evolution of the STDS

A time-transgressive deformation within the STDS, i.e. up-section migration of progressively lower-temperature deformation through time, has been suggested in different Himalayan areas (Iaccarino et al., 2017b; Kellett et al., 2019, with references; Long et al., 2019). For the central Himalaya, where carbonate-rich rocks are very abundant, progressive evolution of the STDS shear zone, from deeper to higher structural levels, is schematized in *Fig. 7.8* according to lithospgeric/strength profiles. At deeper structural level, strain softening was enhanced by higher temperatures and weaker mineral phases behavior (e.g. calcite, *Fig. 7.8*), which therefore recorded lower differential stress. For “normal” continental geothermal gradients (25–40 °C/km) and “wet” marbles, a differential stress of 10 MPa at temperatures above 450 °C is enough to maintain ductile flow in the middle crust. These rocks within the shear zone were progressively affected by strain hardening and a viscosity increase, as the shear zone cooled during exhumation towards higher crustal levels (*Fig. 7.8*). As strain hardening occurred, differential stress increased by one order of magnitude at same strain rates in the upper crust. Moreover, in a system where strain rate is constant, stress is a function of tectonic force applied to the shear zone. In that situation, the cooler and stronger section of the shear zone requires a higher concentration of stress. The decrease in kinematic vorticity overtime should results in a a narrowing of the shear zone (Fossen and Cavalcante, 2017).

In the Himalaya, the "apparent" temperature field gradient within the STDS is one order of magnitude higher than typical geothermal gradients, being of the order of ~160–260 °C/km (Waters et al., 2019; Long et al., 2019) and locally up to 300–400 °C/km (Jessup et al., 2008; Cottle et al., 2011; Law et al., 2011; Kellett and Grujic, 2012). These extreme temperature field gradients have been interpreted as indicating a strong telescoping of isotherms during shearing on the STDS, accompanied by intense vertical flattening of the orogen (Corrie et al., 2012; Law et al., 2011). However, models for attenuation/telescoping of the isotherms within fundamental Himalayan fault zones such as the STDS and MCT are still debated (Kellett et al., 2019). As suggested by Law et al. (2011), vertical shortening can be due to lithospheric loading; therefore, it is possible to expect a decrease in the shortening from $D2_{early}$ to $D2_{late}$, where the latter is the pervasive shortening phase defined in this thesis for the Kali Gandaki valley and in the Manaslu area. Besides being minimum estimates for the strain (e.g. see also Law et al., 2004, 2011), shortening perpendicular to the flow plane for the STDS is of the order of 14-30%, slightly high

compared with the literature database (e.g. Law et al., 2004 for the Everest area). These authors proposed perpendicular shortening of 10–30% on recrystallized quartz grains (at lower strain rates of 10^{-14}–10^{-13} s^{-1}), therefore concerning the $D2_{early}$ stage, and of feldspar porphyroclasts. This indicates minor shortening variation during STDS ductile activity. It is worthy of note that the low shortening estimates are linked to the strong underestimation of the R_{XZ} in the work for this thesis in the Himalayan literature database. Strong pure shear component, active during the $D2_{late}$, support the orogen scale general stretching and flattening model for the central-eastern Himalaya proposed by Corrie et al. (2012), which in turn would enhance telescoping of isotherms (Law et al., 2004, 2011; Long and Kohn, 2020).

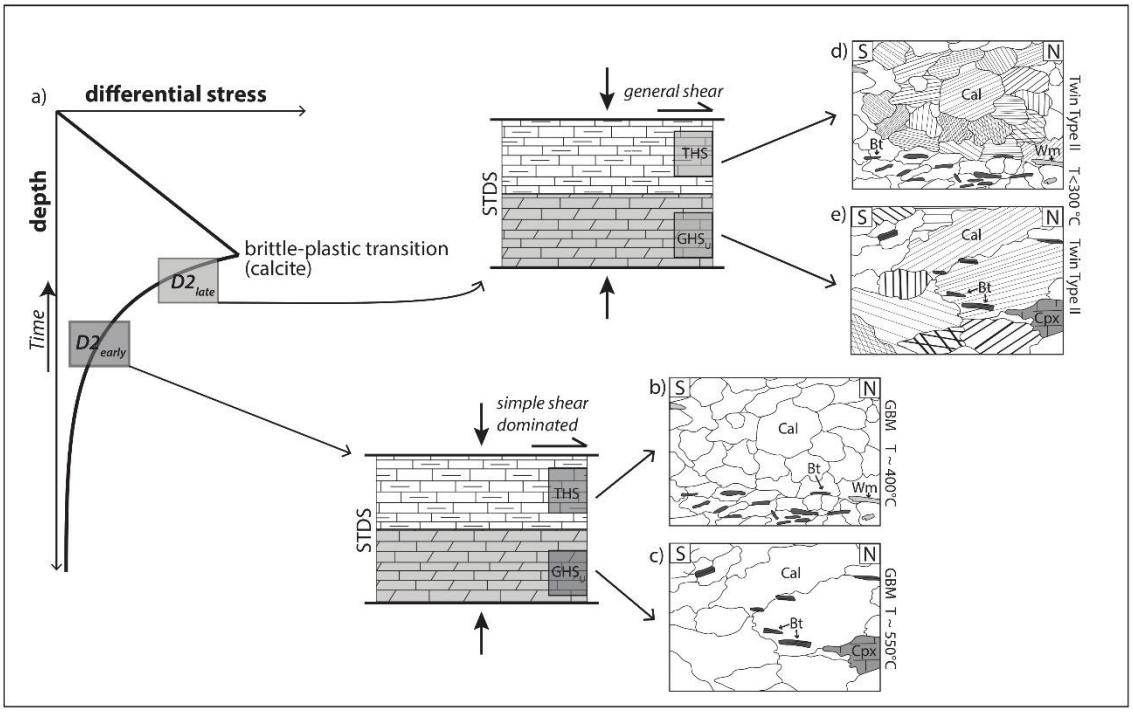

Figure 7. 8. *Schematic strength profile illustrating typical vertical variations in lithosphere strength/differential stress (not to scale). Two main stages, at different depth and stress conditions, are proposed for the activity of the STDS in central Himalaya.*

7.4. Discussion: post-kinematic event in the Tethyan Himalayan Sequence

7.4.1. Summary of microstructure, microchemistry, and ^{40}Ar–^{39}Ar age

Three deformation phases, linked to different P-T histories and structures, are well distinguished in Himalaya: the collisional stage, or D1, the south-directed exhumation stage, or D2, and the crustal thinning stage (east-west flow), or D3. Despite a lateral age variability, distinct temporal ranges are 48/44-25 Ma for the D1 (Hodges et al., 1996; Godin et al., 1999, 2001; Carosi et al., 2010; Dunkl et al., 2011); 27-15 Ma for the D2 (Guillot et al., 1994; Godin et al., 2006b; Crouzet et al., 2007; Leloup et al., 2010; Dunkl et al., 2011; Carosi et al., 2013; Iaccarino et al., 2017b; Soucy La Roche et al., 2018a, b; Lihter et al., 2020), with cooling ages in the late Miocene (e.g., McDermott et al., 2015); and, 17-15 Ma for the onset of the D3, mainly recorded in the northern Himalaya (Godin, 2003; Dunkl et al., 2011; Lee et al., 2011; Nagy et al., 2015; Larson et al., 2019; Brubacher et al., 2020; see Jessup et al., 2019 for a review). In this Ph.D. thesis work, three representative samples from different structural positions within the THS in the Lower Dolpo area were characterized for different microstructural domains (*Fig. 7.9*).

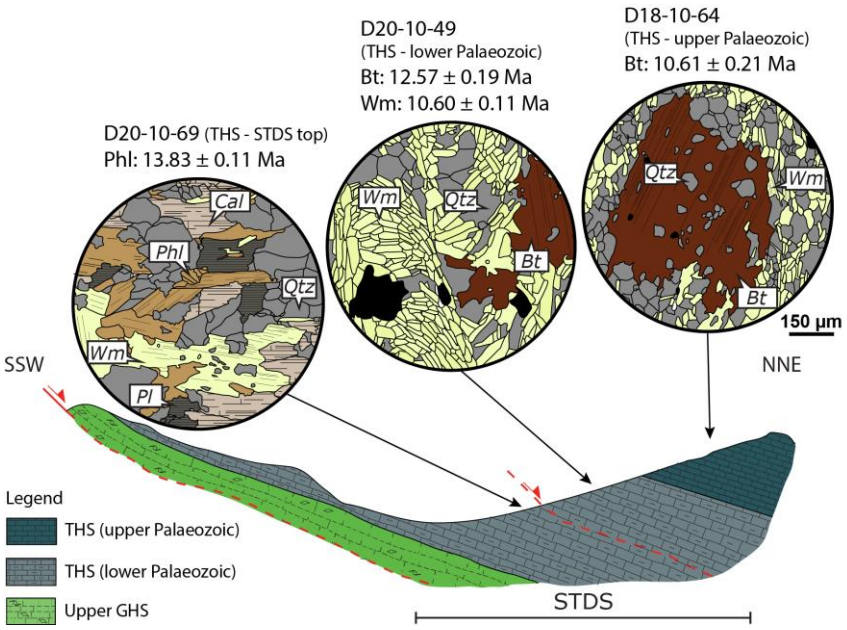

Figure 7. 9. *Main features of the dated samples. Microstructures are highlighted and redrawn from BSE mosaics in* Fig. 6.3. *Mineral abbreviations: Bt, biotite; Cal, calcite; Phl, phlogopite; Pl, plagioclase; Qtz, quartz; Wm, white mica.*

The three samples are representative of three different lithologies occurring in the THS unit:

- Sample D20-10-69 is a greenschist facies impure marble at the top of the STDS, in which only a continuous foliation, in literature the S2, occurs.
- Sample D20-10-49 is a carbonate-bearing metapelite above the STDS (lower Palaeozoic series), with polyphasic structures commonly associated, in literature, with S1 continuous foliation, S2 spaced foliation, and post kinematic biotite (M3).
- Sample D18-10-64 is a carbonate-bearing metapelite of the low-grade metasediments (upper Palaeozoic series), in which the M3 post-kinematic biotite occurs.

Fine-grained phlogopite of the D20-10-69 sample is oriented on the main S2 foliation together with calcite (*Fig. 6.1*). Calcite of the D20-10-69 sample shares common features with the previously characterized sample D19-10-65C (*par. 5*), as the important volumetric abundance and the interconnection of grains elongated parallel to the S2 through GBM dynamic recrystallization. This indicates that the S2 foliation of the impure marble developed at temperatures of 400-450 °C (consistent with the previously characterized THS marbles of *Chapter 5*). However, straight grain boundaries, as described for sample D21-10-81 (*par. 5*), indicate that calcite suffered annealing and/or static recrystallization after the end of S2 foliation development. Poikilitic structure of phengitic muscovite and high-angle laths of phlogopite subparallel to the S2 foliation (e.g. *Fig. 7.9*) indicate that micas likely experienced mimetic recrystallization (Vernon, 2018). Step-heating ^{40}Ar–^{39}Ar ages indicate ca. 14 Ma for phlogopite, which are quite "young" ages for the D2 event (concluded at ca. 23-24 Ma in the Lower Dolpo, see Carosi et al., 2013).

White micas of sample D20-10-49 are oriented almost on the two superimposed tectonic S1 and S2 foliations (see also Carosi et al., 2002). However, little decussate structure and mimetic recrystallization indicate that a later static recrystallization of the phengitic muscovite in sample D20-10-49 occurred after the end of foliation development (see *Fig. 7.9*). Poikilitic structure of

annitic biotite also support the view that late static (re)crystallization occurred after the end of foliation development. According to Henry et al. (2005) Ti-in-biotite thermometer, this late (re)crystallization occurred at MT conditions of 500-545 °C. Microchemical and isotopic investigations provide homogeneous compositions for white micas on both S1 and S2 foliations. Neglectable compositional differences may derive from minor and local factors at a lower scale. Such homogeneous composition provided unsolvable ages for both S1 and S2 foliations (12.54 ± 0.18 Ma) and the post-kinematic biotite (M3) (12.57 ± 0.24 Ma), with a mean age of 12.58 ± 0.08 Ma (*Fig. 6.5*). For annitic biotite, a lack of compositional internal variations rules out an isotopic inheritance from the previous deformation events, supporting the view that the biotite ages reflect a crystallization or a cooling age from MT conditions of 500-545 °C (Villa, 1998). *Vice versa*, for white micas such homogeneous composition may be explained as (*i*) a cooling age as a consequence of a crystallization on both S1 and S2 foliations at similar conditions of pressure and temperature or, alternatively, as (*ii*) a later recrystallization occurring together with static biotite growth. The first hypothesis can be explained as follows: the THS remained stationary, at the same structural level, from the D1 to the D2 phase, without changing bulk rock composition, pressure and temperature conditions. In general, this occurs either in the case in which the unit remains stationary during deformation development (only the footwall moves along the STDS shear zone), or if D1 and D2 events develop in such close times, and with fast cooling rates, that they do not allow significant changes in mineral chemistry. However, this is unlikely true as it requires that both the D1 and D2 events developed at a depth of almost 15 km and at temperatures of about 500-550 °C. These conditions are in contrast with the temperature estimations of this Ph.D. thesis work for the D2 phase in the Lower Dolpo (see *par. 7.5*), and with the other PT estimations along the belt showing clockwise paths (e.g. Jessup et al., 2008; Iaccarino et al., 2015; 2017b, see Kellett et al., 2019 for a review).

The uppermost D18-10-64 sample presents homogeneous unaltered millimeter-size biotite crystals which, according to Henry et al. (2005) thermometer and Massonne and Szpurka (1997) barometer, developed at temperatures of 520-550 °C, pressure of 500-590 MPa, and at ca. 10-11 Ma. As for the lowermost D20-10-69 sample, this analysis does not allow distinguishing whether this is a cooling age or a recrystallization age linked to static annealing. Nonetheless, as for the lowermost D20-10-69 sample, 10-11 Ma are very “young” ages for the D2 event.

7.4.2. Cooling ages or recrystallization ages? Data discussion

A recurrent issue involved in ^{40}Ar–^{39}Ar data interpretation is whether ages reflect the time of cooling below a specific closure temperature (Dunlap, 1997; Schneider et al., 2013, Engi et al., 2017, Halama et al., 2018) or (re)crystallization ages Villa (1998). Diocthaedral micas are less susceptible to isotope resetting than coexisting trioctahedral micas, regardless of the effective loss mechanism due to volume diffusion, recrystallization or alteration (Dahl, 1996). Several field-based studies have demonstrated a negligible re-equilibration of Ar isotopes in white mica re-equilibrated under temperature conditions lower than 500-550°C (e.g. Di Vincenzo et al., 2004; Augier et al., 2005; Villa et al., 2014; Montemagni et al., 2018, 2020). Moreover, Ar isotopes diffusion can be efficient for decompression at medium-high temperature and/or for low pressure conditions (Warren et al. 2012). It is therefore necessary to understand what ^{40}Ar–^{39}Ar ages are related to, linking them to paleotemperature/pressure estimates.

Micas crystallized at pressures and temperatures of ca. 0.5-0.6 GPa (ca. 15-18 km deep) and 500-550 °C. This P-T has been also suggested for the STDS in the Everest area, eastward to the Lower Dolpo, by Waters et al. (2019) by looking biotite-calcite-bearing phyllites of the THS (comparable with the herein presented samples) and using the Ti-in-biotite and the Ti-in-quartz geothermometers. Nevertheless, temperatures of 500-550 °C (as obtained herein for samples D20-10-49 and D18-10-64), are surprisingly high for the D2 phase in the THS and the STDS hanging wall in central Himalaya (see *par.7.2.3*, *par. 7.3.1*). As biotite poikiloblasts show evidence of post-kinematic growth, Ti-in-biotite temperature estimates (derived for the static biotite of samples D18-10-64 and D20-10-49) can be interpreted, in principle, as due to a thermal effect produced shortly after the movement of the STDS (post-kinematic event), as the thick detachment coupled a hot footwall (GHS) with a cold hangingwall (THS). Alternatively, these medium/high temperatures can be linked to a later thermal event in the Lower Dolpo region, linked to the crustal thinning and/or pluton inclusions. In both cases, the event that led to the (re)crystallization of biotite is post-kinematic with respect to the last ductile activity of the STDS. In light of the retentive properties for biotite, based on both experimental works (e.g. Harrison et al., 1985) and natural examples (e.g. Villa, 1998), for T>500 °C Ar ages of biotite should be taken in principle as cooling ages (after the thermal relaxation due to the STDS shearing) and therefore considered to represent a minimum age for static micas crystallization. The same considerations can apply to phlogopite of sample D20-10-69, where phlogopite crystals oriented subparallel to the S2 foliation (sample D20-10-49 at the STDS hanging wall) could yield a cooling age of ca. 14 Ma, following cessation of the STDS activity. *Vice versa*, biotite $^{40}Ar/^{39}Ar$ ages from the uppermost sample D18-10-64 could be interpret to provode a later crystallization age at ca. 11 Ma. Consequently, white micas in the middle-located sample (D20-10-49) can reflect ages of ca. 12-13 Ma as a partial reset of the $^{40}Ar/^{39}Ar$ systematic during M3 event. However, this hypothesis does not explain the uniform chemical and ages compositions for both white mica and biotite, at least in sample D20-10-49. Also, there is a substantial gap in apparent ages between the end of the STDS in the lower Dolpo (c. 23-24 Ma, Carosi et al., 2013) and the ^{40}Ar–^{39}Ar ages estimated for phlogopite, biotite and white micas (14-11 Ma). An alternative interpretation is that all the studied samples underwent a later thermal overprint at 500-550 °C that re-equilibrated wholly, or in part, white mica by volume diffusion. Therefore, 14-11 Ma would reflect the ages of the late thermal event.

Several geological and geochronological constraints from the literature (*Fig. 7.10 a, b*) indicate that the tectono-metamorphic events that produced both the S1 and the S2 structures occurred much earlier than the middle Miocene. Especially for the D2 ages, between the western Dolpo and the Marsyandi valley, Crouzet et al. (2007) proposed (through K/Ar dating on illite-rich fractions and zircon fission track thermochronology) 30–25 Ma for the metamorphic peak in the Devonian to Triassic metasediments of the THS (*Fig. 7.10a*). Through ^{40}Ar–^{39}Ar step-heating geochronology on white mica and monazite U–Th/Pb petrochronology, it was suggested for the Jajarkot Klippe, SW of the study area, that the S2 foliation developed in the THS between 27-19 Ma (*Fig. 7.10a*, Soucy La Roche et al., 2018b). Moreover, a complete cooling below ~450 °C occurred at ca. 17 Ma in the GHS rocks (at the STDS footwall) in the Karnali klippe (^{40}Ar–^{39}Ar analysis of micas, Soucy La Roche et al., 2018a). These ages are consistent with ^{40}Ar–^{39}Ar step-heating age results on white mica in the Annapurna area of Central Nepal (*Fig. 7.10a*), yielding ages of 22 and 18 Ma for the ductile shearing and the late D2-related folding of the THS, respectively (Godin et al., 2001).

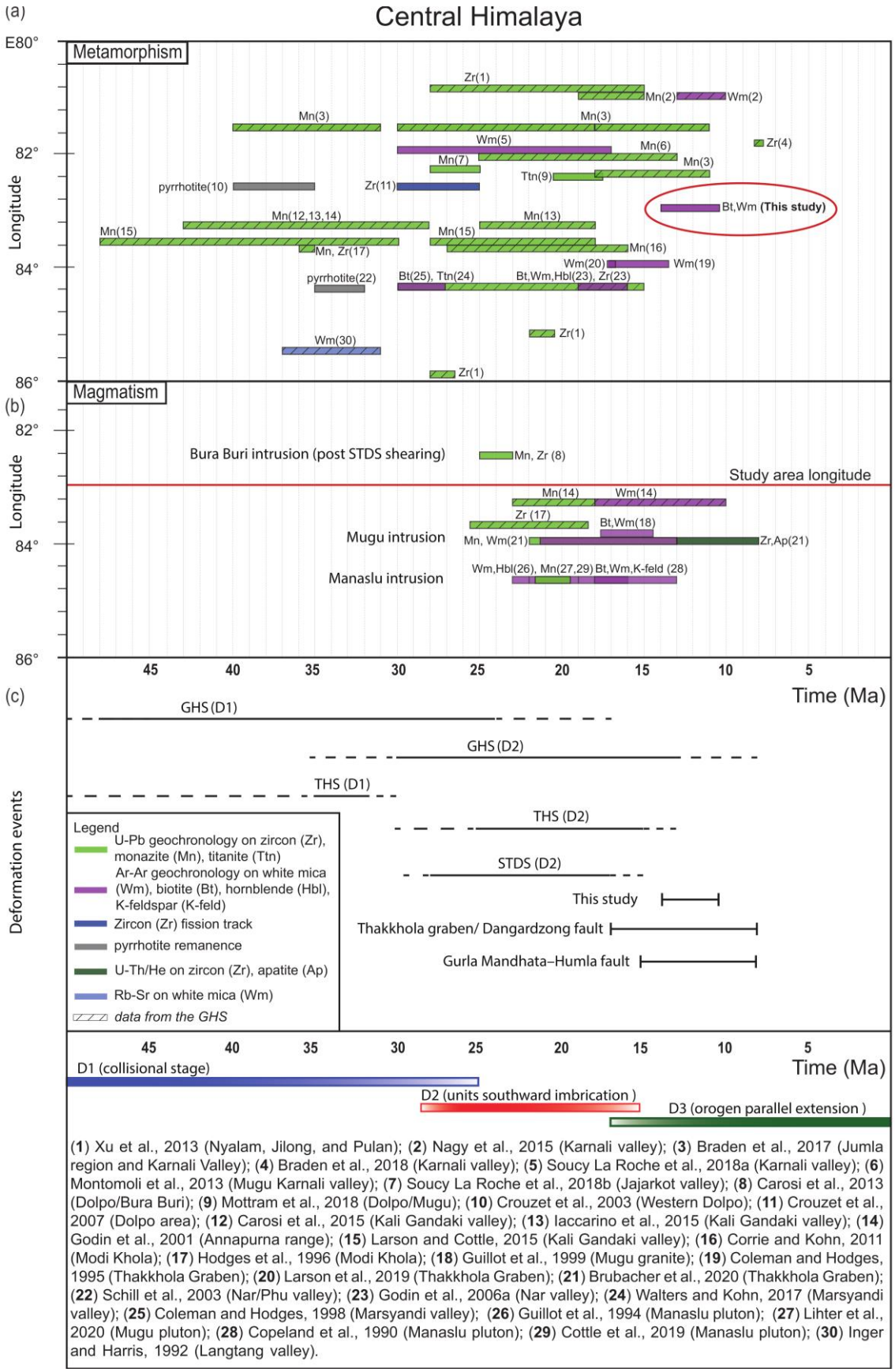

Figure 7. 10. *Compilation of deformation and magmatic age events in the central Himalaya. (**a**) Main deformation/ metamorphic phases ages from different geochronological methods. Dashed bars correspond to investigations carried out on the GHS, whereas non-dashed bars refer to THS deformation ages. Numbers correspond to the reference list below. (**b**) Estimated ages for the main syn- and post-tectonic intrusion (with respect to the D2 phase). (**c**) Simplified compilation of the main tectonic events and reference list.*

According to Carosi et al. (2013), the minimum age of the D2 ductile shearing in the Lower Dolpo, only 50 km to the NW of the study area, is of ca. 24 Ma (zircon and monazite U-Pb ages), constrained by the undeformed Bura Buri leucogranite intrusion into both the GHS_U and the THS (*Fig. 7.10b*). This minimum age of ca. 24 Ma constrained through magmatic intrusion and cross-cutting relation is consistent with those of Guillot et al. (1999) and Lihter et al. (2020) for the impressive Mugu Leucogranite, intruded into the STDS hanging wall (Upper Mustang region of west-central Nepal, *Fig. 7.10b*). These authors provided a minimum age of ca. 21-19 Ma for the STDS shearing (through ^{208}Pb–^{232}Th dating on monazite), suggesting that the intrusion occurred at a depth of about 18 km (based on garnet–biotite-muscovite-plagioclase barometer), followed by a rapid exhumation at ~15-16 Ma (Guillot et al., 1999; Lihter et al., 2020). This is strongly compatible with the estimates of Copeland et al. (1990) and Guillot et al. (1994) for the close Manaslu leucogranite, providing (through ^{40}Ar–^{39}Ar analyses) a minimum age for the STDS at 22-23 Ma, and a rapid cooling at 19-16 Ma at a depth of ~8-15 km (*Fig. 7.10b*).

Regionally, the time span estimated in this thesis (14-11 Ma) corresponds to the D3 tectonic phase (*Fig. 7.10c*). In the far-western Nepal, relatively close to the Lower Dolpo, the almost N-S Gurla Mandhata–Humla fault (related to the D3 event, see Murphy et al., 2002; Murphy and Copeland, 2005) has been constrained at 13 to 10 Ma (muscovite ^{40}Ar–^{39}Ar ages) by Nagy et al. (2015). Several lines of evidence, therefore, suggest that the ^{40}Ar–^{39}Ar ages of 14-11 Ma likely reflect re-crystallization processes. Furthermore, if the apparent ages were cooling ages, Ar isotope mobility ruled by a volume diffusion process would produce discernible effects in the age of coexisting biotite and white mica of sample D20-10-49, which is not the case. This allows us to conclude that white mica recrystallized, wholly or in part, synchronously with the static biotite blastesis during the D3 phase. This implies that white micas recrystallized at temperatures of 500-550 °C, as calculated for dark micas using the geothermometer of Henry et al. (2005), at a depth of 15-18 km (according to Massonne and Szpurka, 1997 geothermometer and classic pressure gradients of 0.033 GPa/km for a for an average rock density of 2,700 kg/m^3).

7.4.3. Late thermal event in the Lower Dolpo region

Static mica in the STDS hanging wall has been recognized in several areas of the belt. Biotite post-kinematic mm-size crystals have been described in Bhutan by Gansser (1983), in the Kali Gandaki valley (Carosi et al., personal communication), and in the Manaslu range (Carosi et al., personal communication). Moreover, also white mica static growth in the upper part of the GHS, dated at ca. 14 Ma, has been described in NW India by Montemagni et al. (2018). Nevertheless, post-kinematic biotite and the tectonic significance of this later blastesis have been poorly characterized until now.

As aforementioned, one of the possible causes can be a thermal effect induced by the STDS movement, as the kilometre-thick ductile shear zone coupled hot mid-crustal rocks of the GHS, in the footwall, and marine sediments of the THS, in the hanging wall. A thermal effect can have been protracted even shortly after the movement, causing a thermal relaxation and post-kinematic recrystallization. However, this would not explain the wide time gap between the end of the STDS movement (c. 24 Ma in the Lower Dolpo), and the proposed ages for the post-kinematic event (14-11 Ma). An alternative hypothesis proposed in the previous paragraph is that the thermal event is due to the D3 phase of crustal thinning leading to a regional thermal

event and/or to local crustal melting processes. Near the study area, there are no magmatic intrusions that can be connected with this tectonic event. Nevertheless, in the central-eastern Himalaya (Makalu area), Streule et al. (2010) and Visonà et al. (2012) documented andalusite/cordierite-bearing granites intruding into the upper GHS at ~16-15 Ma under P-T conditions of <0.4-0.6 GPa and 600-700°C. The occurrence of young (16-11 Ma) andalusite-bearing granites has been explained by Visonà and Lombardo (2002) as resulting from low-pressure heating, with a heat source located immediately underneath the STDS (Visonà et al., 2012). This interpretation is quite consistent with that proposed in this thesis. A lack of LP/HT magmatic intrusions in the Lower Dolpo can be due to erosion and weathering processes or to the lack of partial melting in central Himalaya. The Lower Dolpo is a quite arid region; nevertheless, in the THS in the close Marsyandi valley, Garzanti et al. (2007) estimated erosion rates of ca. 1-2 mm/a increasing toward the GHS, underneath the STDS, up to ca. 5 mm/a in the hangingwall of the MCTz, where the summer monsoon reaches its peak intensity (up to 5 m/a). Such high erosion rates, mainly focused in the GHS and accelerated in the late Miocene (8-10 Ma, Lang et al., 2016; Govin et al., 2020) and the late Pliocene (2.5-0.9 Ma, Huntington et al., 2006; Gemignani et al., 2018; Govin et al., 2020), may be responsible for the lack of exposed plutonic bodies in the nearby areas. Therefore, the lack of intrusion does not rule out an intrusion of plutonic bodies before the erosion rate increases, yet supports a thermal event due to the crustal thinning of the D3 phase. Indeed, in both cases, a progressive age propagation occurs from 14 Ma to 11 Ma toward the structural top (*Fig. 7.9*). This observation, made on only a few samples, supports (i) a fast exhumation of rocks linked to the climate-induced erosion or, alternatively, (ii) a decrease in ages towards higher structural levels. In accordance with rapid erosion during the Late Miocene (i), it is possible that the rocks geographically located further to the south along the studied valley, in proximity to the GHS, were eroded and denudated rapidly, reaching the phlogopite closure temperature earlier than the rocks exposed more to the north, where erosion rates are estimated to be slower. However, it is important to note that the estimated age of ca. 14 Ma is older than the abrupt increase of erosive processes, and that, up to ca. 8 Ma, P-T-t data suggest a significant exhumation had already occurred (e.g. Govin et al., 2020 with references). A decrease in ages towards higher structural levels (ii) can imply an up-section heat flow propagation, crossing the kilometer-thick volume over time. On the basis of the samples studied alone, it is not possible to make further speculations. Regional-scale crustal thinning and heating, supported by the development of the close N-S trending grabens (e.g. Thakkhola Graben) could be a sufficient explanation for the thermal event in the Lower Dolpo.

8. Conclusion

In this thesis work, three key areas in the central Himalaya were studied (from east to west, the Manaslu valleys, the Kali Gandaki valley, and the Lower Dolpo region). Investigations from the macro to the microscale, up to the crystalline lattice scale, were combined with a multidisciplinary approach to characterize the MCTz and the STDS. Analyses on four N-S transects, perpendicular to the Himalayan strike, indicate that:

- On equal structural level within the MCTz, samples collected in two different areas (Manaslu valleys and Lower Dolpo region) compare remarkably in terms of structure/microstructure, metamorphic facies and mineral texture. Microstructures and textures developed during top-to-the-south/southwest non-coaxial ductile flow in a plain strain regime. Quartz and dolomite textures, and quartz, dolomite and feldspar microstructures indicate an increase of deformation temperature (from ~400–450 °C up to ~700 °C) traced structurally up-section along the MCTz profile, consistent with the distribution of Barrovian index-minerals (for the "inverted metamorphism") and independent petrological constraints. Kinematic vorticity estimates at the top of the MCTz (Manaslu area) support a general shear flow, with Wn=0.69–0.77 (48–56% of simple shear) and a "decelerating strain path".

- The STDS is characterized by a complex architecture. In the Marsyandi valley (Manaslu area) it was possible to investigate a lower ductile branch of the STDS, wholly within the GHS_U (Chame Detachment), and an upper ductile shear zone, between the GHS_U and the THS (from the Budhi Gandaki to the Marsyandi valleys). This last ductile branch, or STDS *sensu stricto*, continues into the Annapurna Detachment, in the Kali Gandaki valley, and into the STDS in Lower Dolpo. Shearing on the STDS involved marbles and calcsilicates-rich marbles and orthogneiss of the upper portions of the Greater Himalayan Sequence (GHS_U) at the shear zone base, and low-grade marble of the Tethyan Himalayan Sequence (THS) at the top. Temperature conditions associated with microstructures and metamorphic mineral assemblages sharply decrease up-section within the shear zone.

- The STDS records a progressive evolution, with two stages of shearing, $D2_{early}$ and a $D2_{late}$, occurring during exhumation of the ductile branch. The $D2_{early}$ and a $D2_{late}$ recorded different thermal and lithospheric stress regimes. Decreasing temperatures from the $D2_{early}$ (650–400 °C traced up-section) to the $D2_{late}$ event (T=300–400 °C) are recorded in the STDS, as indicated by calcite microstructures within the shear zone. Constant strain rates and lowering in temperature conditions enhanced strain hardening of the STDS ductile branch. Therefore, differential stress increased at higher structural levels. Minor kinematic vorticity variations are recorded for the Annapurna Detachment of the Kali Gandaki valley, supporting a general shear flow (Wm=0.45–0.79, corresponding to simple shear contributions of 30–58%). Stronger variations are recorded in the Manaslu and Lower Dolpo region, where a kinematic vorticity and temperature lowering occurred from the $D2_{early}$ (Wm=0.97–0.99, corresponding to simple shear contributions of 84–91%) to the $D2_{late}$ event (Wm=0.31–0.52, corresponding to simple shear contributions of 20–35%). Therefore, the STDS experienced a (temporal) "decelerating strain path" as rocks cooled down during progressive tectonic exhumation. This is not equal along the whole length of the STDS, which shows lateral variations along the belt. A strong pure shear component at higher structural levels enhanced the telescoping of isotherms within the shear zone.

- After the end of STDS ductile shearing, occurred at ca. 23-24 Ma in the Lower Dolpo region, a D3 phase is highlighted by post-kinematic millimeter-size biotite crystals. Integrating microstructural, microchemical and geochronological data on samples collected above the upper limit of the STDS allowed us to describe how two superposed tectonic foliations (S1 and S2) and a late static mica growth (M3) are recorded. Static biotite is observable along the THS base in several parts of Himalaya; nevertheless, before this Ph.D. thesis work, minor investigations had been conducted.
- Detailed microstructural and microtextural analysis supported a late mimetic static recrystallization of white micas aligned along both the S1 and S2 foliations, and for S2 biotite (at lower structural levels), together with the development of poikiloblastic biotite (at higher structural levels). Microchemical analyses highlighted neglectable compositional variation in the investigated micas, supporting a chemical equilibration of the mica crystals.
- Micas ^{40}Ar–^{39}Ar laser step-heating and *in-situ* analyses of different structural levels of the THS (from STDS hanging wall to Upper Palaeozoic low-grade metasediments) and on different microstructural positions (for S1 and S2 foliations, and M3 poikiloblasts) yielded an up-section age variation from ca. 14 to ca. 11 Ma. When microstructures were analyzed separately through the ^{40}Ar–^{39}Ar *in-situ* technique, mica from both the S1 and S2 foliations and static biotite (M3) gave indistinguishable ages at ~12.6 Ma.
- Coupled with micas chemical re-equilibration and static recrystallization, geochronological investigations support the view that the static recrystallization resulted from a late-thermal event (M3). This thermal event (T=500-550 °C) occurred when THS rocks were at low structural levels (around 15-18 km in depth) after the end of the STDS shearing. The thermal event reopened the ^{40}Ar–^{39}Ar systematics in micas.
- This thermal event M3 was linked to the E-W orogen-parallel extension tectonic, testified to in the Himalaya by the numerous N-S trending grabens and late domes associated with anatexis along the northern Himalaya. The upward age propagation occurred as the heat source reached higher structural levels over time.

Acknowledgments

I am sincerely grateful to my supervisors, Prof. Chiara Montomoli and Dr. Salvatore Iaccarino, who introduced me to a multidisciplinary approach to study tectonics at all scales. It is truly regenerating to work with tireless researchers who are always passionate and open to constructive criticism. I also thank Prof. Rodolfo Carosi for his support with the project and in-depth constructive discussions. Thank you all for sharing with me your enthusiasm for research, your great experience, and for supporting me during all these intense years with such dedication. Also, thanks for all the opportunities you gave to me. I will keep the expedition in the Himalaya in my heart.

I am also very thankful to Dr. Gianfranco Di Vincenzo from the IGC-CNR of Pisa, for having followed the geochronology part of this thesis with a critical and meticulous approach.

During this Ph.D., I had the opportunity to spend several months abroad, meeting internationally renowned researchers. Among them, I would like to thank prof. Richard D. Law, for his exquisite kindness, helpfulness, and hospitality at the Virginia Tech Department of Geosciences. Thank you for your in-depth course on deformation mechanisms, for empowered me in quartz analysis, and for involving me in the field trips in the Appalachian provinces. I would also have liked to thank Dr. Luca Fedele for his welcome. I know Virginia Tech miss him very much, and I won't be able to forget his cheerful company and help. I also sincerely thank Dr. Andy J. Parsons for his kind helpfulness and his great advice.

I express my gratitude to Dr. Bernd Leiss, for hosting me almost six months in Göttingen, during all my studies. Much of the data examined in this thesis were collected during those periods at the Georg-August University of Göttingen, and from the combined work with Dr. Walter Jens with the crystal fabric microanalyzer. Thank you, Bernd, for introducing me to calcite and dolomite texture analysis. I would also like to thank Prof. Michael Stipp and Dr. Rüdiger Kilian, from the Martin-Luther University of Halle-Wittenberg, for in-depth and thought-provoking discussions on paleopiezometry, texture interpretations and kinematic vorticity. Dr. R. Kuehn is also gratefully thanked for acquiring neutron diffraction data for one sample at the IBR-2 reactors in Dubna, Russia.

Dr. Kyle P. Larson, Riccardo Graziani, and the staff at the University of British Columbia Okanagan are also acknowledged for hosting me at the Department of Earth, Environmental and Geographic Sciences. Thanks to the analyzes carried out there, it was possible for me to refine the results obtained on several analyzed transects.

Dr. Chiara Montemagni and Dr. Matteo Simonetti are thanked for being great teammates during the traineeship periods abroad, e.g. at Virginia Tech. Especially Chiara, during the Himalayan field trip, was an exemplary teammate, with motivational speeches and enthusiasm. A warm thanks also goes to Katherine A. Ford, for her lovely welcome in the Göttingen academia, and for sharing some of her geological field trips with me.

Finally, Prof. Lorella Francalanci is warmly acknowledged for the effective support provided as Ph.D. coordinator during the years. The reviewers, Dr. Fondriest Michele and Dr. Gemignani Lorenzo, are gratefully thanked for their comments that improved the quality of the manuscript. This research is part of a Ph.D. program funded by the Tuscany Regional Pegaso doctoral grant.

References

Aikman, A. B., Harrison, T. M., and Lin, D. (2008). Evidence for early (> 44 Ma) Himalayan crustal thickening, Tethyan Himalaya, southeastern Tibet. Earth and Planetary Science Letters, 274(1-2), 14-23.

An, W., Hu, X., Garzanti, E., Wang, J. G., and Liu, Q. (2021). New precise dating of the India-Asia collision in the Tibetan Himalaya at 61 Ma. Geophysical Research Letters, 48(3), e2020GL090641.

Antolín, B., Appel, E., Montomoli, C., Dunkl, I., Ding, L., Gloaguen, R., and El Bay, R. (2011). Kinematic evolution of the eastern Tethyan Himalaya: constraints from magnetic fabric and structural properties of the Triassic flysch in SE Tibet. Geological Society, London, Special Publications, 349(1), 99-121.

Antolín, B., Godin, L., Wemmer, K., and Nagy, C. (2013). Kinematics of the Dadeldhura klippe shear zones (W Nepal): implications for the foreland evolution of the Himalayan metamorphic core. Terra Nova, 25(4), 282-291.

Augier, R., Agard, P., Monié, P., Jolivet, L., Robin, C., and Booth-Rea, G. (2005). Exhumation, doming and slab retreat in the Betic Cordillera (SE Spain): in situ40Ar/39Ar ages and P–T–d–t paths for the Nevado-Filabride complex. Journal of Metamorphic Geology, 23(5), 357-381.

Baëta, R. D., and Ashbee, K. H. G. (1969). Slip systems in quartz: I. Experiments. American Mineralogist: Journal of Earth and Planetary Materials, 54(11-12), 1551-1573.

Barber, D. J., Heard, H. C., and Wenk, H. R. (1981). Deformation of dolomite single crystals from 20–800 C. Physics and Chemistry of Minerals, 7(6), 271-286.

Barber, D. J., Wenk, H. R., Gomez-Barreiro, J., Rybacki, E., and Dresen, G. (2007). Basal slip and texture development in calcite: new results from torsion experiments. Physics and Chemistry of Minerals, 34(2), 73-84.

Barnhoorn, A., Bystricky, M., Burlini, L., and Kunze, K. (2004). The role of recrystallisation on the deformation behaviour of calcite rocks: large strain torsion experiments on Carrara marble. Journal of Structural Geology, 26(5), 885-903.

Barnhoorn, A., Bystricky, M., Burlini, L., and Kunze, K. (2005). Post-deformational annealing of calcite rocks. Tectonophysics, 403(1-4), 167-191.

Bauer, H., Rogowitz, A., Grasemann, B., and Decker, K. (2018). Intracrystalline deformation of calcite in the upper brittle crust. Geology, 46(4), 375-378.

Beaumont, C., Jamieson, R. A., Nguyen, M. H., and Lee, B. (2001). Himalayan tectonics explained by extrusion of a low-viscosity crustal channel coupled to focused surface denudation. Nature, 414(6865), 738-742.

Beaumont, C., Jamieson, R. A., Nguyen, M. H., and Medvedev, S. (2004). Crustal channel flows: 1. Numerical models with applications to the tectonics of the Himalayan-Tibetan orogen. Journal of Geophysical Research: Solid Earth, 109(B6).

Behyari, M., and Shahbazi, M. (2019). Strain and vorticity analysis in the Zagros suture zone (W Iran): Implications for Neo-Tethys post-collision events. Journal of Structural Geology, 126, 198-209.

Bertoldi, L., Massironi, M., Visonà, D., Carosi, R., Montomoli, C., Gubert, F., ... and Pelizzo, M. G. (2011). Mapping the Buraburi granite in the Himalaya of Western Nepal: remote sensing analysis in a collisional belt with vegetation cover and extreme variation of topography. Remote Sensing of Environment, 115(5), 1129-1144.

Bestmann, M., Kunze, K., and Matthews, A. (2000). Evolution of a calcite marble shear zone complex on Thassos Island, Greece: microstructural and textural fabrics and their kinematic significance. Journal of Structural Geology, 22(11-12), 1789-1807.

Bhandari, A., and Jiang, D. (2021). A multiscale numerical modeling investigation on the significance of flow partitioning for the development of quartz c-axis fabrics. Journal of Geophysical Research: Solid Earth, 126(2), e2020JB021040.

Blacic, J. D. (1975). Plastic-deformati on mechanisms in quartz: the effect of water. Tectonophysics, 27(3), 271-294.

Blisniuk, P. M., Hacker, B. R., Glodny, J., Ratschbacher, L., Bi, S., Wu, Z., ... and Calvert, A. (2001). Normal faulting in central Tibet since at least 13.5 Myr ago. Nature, 412(6847), 628-632.

Blumenfeld, P., Mainprice, D., and Bouchez, J. L. (1986). C-slip in quartz from subsolidus deformed granite. Tectonophysics, 127(1-2), 97-115.

Bodenhausen, J. W. A., De Booy, T., Egeler, C. G., and Nijhuis, H. J. (1964). On the geology of central west Nepal—A preliminary note. In Report on 22nd International Geological Congress Delhi (Vol. 11, pp. 101-122).

Bordet, P., Colchen, M., Krummenacher, D., Le Fort, P., Mouterde, R., and Remy, M. (1971). Recherches géologiques dans l'Himalaya du Népal, région de la Thakkhola (p. 279). Édition du Centre national de la recherche scientifique.

Bosse, V., and Villa, I. M. (2019). Petrochronology and hygrochronology of tectono-metamorphic events. Gondwana research, 71, 76-90.

Braden, Z., Godin, L., and Cottle, J. M. (2017). Segmentation and rejuvenation of the Greater Himalayan sequence in western Nepal revealed by in situ U–Th/Pb monazite petrochronology. Lithos, 284, 751-765.

Braden, Z., Godin, L., Cottle, J., and Yakymchuk, C. (2018). Renewed late Miocene (< 8 Ma) hinterland ductile thrusting, western Nepal Himalaya. Geology, 46(6), 503-506.

Brandstätter, J., Kurz, W., and Rogowitz, A. (2017). Microstructural analysis and calcite piezometry on hydrothermal veins: Insights into the deformation history of the Cocos Plate at Site U1414 (IODP Expedition 344). Tectonics, 36(8), 1562-1579.

Brown, R. L., and Nazarchuk, J. H. (1993). Annapurna Detachment fault in the Greater Himalaya of central Nepal. Geological Society, London, Special Publications, 74(1), 461-473.

Brubacher, A. D., Larson, K. P., Cottle, J. M., Matthews, W., and Camacho, A. (2020). Progressive development of EW extension across the Tibetan plateau: A case study of the Thakkhola graben, west-central Nepal. International Geology Review, 1-20.

Brunel, M., and Kienast, J. R. (1986). Étude pétro-structurale des chevauchements ductiles himalayens sur la transversale de l'Everest–Makalu (Népal oriental). Canadian journal of earth Sciences, 23(8), 1117-1137.

Bucher, K., and Grapes, R. (2011). Petrogenesis of metamorphic rocks. Springer Science & Business Media.

Bunge, H. J. (1969). Mathematische Methoden der Texturanalyse. Akademie-Verlag, Berlin.

Bunge, H.J. (1982). Texture analysis in materials science: mathematical methods. Butterworth-Heinemann.

Burbank, D. W., Beck, R. A., and Mulder, T. (1996). The Himalayan foreland basin. World and regional geology, 149-188.

Burchfiel, B. C., and Royden, L. H. (1985). North-south extension within the convergent Himalayan region. Geology, 13(10), 679-682.

Burchfiel, B. C., Zhiliang, C., Hodges, K. V., Yuping, L., Royden, L. H., and Changrong, D. (1992). The South Tibetan Detachment system, Himalayan orogen: Extension contemporaneous with and parallel to shortening in a collisional mountain belt. Geological Society of America, 269, 1-41.

Burg, J. P., and Chen, G. M. (1984). Tectonics and structural zonation of southern Tibet, China. Nature, 311(5983), 219-223.

Burgess, W. P., Yin, A., Dubey, C. S., Shen, Z. K., and Kelty, T. K. (2012). Holocene shortening across the Main Frontal Thrust zone in the eastern Himalaya. Earth and Planetary Science Letters, 357, 152-167.

Burkhard, M. (1993). Calcite twins, their geometry, appearance and significance as stress-strain markers and indicators of tectonic regime: a review. Journal of Structural Geology, 15(3-5), 351-368.

Caby, R., Pêcher, A., and LeFort, P. (1983). Le grand chevauchement central himalayen. Nouvelles données sur le métamorphisme inverse à la base de la Dalle du Tibet. (The Himalayan Main Central Thrust: new data about the reverse metamorphism at the bottom of the Tibetan Slab). Revue de géologie dynamique et de géographie physique Paris, 24(2), 89-100.

Capedri, S., Venturelli, G., and Photiades, A. (2004). Accessory minerals and δ18O and δ13C of marbles from the Mediterranean area. Journal of Cultural Heritage, 5(1), 27-47.

Carosi, R., Gemignani, L., Godin, L., Iaccarino, S., Montomoli, C., and Rai, S. (2014). A geological journey through the deepest gorge on Earth: The Kali Gandaki valley section, west-central Nepal. In: Geological field trips in the Himalaya, Karakoram and Tibet. Journal of the Virtual Explorer, Electronic Edition, ISSN 1441-8142.

Carosi, R., Lombardo, B., Molli, G., Musumeci, G., and Pertusati, P. C. (1998). The South Tibetan Detachment system in the Rongbuk valley, Everest region. Deformation features and geological implications. Journal of Asian Earth Sciences, 16(2-3), 299-311.

Carosi, R., Montomoli, C., and Iaccarino, S. (2018). 20 years of geological mapping of the metamorphic core across Central and Eastern Himalayas. Earth-Science Reviews, 177, 124-138.

Carosi, R., Montomoli, C., Iaccarino, S., Massonne, H. J., Rubatto, D., Langone, A., ... and Visonà, D. (2016). Middle to late Eocene exhumation of the Greater Himalayan Sequence in the Central Himalayas: Progressive accretion from the Indian plate. The Bulletin of the Geological Society of America, 128(11-12), 1571-1592.

Carosi, R., Montomoli, C., Iaccarino, S., and Visonà, D. (2019). Structural evolution, metamorphism and melting in the Greater Himalayan Sequence in central-western Nepal. Geological Society, London, Special Publications, 483(1), 305-323.

Carosi, R., Montomoli, C., Langone, A., Turina, A., Cesare, B., Iaccarino, S., ... and Ronchi, A. (2015). Eocene partial melting recorded in peritectic garnets from kyanite-gneiss, Greater Himalayan Sequence, central Nepal. Geological Society, London, Special Publications, 412(1), 111-129.

Carosi, R., Montomoli, C., Rubatto, D., and Visonà, D. (2010). Late Oligocene high-temperature shear zones in the core of the Higher Himalayan Crystallines (Lower Dolpo, western Nepal). Tectonics, 29(4).

Carosi, R., Montomoli, C., Rubatto, D., and Visonà, D. (2013). Leucogranite intruding the South Tibetan Detachment in western Nepal: implications for exhumation models in the Himalayas. Terra Nova, 25(6), 478-489.

Carosi, R., Montomoli, C., and Visonà, D. (2002). Is there any Detachment in the Lower Dolpo (western Nepal)?. Comptes Rendus Geoscience, 334(12), 933-940.

Carosi, R., Montomoli, C., and Visonà, D. (2007). A structural transect in the Lower Dolpo: Insights on the tectonic evolution of Western Nepal. Journal of Asian Earth Sciences, 29(2-3), 407-423.

Casey, M., Rutter, E. H., Schmid, S. M., Siddans, A. W. B., and Whalley, J. S. (1978). Texture development in experimentally deformed calcite rocks. In: Proceedings 5th International Conference on Textures of Materials. Springer Verlag (pp. 231-240).

Chambers, J., Parrish, R., Argles, T., Harris, N., and Horstwood, M. (2011). A short-duration pulse of ductile normal shear on the outer South Tibetan Detachment in Bhutan: Alternating channel flow and critical taper mechanics of the eastern Himalaya. Tectonics, 30(2).

Colchen, M. (1981). Geological Map of Annapurna-Manaslu-Ganesh Himalaya of Nepal. Zagros, Hindu Kush, Himalaya Geodynamic Evolution, 3, 323p.

Colchen, M. (1999). The Thakkhola–Mustang graben in Nepal and the late Cenozoic extension in the Higher Himalayas. Journal of Asian Earth Sciences, 17(5-6), 683-702.

Colchen, M., Le Fort, P., and Pecher. A. (1980). Carte geologique Annapurna- Manaslu- Ganesh, Himalaya du Nepal. Echelle 1:200.000. Centre national de la recherche scientifique - Paris.

Colchen, M., Le Fort, P., and Pêcher, A. (1986). Recherches geologiques dans l'Himalaya du Nepal: Annapurna-Manaslu-Ganesh Himal; notice de la carte géologique au 1/200 000e; edition bilingue français-anglais. Edition du Centre National de la Recherche Scientifique – Paris.

Coleman, M. E. (1996). Orogen-parallel and orogen-perpendicular extension in the central Nepalese Himalayas. Geological Society of America Bulletin, 108(12), 1594-1607.

Coleman, M., and Hodges, K. (1995). Evidence for Tibetan plateau uplift before 14 Myr ago from a new minimum age for east–west extension. Nature, 374(6517), 49-52.

Coleman, M. E., and Hodges, K. V. (1998). Contrasting Oligocene and Miocene thermal histories from the hanging wall and footwall of the South Tibetan Detachment in the central Himalaya from 40Ar/39Ar thermochronology, Marsyandi Valley, central Nepal. Tectonics, 17(5), 726-740.

Copeland, P., Harrison, T. M., and Le Fort, P. (1990). Age and cooling history of the Manaslu granite: implications for Himalayan tectonics. Journal of Volcanology and Geothermal Research, 44(1-2), 33-50.

Corrie, S. L., and Kohn, M. J. (2011). Metamorphic history of the central Himalaya, Annapurna region, Nepal, and implications for tectonic models. Geological Society of America Bulletin, 123(9-10), 1863-1879.

Corrie, S. L., Kohn, M. J., McQuarrie, N., and Long, S. P. (2012). Flattening the Bhutan Himalaya. Earth and Planetary Science Letters, 349, 67-74.

Corthouts, T. L., Lageson, D. R., and Shaw, C. A. (2016). Polyphase deformation, dynamic metamorphism, and metasomatism of Mount Everest's summit limestone, east central Himalaya, Nepal/Tibet. Lithosphere, 8(1), 38-57.

Cottle, J., Lederer, G., and Larson, K. (2019). The monazite record of pluton assembly: Mapping manaslu using petrochronology. Chemical Geology, 530, 119309.

Cottle, J. M., Searle, M. P., Jessup, M. J., Crowley, J. L., and Law, R. D. (2015). Rongbuk re-visited: geochronology of leucogranites in the footwall of the South Tibetan Detachment System, Everest Region, Southern Tibet. Lithos, 227, 94-106.

Cottle, J. M., Waters, D. J., Riley, D., Beyssac, O., and Jessup, M. J. (2011). Metamorphic history of the South Tibetan Detachment System, Mt. Everest region, revealed by RSCM thermometry and phase equilibria modelling. Journal of Metamorphic Geology, 29(5), 561-582.

Crouzet, C., Dunkl, I., Paudel, L., Arkai, P., Rainer, T. M., Balogh, K., and Appel, E. (2007). Temperature and age constraints on the metamorphism of the Tethyan Himalaya in Central Nepal: A multidisciplinary approach. Journal of Asian Earth Sciences, 30(1), 113-130.

Crouzet, C., Gautam, P., Schill, E., and Appel, E. (2003). Multicomponent magnetization in western Dolpo (Tethyan Himalaya, Nepal): tectonic implications. Tectonophysics, 377(1-2), 179-196.

Dahl, P. S. (1996). The crystal-chemical basis for Ar retention in micas: inferences from interlayer partitioning and implications for geochronology. Contributions to Mineralogy and Petrology, 123(1), 22-39.

Davis, D., Suppe, J., and Dahlen, F. A. (1983). Mechanics of fold-and-thrust belts and accretionary wedges. Journal of Geophysical Research: Solid Earth, 88(B2), 1153-1172.

De Bresser, J. T., and Spiers, C. J. (1993). Slip systems in calcite single crystals deformed at 300–800 C. Journal of Geophysical Research: Solid Earth, 98(B4), 6397-6409.

De Bresser, J. H. P., and Spiers, C. J. (1997). Strength characteristics of the r, f, and c slip systems in calcite. Tectonophysics, 272(1), 1-23.

DeCelles, P. G., Carrapa, B., Ojha, T. P., Gehrels, G. E., and Collins, D. (2020). Structural and Thermal Evolution of the Himalayan Thrust Belt in Midwestern Nepal (Vol. 547). Geological Society of America.

DeCelles, P. G., Gehrels, G. E., Najman, Y., Martin, A. J., Carter, A., and Garzanti, E. (2004). Detrital geochronology and geochemistry of Cretaceous–Early Miocene strata of Nepal: implications for timing and diachroneity of initial Himalayan orogenesis. Earth and Planetary Science Letters, 227(3-4), 313-330.

DeCelles, P. G., Robinson, D. M., Quade, J., Ojha, T. P., Garzione, C. N., Copeland, P., and Upreti, B. N. (2001). Stratigraphy, structure, and tectonic evolution of the Himalayan fold-thrust belt in western Nepal. Tectonics, 20(4), 487-509.

Deer, W. A., Howie, R. A., and Zussman, J. (1962). Rock-Forming Minerals, Volume 1 (Ortho and Ring Silicates). London, Longmons.

Delle Piane, C., Burlini, L., Kunze, K., Brack, P., and Burg, J. P. (2008). Rheology of dolomite: Large strain torsion experiments and natural examples. Journal of Structural Geology, 30(6), 767-776.

Dewey, J. F., and Bird, J. M. (1970). Mountain belts and the new global tectonics. Journal of Geophysical Research, 75(14), 2625-2647.

Di Vincenzo, G., Carosi, R., and Palmeri, R. (2004). The relationship between tectono-metamorphic evolution and argon isotope records in white mica: constraints from in situ 40Ar–39Ar laser analysis of the Variscan basement of Sardinia. Journal of Petrology, 45(5), 1013-1043.

Dunkl, I., Antolín, B., Wemmer, K., Rantitsch, G., Kienast, M., Montomoli, C., ... and Von Eynatten, H. (2011). Metamorphic evolution of the Tethyan Himalayan flysch in SE Tibet. Geological Society, London, Special Publications, 353(1), 45-69.

Ebert, A., Herwegh, M., Berger, A., and Pfiffner, A. (2008). Grain coarsening maps for polymineralic carbonate mylonites: A calibration based on data from different Helvetic nappes (Switzerland). Tectonophysics, 457(3-4), 128-142.

Engi, M., Lanari, P., and Kohn, M.J. (2017). Significant ages—An introduction to petrochronology. Reviews in Mineralogy and Geochemistry, 83, 1-12.

Erskine, B. G., Heidelbach, F., and Wenk, H. R. (1993). Lattice preferred orientations and microstructures of deformed Cordilleran marbles: correlation of shear indicators and determination of strain path. Journal of Structural Geology, 15(9-10), 1189-1205.

Faleiros, F. M., Moraes, R. D., Pavan, M., and Campanha, G. D. C. (2016). A new empirical calibration of the quartz c-axis fabric opening-angle deformation thermometer. Tectonophysics, 671, 173-182.

Fazio, E., Punturo, R., Cirrincione, R., Kern, H., Pezzino, A., Wenk, H. R., ... and Mamtani, M. A. (2017). Quartz preferred orientation in naturally deformed mylonitic rocks (Montalto shear zone–Italy): a comparison of results by different techniques, their advantages and limitations. International Journal of Earth Sciences, 106(7), 2259-2278.

Ferrill, D. A. (1998). Critical re-evaluation of differential stress estimates from calcite twins in coarse-grained limestone. Tectonophysics, 285(1-2), 77-86.

Ferrill, D. A., Morris, A. P., Evans, M. A., Burkhard, M., Groshong Jr, R. H., and Onasch, C. M. (2004). Calcite twin morphology: a low-temperature deformation geothermometer. Journal of Structural Geology, 26(8), 1521-1529.

Fossen, H. (2010). Structural geology, 1st edition Cambridge University Press.

Fossen, H., and Cavalcante, G. C. G. (2017). Shear zones–A review. Earth-Science Reviews, 171, 434-455.

Fossen, H., Cavalcante, G. C. G., Pinheiro, R. V. L., and Archanjo, C. J. (2019). Deformation–progressive or multiphase?. Journal of Structural Geology, 125, 82-99.

Frank, W., and Fuchs, G. R. (1970). Geological investigations in west Nepal and their significance for the geology of the Himalayas. Geologische Rundschau, 59(2), 552-580.

Fraser, G., Worley, B., and Sandiford, M. (2000). High-precision geothermobarometry across the High Himalayan metamorphic sequence, Langtang Valley, Nepal. Journal of Metamorphic Geology, 18(6), 665-681.

Frassi, C. (2015). Dominant simple-shear deformation during peak metamorphism for the lower portion of the Greater Himalayan Sequence in West Nepal: New implications for hybrid channel flow-type mechanisms in the Dolpo region. Journal of Structural Geology, 81, 28-44.

Fry, N. (1979). Random point distributions and strain measurement in rocks. Tectonophysics, 60(1-2), 89-105.

Fuchs, G. (1977). The geology of the Karnali and Dolpo regions, western Nepal. Jahrbuch der Geologischen Bundesanstalt Wien 120, 165-217.

Fuchs, G. (1981). Outline of the geology of the Himalaya. Mitteilungen der Österreichischen Geologischen Gesellschaft, 74(75), 101-127.

Fuchs, G., Widder, R. W., and Tuladhar, R. (1988). Contributions to the geology of the Annapurna Range (Manang area, Nepal). Jahrbuch der Geologischen Bundesanstalt, 131(4), 593-607.

Gaetani, M., and Garzanti, E. (1991). Multicyclic history of the northern India continental margin (northwestern Himalaya). American Association of Petroleum Geologists Bulletin, 75(9), 1427-1446.

Gansser, A. (1981). The geodynamic history of the Himalaya. Zagros Hindu Kush Himalaya Geodynamic Evolution, 3, 111-121.

Gansser, A. (1983). Geology of the Bhutan Himalaya. Birkhauser Verlag, Boston, Massachusetts

Garzanti, E. (1999). Stratigraphy and sedimentary history of the Nepal Tethys Himalaya passive margin. Journal of Asian Earth Sciences, 17(5-6), 805-827.

Garzanti, E., Liang, W., Andò, S., Clift, P. D., Resentini, A., Vermeesch, P., and Vezzoli, G. (2020). Provenance of Thal Desert sand: Focused erosion in the western Himalayan syntaxis and foreland-basin deposition driven by latest Quaternary climate change. Earth-Science Reviews, 103220.

Garzanti, E., Vezzoli, G., Andò, S., Lavé, J., Attal, M., France-Lanord, C., and DeCelles, P. (2007). Quantifying sand provenance and erosion (Marsyandi River, Nepal Himalaya). Earth and Planetary Science Letters, 258(3-4), 500-515.

Garzione, C. N., DeCelles, P. G., Hodkinson, D. G., Ojha, T. P., and Upreti, B. N. (2003). East-west extension and Miocene environmental change in the southern Tibetan plateau: Thakkhola graben, central Nepal. Geological Society of America Bulletin, 115(1), 3-20.

Gemignani, L., van der Beek, P. A., Braun, J., Najman, Y., Bernet, M., Garzanti, E., and Wijbrans, J. R. (2018). Downstream evolution of the thermochronologic age signal in the Brahmaputra catchment (eastern Himalaya): Implications for the detrital record of erosion. Earth and Planetary Science Letters, 499, 48-61.

Godin, L. (2003). Structural evolution of the Tethyan sedimentary sequence in the Annapurna area, central Nepal Himalaya. Journal of Asian Earth Sciences, 22(4), 307-328.

Godin, L., Ahenda, M., Grujic, D., Stevenson, R., and Cottle, J. (2021). Protolith affiliation and tectonometamorphic evolution of the Gurla Mandhata core complex, NW Nepal Himalaya. Geosphere, 17, https://doi.org/10.1130/GES02326.1.

Godin, L., Brown, R. L., and Hanmer, S. (1999a). High strain zone in the hanging wall of the Annapurna Detachment, central Nepal Himalaya. Special Papers-Geological Society of America, 199-210.

Godin, L., Brown, R. L., Hanmer, S., and Parrish, R. (1999b). Back folds in the core of the Himalayan orogen: An alternative interpretation. Geology, 27(2), 151-154.

Godin, L., Gleeson, T. P., Searle, M. P., Ullrich, T. D., and Parrish, R. R. (2006a). Locking of southward extrusion in favour of rapid crustal-scale buckling of the Greater Himalayan sequence, Nar valley, central Nepal. Geological Society, London, Special Publications, 268(1), 269-292.

Godin, L., Grujic, D., Law, R. D., and Searle, M. P. (2006b). Channel flow, ductile extrusion and exhumation in continental collision zones: an introduction. Geological Society, London, Special Publications, 268(1), 1-23.

Godin, L., Parrish, R. R., Brown, R. L., and Hodges, K. V. (2001). Crustal thickening leading to exhumation of the Himalayan metamorphic core of central Nepal: Insight from U-Pb geochronology and 40Ar/39Ar thermochronology. Tectonics, 20(5), 729-747.

Goscombe, B., Gray, D., and Hand, M. (2006). Crustal architecture of the Himalayan metamorphic front in eastern Nepal. Gondwana Research, 10(3-4), 232-255.

Govin, G., van der Beek, P., Najman, Y., Millar, I., Gemignani, L., Huyghe, P., ... Wijbrans, J. (2020). Early onset and late acceleration of rapid exhumation in the Namche Barwa syntaxis, eastern Himalaya. Geology, 48(12), 1139-1143.

Gradstein, F. M., Rad, U. V., Westermann, G. E., Wiedmann, J., and Gibling, M. R. (1992). Stratigraphy and depositional history of the Mesozoic continental margin of central Nepal. Jahrbuch der Geologischen Bundesanstalt, Regionale Geologie Ausland, (77), 1-141.

Grasemann, B., Fritz, H., and Vannay, J. C. (1999). Quantitative kinematic flow analysis from the Main Central Thrust Zone (NW-Himalaya, India): implications for a decelerating strain path and the extrusion of orogenic wedges. Journal of Structural Geology, 21(7), 837-853.

Graziani, R., Larson, K. P., and Soret, M. (2020). The effect of hydrous mineral content on competitive strain localization mechanisms in felsic granulites. Journal of Structural Geology, 134, 104015.

Grujic, D., Ashley, K. T., Coble, M. A., Coutand, I., Kellett, D. A., Larson, K. P., ... and Whynot, N. (2020). Deformational temperatures across the Lesser Himalayan Sequence in eastern Bhutan and their implications for the deformation history of the Main Central Thrust. Tectonics, 39(4), e2019TC005914.

Grujic, D., Casey, M., Davidson, C., Hollister, L. S., Kündig, R., Pavlis, T., and Schmid, S. (1996). Ductile extrusion of the Higher Himalayan Crystalline in Bhutan: evidence from quartz microfabrics. Tectonophysics, 260(1-3), 21-43.

Guillot, S., Cosca, M., Allemand, P., and Le Fort, P. (1999). Contrasting metamorphic and geochronologic evolution along the Himalayan belt. Special Papers-Geological Society of America, 117-128.

Guillot, S., Hodges, K., Fort, P. L., and Pêcher, A. (1994). New constraints on the age of the Manaslu leucogranite: Evidence for episodic tectonic denudation in the central Himalayas. Geology, 22(6), 559-562.

Guillot, S., Le Fort, P., Pêcher, A., Barman, M. R., and Aprahamian, J. (1995). Contact metamorphism and depth of emplacement of the Manaslu granite (central Nepal). Implications for Himalayan orogenesis. Tectonophysics, 241(1-2), 99-119.

Guillot, S., Mahéo, G., de Sigoyer, J., Hattori, K. H., and Pecher, A. (2008). Tethyan and Indian subduction viewed from the Himalayan high-to ultrahigh-pressure metamorphic rocks. Tectonophysics, 451(1-4), 225-241.

Guillot, S., Pêcher, A., Rochette, P., and Le Fort, P. (1993). The emplacement of the Manaslu granite of central Nepal: field and magnetic susceptibility constraints. Geological Society, London, Special Publications, 74(1), 413-428.

Hammes, D.M., and Peternell, M., (2016). FAME: Software for analysing rock microstructures. Computers & Geosciences, 90, Part A, 24-33. https://doi.org/10.1016/j.cageo.2016.02.010.

Handy, M. R. (1994). Flow laws for rocks containing two non-linear viscous phases: a phenomenological approach. Journal of Structural Geology, 16(3), 287-301.

Harrison, T. M., Duncan, I. A. N., and Mcdougall, I. A. N. (1985). Diffusion of ^{40}Ar in biotite: temperature, pressure and compositional effects. Geochimica et Cosmochimica Acta, 49(11), 2461-2468.

Heilbronner, R., and Pauli, C. (1993). Integrated spatial and orientation analysis of quartz c-axes by computer-aided microscopy. Journal of Structural Geology, 15(3-5), 369-382.

Henry, D. J., Guidotti, C. V., and Thomson, J. A. (2005). The Ti-saturation surface for low-to-medium pressure metapelitic biotites: Implications for geothermometry and Ti-substitution mechanisms. American mineralogist, 90(2-3), 316-328.

Herwegh, M., and Berger, A. (2004). Deformation mechanisms in second-phase affected microstructures and their energy balance. Journal of Structural Geology, 26(8), 1483-1498.

Herwegh, M., Berger, A., Ebert, A., and Brodhag, S. (2008). Discrimination of annealed and dynamic fabrics: consequences for strain localization and deformation episodes of large-scale shear zones. Earth and planetary science letters, 276(1-2), 52-61.

Herwegh, M., Xiao, X., and Evans, B. (2003). The effect of dissolved magnesium on diffusion creep in calcite. Earth and Planetary Science Letters, 212(3-4), 457-470.

Hielscher, R., and Schaeben, H. (2008). A novel pole figure inversion method: specification of the MTEX algorithm. Journal of Applied Crystallography, 41(6), 1024-1037.

Hippertt, J. F. (1994). Microstructures and c-axis fabrics indicative of quartz dissolution in sheared quartzites and phyllonites. Tectonophysics, 229(3-4), 141-163.

Hobbs, B. E., Means, W. D., and Williams, P. F. (1976). An outline of structural geology. Wiley, New York.

Hodges, K. V. (2000). Tectonics of the Himalaya and southern Tibet from two perspectives. Geological Society of America Bulletin, 112(3), 324-350.

Hodges, K. V., Parrish, R. R., Housh, T. B., Lux, D. R., Burchfiel, B. C., Royden, L. H., and Chen, Z. (1992). Simultaneous Miocene extension and shortening in the Himalayan orogen. Science, 258(5087), 1466-1470.

Hodges, K. V., Parrish, R. R., and Searle, M. P. (1996). Tectonic evolution of the central Annapurna range, Nepalese Himalayas. Tectonics, 15(6), 1264-1291.

Holyoke III, C. W., Kronenberg, A. K., and Newman, J. (2013). Dislocation creep of polycrystalline dolomite. Tectonophysics, 590, 72-82.

Holyoke III, C. W., and Tullis, J. (2006). Mechanisms of weak phase interconnection and the effects of phase strength contrast on fabric development. Journal of Structural Geology, 28(4), 621-640.

Hu, X., Garzanti, E., Wang, J., Huang, W., An, W., and Webb, A. (2016). The timing of India-Asia collision onset–Facts, theories, controversies. Earth-Science Reviews, 160, 264-299.

Hubbard, M. S. (1989). Thermobarometric constraints on the thermal history of the Main Central Thrust Zone and Tibetan Slab, eastern Nepal Himalaya. Journal of Metamorphic Geology, 7(1), 19-30.

Humphreys, F.J. (2001). Review grain and subgrain characterisation by electron backscatter diffraction. Journal of materials science, 36(16), 3833-3854.

Hunter, N. J., Hasalová, P., Weinberg, R. F., and Wilson, C. J. (2016). Fabric controls on strain accommodation in naturally deformed mylonites: The influence of interconnected micaceous layers. Journal of Structural Geology, 83, 180-193.

Hunter, N. J., Weinberg, R. F., Wilson, C. J., Luzin, V., and Misra, S. (2018). Microscopic anatomy of a “hot-on-cold” shear zone: Insights from quartzites of the Main Central Thrust in the Alaknanda region (Garhwal Himalaya). Geological Society of America Bulletin, 130(9-10), 1519-1539.

Huntington, K. W., Blythe, A. E., Hodges, K. V. (2006). Climate change and Late Pliocene acceleration of erosion in the Himalaya. Earth and Planetary Science Letters, 252(1-2), 107-118.

Hurtado Jr, J. M., Hodges, K. V., and Whipple, K. X. (2001). Neotectonics of the Thakkhola graben and implications for recent activity on the South Tibetan fault system in the central Nepal Himalaya. Geological Society of America Bulletin, 113(2), 222-240.

Iaccarino, S., Montomoli, C., Carosi, R., Massonne, H. J., Langone, A., and Visonà, D. (2015). Pressure–temperature–time–deformation path of kyanite-bearing migmatitic paragneiss in the Kali Gandaki valley (Central Nepal): investigation of Late Eocene–Early Oligocene melting processes. Lithos, 231, 103-121.

Iaccarino, S., Montomoli, C., Carosi, R., Massonne, H. J., and Visonà, D. (2017a). Geology and tectono-metamorphic evolution of the Himalayan metamorphic core: insights from the Mugu Karnali transect, Western Nepal (Central Himalaya). Journal of Metamorphic Geology, 35(3), 301-325.

Iaccarino, S., Montomoli, C., Carosi, R., Montemagni, C., Massonne, H. J., Langone, A., ... and Visonà, D. (2017b). Pressure-temperature-deformation-time constraints on the South Tibetan Detachment system in the Garhwal Himalaya (NW India). Tectonics, 36(11), 2281-2304.

Iaccarino, S., Montomoli, C., Montemagni, C., Massonne, H. J., Langone, A., Jain, A. K., ... and Carosi, R. (2020). The Main Central Thrust zone along the Alaknanda and Dhauli Ganga valleys (Garhwal Himalaya, NW India): Insights into an inverted metamorphic sequence. Lithos, 372, 105669.

Imayama, T., Takeshita, T., and Arita, K. (2010). Metamorphic P–T profile and P–T path discontinuity across the far-eastern Nepal Himalaya: investigation of channel flow models. Journal of Metamorphic Geology, 28(5), 527-549.

Inger, S., and Harris, N. B. W. (1992). Tectonothermal evolution of the High Himalayan crystalline sequence, Langtang Valley, northern Nepal. Journal of Metamorphic Geology, 10(3), 439-452.
Jamison, W. R., and Spang, J. H. (1976). Use of calcite twin lamellae to infer differential stress. Geological Society of America Bulletin, 87(6), 868-872.

Jessup, M. J., Langille, J. M., Diedesch, T. F., and Cottle, J. M. (2019). Gneiss dome formation in the Himalaya and southern Tibet. Geological Society, London, Special Publications, 483(1), 401-422.

Jessup, M. J., Law, R. D., Searle, M. P., and Hubbard, M. S. (2006). Structural evolution and vorticity of flow during extrusion and exhumation of the Greater Himalayan Slab, Mount Everest Massif, Tibet/Nepal: implications for orogen-scale flow partitioning. Geological Society, London, Special Publications, 268(1), 379-413.

Jessup, M. J., Newell, D. L., Cottle, J. M., Berger, A. L., and Spotila, J. A. (2008). Orogen-parallel extension and exhumation enhanced by denudation in the trans-Himalayan Arun River gorge, Ama Drime Massif, Tibet-Nepal. Geology, 36(7), 587-590.

Jiang, D. (1994a). Vorticity determination, distribution, partitioning and the heterogeneity and non-steadiness of natural deformations. Journal of Structural Geology, 16(1), 121-130.

Jiang, D. (1994b). Flow variation in layered rocks subjected to bulk flow of various kinematic vorticities: theory and geological implications. Journal of Structural Geology, 16(8), 1159-1172.

Jiang, D., and Williams, P. F. (1999). A fundamental problem with the kinematic interpretation of geological structures. Journal of Structural Geology, 21(8-9), 933-937.

Kanyan, L., Jain, A. K., and Singh, S. (2021). Vorticity patterns along the Main Central Thrust Zone, Alaknanda–Dhauli Ganga Valleys (Garhwal), Uttarakhand Himalaya. Journal of Earth System Science, 130(1), 1-21.

Kaushal, R. K., Singh, V., Mukul, M., and Jain, V. (2017). Identification of deformation variability and active structures using geomorphic markers in the Nahan salient, NW Himalaya, India. Quaternary International, 462, 194-210.

Kellett, D. A., Cottle, J. M., and Larson, K. P. (2019). The South Tibetan Detachment System: history, advances, definition and future directions. Geological Society, London, Special Publications, 483(1), 377-400.

Kellett, D. A., and Grujic, D. (2012). New insight into the South Tibetan Detachment system: Not a single progressive deformation. Tectonics, 31(2).

Kennedy, L. A., and White, J. C. (2001). Low-temperature recrystallization in calcite: Mechanisms and consequences. Geology, 29(11), 1027-1030.

Kern, H., and Wenk, H. R. (1983). Calcite texture development in experimentally induced ductile shear zones. Contributions to Mineralogy and Petrology, 83(3-4), 231-236.

Khanal, S., and Robinson, D. M. (2013). Upper crustal shortening and forward modeling of the Himalayan thrust belt along the Budhi-Gandaki River, central Nepal. International Journal of Earth Sciences, 102(7), 1871-1891.

Khanal, G. P., Wang, J. M., Wu, F. Y., Wang, J. G., and Yang, L. (2020). In-sequence buoyancy extrusion of the Himalayan Metamorphic Core, central Nepal: Constraints from monazite petrochronology and thermobarometry. Journal of Asian Earth Sciences, 199, 104406.

Kilian, R., and Heilbronner, R. (2017). Analysis of crystallographic preferred orientations of experimentally deformed Black Hills Quartzite. Solid Earth, 8(5), 1095.

Kilian, R., Heilbronner, R., and Stünitz, H. (2011). Quartz microstructures and crystallographic preferred orientation: which shear sense do they indicate?. Journal of Structural Geology, 33(10), 1446-1466.

Kohlstedt, D. L., Evans, B., and Mackwell, S. J. (1995). Strength of the lithosphere: Constraints imposed by laboratory experiments. Journal of Geophysical Research: Solid Earth, 100(B9), 17587-17602.

Kohn, M.J. (2008). PTt data from central Nepal support critical taper and repudiate large-scale channel flow of the Greater Himalayan Sequence. Geological Society of America Bulletin, 120(3-4), 259-273.

Kohn, M. J., Engi, M., and Lanari, P. (2017). Petrochronology. Methods and Applications, Mineralogical Society of America Reviews in Mineralogy and Geochemistry, 83, 575.

Kohn, M. J., Paul, S. K., and Corrie, S. L. (2010). The lower Lesser Himalayan sequence: A Paleoproterozoic arc on the northern margin of the Indian plate. Geological Society of America Bulletin, 122(3-4), 323-335.

Kohn, M. J., Wieland, M. S., Parkinson, C. D., and Upreti, B. N. (2004). Miocene faulting at plate tectonic velocity in the Himalaya of central Nepal. Earth and Planetary Science Letters, 228(3-4), 299-310.

Koppers, A. A. (2002). ArArCALC—software for $^{40}Ar/^{39}Ar$ age calculations. Computers & Geosciences, 28(5), 605-619.

Kruhl, J. H. (1996). Prism-and basal-plane parallel subgrain boundaries in quartz: A microstructural geothermobarometer. Journal of Metamorphic Geology, 14(5), 581-589.

Kruhl, J. H. (1998). Prism-and basal-plane parallel subgrain boundaries in quartz: a microstructural geothermobarometer-Reply. Journal of Metamorphic Geology, 16(1), 142-146.

Kuiper, K. F., Deino, A., Hilgen, F. J., Krijgsman, W., Renne, P. R., and Wijbrans, A. J. (2008). Synchronizing rock clocks of Earth history. Science, 320(5875), 500-504.

Kurz, W., and Neubauer, F. (1996). Deformation partitioning during updoming of the Sonnblick area in the Tauern Window (Eastern Alps, Austria). Journal of Structural Geology, 18(11), 1327-1343.

Kurz, W., Neubauer, F., Unzog, W., Genser, J., and Wang, X. (2000). Microstructural and textural development of calcite marbles during polyphase deformation of Penninic units within the Tauern Window (Eastern Alps). Tectonophysics, 316(3-4), 327-342.

Lacombe, O. (2010). Calcite twins, a tool for tectonic studies in thrust belts and stable orogenic forelands. Oil & Gas Science and Technology–Revue d'IFP Energies nouvelles, 65(6), 809-838.

Lacombe, O., and Laurent, P. (1996). Determination of deviatoric stress tensors based on inversion of calcite twin data from experimentally deformed monophase samples: preliminary results. Tectonophysics, 255(3-4), 189-202.

Lafrance, B., White, J.C., and Williams, P.F. (1994). Natural calcite c-axis fabrics: an alternate interpretation. Tectonophysics, 229(1-2), 1-18.

Lang, K. A., Huntington, K. W., Burmester, R., Housen, B. (2016). Rapid exhumation of the eastern Himalayan syntaxis since the late Miocene. Bulletin, 128(9-10), 1403-1422.

Larson, K.M., Bürgmann, R., Bilham, R., and Freymueller, J.T. (1999). Kinematics of the India-Eurasia collision zone from GPS measurements. Journal of Geophysical Research: Solid Earth, 104(B1), 1077-1093.

Larson, K.P., Ambrose, T. K., Webb, A. A. G., Cottle, J.M., and Shrestha, S. (2015). Reconciling Himalayan midcrustal discontinuities: the Main Central thrust system. Earth and Planetary Science Letters, 429, 139-146.

Larson, K.P., Cottle, J., Lederer, G., and Rai, S. M. (2017). Defining shear zone boundaries using fabric intensity gradients: An example from the east-central Nepal Himalaya. Geosphere, 13(3), 771-781.

Larson, K. P., and Godin, L. (2009). Kinematics of the Greater Himalayan sequence, Dhaulagiri Himal: implications for the structural framework of central Nepal. Journal of the Geological Society, 166(1), 25-43.

Larson, K.P., Godin, L., and Price, R. A. (2010). Relationships between displacement and distortion in orogens: Linking the Himalayan foreland and hinterland in central Nepal. The Bulletin of the Geological Society of America, 122(7-8), 1116-1134.

Larson, K.P., Graziani, R., Cottle, J. M., Apen, F., Corthouts, T., and Lageson, D. (2020). The structural evolution of the Qomolangma Formation, Mount Everest, Nepal. Journal of Structural Geology, 138, 104123.

Larson, K.P., Kellett, D. A., Cottle, J. M., Camacho, A., and Brubacher, A. D. (2019). Mid-Miocene initiation of E-W extension and recoupling of the Himalaya. Terra Nova, 32(2), 151-158.

Law, R. D. (2014). Deformation thermometry based on quartz c-axis fabrics and recrystallization microstructures: A review. Journal of Structural Geology, 66, 129-161.

Law, R. D., Jessup, M. J., Searle, M. P., Francsis, M. K., Waters, D. J., and Cottle, J. M. (2011). Telescoping of isotherms beneath the South Tibetan Detachment system, Mount Everest Massif. Journal of Structural Geology, 33(11), 1569-1594.

Law, R. D., Searle, M. P., and Simpson, R. L. (2004). Strain, deformation temperatures and vorticity of flow at the top of the Greater Himalayan Slab, Everest Massif, Tibet. Journal of the Geological Society, 161(2), 305-320.

Law, R. D., Stahr Iii, D. W., Francsis, M. K., Ashley, K. T., Grasemann, B., and Ahmad, T. (2013). Deformation temperatures and flow vorticities near the base of the Greater Himalayan Series, Sutlej Valley and Shimla Klippe, NW India. Journal of Structural Geology, 54, 21-53.

Le Fort, P. (1971). Les formations cristallophylliennes de la Thakkhola. Recherches géologiques dans l'Himalaya du Népal, région de la Thakkhola. Centre National de la Recherche Scientifique, Paris, 41-81.

Le Fort, P. (1975). Himalayas: the collided range. Present knowledge of the continental arc. American Journal of Science, 275(1), 1-44.

Le Fort, P. (1981). Manaslu leucogranite: a collision signature of the Himalaya: a model for its genesis and emplacement. Journal of Geophysical Research: Solid Earth, 86(B11), 10545-10568.

Lee, J., Hager, C., Wallis, S. R., Stockli, D. F., Whitehouse, M. J., Aoya, M., and Wang, Y. (2011). Middle to late Miocene extremely rapid exhumation and thermal reequilibration in the Kung Co rift, southern Tibet. Tectonics, 30(2).

Leiss, B., and Barber, D. J. (1999). Mechanisms of dynamic recrystallization in naturally deformed dolomite inferred from EBSP analyses. Tectonophysics, 303(1-4), 51-69.

Leiss, B., and Molli, G. (2003). 'High-temperature'texture in naturally deformed Carrara marble from the Alpi Apuane, Italy. Journal of Structural Geology, 25(4), 649-658.

Leiss, B., Siegesmund, S., and Weber, K. (1999). Texture asymmetries as shear sense indicators in naturally deformed mono-and polyphase carbonate rocks. Texture, Stress, and Microstructure, 33(1-4), 61-74.

Leloup, P. H., Mahéo, G., Arnaud, N., Kali, E., Boutonnet, E., Liu, D., ... and Haibing, L. (2010). The South Tibet Detachment shear zone in the Dinggye area: Time constraints on extrusion models of the Himalayas. Earth and Planetary Science Letters, 292(1-2), 1-16.

Lihter, I., Larson, K. P., Shrestha, S., Cottle, J. M., and Brubacher, A. D. (2020). Contact metamorphism of the Tethyan Sedimentary Sequence, Upper Mustang region, west-central Nepal. Geological Magazine, 157(11), 1917-1932.

Lister, G. S. (1977). Discussion: crossed-girdle c-axis fabrics in quartzites plastically deformed by plane strain and progressive simple shear. Tectonophysics, 39(1-3), 51-54.

Lister, G. S., and Hobbs, B. E. (1980). The simulation of fabric development during plastic deformation and its application to quartzite: the influence of deformation history. Journal of Structural Geology, 2(3), 355-370.

Lombardo, B., Pertusati, P., and Borghi, S. (1993). Geology and tectonomagmatic evolution of the eastern Himalaya along the Chomolungma-Makalu transect. Geological Society, London, Special Publications, 74(1), 341-355.

Long, S. P., and Kohn, M. J. (2020). Distributed ductile thinning during thrust emplacement: A commonly overlooked exhumation mechanism. Geology, 48(4), 368-373.

Long, S., McQuarrie, N., Tobgay, T., and Grujic, D. (2011). Geometry and crustal shortening of the Himalayan fold-thrust belt, eastern and central Bhutan. Geological Society of America Bulletin, 123(7-8), 1427-1447.

Long, S. P., Mullady, C. L., Starnes, J. K., Gordon, S. M., Larson, K. P., Pianowski, L. S., ... and Soignard, E. (2019). A structural model for the South Tibetan Detachment system in northwestern Bhutan from integration of temperature, fabric, strain, and kinematic data. Lithosphere, 11(4), 465-487.

López Sánchez, M. A., Llana Fúnez, S., Menegon, L., Pennacchioni, G., Stipp, M., Mancktelow, N., and Law, R. (2015). An evaluation of different measures of dynamically recrystallized grain size for paleopiezometry or paleowattometry studies. Solid Earth, 6(2), 475-495.

Mainprice, D., Bachmann, F., Hielscher, R., and Schaeben, H. (2015). Descriptive tools for the analysis of texture projects with large datasets using MTEX: strength, symmetry and components. Geological Society, London, Special Publications, 409(1), 251-271.

Mainprice, D., Bouchez, J. L., Blumenfeld, P., and Tubià, J. M. (1986). Dominant c slip in naturally deformed quartz: implications for dramatic plastic softening at high temperature. Geology, 14(10), 819-822.

Marques, F. O., Mandal, N., Ghosh, S., Ranalli, G., and Bose, S. (2018). Channel flow, tectonic overpressure, and exhumation of high-pressure rocks in the Greater Himalayas. Solid Earth, 9(5), 1061-1078.

Martin, A. J. (2017). A review of definitions of the Himalayan Main Central Thrust. International Journal of Earth Sciences, 106(6), 2131-2145.

Massonne, H.J., and Szpurka, Z. (1997=. Thermodynamic properties of white micas on the basis of high-pressure experiments in the systems K_2O–MgO–Al_2O_3–SiO_2–H_2O and K_2O–FeO–Al_3O_3–SiO_2–H_2O. Lithos, 41, 229-250.

Means, W. D., Hobbs, B. E., Lister, G. S., and Williams, P. F. (1980). Vorticity and non-coaxiality in progressive deformations. Journal of Structural Geology, 2(3), 371-378.

Molnar, P., & Stock, J. M. (2009). Slowing of India's convergence with Eurasia since 20 Ma and its implications for Tibetan mantle dynamics. Tectonics, 28(3).

Montemagni, C., Carosi, R., Fusi, N., Iaccarino, S., Montomoli, C., Villa, I. M., and Zanchetta, S. (2020). Three-dimensional vorticity and time-constrained evolution of the Main Central Thrust zone, Garhwal Himalaya (NW India). Terra Nova, 32(3), 215-224.

Montemagni, C., Iaccarino, S., Montomonli, C., Carosi, R., Jain, A. K., and Villa, I. M. (2018). Age constraints on the deformation style of the South Tibetan Detachment System in Garhwal Himalaya. Italian journal of Geosciences, 137(2), 175-187.

Montomoli, C., Carosi, R., and Iaccarino, S. (2015). Tectonometamorphic discontinuities in the Greater Himalayan Sequence: a local or a regional feature?. Geological Society, London, Special Publications, 412(1), 25-41.

Montomoli, C., Carosi, R., Rubatto, D., Visonà, D., and Iaccarino, S. (2017). Tectonic activity along the inner margin of the South Tibetan Detachment constrained by syntectonic leucogranite emplacement in Western Bhutan. Italian journal of Geosciences, 136(1), 5-14.

Montomoli, C., Iaccarino, S., Carosi, R., Langone, A., and Visonà, D. (2013). Tectonometamorphic discontinuities within the Greater Himalayan Sequence in Western Nepal (Central Himalaya): insights on the exhumation of crystalline rocks. Tectonophysics, 608, 1349-1370.

Morales, L. F., Lloyd, G. E., and Mainprice, D. (2014). Fabric transitions in quartz via viscoplastic self-consistent modeling part I: Axial compression and simple shear under constant strain. Tectonophysics, 636, 52-69.

Morales, L. F., Mainprice, D., Lloyd, G. E., and Law, R. D. (2011). Crystal fabric development and slip systems in a quartz mylonite: an approach via transmission electron microscopy and viscoplastic self-consistent modelling. Geological Society, London, Special Publications, 360(1), 151-174.

Morgan, S. S., and Law, R. D. (2004). Unusual transition in quartzite dislocation creep regimes and crystal slip systems in the aureole of the Eureka Valley–Joshua Flat–Beer Creek pluton, California: a case for anhydrous conditions created by decarbonation reactions. Tectonophysics, 384(1-4), 209-231.

Mottram, C. M., Cottle, J. M., and Kylander-Clark, A. R. (2019). Campaign-style U-Pb titanite petrochronology: Along-strike variations in timing of metamorphism in the Himalayan metamorphic core. Geoscience Frontiers, 10(3), 827-847.

Müller, W. (2003). Strengthening the link between geochronology, textures and petrology. Earth and Planetary Science Letters, 206(3-4), 237-251.

Murphy, M. A., and Copeland, P. (2005). Transtensional deformation in the central Himalaya and its role in accommodating growth of the Himalayan orogen. Tectonics, 24(4).

Murphy, M. A., Yin, A., Kapp, P., Harrison, T. M., Manning, C. E., Ryerson, F. J., ... and Jinghui, G. (2002). Structural evolution of the Gurla Mandhata Detachment system, southwest Tibet: Implications for the eastward extent of the Karakoram fault system. Geological Society of America Bulletin, 114(4), 428-447.

Nagy, C., Godin, L., Antolín, B., Cottle, J., and Archibald, D. (2015). Mid-Miocene initiation of orogen-parallel extension, NW Nepal Himalaya. Lithosphere, 7(5), 483-502.

Najman, Y., Jenks, D., Godin, L., Boudagher-Fadel, M., Millar, I., Garzanti, E., ... and Bracciali, L. (2017). The Tethyan Himalayan detrital record shows that India–Asia terminal collision occurred by 54 Ma in the Western Himalaya. Earth and Planetary Science Letters, 459, 301-310.

Negrini, M., Smith, S. A., Scott, J. M., and Tarling, M. S. (2018). Microstructural and rheological evolution of calcite mylonites during shear zone thinning: Constraints from the Mount Irene shear zone, Fiordland, New Zealand. Journal of Structural Geology, 106, 86-102.

Nelson, K. D., Zhao, W., Brown, L. D., Kuo, J., Che, J., Liu, X., ... and Edwards, M. (1996). Partially molten middle crust beneath southern Tibet: synthesis of project INDEPTH results. Science, 274(5293), 1684-1688.

Neupane, B., Zhao, J., Allen, C. M., Ju, Y., Baral, U., and Gyawali, B. R. (2020). Provenance of Jurassic-Cretaceous Tethyan Himalayan sequences in the Thakkhola Section-Nepal, inferring pre-collisional tectonics of the central Himalaya. Journal of Asian Earth Sciences, 192, 104288.

Ningthoujam, P. S., Dubey, C. S., Lolee, L. K., Shukla, D. P., Naorem, S. S., and Singh, S. K. (2015). Tectonic studies and crustal shortening across Easternmost Arunachal Himalaya. Journal of Asian Earth Sciences, 111, 339-349.

Okudaira, T., Takeshita, T., and Toriumi, M. (1998). Prism-and basal-plane parallel subgrain boundaries in quartz: a microstructural geothermobarometer. Journal of Metamorphic Geology, 16(1), 141-142.

Olgaard, D. L. (1990). The role of second phase in localizing deformation. Geological Society, London, Special Publications, 54(1), 175-181.

Parsons, A. J., Law, R. D., Lloyd, G. E., Phillips, R. J., and Searle, M. P. (2016a). Thermo-kinematic evolution of the Annapurna-Dhaulagiri Himalaya, central Nepal: The Composite Orogenic System. Geochemistry, Geophysics, Geosystems, 17(4), 1511-1539.

Parsons, A. J., Law, R. D., Searle, M. P., Phillips, R. J., and Lloyd, G. E. (2016b). Geology of the Dhaulagiri-Annapurna-Manaslu Himalaya, Western Region, Nepal. 1: 200,000. Journal of Maps, http://dx.doi.org/10.1080/17445647.2014.984784

Parsons, A. J., Hosseini, K., Palin, R., and Sigloch, K. (2020). Geological, geophysical and plate kinematic constraints for models of the India-Asia collision and the post-Triassic central Tethys oceans. Earth-Science Reviews, 103084.

Passchier, C.W., and Trouw, R.A. (2005). Microtectonics, 2nd Revised and Enlarged Edition. Springer Science Business Media, Würzburg, Germany. https://doi.org/10.1007/3-540-29359-0

Passchier, C. W. (1997). The fabric attractor. Journal of Structural Geology, 19(1), 113-127.

Paudel, L. P., and Arita, K. (2000). Tectonic and polymetamorphic history of the Lesser Himalaya in central Nepal. Journal of Asian Earth Sciences, 18(5), 561-584.

Paul, J., Bürgmann, R., Gaur, V. K., Bilham, R., Larson, K. M., Ananda, M. B., ... and Kumar, D. (2001). The motion and active deformation of India. Geophysical Research Letters, 28(4), 647-650.

Pêcher, A. (1975). The Main Central Thrust of the Nepal Himalaya and the related metamorphism in the Modi Khola cross-section (Annapurna Range). Himalayan Geology, 5, 115-132.

Pêcher, A., (1978). Déformations et métamorphisme associés à une zone de cisaillement. Exemple du grand chevauchement central himalayen (M.C.T.), transversale des Annapurna et du Manaslu, Népal [Ph.D. thesis]. Grenoble, University of Grenoble, 310 p.

Pécher, A., Bouchez, J. L., and Le Fort, P. (1991). Miocene dextral shearing between Himalaya and Tibet. Geology, 19(7), 683-685.

Philpotts, A. R. (1990). Principles of Igneous and Metamorphic Petrology. Prentice-Hall International.

Platt, J. P., and De Bresser, J. H. (2017). Stress dependence of microstructures in experimentally deformed calcite. Journal of Structural Geology, 105, 80-87.

Platt, J. P. (1993). Exhumation of high-pressure rocks: A review of concepts and processes. Terra nova, 5(2), 119-133.

Ramberg, H. (1975). Particle paths, displacement and progressive strain applicable to rocks. Tectonophysics, 28(1-2), 1-37.

Ramsay, J. G. (1980). Shear zone geometry: a review. Journal of Structural Geology, 2(1-2), 83-99.

Ranalli, G., and Murphy, D. C. (1987). Rheological stratification of the lithosphere. Tectonophysics, 132(4), 281-295.

Ratschbacher, L., Frisch, W., Liu, G., and Chen, C. (1994). Distributed deformation in southern and western Tibet during and after the India-Asia collision. Journal of Geophysical Research: Solid Earth, 99(B10), 19917-19945.

Ratschbacher, L., Wenk, H. R., and Sintubin, M. (1991). Calcite textures: examples from nappes with strain-path partitioning. Journal of Structural Geology, 13(4), 369-384.

Renner, J., Evans, B., and Siddiqi, G. (2002). Dislocation creep of calcite. Journal of Geophysical Research: Solid Earth, 107(B12), ECV-6.

Robert, X., van der Beek, P., Braun, J., Perry, C., and Mugnier, J. L. (2011). Control of detachment geometry on lateral variations in exhumation rates in the Himalaya: Insights from low-temperature thermochronology and numerical modeling. Journal of Geophysical Research: Solid Earth, 116(B5).

Robinson, D. M., and Martin, A. J. (2014). Reconstructing the Greater Indian margin: A balanced cross section in central Nepal focusing on the Lesser Himalayan duplex. Tectonics, 33(11), 2143-2168.

Robinson, D. M., DeCelles, P. G., and Copeland, P. (2006). Tectonic evolution of the Himalayan thrust belt in western Nepal: Implications for channel flow models. Geological Society of America Bulletin, 118(7-8), 865-885.

Rogowitz, A., Grasemann, B., Huet, B., and Habler, G. (2014). Strain rate dependent calcite microfabric evolution–An experiment carried out by nature. Journal of Structural Geology, 69, 1-17.

Rowe, K. J., and Rutter, E. H. (1990). Palaeostress estimation using calcite twinning: experimental calibration and application to nature. Journal of Structural Geology, 12(1), 1-17.

Rutter, E. H. (1974). The influence of temperature, strain rate and interstitial water in the experimental deformation of calcite rocks. Tectonophysics, 22(3-4), 311-334.

Rutter, E. H. (1995). Experimental study of the influence of stress, temperature, and strain on the dynamic recrystallization of Carrara marble. Journal of Geophysical Research: Solid Earth, 100(B12), 24651-24663.

Rutter, E. H., Faulkner, D. R., Brodie, K. H., Phillips, R. J., and Searle, M. P. (2007). Rock deformation processes in the Karakoram fault zone, Eastern Karakoram, Ladakh, NW India. Journal of Structural Geology, 29(8), 1315-1326.

Rybacki, E., Evans, B., Janssen, C., Wirth, R., and Dresen, G. (2013). Influence of stress, temperature, and strain on calcite twins constrained by deformation experiments. Tectonophysics, 601, 20-36.

Rybacki, E., Janssen, C., Wirth, R., Chen, K., Wenk, H. R., Stromeyer, D., and Dresen, G. (2011). Low-temperature deformation in calcite veins of SAFOD core samples (San Andreas Fault)—microstructural analysis and implications for fault rheology. Tectonophysics, 509(1-2), 107-119.

Sander, B. (1950). Einfuhrung in die gefugekunde der geologischen korper.: Die korngefug. Springer-Verlag, Wien Berlin Heidelberg. https://doi.org/10.1007/978-3-7091-7759-4.

Sarkarinejad, K., and Heibati, Z. (2017). Vorticity analysis in the Zagros orogen, Shiraz area, Iran. International Journal of Earth Sciences, 106(6), 2041-2065.

Schaeben, H. (1997). A simple standard orientation density function: The hyperspherical de la Vallée Poussin kernel. Physica Status Solidi (B), 200(2), 367-376.

Schaeben, H. (2007). Comment on "The misorientation index: Development of a new method for calculating the strength of lattice-preferred orientation" by Philip Skemer, Ikuo Katayama, Zhenting Jiang, Shun-ichiro Karato. Tectonophysics, 441(1-4), 115-117.

Schaeben, H., Hielscher, R., Fundenberger, J. J., Potts, D., and Prestin, J. (2007). Orientation density function-controlled pole probability density function measurements: automated adaptive control of texture goniometers. Journal of Applied Crystallography, 40(3), 570-579.

Schelling, D. (1992). The tectonostratigraphy and structure of the eastern Nepal Himalaya. Tectonics, 11(5), 925-943.

Schelling, D., and Arita, K. (1991). Thrust tectonics, crustal shortening, and the structure of the far-eastern Nepal Himalaya. Tectonics, 10(5), 851-862.

Schill, E., Appel, E., Godin, L., Crouzet, C., Gautam, P., and Regmi, K. R. (2003). Record of deformation by secondary magnetic remanences and magnetic anisotropy in the Nar/Phu valley (central Himalaya). Tectonophysics, 377(1-2), 197-209.

Schmid, S. M., and Casey, M. (1986). Complete fabric analysis of some commonly observed quartz c-axis patterns. Geophysical Monograph, 36(6), 263-286.

Schmid, S. M., Panozzo, R., and Bauer, S. (1987). Simple shear experiments on calcite rocks: rheology and microfabric. Journal of Structural Geology, 9(5-6), 747-778.

Schmid, S. M., Paterson, M. S., and Boland, J. N. (1980). High temperature flow and dynamic recrystallization in Carrara marble. Tectonophysics, 65(3-4), 245-280.

Schneider, C., and Masch, L. (1993). The metamorphism of the Tibetan series from the Manang area, Marsyandi valley, central Nepal. Geological Society, London, Special Publications, 74(1), 357-374.

Searle, M. P., and Godin, L. (2003). The South Tibetan Detachment and the Manaslu leucogranite: A structural reinterpretation and restoration of the Annapurna-Manaslu Himalaya, Nepal. The Journal of Geology, 111(5), 505-523.

Searle, M. P. (1999). Emplacement of Himalayan leucogranites by magma injection along giant sill complexes: examples from the Cho Oyu, Gyachung Kang and Everest leucogranites (Nepal Himalaya). Journal of Asian Earth Sciences, 17(5-6), 773-783.

Searle, M. P. (2010). Low-angle normal faults in the compressional Himalayan orogen; Evidence from the Annapurna–Dhaulagiri Himalaya, Nepal. Geosphere, 6(4), 296-315.

Searle, M., Avouac, J. P., Elliott, J., and Dyck, B. (2017). Ductile shearing to brittle thrusting along the Nepal Himalaya: Linking Miocene channel flow and critical wedge tectonics to 25th April 2015 Gorkha earthquake. Tectonophysics, 714, 117-124.

Searle, M. P., Cottle, J. M., Streule, M. J., and Waters, D. J. (2009). Crustal melt granites and migmatites along the Himalaya: melt source, segregation, transport and granite emplacement mechanisms. Transactions of the Royal Society of Edinburgh, 100, 219-233.

Searle, M. P., Law, R. D., Godin, L., Larson, K. P., Streule, M. J., Cottle, J. M., and Jessup, M. J. (2008). Defining the Himalayan main central thrust in Nepal. Journal of the Geological Society, 165(2), 523-534.

Searle, M. P., and Rex, A. J. (1989). Thermal model for the Zanskar Himalaya. Journal of Metamorphic Geology, 7(1), 127-134.

Searle, M. P., Simpson, R. L., Law, R. D., Parrish, R. R., and Waters, D. J. (2003). The structural geometry, metamorphic and magmatic evolution of the Everest massif, High Himalaya of Nepal–South Tibet. Journal of the Geological Society, 160(3), 345-366.

Simpson, C., and De Paor, D. G. (1997). Practical analysis of general shear zones using the porphyroclast hyperbolic distribution method: an example from the Scandinavian Caledonides. In Evolution of geological structures in micro-to macro-scales (pp. 169-184). Springer, Dordrecht.

Skemer, P., and Karato, S. I. (2007). Reply to Comment on “The Misorientation index: Development of a new method for calculating the strength of lattice-preferred orientation”. Tectonophysics, 441(1-4), 119-120.

Skemer, P., Katayama, I., Jiang, Z., and Karato, S. I. (2005). The misorientation index: Development of a new method for calculating the strength of lattice-preferred orientation. Tectonophysics, 411(1-4), 157-167.

Smith, S. A. F., Di Toro, G., Kim, S., Ree, J. H., Nielsen, S., Billi, A., and Spiess, R. (2013). Coseismic recrystallization during shallow earthquake slip. Geology, 41(1), 63-66.

Song, W. J., and Ree, J. H. (2007). Effect of mica on the grain size of dynamically recrystallized quartz in a quartz–muscovite mylonite. Journal of Structural Geology, 29(12), 1872-1881.

Soucy La Roche, R., Godin, L., Cottle, J. M., and Kellett, D. A. (2018a). Preservation of the early evolution of the Himalayan middle crust in foreland klippen: insights from the Karnali klippe, west Nepal. Tectonics, 37(5), 1161-1193.

Soucy La Roche, R., Godin, L., Cottle, J. M., and Kellett, D. A. (2018b). Tectonometamorphic evolution of the tip of the Himalayan metamorphic core in the Jajarkot klippe, west Nepal. Journal of Metamorphic Geology, 37(2), 239-269.

Spanos, D., Xypolias, P., and Koukouvelas, I. (2015). Vorticity analysis in calcite tectonites: An example from the Attico-Cycladic massif (Attica, Greece). Journal of Structural Geology, 80, 120-132.

Spiers, C. J. (1982). The development of deformation textures in calcite rocks [Ph.D. thesis]. London, University of London, 251 p.

Spiers, C. J., and Rutter, E. H. (1984). A calcite twinning palaeopiezometer. In: Progress in Experimental Petrology. Natural Environment Research Council publication series, 25, 241-245.

Srivastava, P., and Mitra, G. (1994). Thrust geometries and deep structure of the outer and lesser Himalaya, Kumaon and Garhwal (India): Implications for evolution of the Himalayan fold-and-thrust belt. Tectonics, 13(1), 89-109.

Stampfli, G. M., and Borel, G. D. (2002). A plate tectonic model for the Paleozoic and Mesozoic constrained by dynamic plate boundaries and restored synthetic oceanic isochrons. Earth and Planetary Science Letters, 196(1-2), 17-33.

Starnes, J. K., Long, S. P., Gordon, S. M., Zhang, J., and Soignard, E. (2020). Using quartz fabric intensity parameters to delineate strain patterns across the Himalayan Main Central thrust. Journal of Structural Geology, 131, 103941.

Stipp, M., Stünitz, H., Heilbronner, R., and Schmid, S. M. (2002). The eastern Tonale fault zone: a 'natural laboratory'for crystal plastic deformation of quartz over a temperature range from 250 to 700 C. Journal of Structural Geology, 24(12), 1861-1884.

Stipp, M., and Tullis, J. (2003). The recrystallized grain size piezometer for quartz. Geophysical Research Letters, 30(21).

Streule, M. J., Searle, M. P., Waters, D. J., and Horstwood, M. S. (2010). Metamorphism, melting, and channel flow in the Greater Himalayan Sequence and Makalu leucogranite: Constraints from thermobarometry, metamorphic modeling, and U-Pb geochronology. Tectonics, 29(5).

Sundell, K. E., Taylor, M. H., Styron, R. H., Stockli, D. F., Kapp, P., Hager, C., ... and Ding, L. (2013). Evidence for constriction and Pliocene acceleration of east-west extension in the North Lunggar rift region of west central Tibet. Tectonics, 32(5), 1454-1479.

Toy, V. G., Prior, D. J., and Norris, R. J. (2008). Quartz fabrics in the Alpine Fault mylonites: Influence of pre-existing preferred orientations on fabric development during progressive uplift. Journal of Structural Geology, 30(5), 602-621.

Trimby, P. W., and Prior, D. J. (1999). Microstructural imaging techniques: a comparison between light and scanning electron microscopy. Tectonophysics, 303(1-4), 71-81.

Tripathy, V., and Saha, D. (2015). Inversion of calcite twin data, paleostress reconstruction and multiphase weak deformation in cratonic interior–Evidence from the Proterozoic Cuddapah basin, India. Journal of Structural Geology, 77, 62-81.

Truesdell, C. (1954). The Kinematics of Vorticity. Indiana University Press, Bloomington.

Truesdell, C. (2018). The kinematics of vorticity. Courier Dover Publications, 232 p.

Tullis, J., and Wenk, H. R. (1994). Effect of muscovite on the strength and lattice preferred orientations of experimentally deformed quartz aggregates. Materials Science and Engineering: A, 175(1-2), 209-220.

Turner, F.J. (1949). Preferred orientation of calcite in Yule marble. American Journal of Science, 247(9), 593-621.

Turner F.J. (1968). Metamorphic petrology, mineralogical and field aspects. McGraw Hill, New York.

Upreti, B. N., Rai, S. M, Sakai, H., Koirala, D. R., Takigami, Y. (2003). Early Proterozoic granite of the Taplejung window, far eastern lesser Nepal Himalaya. Journal of Nepal Geological Society, 28, 9-18.

Valli, F., Arnaud, N., Leloup, P. H., Sobel, E. R., Mahéo, G., Lacassin, R., ... and Xu, Z. (2007). Twenty million years of continuous deformation along the Karakorum fault, western Tibet: A thermochronological analysis. Tectonics, 26(4).

Vannay, J. C., and Grasemann, B. (2001). Himalayan inverted metamorphism and syn-convergence extension as a consequence of a general shear extrusion. Geological Magazine, 138(3), 253-276.

Vannay, J. C., and Hodges, K. V. (1996). Tectonometamorphic evolution of the Himalayan metamorphic core between the Annapurna and Dhaulagiri, central Nepal. Journal of Metamorphic Geology, 14(5), 635-656.

Villa, I. M. (1998). Isotopic closure. Terra Nova, 10, 42–47.

Villa, I. M. (2006). From nanometer to megameter: Isotopes, atomic-scale processes, and continent-scale tectonic models. Lithos, 87(3-4), 155-173.

Villa, I. M., Bucher, S., Bousquet, R., Kleinhanns, I. C., and Schmid, S. M. (2014). Dating polygenetic metamorphic assemblages along a transect across the Western Alps. Journal of Petrology, 55(4), 803-830.

Visonà, D., and Lombardo, B. (2002). Two-mica and tourmaline leucogranites from the Everest–Makalu region (Nepal–Tibet). Himalayan leucogranite genesis by isobaric heating?. Lithos, 62(3-4), 125-150.

Visonà, D., Carosi, R., Montomoli, C., Tiepolo, M., and Peruzzo, L. (2012). Miocene andalusite leucogranite in central-east Himalaya (Everest–Masang Kang area): low-pressure melting during heating. Lithos, 144, 194-208.

Waldron, J. W., and Wallace, K. D. (2007). Objective fitting of ellipses in the centre-to-centre (Fry) method of strain analysis. Journal of Structural Geology, 29(9), 1430-1444.

Wallis, S. R. (1992). Vorticity analysis in a metachert from the Sanbagawa Belt, SW Japan. Journal of Structural Geology, 14(3), 271-280.

Wallis, S. (1995). Vorticity analysis and recognition of ductile extension in the Sanbagawa belt, SW Japan. Journal of Structural Geology, 17(8), 1077-1093.

Wallis, S., Platt, J. P., and Knott, S. D. (1993). Recognition of syn-convergence extension in accretionary wedges with examples from the Calabrian Arc and the Eastern Alps. American Journal of Science, 293(5), 463-494.

Walters, J. B., and Kohn, M. J. (2017). Protracted thrusting followed by late rapid cooling of the Greater Himalayan Sequence, Annapurna Himalaya, Central Nepal: insights from titanite petrochronology. Journal of Metamorphic Geology, 35(8), 897-917.

Wang, J. M., Rubatto, D., and Zhang, J. J. (2015). Timing of partial melting and cooling across the Greater Himalayan Crystalline Complex (Nyalam, Central Himalaya): In-sequence thrusting and its implications. Journal of Petrology, 56(9), 1677-1702.

Wang, J. M., Zhang, J. J., Liu, K., Zhang, B., Wang, X. X., Rai, S., and Scheltens, M. (2016). Spatial and temporal evolution of tectonometamorphic discontinuities in the central Himalaya: Constraints from P–T paths and geochronology. Tectonophysics, 679, 41-60.

Warren, C. J., Singh, A. K., Roberts, N. M., Regis, D., Halton, A. M., and Singh, R. B. (2014). Timing and conditions of peak metamorphism and cooling across the Zimithang Thrust, Arunachal Pradesh, India. Lithos, 200, 94-110.

Waters, D. J. (2019). Metamorphic constraints on the tectonic evolution of the High Himalaya in Nepal: the art of the possible. Geological Society, London, Special Publications, 483(1), 325-375.

Waters, D. J., Law, R. D., Searle, M. P., and Jessup, M. J. (2019). Structural and thermal evolution of the South Tibetan Detachment shear zone in the Mt Everest region, from the 1933 sample collection of LR Wager. Geological Society, London, Special Publications, 478(1), 335-372.

Webb, A. A. G., Yin, A., Harrison, T. M., Célérier, J., and Burgess, W. P. (2007). The leading edge of the Greater Himalayan Crystalline complex revealed in the NW Indian Himalaya: Implications for the evolution of the Himalayan orogen. Geology, 35(10), 955-958.

Weinberg, R. F. (2016). Himalayan leucogranites and migmatites: nature, timing and duration of anatexis. Journal of Metamorphic Geology, 34(8), 821-843.

Wells, R. K., Holyoke III, C. W., Newman, J., and Kronenberg, A. (2019). Lattice-preferred orientation development in experimental and natural fine-grained dolomite shear zones. Journal of Structural Geology, 128, 103874.

Wenk, H. R., Takeshita, T., Bechler, E., Erskine, B. G., and Matthies, S. (1987). Pure shear and simple shear calcite textures. Comparison of experimental, theoretical and natural data. Journal of Structural Geology, 9(5-6), 731-745.

Xu, Z., Wang, Q., Pêcher, A., Liang, F., Qi, X., Cai, Z., ... and Cao, H. (2013). Orogen-parallel ductile extension and extrusion of the Greater Himalaya in the late Oligocene and Miocene. Tectonics, 32(2), 191-215.

Xypolias, P. (2009). Some new aspects of kinematic vorticity analysis in naturally deformed quartzites. Journal of Structural Geology, 31(1), 3-10.

Xypolias, P. (2010). Vorticity analysis in shear zones: a review of methods and applications. Journal of Structural Geology, 32(12), 2072-2092.

Xypolias, P., Chatzaras, V., Beane, R., and Papadopoulou, S. (2013). Heterogeneous constrictional deformation in a ductile shear zone resulting from the transposition of a lineation-parallel fold. Journal of Structural Geology, 52, 44-59.

Yakymchuk, C., and Godin, L. (2012). Coupled role of deformation and metamorphism in the construction of inverted metamorphic sequences: an example from far-northwest Nepal. Journal of Metamorphic Geology, 30(5), 513-535.

Yin, A. (2006). Cenozoic tectonic evolution of the Himalayan orogen as constrained by along-strike variation of structural geometry, exhumation history, and foreland sedimentation. Earth-Science Reviews, 76(1-2), 1-131.

APPENDIX - Electron microprobe analyses

Table A.1. Electron microprobe analyses of biotite (wt% oxides) and atoms per formula unit (a.p.f.u.) recalculated based on 11 oxygens (sample D20-10-69). Abbreviation: *b.d.l.*, below detection limit; $Total_{c}$, total recorrected; Al_{T}, Tetrahedral coordination of aluminum; Al_{O}, Octahedral coordination of aluminum.

	D69// Bt1	D69// Bt2	D69// Bt3	D69// Bt4	D69// Bt5	D69// Bt6	D69// Bt7	D69// Bt8	D69// Bt9	D69// Bt10	D69// Bt31	D69// Bt32
SiO_2	38.05	37.90	38.16	37.73	37.58	37.80	37.84	37.83	38.11	37.54	37.92	38.11
TiO_2	1.98	2.08	2.40	2.17	2.10	2.04	2.21	1.88	2.15	2.18	2.43	2.34
Al_2O_3	17.03	17.09	16.63	17.34	16.96	17.45	17.35	17.47	17.29	17.30	16.95	16.68
FeO	11.89	12.02	11.90	12.06	11.56	11.85	11.86	11.96	11.70	11.85	11.60	11.76
MnO	*b.d.l.*	0.03	*b.d.l.*	*b.d.l.*	0.04	*b.d.l.*	0.02	*b.d.l.*	*b.d.l.*	0.05	0.02	0.03
MgO	15.56	15.51	15.47	15.32	15.33	15.04	15.31	15.30	15.32	15.35	15.15	15.19
CaO	0.11	0.11	0.03	0.15	0.07	0.15	*b.d.l.*	0.06	0.03	0.01	0.10	0.06
Na_2O	0.02	0.09	0.05	0.07	0.07	0.10	0.08	0.09	0.09	0.06	0.11	0.03
K_2O	10.40	10.09	10.26	10.35	10.32	10.24	10.05	10.31	10.27	10.37	10.11	10.11
BaO	0.13	0.13	0.12	0.17	0.15	0.12	0.11	0.11	0.06	0.07	0.17	0.07
F^-	0.53	0.60	0.46	0.35	0.31	0.30	0.49	0.53	0.45	0.43	0.51	0.49
Cl^-	0.02	0.02	0.03	0.02	0.03	0.02	0.02	0.02	0.02	0.02	0.03	0.02
H_2O	3.81	3.77	3.84	3.90	3.87	3.90	3.82	3.80	3.85	3.84	3.80	3.80
Total	99.54	99.44	99.35	99.64	98.39	99.01	99.15	99.37	99.32	99.06	98.88	98.68
$Total_{c.}$	99.31	99.19	99.15	99.49	98.25	98.88	98.94	99.14	99.13	98.87	98.66	98.47
Si	2.806	2.798	2.817	2.782	2.800	2.796	2.794	2.794	2.807	2.781	2.809	2.827
Al_{T}	1.194	1.202	1.184	1.218	1.200	1.204	1.206	1.206	1.193	1.219	1.191	1.173
Ti	0.110	0.115	0.133	0.120	0.118	0.114	0.123	0.104	0.119	0.121	0.135	0.130
Al_{O}	0.287	0.284	0.263	0.288	0.289	0.318	0.304	0.314	0.308	0.292	0.289	0.285
Fe^2	0.733	0.742	0.735	0.743	0.720	0.734	0.732	0.739	0.721	0.734	0.719	0.730
Mn	*b.d.l.*	0.002	*b.d.l.*	*b.d.l.*	0.003	*b.d.l.*	0.001	*b.d.l.*	*b.d.l.*	0.003	0.001	0.002
Mg	1.711	1.706	1.703	1.684	1.703	1.659	1.686	1.685	1.682	1.695	1.673	1.680
Ca	0.009	0.009	0.003	0.012	0.006	0.012	*b.d.l.*	0.005	0.003	0.001	0.008	0.004
Na	0.003	0.013	0.008	0.011	0.011	0.014	0.011	0.013	0.013	0.008	0.015	0.004
K	0.978	0.950	0.966	0.974	0.981	0.966	0.947	0.971	0.965	0.980	0.955	0.957
Ba	0.004	0.004	0.003	0.005	0.004	0.004	0.003	0.003	0.002	0.002	0.005	0.002
F	0.122	0.140	0.106	0.081	0.073	0.070	0.114	0.124	0.104	0.100	0.119	0.116
Cl	0.003	0.003	0.003	0.003	0.004	0.003	0.003	0.003	0.003	0.002	0.003	0.003
H	1.875	1.857	1.890	1.916	1.922	1.927	1.884	1.874	1.894	1.898	1.878	1.882
xAl	0.14	0.14	0.13	0.14	0.14	0.16	0.15	0.16	0.15	0.15	0.14	0.14
Mg/(Mg+ Fe)	0.70	0.70	0.70	0.69	0.70	0.69	0.70	0.70	0.70	0.70	0.70	0.70

Table A.1

	D69//Bt33	D69//Bt34	D69//Bt35	D69//Bt36	D69//Bt37	D69//Bt38	D69//Bt39	D69//Bt40	D69//Bt41	D69//Bt42	D69//Bt43	D69//Bt44
SiO_2	37.82	37.82	37.84	37.80	37.55	37.64	37.69	37.76	37.96	37.69	37.85	37.78
TiO_2	1.73	1.99	2.31	2.00	1.85	2.03	2.30	2.36	2.26	2.16	2.10	1.95
Al_2O_3	17.60	17.16	17.31	16.97	17.08	17.07	16.96	17.00	17.36	17.18	17.34	17.26
FeO	12.14	11.92	11.55	11.98	12.06	11.89	11.67	12.01	11.87	11.60	11.64	11.65
MnO	0.02	0.01	*b.d.l.*	*b.d.l.*	*b.d.l.*	*b.d.l.*	0.03	*b.d.l.*	*b.d.l.*	0.05	0.01	*b.d.l.*
MgO	15.27	15.43	14.95	15.11	15.34	15.07	15.03	15.17	15.32	15.42	15.21	15.38
CaO	0.10	0.02	*b.d.l.*	*b.d.l.*	0.06	0.05	0.18	0.19	0.04	0.07	0.05	0.03
Na_2O	0.09	0.08	0.11	0.03	0.05	0.06	0.06	0.05	0.09	0.09	0.05	0.06
K_2O	10.26	10.30	10.20	10.18	10.22	10.20	10.38	10.31	10.27	10.26	10.19	10.54
BaO	0.07	0.10	0.11	0.11	0.07	0.13	0.16	0.14	0.11	0.11	0.16	0.08
F^-	0.42	0.48	0.45	0.53	0.47	0.54	0.47	0.55	0.28	0.36	0.31	0.34
Cl^-	0.03	0.02	0.02	0.03	0.04	0.03	0.03	0.03	0.02	0.03	0.03	0.03
H_2O	3.86	3.82	3.82	3.77	3.79	3.76	3.80	3.79	3.94	3.87	3.90	3.88
Total	99.40	99.13	98.66	98.51	98.59	98.49	98.76	99.35	99.53	98.89	98.83	98.97
$Total_{c.}$	99.22	98.92	98.47	98.28	98.38	98.25	98.56	99.11	99.41	98.73	98.70	98.82
Si	2.791	2.799	2.806	2.815	2.797	2.805	2.802	2.794	2.793	2.792	2.802	2.799
Al_{T}	1.209	1.201	1.194	1.185	1.204	1.195	1.198	1.206	1.207	1.208	1.198	1.202
Ti	0.096	0.111	0.129	0.112	0.104	0.114	0.129	0.131	0.125	0.120	0.117	0.109
Al_{O}	0.322	0.296	0.318	0.304	0.296	0.305	0.289	0.276	0.298	0.292	0.314	0.305
Fe^2	0.749	0.738	0.716	0.746	0.752	0.741	0.725	0.743	0.730	0.719	0.721	0.721
Mn	0.001	*b.d.l.*	*b.d.l.*	*b.d.l.*	*b.d.l.*	*b.d.l.*	0.002	*b.d.l.*	*b.d.l.*	0.003	0.001	*b.d.l.*
Mg	1.680	1.702	1.652	1.677	1.703	1.674	1.665	1.674	1.680	1.703	1.679	1.699
Ca	0.008	0.001	*b.d.l.*	*b.d.l.*	0.005	0.004	0.015	0.015	0.004	0.006	0.004	0.002
Na	0.013	0.011	0.015	0.004	0.008	0.009	0.009	0.008	0.013	0.013	0.007	0.008
K	0.966	0.973	0.965	0.967	0.971	0.970	0.985	0.973	0.964	0.969	0.962	0.996
Ba	0.002	0.003	0.003	0.003	0.002	0.004	0.005	0.004	0.003	0.003	0.005	0.002
F	0.098	0.111	0.105	0.124	0.111	0.128	0.110	0.128	0.065	0.085	0.072	0.080
Cl	0.003	0.002	0.003	0.004	0.005	0.004	0.004	0.004	0.003	0.004	0.004	0.003
H	1.899	1.887	1.892	1.871	1.884	1.869	1.886	1.869	1.932	1.912	1.924	1.917
xAl	0.16	0.15	0.16	0.15	0.15	0.15	0.14	0.14	0.15	0.15	0.16	0.15
Mg/(Mg+Fe)	0.69	0.70	0.70	0.69	0.69	0.69	0.70	0.69	0.70	0.70	0.70	0.70

Table A.1

	D69//Bt45	D69//Bt46	D69//Bt47	D69//Bt48	D69//Bt49	D69//Bt50	D69//Bt65	D69//Bt66	D69//Bt67	D69//Bt68	D69//Bt69	D69//Bt70
SiO_2	38.26	37.78	37.82	37.97	38.22	37.74	37.86	37.58	38.07	37.45	37.67	38.05
TiO_2	2.04	2.02	2.07	2.31	2.53	2.32	2.22	2.05	2.09	2.22	2.17	2.06
Al_2O_3	17.48	17.43	17.46	17.00	16.91	17.43	17.06	16.82	17.30	17.33	17.24	17.45
FeO	11.79	11.58	11.87	11.65	11.93	11.90	11.90	11.43	11.78	11.90	11.96	12.08
MnO	*b.d.l.*	0.05	*b.d.l.*	0.01	*b.d.l.*	0.05	0.01	0.01	0.02	*b.d.l.*	0.03	0.01
MgO	15.43	15.50	15.49	15.16	15.21	15.09	15.45	15.58	15.82	15.50	15.57	15.36
CaO	0.03	0.12	0.11	0.24	0.17	0.13	*b.d.l.*	0.06	0.03	0.05	0.04	0.02
Na_2O	0.09	0.04	0.08	0.11	0.07	0.02	0.06	0.06	0.06	0.09	0.09	0.03
K_2O	10.28	10.31	10.40	10.01	10.28	10.44	10.32	10.04	10.18	10.25	10.19	10.26
BaO	0.09	0.13	0.08	0.11	0.09	0.11	0.12	0.12	0.11	0.10	0.09	0.09
F^-	0.48	0.57	0.40	0.58	0.40	0.43	0.41	0.39	0.46	0.41	0.43	0.56
Cl^-	0.02	0.03	0.02	0.03	0.03	0.02	0.02	0.03	0.03	0.03	0.02	0.02
H_2O	3.86	3.78	3.88	3.77	3.88	3.86	3.86	3.83	3.86	3.85	3.85	3.81
Total	99.85	99.36	99.67	98.94	99.71	99.54	99.29	98.00	99.83	99.18	99.34	99.80
$Total_{c.}$	99.64	99.11	99.50	98.69	99.53	99.35	99.11	97.83	99.63	99.00	99.15	99.56
Si	2.804	2.788	2.783	2.811	2.810	2.784	2.797	2.805	2.793	2.771	2.782	2.796
Al_{T}	1.196	1.212	1.217	1.189	1.190	1.216	1.203	1.195	1.207	1.229	1.218	1.204
Ti	0.112	0.112	0.115	0.129	0.140	0.129	0.123	0.115	0.115	0.123	0.120	0.114
Al_{O}	0.314	0.304	0.297	0.294	0.275	0.299	0.282	0.285	0.288	0.283	0.282	0.308
Fe^2	0.723	0.715	0.730	0.721	0.734	0.734	0.735	0.714	0.723	0.736	0.738	0.742
Mn	*b.d.l.*	0.003	*b.d.l.*	*b.d.l.*	*b.d.l.*	0.003	*b.d.l.*	0.001	0.002	*b.d.l.*	0.002	0.001
Mg	1.686	1.705	1.700	1.673	1.667	1.659	1.701	1.734	1.730	1.710	1.714	1.683
Ca	0.002	0.009	0.009	0.019	0.013	0.010	*b.d.l.*	0.005	0.003	0.004	0.003	0.001
Na	0.013	0.006	0.011	0.016	0.009	0.003	0.009	0.009	0.008	0.013	0.012	0.005
K	0.962	0.971	0.976	0.946	0.964	0.983	0.973	0.956	0.953	0.968	0.960	0.962
Ba	0.003	0.004	0.002	0.003	0.003	0.003	0.004	0.003	0.003	0.003	0.003	0.003
F	0.111	0.134	0.092	0.135	0.093	0.101	0.096	0.092	0.106	0.096	0.099	0.130
Cl	0.003	0.003	0.003	0.004	0.004	0.002	0.003	0.004	0.004	0.004	0.003	0.003
H	1.886	1.863	1.906	1.861	1.903	1.897	1.901	1.905	1.891	1.900	1.898	1.867
xAl	0.16	0.15	0.15	0.15	0.14	0.15	0.14	0.14	0.14	0.14	0.14	0.15
Mg/(Mg+Fe)	0.70	0.71	0.70	0.70	0.69	0.69	0.70	0.71	0.71	0.70	0.70	0.69

Table A.2. Electron microprobe analyses of biotite (wt% oxides) and atoms per formula unit (a.p.f.u.) recalculated based on 11 oxygens (sample D20-10-49). Abbreviation: *b.d.l.*, below detection limit; $Total_{c}$, total recorrected; Al_{T}, Tetrahedral coordination of aluminum; Al_{O}, Octahedral coordination of aluminum.

	49// Bt1	49// Bt2	49// Bt3	49// Bt4	49// Bt6	49// Bt7	49// Bt8	49// Bt9	49// Bt10	49// Bt11	49// Bt12	49// Bt13
SiO_2	35.92	35.24	35.40	35.31	35.71	35.60	35.48	35.25	36.18	36.74	36.15	34.86
TiO_2	3.12	3.00	2.94	3.14	3.23	3.42	3.29	3.03	2.94	3.42	3.01	3.04
Al_2O_3	16.15	15.96	16.02	15.57	15.83	15.83	15.81	16.00	17.10	15.84	17.73	15.49
FeO	21.14	21.39	21.28	21.34	21.27	21.24	21.19	21.57	19.75	20.30	18.70	20.39
MnO	0.00	0.00	0.03	0.01	0.04	0.00	0.00	0.00	0.08	0.00	0.03	0.06
MgO	9.31	9.15	9.22	9.32	9.21	9.06	9.28	9.23	8.15	8.55	7.76	9.47
CaO	0.04	0.00	0.01	0.03	0.02	0.00	0.02	0.03	0.01	0.03	0.00	0.00
Na_2O	0.07	0.06	0.06	0.06	0.03	0.04	0.05	0.06	0.08	0.06	0.07	0.05
K_2O	9.75	9.95	9.91	10.04	10.09	9.88	9.76	10.00	9.84	9.72	10.09	9.76
BaO	0.19	0.17	0.23	0.24	0.17	0.22	0.20	0.17	0.19	0.21	0.29	0.27
F^-	0.31	0.26	0.27	0.40	0.35	0.33	0.34	0.38	0.37	0.26	0.27	0.34
Cl^-	0.01	0.00	0.01	0.00	0.01	0.00	0.00	0.00	0.00	0.00	0.01	0.00
H_2O	3.75	3.73	3.73	3.66	3.72	3.72	3.70	3.68	3.70	3.77	3.74	3.63
Total	99.75	98.91	99.10	99.12	99.66	99.31	99.12	99.40	98.39	98.90	97.86	97.36
$Total_{c.}$	99.62	98.80	98.99	98.95	99.52	99.17	98.98	99.25	98.23	98.80	97.74	97.22
Si	2.762	2.745	2.750	2.751	2.759	2.758	2.752	2.737	2.799	2.832	2.800	2.753
Al_{T}	1.238	1.255	1.250	1.249	1.241	1.242	1.248	1.263	1.201	1.169	1.200	1.247
Ti	0.180	0.176	0.172	0.184	0.188	0.199	0.192	0.177	0.171	0.198	0.175	0.181
Al_{O}	0.226	0.211	0.217	0.180	0.201	0.203	0.198	0.201	0.358	0.270	0.418	0.195
Fe^2	1.360	1.393	1.382	1.390	1.374	1.376	1.375	1.400	1.278	1.309	1.211	1.347
Mn	*b.d.l.*	*b.d.l.*	0.002	0.001	0.002	*b.d.l.*	*b.d.l.*	*b.d.l.*	0.005	*b.d.l.*	0.002	0.004
Mg	1.068	1.063	1.068	1.083	1.060	1.046	1.074	1.069	0.940	0.982	0.896	1.115
Ca	0.004	*b.d.l.*	0.001	0.002	0.002	*b.d.l.*	0.002	0.002	0.001	0.002	*b.d.l.*	*b.d.l.*
Na	0.011	0.010	0.009	0.009	0.004	0.006	0.008	0.009	0.012	0.009	0.011	0.008
K	0.956	0.989	0.982	0.998	0.994	0.976	0.966	0.991	0.971	0.956	0.997	0.983
Ba	0.006	0.005	0.007	0.007	0.005	0.007	0.006	0.005	0.006	0.006	0.009	0.009
F	0.074	0.064	0.066	0.099	0.084	0.080	0.084	0.093	0.091	0.063	0.066	0.085
Cl	0.001	0.001	0.001	*b.d.l.*	0.001	*b.d.l.*	*b.d.l.*	*b.d.l.*	0.001	*b.d.l.*	0.001	*b.d.l.*
H	1.925	1.936	1.933	1.901	1.915	1.920	1.916	1.907	1.909	1.937	1.933	1.915
xAl	1.46	1.47	1.47	1.43	1.44	1.44	1.45	1.46	1.56	1.44	1.62	1.44
Mg/ (Mg+Fe)	0.44	0.43	0.44	0.44	0.44	0.43	0.44	0.43	0.42	0.43	0.43	0.45

Appendix

Table A2.

	49// Bt14	49// Bt15	49// Bt16	49// Bt17	49// Bt18	49// Bt19	49// Bt20	49// Bt21	49// Bt22	49// Bt41	49// Bt42	49// Bt43
SiO_2	35.54	35.43	35.35	34.79	35.14	35.37	35.27	35.26	35.29	35.24	35.24	34.34
TiO_2	3.12	3.14	3.08	3.17	3.06	3.25	3.30	3.12	3.26	3.19	3.10	3.03
Al_2O_3	15.84	15.82	15.76	15.72	15.53	15.80	15.78	15.55	15.48	15.54	15.80	15.52
FeO	20.66	20.95	20.70	20.70	21.71	21.40	21.43	21.42	21.06	20.86	20.83	21.68
MnO	*b.d.l.*	0.01	*b.d.l.*	0.03	*b.d.l.*	0.05	0.01	*b.d.l.*	0.08	0.03	0.07	0.02
MgO	9.40	9.41	9.44	9.11	9.14	9.15	9.15	9.09	8.96	9.24	9.32	8.99
CaO	0.02	*b.d.l.*	*b.d.l.*	*b.d.l.*	*b.d.l.*	0.01	0.01	*b.d.l.*	*b.d.l.*	*b.d.l.*	0.01	0.01
Na_2O	0.02	0.04	0.01	0.04	0.06	0.08	0.02	0.05	0.05	0.03	0.01	0.05
K_2O	9.82	9.85	9.96	9.93	9.90	10.20	9.80	9.92	9.83	9.83	9.76	9.86
BaO	0.27	0.25	0.24	0.19	0.19	0.26	0.23	0.23	0.22	0.28	0.16	0.24
F^-	0.34	0.38	0.23	0.47	0.29	0.25	0.27	0.17	0.34	0.42	0.31	0.31
Cl^-	0.01	*b.d.l.*	*b.d.l.*	*b.d.l.*	*b.d.l.*	*b.d.l.*	0.01	*b.d.l.*	0.01	*b.d.l.*	*b.d.l.*	0.01
H_2O	3.69	3.68	3.73	3.58	3.70	3.75	3.72	3.75	3.66	3.63	3.69	3.63
Total	98.72	98.96	98.50	97.71	98.73	99.58	98.99	98.54	98.25	98.28	98.31	97.68
$Total_{c.}$	98.57	98.80	98.40	97.51	98.61	99.47	98.87	98.47	98.10	98.10	98.18	97.54
Si	2.764	2.754	2.757	2.744	2.749	2.743	2.745	2.758	2.767	2.761	2.754	2.724
Al_{T}	1.236	1.246	1.243	1.256	1.251	1.257	1.255	1.242	1.233	1.239	1.246	1.276
Ti	0.182	0.184	0.181	0.188	0.180	0.190	0.193	0.184	0.192	0.188	0.182	0.181
Al_{O}	0.215	0.203	0.206	0.205	0.182	0.187	0.193	0.192	0.198	0.196	0.209	0.175
Fe^2	1.343	1.362	1.351	1.365	1.421	1.388	1.395	1.401	1.381	1.367	1.361	1.438
Mn	*b.d.l.*	0.001	*b.d.l.*	0.002	*b.d.l.*	0.004	*b.d.l.*	*b.d.l.*	0.005	0.002	0.005	0.002
Mg	1.089	1.090	1.098	1.071	1.067	1.058	1.062	1.060	1.047	1.079	1.085	1.063
Ca	0.002	*b.d.l.*	*b.d.l.*	*b.d.l.*	*b.d.l.*	0.001	0.001	*b.d.l.*	*b.d.l.*	*b.d.l.*	0.001	0.001
Na	0.002	0.007	0.001	0.006	0.010	0.013	0.004	0.007	0.008	0.005	0.001	0.008
K	0.974	0.976	0.991	0.999	0.989	1.009	0.973	0.990	0.983	0.982	0.973	0.998
Ba	0.008	0.008	0.007	0.006	0.006	0.008	0.007	0.007	0.007	0.009	0.005	0.007
F	0.084	0.094	0.057	0.118	0.071	0.061	0.067	0.042	0.085	0.103	0.078	0.078
Cl	0.001	*b.d.l.*	*b.d.l.*	*b.d.l.*	*b.d.l.*	*b.d.l.*	0.001	*b.d.l.*	0.001	*b.d.l.*	*b.d.l.*	0.001
H	1.915	1.906	1.943	1.882	1.929	1.939	1.932	1.958	1.914	1.897	1.922	1.921
xAl	1.45	1.45	1.45	1.46	1.43	1.44	1.45	1.43	1.43	1.44	1.46	1.45
Mg/ (Mg+Fe)	0.45	0.45	0.45	0.44	0.43	0.43	0.43	0.43	0.43	0.44	0.44	0.43

Table A2.

	49//Bt44	49//Bt45	49//Bt46	49//Bt47	49//Bt48	49//Bt102	49//Bt103	49//Bt104	49//Bt105	49//Bt106
SiO_2	35.21	35.06	35.34	35.37	35.72	35.51	35.26	35.13	35.15	35.33
TiO_2	3.30	3.27	3.27	3.36	3.17	3.08	2.95	3.16	3.15	3.22
Al_2O_3	15.26	15.52	15.62	15.69	16.29	15.70	15.66	15.57	15.75	15.71
FeO	21.22	21.73	21.08	21.07	20.98	21.45	21.49	21.61	21.27	21.06
MnO	0.01	0.01	0.02	*b.d.l.*	0.07	0.01	*b.d.l.*	0.03	0.04	0.05
MgO	9.15	9.20	9.17	9.10	8.89	9.09	9.32	9.08	9.20	9.35
CaO	*b.d.l.*	0.01	*b.d.l.*	*b.d.l.*	*b.d.l.*	*b.d.l.*	0.03	0.05	*b.d.l.*	0.01
Na_2O	0.07	0.05	0.08	0.05	0.04	0.02	0.09	0.05	0.07	0.06
K_2O	10.09	9.95	9.90	9.88	9.69	9.91	9.76	9.71	9.87	9.90
BaO	0.21	0.23	0.20	0.20	0.27	0.17	0.24	0.26	0.23	0.23
F^-	0.38	0.35	0.30	0.46	0.28	0.38	0.19	0.29	0.26	0.31
Cl^-	*b.d.l.*	0.01	*b.d.l.*	0.01	*b.d.l.*	*b.d.l.*	*b.d.l.*	0.01	*b.d.l.*	0.01
H_2O	3.64	3.67	3.70	3.63	3.74	3.67	3.75	3.69	3.72	3.71
Total	98.53	99.05	98.68	98.83	99.16	98.99	98.74	98.65	98.70	98.94
$Total_{c.}$	98.37	98.90	98.55	98.63	99.04	98.83	98.67	98.52	98.59	98.81
Si	2.760	2.738	2.757	2.756	2.763	2.764	2.752	2.749	2.745	2.749
Al_{T}	1.240	1.262	1.243	1.244	1.237	1.236	1.248	1.251	1.255	1.251
Ti	0.195	0.192	0.192	0.197	0.184	0.180	0.173	0.186	0.185	0.188
Al_{O}	0.170	0.166	0.193	0.197	0.249	0.204	0.192	0.185	0.194	0.191
Fe^2	1.391	1.420	1.375	1.373	1.358	1.396	1.402	1.414	1.389	1.371
Mn	*b.d.l.*	*b.d.l.*	0.001	*b.d.l.*	0.005	*b.d.l.*	*b.d.l.*	0.002	0.003	0.004
Mg	1.069	1.071	1.067	1.057	1.025	1.055	1.084	1.060	1.070	1.085
Ca	*b.d.l.*	0.001	*b.d.l.*	*b.d.l.*	*b.d.l.*	*b.d.l.*	0.003	0.004	*b.d.l.*	0.001
Na	0.010	0.007	0.012	0.008	0.007	0.004	0.014	0.008	0.010	0.009
K	1.009	0.991	0.986	0.982	0.957	0.984	0.972	0.969	0.983	0.983
Ba	0.006	0.007	0.006	0.006	0.008	0.005	0.007	0.008	0.007	0.007
F	0.094	0.087	0.075	0.113	0.070	0.093	0.046	0.072	0.063	0.076
Cl	0.001	0.001	*b.d.l.*	0.001	*b.d.l.*	*b.d.l.*	*b.d.l.*	0.001	*b.d.l.*	0.001
H	1.905	1.911	1.925	1.887	1.930	1.907	1.954	1.927	1.937	1.924
xAl	1.41	1.43	1.44	1.44	1.49	1.44	1.44	1.44	1.45	1.44
Mg/ (Mg+Fe)	0.44	0.43	0.44	0.44	0.43	0.43	0.44	0.43	0.44	0.44

Table A.3. Electron microprobe analyses of biotite (wt% oxides) and atoms per formula unit (a.p.f.u.) recalculated based on 11 oxygens (sample D18-10-64). Abbreviation: *b.d.l.*, below detection limit; $Total_{c}$, total recorrected; Al_{T}, Tetrahedral coordination of aluminum; Al_{O}, Octahedral coordination of aluminum.

	64// Bt1	64// Bt2	64// Bt3	64// Bt4	64// Bt5	64// Bt6	64// Bt7	64// Bt8	64// Bt9	64// Bt10	64// Bt11	64// Bt12	64// Bt13
SiO_2	35.99	35.96	35.84	35.78	35.78	36.02	36.15	35.91	35.94	36.16	35.42	35.80	35.72
TiO_2	3.43	3.38	3.39	3.46	3.15	3.15	3.27	3.30	3.33	3.25	3.28	3.22	3.28
Al_2O_3	14.97	15.28	15.26	15.34	15.61	15.15	15.08	15.62	15.27	15.47	15.33	15.67	15.39
FeO	22.09	21.87	21.87	21.46	21.41	21.65	21.35	21.92	21.72	21.58	21.70	21.90	21.92
MnO	*b.d.l.*	0.05	0.03	*b.d.l.*	0.07	0.04	*b.d.l.*	*b.d.l.*	*b.d.l.*	0.05	0.02	0.03	*b.d.l.*
MgO	8.93	8.77	8.84	8.68	8.70	8.90	8.98	8.74	8.79	8.86	8.62	8.69	8.52
CaO	*b.d.l.*	0.02	0.09	0.11	0.07	0.23	*b.d.l.*	0.02	0.01	*b.d.l.*	0.03	*b.d.l.*	*b.d.l.*
Na_2O	0.04	0.04	0.06	0.05	0.09	0.04	0.05	0.08	0.06	0.03	0.04	0.04	0.06
K_2O	10.22	9.96	10.05	9.97	9.82	9.84	10.06	10.04	9.95	9.97	9.84	10.14	9.92
BaO	0.16	0.16	0.19	0.26	0.19	0.19	0.13	0.13	0.19	0.19	0.26	0.15	0.18
F^-	0.29	0.33	0.23	0.41	0.36	0.35	0.19	0.31	0.33	0.36	0.24	0.16	0.27
Cl^-	*b.d.l.*	*b.d.l.*	*b.d.l.*	0.01	*b.d.l.*	*b.d.l.*	*b.d.l.*	*b.d.l.*	0.01	0.01	0.01	*b.d.l.*	0.01
H_2O	3.73	3.71	3.76	3.66	3.68	3.69	3.77	3.73	3.70	3.71	3.71	3.79	3.72
Total	99.86	99.54	99.61	99.19	98.93	99.26	99.03	99.80	99.30	99.63	98.49	99.57	98.98
$Total_{c.}$	99.74	99.40	99.51	99.02	98.78	99.11	98.95	99.67	99.16	99.47	98.38	99.51	98.86
Si	2.788	2.787	2.778	2.783	2.784	2.798	2.808	2.776	2.791	2.795	2.776	2.773	2.785
Al_{T}	1.212	1.213	1.222	1.217	1.216	1.202	1.192	1.225	1.209	1.205	1.224	1.227	1.215
Ti	0.154	0.184	0.172	0.190	0.217	0.185	0.188	0.199	0.189	0.204	0.192	0.204	0.200
Al_{O}	0.200	0.197	0.198	0.202	0.185	0.184	0.191	0.192	0.194	0.189	0.193	0.188	0.192
Fe^2	1.431	1.418	1.418	1.396	1.393	1.407	1.386	1.417	1.411	1.395	1.423	1.419	1.430
Mn	*b.d.l.*	0.004	0.002	*b.d.l.*	0.005	0.003	*b.d.l.*	*b.d.l.*	*b.d.l.*	0.003	0.001	0.002	*b.d.l.*
Mg	1.031	1.013	1.021	1.007	1.010	1.031	1.040	1.007	1.017	1.021	1.007	1.004	0.991
Ca	*b.d.l.*	0.002	0.008	0.009	0.006	0.019	*b.d.l.*	0.002	0.001	*b.d.l.*	0.003	*b.d.l.*	*b.d.l.*
Na	0.007	0.006	0.010	0.007	0.014	0.006	0.007	0.011	0.009	0.004	0.006	0.005	0.009
K	1.010	0.985	0.994	0.990	0.975	0.976	0.997	0.991	0.986	0.983	0.984	1.002	0.987
Ba	0.005	0.005	0.006	0.008	0.006	0.006	0.004	0.004	0.006	0.006	0.008	0.005	0.005
F	0.071	0.082	0.055	0.101	0.087	0.087	0.046	0.076	0.080	0.088	0.060	0.040	0.066
Cl	*b.d.l.*	*b.d.l.*	*b.d.l.*	0.001	*b.d.l.*	*b.d.l.*	*b.d.l.*	0.001	0.001	0.001	0.001	*b.d.l.*	0.001
H	1.928	1.918	1.945	1.897	1.912	1.913	1.954	1.924	1.919	1.911	1.940	1.960	1.933
xAl	0.08	0.09	0.09	0.10	0.11	0.09	0.09	0.10	0.09	0.10	0.10	0.10	0.10
Mg/ (Mg+Fe)	0.42	0.42	0.42	0.42	0.42	0.42	0.43	0.42	0.42	0.42	0.41	0.41	0.41

Table A.3

	64// Bt14	64// Bt15	64// Bt16	64// Bt17	64// Bt18	64// Bt19	64// Bt20	64// Bt21	64// Bt22	64// Bt23	64// Bt24	64// Bt25
SiO_2	35.46	35.92	35.31	35.08	35.13	35.46	35.54	35.07	34.89	35.31	35.49	35.30
TiO_2	3.23	3.24	3.25	3.11	3.18	3.35	3.19	3.26	3.22	3.33	3.33	3.36
Al_2O_3	15.35	15.44	15.65	15.59	15.55	15.70	15.85	14.78	15.15	14.83	15.37	15.43
FeO	21.54	21.84	21.78	22.00	22.19	21.70	21.36	21.68	21.42	21.78	21.74	21.73
MnO	0.03	0.01	0.03	0.04	0.01	*b.d.l.*	0.07	0.07	0.01	*b.d.l.*	0.05	0.06
MgO	8.92	8.65	8.56	8.64	8.81	8.64	8.72	8.99	8.95	8.60	8.64	8.70
CaO	0.01	0.02	0.02	0.01	0.04	*b.d.l.*	0.11	0.19	0.24	0.02	0.06	0.02
Na_2O	0.06	0.09	0.05	0.08	0.01	0.04	0.09	0.04	0.07	0.03	0.04	0.06
K_2O	10.03	10.06	9.83	9.71	9.68	9.92	9.47	8.64	8.85	9.85	10.12	10.01
BaO	0.17	0.16	0.22	0.17	0.24	0.12	0.18	0.23	0.21	0.21	0.19	0.19
F^-	0.31	0.40	0.16	0.30	0.28	0.35	0.23	0.34	0.29	0.31	0.14	0.37
Cl^-	*b.d.l.*	*b.d.l.*	*b.d.l.*	0.01	0.01	*b.d.l.*	*b.d.l.*	0.01	*b.d.l.*	*b.d.l.*	*b.d.l.*	0.01
H_2O	3.69	3.68	3.75	3.67	3.70	3.68	3.74	3.61	3.64	3.65	3.77	3.65
Total	98.79	99.50	98.61	98.42	98.83	98.97	98.56	96.92	96.94	97.93	98.96	98.90
$Total_{-c.}$	98.66	99.33	98.54	98.29	98.71	98.83	98.46	96.77	96.82	97.80	98.90	98.74
Si	2.770	2.787	2.762	2.755	2.749	2.763	2.770	2.783	2.767	2.788	2.770	2.760
Al_{-T}	1.230	1.213	1.238	1.245	1.251	1.237	1.230	1.217	1.233	1.212	1.230	1.240
Ti	0.184	0.199	0.206	0.198	0.183	0.205	0.226	0.165	0.183	0.169	0.185	0.182
Al_{-O}	0.190	0.189	0.191	0.184	0.187	0.196	0.187	0.195	0.192	0.198	0.196	0.198
Fe^2	1.407	1.417	1.425	1.445	1.453	1.414	1.392	1.439	1.420	1.438	1.419	1.421
Mn	0.002	0.001	0.002	0.003	0.001	*b.d.l.*	0.005	0.005	0.001	*b.d.l.*	0.003	0.004
Mg	1.040	1.001	0.998	1.012	1.028	1.004	1.013	1.063	1.058	1.012	1.005	1.015
Ca	0.001	0.001	0.001	0.001	0.004	*b.d.l.*	0.009	0.017	0.020	0.002	0.005	0.001
Na	0.008	0.013	0.008	0.012	0.002	0.006	0.014	0.006	0.010	0.005	0.007	0.009
K	1.000	0.996	0.981	0.973	0.967	0.986	0.942	0.875	0.895	0.992	1.008	0.999
Ba	0.005	0.005	0.007	0.005	0.007	0.004	0.005	0.007	0.006	0.007	0.006	0.006
F	0.076	0.097	0.040	0.075	0.070	0.085	0.056	0.085	0.073	0.078	0.034	0.093
Cl	0.001	*b.d.l.*	*b.d.l.*	0.001	0.002	*b.d.l.*	*b.d.l.*	0.002	*b.d.l.*	*b.d.l.*	*b.d.l.*	0.001
H	1.924	1.903	1.960	1.924	1.929	1.915	1.944	1.914	1.927	1.922	1.966	1.906
xAl	0.09	0.10	0.10	0.10	0.09	0.10	0.11	0.08	0.09	0.08	0.09	0.09
Mg/ (Mg+Fe)	0.43	0.41	0.41	0.41	0.41	0.42	0.42	0.43	0.43	0.41	0.42	0.42

Table A.3

	64// Bt26	64// Bt27	64// Bt28	64// Bt29	64// Bt30	64// Bt31	64// Bt32	64// Bt33	64// Bt34	64// Bt35	64// Bt36	64// Bt37
SiO_2	35.45	35.14	35.18	35.55	36.06	35.78	35.61	36.00	35.84	35.59	35.20	34.88
TiO_2	3.23	3.21	3.22	3.43	3.32	3.30	3.39	3.37	3.35	3.26	3.04	3.23
Al_2O_3	15.02	14.99	15.46	15.88	15.53	15.71	15.95	15.36	15.41	15.35	14.98	15.22
FeO	21.35	22.06	22.18	22.20	21.46	22.00	21.69	21.32	21.81	21.83	21.96	22.20
MnO	0.06	*b.d.l.*	0.05	0.05	0.01	0.06	0.06	0.01	0.12	*b.d.l.*	0.10	0.06
MgO	8.84	8.86	8.26	8.54	8.87	8.81	8.68	8.84	8.64	8.73	8.72	8.59
CaO	0.03	0.01	0.02	0.02	0.11	*b.d.l.*	*b.d.l.*	0.02	0.03	0.04	0.05	*b.d.l.*
Na_2O	0.06	0.02	0.05	0.08	0.06	0.01	0.08	0.03	0.07	0.05	0.04	0.07
K_2O	9.87	10.16	9.72	9.92	9.84	10.11	9.94	9.96	9.94	9.93	9.68	10.11
BaO	0.19	0.17	0.18	0.24	0.16	0.17	0.16	0.24	0.21	0.20	0.21	0.17
F^-	0.24	0.26	0.33	0.21	0.27	0.27	0.21	0.24	0.28	0.29	0.43	0.35
Cl^-	0.01	0.01	*b.d.l.*	*b.d.l.*	*b.d.l.*	0.01	*b.d.l.*	*b.d.l.*	*b.d.l.*	0.01	*b.d.l.*	*b.d.l.*
H_2O	3.70	3.69	3.65	3.78	3.75	3.75	3.78	3.75	3.73	3.70	3.59	3.63
Total	98.05	98.57	98.31	99.89	99.45	99.97	99.56	99.13	99.44	98.99	97.99	98.52
$Total_{c.}$	97.94	98.46	98.18	99.80	99.33	99.86	99.48	99.03	99.33	98.86	97.81	98.37
Si	2.788	2.764	2.768	2.750	2.788	2.764	2.756	2.794	2.782	2.777	2.781	2.750
Al_{T}	1.212	1.236	1.232	1.250	1.212	1.236	1.244	1.206	1.218	1.223	1.219	1.250
Ti	0.180	0.154	0.202	0.198	0.203	0.194	0.211	0.199	0.192	0.188	0.176	0.164
Al_{O}	0.191	0.190	0.191	0.200	0.193	0.192	0.198	0.197	0.195	0.191	0.181	0.192
Fe^2	1.404	1.452	1.460	1.437	1.387	1.421	1.404	1.384	1.416	1.424	1.451	1.463
Mn	0.004	*b.d.l.*	0.003	0.003	0.001	0.004	0.004	0.001	0.008	*b.d.l.*	0.007	0.004
Mg	1.037	1.039	0.969	0.984	1.023	1.015	1.002	1.022	1.000	1.016	1.027	1.010
Ca	0.002	0.001	0.002	0.002	0.009	*b.d.l.*	*b.d.l.*	0.002	0.003	0.004	0.004	*b.d.l.*
Na	0.009	0.003	0.007	0.012	0.009	0.002	0.012	0.005	0.011	0.007	0.006	0.010
K	0.991	1.020	0.976	0.979	0.971	0.996	0.981	0.986	0.984	0.988	0.975	1.017
Ba	0.006	0.005	0.006	0.007	0.005	0.005	0.005	0.007	0.006	0.006	0.006	0.005
F	0.059	0.065	0.082	0.050	0.066	0.066	0.050	0.059	0.068	0.072	0.106	0.088
Cl	0.001	0.001	*b.d.l.*	*b.d.l.*	*b.d.l.*	0.001	*b.d.l.*	*b.d.l.*	*b.d.l.*	0.001	*b.d.l.*	0.001
H	1.940	1.934	1.918	1.950	1.935	1.933	1.949	1.941	1.932	1.927	1.893	1.911
xAl	0.09	0.08	0.10	0.10	0.10	0.10	0.11	0.10	0.10	0.09	0.09	0.08
Mg/ (Mg+Fe)	0.43	0.42	0.40	0.41	0.42	0.42	0.42	0.43	0.41	0.42	0.41	0.41

Table A.3

	64// Bt38	64// Bt39	64// Bt40	64// Bt41	64// Bt42	64// Bt43	64// Bt44	64// Bt45	64// Bt46	64// Bt47	64// Bt48	64// Bt49
SiO_2	34.98	35.37	35.02	35.23	34.98	35.08	34.98	34.91	35.55	35.70	35.04	35.71
TiO_2	3.32	3.30	3.19	3.26	3.37	3.40	3.26	3.33	3.32	3.38	3.33	3.32
Al_2O_3	15.21	15.31	15.43	15.53	15.50	15.18	15.26	14.90	14.96	14.98	15.37	15.34
FeO	22.01	22.15	22.27	22.07	21.94	22.48	21.98	22.37	22.15	21.78	21.97	21.93
MnO	0.04	0.05	0.10	0.03	0.03	0.04	0.05	0.02	0.02	*b.d.l.*	0.03	*b.d.l.*
MgO	8.58	8.76	8.50	8.58	8.41	8.35	8.72	8.53	8.81	8.64	8.87	8.79
CaO	0.13	*b.d.l.*	*b.d.l.*	*b.d.l.*	*b.d.l.*	*b.d.l.*	*b.d.l.*	0.02	0.03	*b.d.l.*	0.04	*b.d.l.*
Na_2O	0.08	0.05	0.05	0.08	0.05	0.05	0.03	0.04	0.01	0.02	0.02	0.03
K_2O	9.68	10.04	9.97	9.91	10.01	9.79	9.92	9.82	9.83	9.87	9.80	10.15
BaO	0.17	0.15	0.15	0.14	0.19	0.16	0.22	0.19	0.22	0.25	0.25	0.19
F^-	0.23	0.32	0.31	0.30	0.26	0.13	0.20	0.33	0.36	0.28	0.25	0.35
Cl^-	*b.d.l.*	0.01	*b.d.l.*	*b.d.l.*	*b.d.l.*	*b.d.l.*	*b.d.l.*	*b.d.l.*	0.01	*b.d.l.*	0.01	*b.d.l.*
H_2O	3.70	3.69	3.67	3.69	3.69	3.75	3.71	3.63	3.66	3.70	3.70	3.69
Total	98.14	99.19	98.65	98.82	98.43	98.41	98.33	98.09	98.93	98.60	98.68	99.51
$Total_{-c.}$	98.05	99.06	98.52	98.69	98.32	98.36	98.24	97.96	98.78	98.48	98.57	99.36
Si	2.757	2.761	2.752	2.757	2.752	2.761	2.754	2.763	2.781	2.795	2.748	2.775
Al_{-T}	1.243	1.239	1.248	1.243	1.248	1.239	1.246	1.238	1.219	1.205	1.253	1.225
Ti	0.170	0.170	0.182	0.189	0.188	0.170	0.170	0.152	0.160	0.178	0.168	0.180
Al_{-O}	0.197	0.194	0.188	0.192	0.199	0.201	0.193	0.198	0.195	0.199	0.196	0.194
Fe^2	1.451	1.446	1.464	1.445	1.443	1.480	1.447	1.480	1.449	1.427	1.441	1.425
Mn	0.003	0.003	0.006	0.002	0.002	0.003	0.004	0.001	0.002	*b.d.l.*	0.002	*b.d.l.*
Mg	1.009	1.019	0.996	1.001	0.986	0.980	1.023	1.006	1.027	1.009	1.037	1.018
Ca	0.011	*b.d.l.*	*b.d.l.*	*b.d.l.*	*b.d.l.*	*b.d.l.*	*b.d.l.*	0.001	0.003	*b.d.l.*	0.003	*b.d.l.*
Na	0.013	0.008	0.008	0.012	0.008	0.007	0.005	0.006	0.001	0.003	0.003	0.005
K	0.974	1.000	1.000	0.989	1.005	0.983	0.997	0.992	0.981	0.986	0.980	1.006
Ba	0.005	0.005	0.005	0.004	0.006	0.005	0.007	0.006	0.007	0.008	0.008	0.006
F	0.056	0.078	0.076	0.075	0.064	0.032	0.049	0.082	0.090	0.069	0.063	0.086
Cl	*b.d.l.*	0.001	*b.d.l.*	*b.d.l.*	*b.d.l.*	*b.d.l.*	*b.d.l.*	*b.d.l.*	0.001	*b.d.l.*	0.001	*b.d.l.*
H	1.944	1.922	1.924	1.926	1.935	1.968	1.951	1.918	1.909	1.931	1.936	1.914
xAl	0.09	0.09	0.09	0.09	0.09	0.08	0.09	0.08	0.08	0.09	0.08	0.09
Mg/ (Mg+Fe)	0.41	0.41	0.41	0.41	0.41	0.40	0.41	0.41	0.42	0.41	0.42	0.42

Table A.3

	64//Bt50	64//Bt51	64//Bt52	64//Bt53	64//Bt54	64//Bt55	64//Bt56	64//Bt57	64//Bt58	64//Bt59
SiO_2	35.58	36.04	35.31	35.66	36.02	35.65	34.74	34.80	34.62	35.83
TiO_2	3.23	3.33	3.33	3.32	3.30	3.40	3.22	3.28	3.21	3.39
Al_2O_3	15.44	15.23	15.04	15.82	15.48	15.51	14.98	15.05	14.77	15.49
FeO	21.73	21.76	21.87	22.24	21.81	21.86	20.76	21.11	21.04	21.97
MnO	0.02	0.05	*b.d.l.*	0.05	0.12	0.01	0.06	0.09	0.19	0.02
MgO	8.71	8.85	8.82	8.79	8.80	8.75	9.59	9.43	9.79	8.98
CaO	0.03	*b.d.l.*	0.01	0.02	*b.d.l.*	*b.d.l.*	0.49	0.45	0.55	*b.d.l.*
Na_2O	0.06	0.06	0.04	0.06	*b.d.l.*	0.04	0.12	0.11	0.13	0.01
K_2O	9.81	9.87	9.97	9.93	10.13	10.01	7.20	7.56	6.32	10.00
BaO	0.13	0.21	0.17	0.13	0.18	0.17	0.18	0.20	0.14	0.20
F^-	0.35	0.27	0.29	0.30	0.19	0.18	0.24	0.25	0.33	0.28
Cl^-	0.01	*b.d.l.*	*b.d.l.*	0.01	0.01	0.01	0.01	*b.d.l.*	0.01	*b.d.l.*
H_2O	3.67	3.74	3.68	3.74	3.79	3.77	3.64	3.65	3.59	3.75
Total	98.77	99.42	98.54	100.06	99.83	99.36	95.21	96.00	94.68	99.92
$Total_{c.}$	98.62	99.30	98.42	99.93	99.75	99.28	95.11	95.90	94.54	99.80
Si	2.778	2.794	2.772	2.753	2.783	2.768	2.773	2.765	2.773	2.768
Al_T	1.222	1.206	1.228	1.247	1.217	1.232	1.227	1.235	1.227	1.232
Ti	0.199	0.186	0.163	0.192	0.193	0.188	0.183	0.175	0.167	0.178
Al_O	0.190	0.194	0.197	0.193	0.192	0.199	0.193	0.196	0.193	0.197
Fe^2	1.419	1.411	1.435	1.436	1.409	1.419	1.386	1.403	1.410	1.420
Mn	0.001	0.003	*b.d.l.*	0.003	0.008	0.001	0.004	0.006	0.013	0.002
Mg	1.013	1.023	1.032	1.012	1.014	1.013	1.141	1.117	1.169	1.034
Ca	0.003	*b.d.l.*	0.001	0.002	*b.d.l.*	*b.d.l.*	0.042	0.039	0.047	*b.d.l.*
Na	0.009	0.010	0.006	0.009	*b.d.l.*	0.006	0.018	0.018	0.021	0.001
K	0.977	0.976	0.998	0.978	0.999	0.992	0.733	0.767	0.645	0.986
Ba	0.004	0.006	0.005	0.004	0.005	0.005	0.006	0.006	0.004	0.006
F	0.086	0.067	0.073	0.073	0.046	0.045	0.062	0.064	0.083	0.069
Cl	0.001	0.001	*b.d.l.*	0.001	0.001	0.001	0.001	0.001	0.001	0.001
H	1.913	1.933	1.927	1.926	1.953	1.954	1.938	1.936	1.916	1.931
xAl	0.10	0.09	0.08	0.10	0.10	0.09	0.09	0.09	0.08	0.09
Mg/(Mg+Fe)	0.42	0.42	0.42	0.41	0.42	0.42	0.45	0.44	0.45	0.42

Table A.3

	64//Bt60	64//Bt61	64//Bt62	64//Bt63	64//Bt64	64//Bt65	64//Bt66
SiO_2	35.63	35.42	35.52	34.64	35.78	36.04	35.73
TiO_2	3.32	3.34	3.31	3.24	3.45	3.49	3.44
Al_2O_3	15.35	15.58	15.63	15.38	16.02	15.26	15.42
FeO	21.94	22.33	21.85	20.59	21.66	21.79	21.71
MnO	0.06	0.05	0.02	0.05	0.05	0.02	0.05
MgO	8.74	8.46	8.74	9.30	8.72	8.98	8.86
CaO	0.02	0.01	0.01	0.53	0.01	*b.d.l.*	0.01
Na_2O	0.04	0.05	0.05	0.19	0.01	0.01	0.06
K_2O	10.01	10.19	9.94	6.35	9.69	10.02	9.98
BaO	0.19	0.20	0.15	0.14	0.18	0.24	0.26
F^-	0.28	0.23	0.24	0.23	0.24	0.38	0.21
Cl^-	*b.d.l.*	*b.d.l.*	*b.d.l.*	0.01	0.01	0.01	*b.d.l.*
H_2O	3.72	3.74	3.74	3.63	3.77	3.70	3.77
Total	99.31	99.60	99.19	94.28	99.59	99.93	99.50
$Total_{c.}$	99.19	99.50	99.09	94.18	99.49	99.77	99.41
Si	2.773	2.756	2.763	2.775	2.762	2.784	2.771
Al_T	1.227	1.244	1.237	1.225	1.238	1.216	1.229
Ti	0.181	0.185	0.196	0.227	0.220	0.173	0.181
Al_O	0.194	0.196	0.194	0.196	0.200	0.203	0.201
Fe^2	1.428	1.453	1.421	1.379	1.398	1.408	1.408
Mn	0.004	0.003	0.001	0.004	0.003	0.001	0.003
Mg	1.014	0.981	1.014	1.110	1.003	1.034	1.025
Ca	0.002	0.001	0.001	0.045	0.001	*b.d.l.*	0.001
Na	0.006	0.008	0.007	0.029	0.002	0.001	0.009
K	0.994	1.012	0.986	0.649	0.954	0.987	0.987
Ba	0.006	0.006	0.005	0.005	0.005	0.007	0.008
F	0.069	0.056	0.060	0.059	0.057	0.092	0.052
Cl	*b.d.l.*	*b.d.l.*	*b.d.l.*	0.002	0.001	0.001	*b.d.l.*
H	1.931	1.943	1.940	1.940	1.942	1.907	1.948
xAl	0.09	0.09	0.10	0.11	0.11	0.09	0.09
Mg/(Mg+Fe)	0.42	0.40	0.42	0.45	0.42	0.42	0.42

Table A.4. Electron microprobe analyses of white mica (wt% oxides) and atoms per formula unit (a.p.f.u.) recalculated based on 11 oxygens (sample D20-10-69). Abbreviation: *b.d.l.*, below detection limit; Total$_c$, total recorrected; Al$_T$, Tetrahedral coordination of aluminum; Al$_O$, Octahedral coordination of aluminum; phl, phlogopite; msc, muscovite; cel, celadonite; par, paragonite sum$_O$, a.p.f.u. in octahedral coordination.

	D69// Wm11	D69// Wm12	D69// Wm13	D69// Wm14	D69// Wm15	D69// Wm16	D69// Wm17	D69// Wm18	D69// Wm19	D69// Wm20	D69// Wm21	D69// Wm22
SiO_2	46.34	46.19	46.22	46.02	45.95	46.17	46.77	46.37	45.96	46.44	45.60	45.73
TiO_2	1.27	0.96	0.66	0.67	0.84	0.83	1.34	1.06	0.76	1.26	0.71	0.91
Al_2O_3	31.59	32.03	31.99	32.47	32.11	31.97	31.21	31.65	31.96	31.90	31.81	32.15
FeO	1.27	1.62	1.36	1.27	1.30	1.55	1.28	1.37	1.58	1.18	1.45	1.31
MnO	*b.d.l.*	*b.d.l.*	0.01	0.01	*b.d.l.*	*b.d.l.*	*b.d.l.*	*b.d.l.*	*b.d.l.*	*b.d.l.*	0.02	0.02
MgO	2.15	2.32	2.11	1.90	2.39	2.37	2.06	2.13	2.24	1.89	2.31	1.93
CaO	0.01	0.02	0.02	0.05	0.01	0.03	*b.d.l.*	0.06	0.01	*b.d.l.*	0.12	0.04
Na_2O	0.32	0.39	0.38	0.33	0.34	0.31	0.31	0.28	0.30	0.29	0.30	0.30
K_2O	11.23	11.22	11.32	10.92	11.43	11.15	11.20	11.24	11.31	11.38	11.35	11.24
BaO	0.25	0.22	0.37	0.43	0.34	0.35	0.52	0.27	0.24	0.19	0.29	0.45
F^-	0.11	0.02	0.07	*b.d.l.*	0.01	0.13	0.09	0.03	0.18	0.13	*b.d.l.*	0.08
H_2O	4.36	4.42	4.37	4.41	4.42	4.36	4.38	4.40	4.32	4.36	4.39	4.35
Total	98.92	99.42	98.88	98.48	99.47	99.23	99.17	98.86	98.85	99.01	98.68	98.51
Total$_c$	98.87	99.41	98.86	98.47	99.47	99.17	99.13	98.85	98.78	98.96	98.68	98.48
Si	3.145	3.124	3.146	3.131	3.112	3.129	3.171	3.149	3.129	3.146	3.116	3.125
Al$_T$	0.855	0.876	0.854	0.869	0.888	0.871	0.829	0.851	0.871	0.854	0.884	0.875
Al$_O$	1.672	1.676	1.712	1.734	1.675	1.682	1.665	1.682	1.694	1.694	1.677	1.714
Ti	0.065	0.049	0.034	0.034	0.043	0.042	0.068	0.054	0.039	0.064	0.037	0.047
Fe^2	0.072	0.092	0.078	0.072	0.074	0.088	0.073	0.078	0.090	0.067	0.083	0.075
Mn	*b.d.l.*	*b.d.l.*	*b.d.l.*	0.001	*b.d.l.*	*b.d.l.*	*b.d.l.*	*b.d.l.*	*b.d.l.*	*b.d.l.*	0.001	0.001
Mg	0.218	0.234	0.214	0.193	0.242	0.240	0.208	0.216	0.227	0.191	0.235	0.197
Ca	0.001	0.002	0.001	0.003	0.001	0.002	*b.d.l.*	0.004	0.001	*b.d.l.*	0.009	0.003
Ba	0.007	0.006	0.010	0.012	0.009	0.009	0.014	0.007	0.006	0.005	0.008	0.012
Na	0.042	0.051	0.051	0.043	0.044	0.041	0.041	0.037	0.040	0.038	0.040	0.039
K	0.973	0.968	0.983	0.948	0.988	0.964	0.969	0.974	0.982	0.984	0.989	0.980
F	0.024	0.005	0.014	*b.d.l.*	0.001	0.029	0.019	0.007	0.039	0.028	*b.d.l.*	0.017
Cl	*b.d.l.*	0.001	*b.d.l.*	0.001	*b.d.l.*	0.001	*b.d.l.*	0.001	*b.d.l.*	*b.d.l.*	*b.d.l.*	*b.d.l.*
H	1.976	1.995	1.986	1.999	1.999	1.971	1.981	1.992	1.962	1.972	2.000	1.983
Components												
msc	0.354	0.356	0.357	0.364	0.363	0.357	0.340	0.354	0.365	0.364	0.360	0.364
wm-phl	0.013	0.026	0.019	0.017	0.025	0.026	0.007	0.015	0.025	0.008	0.025	0.017
Al-cel	0.057	0.047	0.057	0.053	0.047	0.051	0.069	0.059	0.049	0.056	0.049	0.051
Fe-Al-cel	0.019	0.018	0.021	0.020	0.014	0.019	0.024	0.021	0.019	0.020	0.017	0.019
par	0.021	0.025	0.024	0.022	0.021	0.020	0.020	0.018	0.020	0.018	0.019	0.019
Ti-Mn-Ca-wm	0.036	0.028	0.022	0.024	0.031	0.027	0.041	0.033	0.023	0.035	0.031	0.031
xOH	0.494	0.499	0.496	0.500	0.500	0.493	0.495	0.498	0.490	0.493	0.500	0.496
sum$_O$	2.027	2.051	2.038	2.034	2.050	2.052	2.014	2.030	2.050	2.016	2.050	2.033

Table A.4.

	D69// Wm23	D69// Wm24	D69// Wm25	D69// Wm26	D69// Wm27	D69// Wm28	D69// Wm29	D69// Wm30	D69// Wm51	D69// Wm52	D69// Wm53
SiO_2	45.51	46.18	46.12	46.32	46.39	45.68	46.24	45.88	46.30	46.19	46.39
TiO_2	0.97	0.82	1.31	0.79	1.21	0.91	1.30	0.78	1.45	0.88	0.76
Al_2O_3	31.44	32.01	31.87	31.68	31.25	31.67	31.51	31.81	32.18	32.57	32.15
FeO	1.52	1.20	1.16	1.16	1.11	1.45	1.18	1.39	1.15	1.31	1.48
MnO	*b.d.l.*	*b.d.l.*	*b.d.l.*	*b.d.l.*	0.01	*b.d.l.*	0.02	0.01	*b.d.l.*	*b.d.l.*	0.02
MgO	2.31	1.95	1.76	1.81	2.06	2.13	1.92	2.11	1.78	1.87	2.41
CaO	*b.d.l.*	0.01	0.05	0.04	0.09	0.04	*b.d.l.*	0.10	0.14	0.08	*b.d.l.*
Na_2O	0.32	0.37	0.38	0.34	0.29	0.33	0.34	0.33	0.33	0.33	0.33
K_2O	11.27	11.21	11.44	11.23	11.36	11.35	11.44	11.29	11.29	11.41	11.24
BaO	0.24	0.22	0.21	0.16	0.55	0.18	0.20	0.23	0.31	0.24	0.42
F^-	*b.d.l.*	*b.d.l.*	*b.d.l.*	0.11	*b.d.l.*	0.04	0.10	0.05	0.01	0.12	0.10
H_2O	4.36	4.40	4.40	4.33	4.39	4.35	4.35	4.36	4.43	4.37	4.40
Total	97.94	98.38	98.71	97.97	98.71	98.14	98.60	98.34	99.37	99.38	99.71
$Total_{\_c}$	97.94	98.38	98.71	97.92	98.71	98.12	98.55	98.32	99.36	99.33	99.66
Si	3.128	3.146	3.142	3.169	3.166	3.133	3.153	3.139	3.131	3.126	3.130
$Al_{\_T}$	0.872	0.854	0.858	0.832	0.834	0.867	0.847	0.861	0.870	0.874	0.870
$Al_{\_O}$	1.674	1.717	1.700	1.723	1.680	1.693	1.685	1.703	1.695	1.724	1.687
Ti	0.050	0.042	0.067	0.041	0.062	0.047	0.067	0.040	0.074	0.045	0.039
Fe^2	0.087	0.069	0.066	0.066	0.063	0.083	0.067	0.080	0.065	0.074	0.084
Mn	*b.d.l.*	*b.d.l.*	*b.d.l.*	*b.d.l.*	0.001	*b.d.l.*	0.001	0.001	*b.d.l.*	*b.d.l.*	0.001
Mg	0.237	0.198	0.178	0.184	0.209	0.218	0.195	0.215	0.179	0.189	0.242
Ca	*b.d.l.*	0.001	0.004	0.003	0.006	0.003	*b.d.l.*	0.008	0.010	0.006	*b.d.l.*
Ba	0.007	0.006	0.006	0.004	0.015	0.005	0.005	0.006	0.008	0.006	0.011
Na	0.043	0.049	0.051	0.045	0.039	0.044	0.045	0.044	0.043	0.044	0.044
K	0.988	0.974	0.994	0.980	0.989	0.993	0.996	0.986	0.974	0.985	0.968
F	*b.d.l.*	*b.d.l.*	*b.d.l.*	0.023	*b.d.l.*	0.009	0.021	0.010	0.001	0.026	0.020
Cl	0.001	*b.d.l.*	*b.d.l.*	*b.d.l.*	0.001	0.001	0.001	*b.d.l.*	0.001	*b.d.l.*	*b.d.l.*
H	1.999	2.000	2.000	1.977	1.999	1.991	1.979	1.990	1.998	1.974	1.980
Components											
msc	0.360	0.362	0.357	0.360	0.340	0.361	0.356	0.357	0.353	0.367	0.357
wm-phl	0.024	0.013	0.006	0.007	0.008	0.020	0.007	0.019	0.007	0.015	0.026
Al-cel	0.049	0.057	0.055	0.065	0.072	0.051	0.059	0.055	0.054	0.049	0.052
Fe-Al-cel	0.018	0.020	0.020	0.023	0.022	0.019	0.020	0.021	0.020	0.019	0.018
par	0.021	0.024	0.024	0.022	0.018	0.021	0.022	0.021	0.021	0.021	0.021
Ti-Mn-Ca-wm	0.028	0.024	0.038	0.024	0.041	0.027	0.036	0.027	0.046	0.028	0.025
xOH	0.500	0.500	0.500	0.494	0.500	0.498	0.495	0.498	0.500	0.493	0.495
$sum_{\_O}$	2.049	2.026	2.012	2.014	2.015	2.041	2.015	2.039	2.013	2.031	2.053

Table A.4.

	D69// Wm54	D69// Wm55	D69// Wm56	D69// Wm57	D69// Wm58	D69// Wm59	D69// Wm60	D69// Wm61	D69// Wm62	D69// Wm63	D69// Wm64
SiO_2	46.15	46.30	46.60	46.71	46.47	46.87	46.49	46.10	46.80	45.87	46.24
TiO_2	0.63	0.86	1.24	0.66	1.64	1.55	0.75	0.73	1.71	0.82	0.92
Al_2O_3	31.85	32.77	31.44	32.21	31.11	31.22	32.19	32.77	31.67	32.41	32.93
FeO	1.20	1.44	1.38	1.39	1.26	1.30	1.31	1.31	1.31	1.16	1.20
MnO	*b.d.l.*	*b.d.l.*	*b.d.l.*	*b.d.l.*	*b.d.l.*	*b.d.l.*	*b.d.l.*	*b.d.l.*	*b.d.l.*	*b.d.l.*	*b.d.l.*
MgO	2.51	2.13	2.39	2.15	2.21	2.24	2.05	1.95	2.10	2.35	1.96
CaO	*b.d.l.*	0.07	0.05	0.06	*b.d.l.*	0.05	0.04	0.15	0.02	0.03	0.02
Na_2O	0.34	0.37	0.32	0.29	0.30	0.28	0.33	0.34	0.33	0.32	0.31
K_2O	11.53	11.17	11.34	11.26	11.16	11.23	11.43	10.98	11.13	11.34	11.44
BaO	0.41	0.25	0.26	0.32	0.57	0.51	0.34	0.47	0.57	0.41	0.23
F^-	0.10	*b.d.l.*	0.11	0.02	0.09	0.22	*b.d.l.*	*b.d.l.*	0.11	0.12	*b.d.l.*
H_2O	4.38	4.46	4.38	4.44	4.38	4.34	4.43	4.43	4.42	4.38	4.45
Total	99.53	99.81	99.53	99.51	99.19	99.82	99.36	99.24	100.16	99.78	99.71
$Total_{\_c}$	99.49	99.81	99.48	99.50	99.15	99.73	99.36	99.24	100.12	99.73	99.71
Si	3.129	3.112	3.149	3.150	3.153	3.161	3.146	3.118	3.143	3.098	3.112
$Al_{\_T}$	0.871	0.888	0.851	0.851	0.847	0.839	0.854	0.882	0.858	0.903	0.888
$Al_{\_O}$	1.674	1.708	1.654	1.709	1.640	1.642	1.713	1.731	1.649	1.677	1.724
Ti	0.032	0.043	0.063	0.034	0.084	0.079	0.038	0.037	0.086	0.042	0.047
Fe^2	0.068	0.081	0.078	0.078	0.071	0.073	0.074	0.074	0.073	0.066	0.067
Mn	*b.d.l.*	*b.d.l.*	*b.d.l.*	*b.d.l.*	*b.d.l.*	*b.d.l.*	*b.d.l.*	*b.d.l.*	*b.d.l.*	*b.d.l.*	*b.d.l.*
Mg	0.254	0.214	0.241	0.216	0.224	0.225	0.207	0.196	0.210	0.237	0.197
Ca	*b.d.l.*	0.005	0.004	0.004	*b.d.l.*	0.003	0.003	0.011	0.002	0.002	0.001
Ba	0.011	0.007	0.007	0.008	0.015	0.014	0.009	0.013	0.015	0.011	0.006
Na	0.045	0.048	0.042	0.038	0.040	0.037	0.044	0.045	0.043	0.043	0.041
K	0.997	0.958	0.978	0.968	0.966	0.967	0.987	0.947	0.953	0.977	0.982
F	0.020	*b.d.l.*	0.024	0.005	0.019	0.047	*b.d.l.*	*b.d.l.*	0.023	0.026	*b.d.l.*
Cl	*b.d.l.*	0.001	*b.d.l.*	*b.d.l.*	*b.d.l.*	*b.d.l.*	*b.d.l.*	*b.d.l.*	*b.d.l.*	0.001	0.001
H	1.979	1.999	1.976	1.995	1.981	1.953	2.000	2.000	1.978	1.973	2.000
Components											
msc	0.357	0.364	0.345	0.359	0.338	0.336	0.360	0.358	0.339	0.365	0.376
wm-phl	0.025	0.023	0.018	0.019	0.010	0.010	0.016	0.019	0.009	0.025	0.018
Al-cel	0.055	0.045	0.060	0.059	0.064	0.067	0.058	0.051	0.059	0.043	0.045
Fe-Al-cel	0.015	0.017	0.020	0.022	0.020	0.022	0.021	0.019	0.021	0.012	0.015
par	0.021	0.024	0.021	0.019	0.020	0.018	0.021	0.022	0.021	0.021	0.020
Ti-Mn-Ca-wm	0.027	0.027	0.037	0.023	0.049	0.048	0.025	0.030	0.051	0.034	0.027
xOH	0.495	0.500	0.494	0.499	0.495	0.488	0.500	0.500	0.494	0.493	0.500
$sum_{\_O}$	2.050	2.047	2.036	2.037	2.020	2.020	2.032	2.038	2.018	2.050	2.035

Table A.5. Electron microprobe analyses of white mica (wt% oxides) and atoms per formula unit (a.p.f.u.) recalculated based on 11 oxygens (sample D20-10-49). Abbreviation: *b.d.l.*, below detection limit; Total$_C$, total recorrected; Al$_T$, Tetrahedral coordination of aluminum; Al$_O$, Octahedral coordination of aluminum; phl, phlogopite; msc, muscovite; cel, celadonite; par, paragonite sum$_O$, a.p.f.u. in octahedral coordination.

	49// Wm23	49// Wm24	49// Wm25	49// Wm26	49// Wm27	49// Wm28	49// Wm29	49// Wm30	49// Wm31	49// Wm32	49// Wm33	49// Wm34
SiO_2	47.10	46.23	45.59	46.37	46.54	46.67	47.69	46.81	45.67	45.76	47.35	47.25
TiO_2	0.89	0.89	0.92	1.04	0.99	0.74	0.76	0.86	1.24	1.19	0.77	0.72
Al_2O_3	28.92	29.52	28.96	29.06	29.89	28.85	29.19	28.37	30.44	30.05	29.09	29.37
FeO	3.71	3.86	3.88	4.10	3.89	3.96	3.89	3.96	3.99	4.04	3.92	3.91
MnO	*b.d.l.*	0.03	0.06	0.05	*b.d.l.*	*b.d.l.*	*b.d.l.*	*b.d.l.*	0.02	*b.d.l.*	0.02	*b.d.l.*
MgO	1.53	1.65	1.67	2.20	1.67	1.85	1.94	1.98	1.31	1.38	1.95	1.86
CaO	0.11	*b.d.l.*	*b.d.l.*	0.02	*b.d.l.*	*b.d.l.*	*b.d.l.*	*b.d.l.*	0.02	0.02	0.01	*b.d.l.*
Na_2O	1.15	0.23	0.23	0.25	0.26	0.27	0.27	0.23	0.29	0.29	0.26	0.27
K_2O	10.35	11.17	11.20	11.01	11.20	10.98	10.89	11.07	11.13	11.08	11.09	11.19
BaO	0.31	0.31	0.32	0.31	0.30	0.31	0.29	0.31	0.28	0.28	0.32	0.33
F^-	0.04	0.24	0.16	0.11	0.06	0.11	0.04	0.12	0.15	0.08	0.06	0.02
H_2O	4.32	4.22	4.20	4.31	4.34	4.28	4.38	4.27	4.29	4.30	4.36	4.37
Total	98.44	98.34	97.21	98.83	99.14	98.02	99.35	97.98	99.05	98.48	99.19	99.29
Total$_C$	98.42	98.24	97.14	98.78	99.11	97.98	99.33	97.93	98.99	98.44	99.16	99.28
Si	3.252	3.200	3.199	3.186	3.190	3.234	3.246	3.248	3.142	3.163	3.239	3.231
Al$_T$	0.748	0.800	0.801	0.814	0.810	0.766	0.754	0.752	0.859	0.837	0.761	0.769
Al$_O$	1.606	1.608	1.594	1.539	1.606	1.590	1.587	1.568	1.610	1.612	1.585	1.598
Ti	0.046	0.047	0.048	0.054	0.051	0.038	0.039	0.045	0.064	0.062	0.039	0.037
Fe^2	0.214	0.223	0.228	0.171	0.223	0.230	0.221	0.230	0.230	0.234	0.224	0.223
Mn	*b.d.l.*	0.002	0.004	0.003	*b.d.l.*	*b.d.l.*	*b.d.l.*	*b.d.l.*	0.001	*b.d.l.*	0.001	*b.d.l.*
Mg	0.157	0.170	0.175	0.226	0.171	0.192	0.197	0.205	0.134	0.143	0.199	0.190
Ca	0.008	*b.d.l.*	*b.d.l.*	0.002	*b.d.l.*	*b.d.l.*	*b.d.l.*	*b.d.l.*	0.002	0.002	0.001	*b.d.l.*
Ba	0.009	0.008	0.009	0.008	0.008	0.008	0.008	0.008	0.008	0.008	0.009	0.009
Na	0.154	0.031	0.031	0.033	0.034	0.037	0.036	0.032	0.039	0.038	0.035	0.036
K	0.912	0.986	1.003	0.965	0.979	0.970	0.946	0.980	0.977	0.977	0.968	0.977
F	0.010	0.053	0.034	0.024	0.013	0.023	0.010	0.026	0.032	0.018	0.012	0.005
Cl	0.001	*b.d.l.*	*b.d.l.*	0.001	0.001	*b.d.l.*	0.001	*b.d.l.*	*b.d.l.*	*b.d.l.*	*b.d.l.*	0.001
H	1.989	1.947	1.965	1.975	1.986	1.977	1.990	1.975	1.968	1.982	1.988	1.995
Components												
msc	0.504	0.658	0.656	0.629	0.659	0.626	0.619	0.612	0.682	0.669	0.620	0.632
wm-phl	0.024	0.050	0.050	0.050	0.051	0.050	0.045	0.047	0.050	0.050	0.049	0.048
Al-cel	0.113	0.090	0.090	0.111	0.086	0.110	0.120	0.121	0.056	0.066	0.117	0.110
Fe-Al-cel	0.154	0.118	0.117	0.085	0.112	0.132	0.134	0.135	0.095	0.107	0.131	0.130
par	0.142	0.030	0.029	0.033	0.033	0.036	0.036	0.031	0.038	0.037	0.035	0.035
Ti-Mn-Ca-wm	0.062	0.055	0.058	0.092	0.059	0.047	0.047	0.053	0.079	0.071	0.048	0.046
xOH	0.995	0.974	0.983	0.988	0.993	0.989	0.995	0.987	0.984	0.991	0.994	0.997
sum$_O$	2.024	2.050	2.050	2.050	2.051	2.050	2.045	2.047	2.050	2.050	2.049	2.048

Table A.5.

	49// Wm35	49// Wm36	49// Wm37	49// Wm38	49// Wm39	49// Wm40	49// Wm58	49// Wm59	49// Wm60	49// Wm61	49// Wm62	49// Wm63
SiO_2	46.37	46.81	46.77	46.48	45.44	47.07	45.82	45.76	46.27	46.40	46.27	46.00
TiO_2	0.89	0.78	0.74	0.82	1.16	0.65	0.94	1.07	0.96	0.99	0.89	0.99
Al_2O_3	29.73	28.95	28.90	28.47	29.92	28.70	28.91	29.46	29.12	28.81	28.59	29.35
FeO	3.74	3.84	3.85	4.18	3.86	3.78	3.84	4.00	3.90	4.11	3.87	3.79
MnO	0.05	0.01	*b.d.l.*	*b.d.l.*	*b.d.l.*	*b.d.l.*	*b.d.l.*	*b.d.l.*	*b.d.l.*	*b.d.l.*	*b.d.l.*	0.03
MgO	1.65	1.91	1.95	1.86	1.45	1.93	1.80	1.58	1.80	1.78	1.94	1.63
CaO	*b.d.l.*	*b.d.l.*	*b.d.l.*	*b.d.l.*	0.01	*b.d.l.*	*b.d.l.*	0.02	*b.d.l.*	0.03	0.02	*b.d.l.*
Na_2O	0.26	0.29	0.29	0.26	0.25	0.29	0.26	0.17	0.24	0.25	0.19	0.28
K_2O	11.22	11.12	11.20	10.97	11.29	11.07	11.15	11.36	11.02	10.95	11.02	11.28
BaO	0.27	0.31	0.30	0.33	0.28	0.28	0.31	0.31	0.31	0.34	0.27	0.35
F^-	0.16	0.16	0.05	*b.d.l.*	0.04	0.12	0.12	0.03	0.03	0.08	0.16	0.11
H_2O	4.27	4.26	4.31	4.31	4.30	4.28	4.23	4.29	4.32	4.28	4.22	4.26
Total	98.62	98.45	98.37	97.68	98.21	98.16	97.41	98.05	98.17	98.02	97.45	98.06
$Total_{\_c}$	98.55	98.38	98.35	97.68	98.19	98.11	97.36	98.03	98.16	97.99	97.38	98.02
Si	3.198	3.233	3.234	3.236	3.155	3.254	3.204	3.184	3.203	3.220	3.227	3.199
$Al_{\_T}$	0.802	0.767	0.766	0.764	0.845	0.746	0.796	0.816	0.797	0.780	0.773	0.801
$Al_{\_O}$	1.614	1.589	1.588	1.573	1.604	1.592	1.587	1.600	1.578	1.576	1.577	1.604
Ti	0.046	0.041	0.039	0.043	0.060	0.034	0.050	0.056	0.050	0.052	0.047	0.052
Fe^2	0.216	0.222	0.223	0.244	0.224	0.219	0.225	0.233	0.226	0.239	0.226	0.221
Mn	0.003	0.001	*b.d.l.*	*b.d.l.*	*b.d.l.*	*b.d.l.*	*b.d.l.*	*b.d.l.*	*b.d.l.*	*b.d.l.*	*b.d.l.*	0.002
Mg	0.169	0.197	0.201	0.193	0.150	0.198	0.188	0.163	0.185	0.184	0.202	0.169
Ca	*b.d.l.*	*b.d.l.*	*b.d.l.*	*b.d.l.*	0.001	*b.d.l.*	*b.d.l.*	0.002	*b.d.l.*	0.002	0.001	*b.d.l.*
Ba	0.007	0.008	0.008	0.009	0.008	0.008	0.009	0.009	0.008	0.009	0.008	0.010
Na	0.035	0.039	0.039	0.035	0.033	0.039	0.035	0.023	0.033	0.034	0.026	0.037
K	0.987	0.980	0.988	0.975	1.000	0.976	0.995	1.009	0.973	0.969	0.980	1.001
F	0.035	0.035	0.011	*b.d.l.*	0.010	0.027	0.027	0.007	0.007	0.017	0.035	0.023
Cl	*b.d.l.*	0.001	0.001	*b.d.l.*	*b.d.l.*	*b.d.l.*	*b.d.l.*	*b.d.l.*	*b.d.l.*	*b.d.l.*	*b.d.l.*	*b.d.l.*
H	1.965	1.964	1.989	2.000	1.990	1.974	1.973	1.993	1.993	1.983	1.965	1.977
Components												
msc	0.660	0.624	0.624	0.616	0.680	0.616	0.646	0.667	0.643	0.623	0.632	0.649
wm-phl	0.048	0.049	0.051	0.053	0.050	0.043	0.050	0.052	0.050	0.050	0.051	0.047
Al-cel	0.090	0.113	0.115	0.109	0.066	0.125	0.097	0.080	0.095	0.101	0.111	0.090
Fe-Al-cel	0.115	0.128	0.127	0.137	0.098	0.137	0.116	0.114	0.116	0.130	0.125	0.118
par	0.034	0.038	0.038	0.034	0.032	0.038	0.034	0.022	0.032	0.033	0.026	0.036
Ti-Mn-Ca-wm	0.053	0.049	0.047	0.052	0.074	0.041	0.058	0.065	0.063	0.063	0.055	0.061
xOH	0.982	0.982	0.994	1.000	0.995	0.987	0.987	0.996	0.996	0.991	0.982	0.989
$sum_{\_O}$	2.048	2.049	2.051	2.053	2.050	2.043	2.050	2.052	2.050	2.050	2.051	2.047

Table A.5.

	49// Wm64	49// Wm65	49// Wm66	49// Wm67	49// Wm68	49// Wm69	49// Wm70	49// Wm71	49// Wm72	49// Wm73	49// Wm74	49// Wm75
SiO_2	45.30	46.34	46.71	46.34	46.29	46.13	45.96	46.07	46.29	46.76	46.08	46.76
TiO_2	1.26	0.86	0.94	0.83	0.81	0.95	0.97	1.11	0.78	0.96	0.86	0.87
Al_2O_3	30.29	28.36	29.00	28.76	28.72	29.01	29.03	29.36	28.81	28.91	29.45	28.64
FeO	3.91	3.94	3.88	4.07	3.69	4.15	3.89	3.94	3.79	3.90	3.94	3.72
MnO	0.01	*b.d.l.*	*b.d.l.*	*b.d.l.*	*b.d.l.*	*b.d.l.*	*b.d.l.*	*b.d.l.*	0.01	0.03	*b.d.l.*	*b.d.l.*
MgO	1.22	1.87	1.84	1.78	1.97	1.64	1.75	1.63	1.90	1.76	1.65	1.96
CaO	0.03	0.02	*b.d.l.*	*b.d.l.*	0.01	0.01	0.04	*b.d.l.*	0.03	0.03	0.01	*b.d.l.*
Na_2O	0.28	0.27	0.29	0.24	0.25	0.24	0.28	0.20	0.25	0.28	0.29	0.23
K_2O	11.13	11.27	11.11	11.32	11.02	11.02	11.10	11.14	11.07	11.16	11.10	11.24
BaO	0.37	0.32	0.31	0.24	0.31	0.22	0.29	0.30	0.29	0.32	0.25	0.27
F^-	0.07	0.07	*b.d.l.*	*b.d.l.*	0.03	*b.d.l.*	0.07	*b.d.l.*	0.15	0.07	0.11	0.08
H_2O	4.28	4.26	4.34	4.31	4.30	4.31	4.27	4.32	4.24	4.31	4.27	4.29
Total	98.14	97.57	98.41	97.90	97.77	97.68	97.65	98.07	97.90	98.47	98.07	98.04
$Total_{\_c}$	98.11	97.54	98.41	97.90	97.76	97.68	97.62	98.07	97.83	98.44	98.02	98.01
Si	3.147	3.240	3.225	3.226	3.217	3.210	3.205	3.194	3.217	3.231	3.196	3.241
$Al_{\_T}$	0.853	0.760	0.775	0.774	0.783	0.790	0.795	0.806	0.783	0.769	0.804	0.759
$Al_{\_O}$	1.627	1.576	1.585	1.585	1.569	1.589	1.591	1.594	1.577	1.585	1.603	1.581
Ti	0.066	0.045	0.049	0.044	0.043	0.050	0.051	0.058	0.041	0.050	0.045	0.045
Fe^2	0.227	0.230	0.224	0.237	0.214	0.241	0.227	0.229	0.220	0.226	0.228	0.216
Mn	*b.d.l.*	*b.d.l.*	*b.d.l.*	*b.d.l.*	*b.d.l.*	*b.d.l.*	*b.d.l.*	*b.d.l.*	0.001	0.002	*b.d.l.*	*b.d.l.*
Mg	0.126	0.195	0.190	0.185	0.205	0.170	0.182	0.168	0.197	0.181	0.171	0.202
Ca	0.002	0.002	*b.d.l.*	*b.d.l.*	0.001	0.001	0.003	*b.d.l.*	0.002	0.002	0.001	*b.d.l.*
Ba	0.010	0.009	0.008	0.007	0.008	0.006	0.008	0.008	0.008	0.009	0.007	0.007
Na	0.037	0.037	0.039	0.033	0.034	0.032	0.039	0.027	0.034	0.037	0.039	0.031
K	0.986	1.005	0.978	1.006	0.977	0.978	0.988	0.986	0.982	0.984	0.982	0.994
F	0.016	0.015	*b.d.l.*	*b.d.l.*	0.006	*b.d.l.*	0.015	*b.d.l.*	0.033	0.014	0.024	0.017
Cl	*b.d.l.*	*b.d.l.*	*b.d.l.*	0.001	*b.d.l.*	*b.d.l.*	0.001	0.001	*b.d.l.*	0.001	0.001	*b.d.l.*
H	1.984	1.985	2.000	1.999	1.994	2.000	1.985	2.000	1.967	1.985	1.975	1.983
Components												
msc	0.680	0.614	0.626	0.636	0.629	0.645	0.635	0.657	0.632	0.620	0.655	0.626
wm-phl	0.047	0.047	0.047	0.051	0.050	0.051	0.051	0.048	0.050	0.043	0.050	0.044
Al-cel	0.057	0.114	0.107	0.102	0.110	0.090	0.096	0.086	0.107	0.107	0.087	0.120
Fe-Al-cel	0.102	0.135	0.126	0.130	0.116	0.127	0.120	0.117	0.120	0.134	0.117	0.128
par	0.036	0.035	0.038	0.032	0.034	0.032	0.037	0.026	0.033	0.036	0.038	0.030
Ti-Mn-Ca-wm	0.078	0.055	0.057	0.050	0.061	0.057	0.061	0.066	0.058	0.060	0.054	0.052
xOH	0.992	0.993	1.000	1.000	0.997	1.000	0.992	1.000	0.984	0.993	0.988	0.991
$sum_{\_O}$	2.047	2.047	2.047	2.051	2.050	2.051	2.051	2.048	2.050	2.043	2.050	2.044

Table A.5.

	49// Wm76	49// Wm77	49// Wm78	49// Wm79	49// Wm80	49// Wm81	49// Wm82	49// Wm83	49// Wm84	49// Wm85	49// Wm86	49// Wm87
SiO_2	45.96	46.65	46.68	46.97	46.78	46.83	46.57	46.55	47.41	46.80	47.28	47.13
TiO_2	0.94	1.00	0.80	0.94	0.91	0.85	0.84	0.98	0.77	0.88	0.96	0.82
Al_2O_3	28.91	29.53	29.04	28.97	29.36	29.19	29.07	29.70	29.24	29.00	29.93	29.57
FeO	3.82	3.82	4.08	4.02	3.91	3.92	3.80	3.67	3.96	3.89	3.90	3.71
MnO	0.03	*b.d.l.*	0.01	0.04	*b.d.l.*	*b.d.l.*	*b.d.l.*	*b.d.l.*	0.01	*b.d.l.*	*b.d.l.*	*b.d.l.*
MgO	1.78	1.85	1.76	1.78	1.81	1.85	1.79	1.82	1.89	1.85	1.40	1.89
CaO	*b.d.l.*	*b.d.l.*	0.04	0.01	*b.d.l.*	0.02	*b.d.l.*	*b.d.l.*	0.07	*b.d.l.*	0.07	0.06
Na_2O	0.24	0.29	0.31	0.29	0.26	0.23	0.31	0.29	0.33	0.23	0.73	0.23
K_2O	11.23	11.11	10.94	11.03	11.08	11.04	11.30	11.07	10.81	11.21	10.66	11.22
BaO	0.33	0.31	0.29	0.30	0.34	0.31	0.34	0.27	0.38	0.29	0.32	0.30
F^-	0.06	0.09	0.07	0.16	0.09	0.01	0.15	0.03	0.17	0.13	*b.d.l.*	0.08
H_2O	4.28	4.33	4.30	4.28	4.32	4.35	4.26	4.35	4.31	4.28	4.40	4.35
Total	97.88	99.08	98.33	98.78	98.87	98.61	98.43	98.74	99.36	98.56	99.64	99.35
$Total_{\_c}$	97.86	99.05	98.30	98.72	98.83	98.61	98.36	98.72	99.29	98.50	99.64	99.32
Si	3.202	3.198	3.226	3.232	3.214	3.223	3.225	3.198	3.236	3.229	3.218	3.220
$Al_{\_T}$	0.799	0.802	0.774	0.768	0.786	0.777	0.775	0.803	0.764	0.771	0.782	0.780
$Al_{\_O}$	1.575	1.584	1.591	1.581	1.592	1.590	1.597	1.602	1.589	1.586	1.619	1.601
Ti	0.049	0.052	0.042	0.048	0.047	0.044	0.044	0.051	0.040	0.046	0.049	0.042
Fe^2	0.223	0.219	0.236	0.232	0.225	0.226	0.220	0.211	0.226	0.225	0.222	0.212
Mn	0.002	*b.d.l.*	0.001	0.002	*b.d.l.*	*b.d.l.*	*b.d.l.*	*b.d.l.*	0.001	*b.d.l.*	*b.d.l.*	*b.d.l.*
Mg	0.185	0.189	0.182	0.183	0.186	0.190	0.185	0.186	0.192	0.190	0.142	0.193
Ca	*b.d.l.*	*b.d.l.*	0.003	*b.d.l.*	*b.d.l.*	0.001	*b.d.l.*	*b.d.l.*	0.005	*b.d.l.*	0.005	0.005
Ba	0.009	0.008	0.008	0.008	0.009	0.008	0.009	0.007	0.010	0.008	0.009	0.008
Na	0.033	0.038	0.042	0.039	0.035	0.031	0.042	0.038	0.044	0.031	0.096	0.030
K	0.998	0.972	0.965	0.968	0.972	0.969	0.999	0.970	0.942	0.987	0.926	0.978
F	0.012	0.020	0.016	0.035	0.020	0.002	0.034	0.006	0.037	0.028	*b.d.l.*	0.017
Cl	0.001	*b.d.l.*	*b.d.l.*	0.001	*b.d.l.*	*b.d.l.*	0.001	*b.d.l.*	0.001	0.001	*b.d.l.*	*b.d.l.*
H	1.987	1.980	1.984	1.965	1.980	1.998	1.966	1.994	1.962	1.972	2.000	1.983
Components												
msc	0.643	0.644	0.621	0.620	0.636	0.634	0.629	0.650	0.602	0.633	0.582	0.636
wm-phl	0.050	0.050	0.050	0.045	0.050	0.050	0.045	0.050	0.048	0.047	0.032	0.047
Al-cel	0.095	0.096	0.103	0.106	0.101	0.106	0.107	0.096	0.116	0.108	0.090	0.111
Fe-Al-cel	0.115	0.111	0.133	0.134	0.123	0.126	0.127	0.109	0.136	0.128	0.141	0.122
par	0.031	0.037	0.041	0.038	0.034	0.031	0.040	0.038	0.044	0.030	0.093	0.030
Ti-Mn-Ca-wm	0.066	0.063	0.052	0.057	0.056	0.054	0.052	0.058	0.055	0.053	0.062	0.055
xOH	0.994	0.990	0.992	0.983	0.990	0.999	0.983	0.997	0.981	0.986	1.000	0.992
$sum_{\_O}$	2.050	2.050	2.050	2.045	2.050	2.050	2.045	2.050	2.048	2.047	2.032	2.047

Table A.5.

	49// Wm88	49// Wm89	49// Wm90	49// Wm91	49// Wm92	49// Wm93	49// Wm94	49// Wm95	49// Wm96	49// Wm97	49// Wm98	49// Wm99	49// Wm100
SiO_2	46.94	46.18	46.57	46.37	45.78	46.83	45.77	46.24	46.70	46.44	46.23	46.23	46.06
TiO_2	0.86	1.03	0.83	0.86	0.93	0.69	1.06	0.93	0.80	0.99	1.03	1.05	1.12
Al_2O_3	29.10	30.75	28.91	28.96	28.36	29.19	28.85	29.30	29.37	29.10	29.06	29.46	29.25
FeO	3.95	3.60	3.91	3.76	3.93	3.95	3.81	3.87	3.89	3.73	4.04	3.77	3.92
MnO	*b.d.l.*	*b.d.l.*	0.02	*b.d.l.*	*b.d.l.*	*b.d.l.*	*b.d.l.*	0.01	0.01	*b.d.l.*	*b.d.l.*	0.01	*b.d.l.*
MgO	1.88	1.50	1.87	1.74	1.84	1.87	1.75	1.68	1.80	1.93	1.75	1.59	1.76
CaO	0.03	0.02	*b.d.l.*	0.01	0.03	*b.d.l.*	*b.d.l.*	0.01	0.01	*b.d.l.*	*b.d.l.*	0.01	*b.d.l.*
Na_2O	0.28	0.22	0.26	0.29	0.23	0.25	0.28	0.26	0.25	0.20	0.26	0.29	0.19
K_2O	11.11	11.28	11.03	11.19	11.19	11.19	11.11	11.06	11.10	11.35	11.03	11.09	11.26
BaO	0.30	0.30	0.30	0.30	0.29	0.32	0.31	0.29	0.31	0.22	0.33	0.32	0.31
F^-	0.14	0.01	0.08	*b.d.l.*	*b.d.l.*	0.20	*b.d.l.*	0.10	0.06	0.13	*b.d.l.*	0.11	0.08
H_2O	4.29	4.40	4.29	4.31	4.26	4.26	4.28	4.28	4.32	4.28	4.33	4.28	4.29
Total	98.90	99.81	98.07	97.78	96.84	98.74	97.24	98.02	98.63	98.55	98.21	98.20	98.26
$Total_{c}$	98.84	99.81	98.03	97.77	96.84	98.66	97.23	97.98	98.61	98.50	98.21	98.15	98.23
Si	3.227	3.145	3.226	3.225	3.224	3.226	3.205	3.207	3.216	3.207	3.202	3.201	3.192
Al_{T}	0.773	0.855	0.774	0.775	0.776	0.775	0.795	0.793	0.784	0.793	0.798	0.799	0.808
Al_{O}	1.585	1.613	1.587	1.599	1.577	1.595	1.586	1.601	1.600	1.575	1.574	1.605	1.582
Ti	0.044	0.053	0.043	0.045	0.049	0.036	0.056	0.048	0.042	0.051	0.054	0.055	0.058
Fe^2	0.227	0.205	0.227	0.219	0.231	0.227	0.223	0.224	0.224	0.215	0.234	0.219	0.227
Mn	*b.d.l.*	*b.d.l.*	0.001	*b.d.l.*	*b.d.l.*	*b.d.l.*	*b.d.l.*	*b.d.l.*	0.001	*b.d.l.*	*b.d.l.*	*b.d.l.*	*b.d.l.*
Mg	0.193	0.152	0.193	0.180	0.193	0.192	0.183	0.174	0.185	0.199	0.181	0.165	0.182
Ca	0.002	0.001	*b.d.l.*	*b.d.l.*	0.002	*b.d.l.*	*b.d.l.*	0.001	0.001	*b.d.l.*	*b.d.l.*	*b.d.l.*	*b.d.l.*
Ba	0.008	0.008	0.008	0.008	0.008	0.009	0.009	0.008	0.008	0.006	0.009	0.009	0.008
Na	0.038	0.029	0.035	0.039	0.032	0.033	0.038	0.036	0.034	0.026	0.036	0.039	0.026
K	0.975	0.980	0.975	0.993	1.006	0.983	0.993	0.979	0.975	1.000	0.975	0.980	0.996
F	0.030	0.001	0.018	*b.d.l.*	*b.d.l.*	0.043	*b.d.l.*	0.022	0.013	0.028	*b.d.l.*	0.024	0.017
Cl	0.001	0.001	*b.d.l.*	0.001	0.001	*b.d.l.*	0.001	*b.d.l.*	*b.d.l.*	*b.d.l.*	*b.d.l.*	0.001	*b.d.l.*
H	1.970	1.998	1.982	1.999	1.999	1.957	1.999	1.978	1.987	1.972	2.000	1.975	1.983
Components													
msc	0.622	0.692	0.630	0.633	0.627	0.640	0.637	0.646	0.641	0.650	0.638	0.647	0.657
wm-phl	0.050	0.050	0.050	0.043	0.051	0.050	0.048	0.048	0.051	0.050	0.050	0.043	0.050
Al-cel	0.109	0.066	0.108	0.106	0.106	0.107	0.096	0.094	0.102	0.102	0.092	0.090	0.089
Fe-Al-cel	0.128	0.088	0.126	0.128	0.127	0.127	0.118	0.121	0.123	0.111	0.119	0.120	0.111
par	0.037	0.028	0.035	0.038	0.031	0.033	0.036	0.035	0.033	0.026	0.035	0.038	0.025
Ti-Mn-Ca-wm	0.055	0.076	0.051	0.053	0.059	0.044	0.064	0.057	0.051	0.062	0.066	0.064	0.067
xOH	0.985	0.999	0.991	1.000	1.000	0.979	1.000	0.989	0.993	0.986	1.000	0.988	0.992
sum_{O}	2.050	2.050	2.050	2.043	2.051	2.050	2.048	2.048	2.051	2.050	2.050	2.043	2.050

Table A.6. Electron microprobe analyses of white mica (wt% oxides) and a.p.f.u. recalculated based on 11 oxygens (sample D18-10-64). Abbreviation: *b.d.l.*, below detection limit; Total$_{c}$, total recorrected; Al$_{T}$, Tetrahedral coordination of aluminum; Al$_{O}$, Octahedral coordination of aluminum; phl, phlogopite; msc, muscovite; cel, celadonite; par, paragonite sum$_{O}$, a.p.f.u. in octahedral coordination.

	64// Wm67	64// Wm68	64// Wm69	64// Wm70	64// Wm71	64// Wm72	64// Wm73	64// Wm74	64// Wm75	64// Wm76	64// Wm77	64// Wm78
SiO_2	48.51	48.69	47.37	48.21	48.17	47.11	47.00	46.25	51.64	50.03	47.46	47.76
TiO_2	0.80	0.57	0.94	0.89	0.83	0.98	1.11	1.24	1.23	1.06	1.11	1.00
Al_2O_3	29.01	28.72	28.90	28.41	28.68	28.31	27.81	27.94	26.55	27.19	28.05	28.51
FeO	3.07	2.99	2.99	3.03	2.81	2.96	3.09	3.49	3.65	3.19	3.46	3.34
MnO	*b.d.l.*	*b.d.l.*	*b.d.l.*	*b.d.l.*	*b.d.l.*	*b.d.l.*	0.01	*b.d.l.*	*b.d.l.*	*b.d.l.*	*b.d.l.*	*b.d.l.*
MgO	2.22	2.28	2.04	2.27	2.20	2.13	2.05	2.24	1.89	1.91	2.24	2.13
CaO	0.02	*b.d.l.*	*b.d.l.*	0.02	*b.d.l.*	0.06	*b.d.l.*	0.03	0.02	0.02	*b.d.l.*	0.03
Na_2O	0.24	0.23	0.20	0.25	0.21	0.21	0.24	0.25	0.23	0.24	0.19	0.23
K_2O	11.20	11.19	11.24	11.12	11.22	11.28	11.19	10.84	10.43	10.82	11.34	11.20
BaO	0.28	0.30	0.25	0.29	0.18	0.28	0.29	0.30	0.20	0.28	0.26	0.25
F^-	0.15	0.14	0.01	0.11	0.02	0.06	0.10	0.12	0.06	*b.d.l.*	0.14	0.02
H_2O	4.37	4.36	4.36	4.34	4.39	4.30	4.25	4.27	4.48	4.43	4.28	4.37
Total	99.85	99.46	98.32	98.94	98.71	97.66	97.13	98.05	100.39	99.17	98.55	98.85
Total$_{c}$	99.79	99.40	98.31	98.89	98.70	97.64	97.09	98.00	100.36	99.17	98.49	98.84
Si	3.278	3.300	3.255	3.289	3.286	3.268	3.279	3.210	3.433	3.384	3.269	3.269
Al$_{T}$	0.722	0.700	0.745	0.711	0.714	0.732	0.721	0.791	0.567	0.616	0.731	0.731
Al$_{O}$	1.589	1.595	1.596	1.574	1.592	1.582	1.566	1.495	1.513	1.552	1.547	1.569
Ti	0.041	0.029	0.048	0.046	0.043	0.051	0.058	0.065	0.062	0.054	0.058	0.051
Fe^2	0.173	0.170	0.172	0.173	0.160	0.172	0.181	0.202	0.203	0.181	0.200	0.191
Mn	*b.d.l.*	*b.d.l.*	*b.d.l.*	*b.d.l.*	*b.d.l.*	*b.d.l.*	0.001	*b.d.l.*	*b.d.l.*	*b.d.l.*	*b.d.l.*	*b.d.l.*
Mg	0.223	0.230	0.210	0.231	0.224	0.220	0.213	0.232	0.188	0.193	0.230	0.218
Ca	0.001	*b.d.l.*	*b.d.l.*	0.002	*b.d.l.*	0.004	*b.d.l.*	0.002	0.002	0.001	*b.d.l.*	0.002
Ba	0.007	0.008	0.007	0.008	0.005	0.008	0.008	0.008	0.005	0.007	0.007	0.007
Na	0.032	0.030	0.027	0.033	0.028	0.028	0.032	0.034	0.029	0.031	0.025	0.030
K	0.966	0.967	0.985	0.968	0.976	0.998	0.996	0.960	0.885	0.934	0.997	0.978
F	0.032	0.031	0.002	0.024	0.004	0.012	0.021	0.025	0.012	*b.d.l.*	0.031	0.005
Cl	*b.d.l.*	*b.d.l.*	*b.d.l.*	*b.d.l.*	*b.d.l.*	*b.d.l.*	0.001	*b.d.l.*	0.001	*b.d.l.*	0.001	0.001
H	1.968	1.969	1.997	1.976	1.996	1.988	1.978	1.975	1.988	2.000	1.968	1.995
Components												
msc	0.607	0.602	0.630	0.591	0.615	0.607	0.598	0.593	0.494	0.534	0.601	0.602
wm-phl	0.026	0.024	0.026	0.023	0.018	0.024	0.019	0.050	-0.035	-0.022	0.034	0.029
Al-cel	0.161	0.178	0.144	0.171	0.170	0.157	0.155	0.117	0.212	0.203	0.148	0.148
Fe-Al-cel	0.125	0.131	0.118	0.128	0.122	0.122	0.132	0.102	0.229	0.190	0.128	0.130
par	0.032	0.030	0.027	0.033	0.028	0.027	0.031	0.034	0.032	0.032	0.025	0.030
Ti-Mn-Ca-wm	0.049	0.037	0.055	0.055	0.048	0.062	0.066	0.103	0.069	0.063	0.065	0.060
xOH	0.984	0.985	0.999	0.988	0.998	0.994	0.989	0.987	0.994	1.000	0.984	0.997
sum$_{O}$	2.026	2.024	2.026	2.023	2.018	2.024	2.019	2.050	1.965	1.979	2.034	2.029
SiO_2	0.563	0.576	0.549	0.572	0.582	0.561	0.541	0.534	0.481	0.516	0.536	0.533
TiO_2	0.032	0.030	0.027	0.033	0.028	0.027	0.031	0.034	0.032	0.032	0.025	0.030
Al tot	2.311	2.295	2.341	2.285	2.306	2.314	2.287	2.285	2.080	2.168	2.278	2.300

Table A.6.

	64// Wm79	64// Wm80	64// Wm81	64// Wm82	64// Wm83	64// Wm84	64// Wm85	64// Wm86	64// Wm87	64// Wm88	64// Wm89
SiO_2	47.97	47.27	47.77	46.64	47.10	47.12	46.64	46.52	46.96	48.63	48.71
TiO_2	1.04	1.06	0.90	0.84	1.11	0.88	0.68	1.07	0.98	0.67	0.78
Al_2O_3	28.14	28.86	28.17	29.48	28.01	28.40	28.48	29.30	29.81	28.37	28.15
FeO	3.24	3.28	3.26	3.14	2.92	2.92	3.08	3.07	3.49	3.66	3.42
MnO	*b.d.l.*	*b.d.l.*	*b.d.l.*	*b.d.l.*	*b.d.l.*	*b.d.l.*	*b.d.l.*	*b.d.l.*	*b.d.l.*	0.03	0.02
MgO	2.23	1.94	2.17	1.78	2.21	1.98	2.07	1.83	1.78	2.32	2.37
CaO	*b.d.l.*	0.03	*b.d.l.*	*b.d.l.*	0.02	0.01	0.02	0.02	*b.d.l.*	0.02	*b.d.l.*
Na_2O	0.25	0.24	0.32	0.21	0.22	0.20	0.57	0.31	0.22	0.20	0.17
K_2O	11.22	11.14	11.06	11.31	11.17	11.10	11.52	11.33	11.20	11.19	11.41
BaO	0.27	0.21	0.28	0.26	0.27	0.26	0.28	0.29	0.21	0.23	0.26
F^-	0.14	0.01	0.14	0.01	0.03	0.03	0.09	0.12	0.07	0.25	0.09
H_2O	4.31	4.36	4.29	4.33	4.30	4.30	4.19	4.26	4.36	4.31	4.37
Total	98.81	98.38	98.36	98.01	97.36	97.21	97.62	98.12	99.08	99.87	99.77
$Total_{c}$	98.75	98.38	98.30	98.00	97.35	97.19	97.53	98.06	99.05	99.77	99.73
Si	3.286	3.249	3.286	3.223	3.273	3.273	3.258	3.219	3.209	3.295	3.305
Al_{T}	0.714	0.752	0.714	0.777	0.727	0.727	0.742	0.781	0.791	0.705	0.695
Al_{O}	1.558	1.586	1.570	1.624	1.566	1.598	1.603	1.608	1.609	1.560	1.555
Ti	0.053	0.055	0.046	0.044	0.058	0.046	0.036	0.056	0.050	0.034	0.040
Fe^2	0.185	0.188	0.188	0.181	0.170	0.170	0.180	0.178	0.200	0.208	0.194
Mn	*b.d.l.*	*b.d.l.*	*b.d.l.*	*b.d.l.*	*b.d.l.*	*b.d.l.*	*b.d.l.*	*b.d.l.*	*b.d.l.*	0.002	0.001
Mg	0.228	0.199	0.222	0.184	0.228	0.205	0.216	0.189	0.182	0.235	0.240
Ca	*b.d.l.*	0.002	*b.d.l.*	*b.d.l.*	0.001	0.001	0.001	0.001	*b.d.l.*	0.002	*b.d.l.*
Ba	0.007	0.006	0.008	0.007	0.008	0.007	0.008	0.008	0.006	0.006	0.007
Na	0.033	0.032	0.043	0.028	0.030	0.027	0.077	0.042	0.029	0.026	0.023
K	0.981	0.977	0.971	0.998	0.990	0.983	1.027	1.000	0.976	0.967	0.988
F	0.031	0.001	0.030	0.002	0.006	0.008	0.021	0.027	0.014	0.053	0.020
Cl	*b.d.l.*	*b.d.l.*	*b.d.l.*	*b.d.l.*	*b.d.l.*	*b.d.l.*	0.028	0.005	0.001	0.001	*b.d.l.*
H	1.969	1.999	1.970	1.997	1.994	1.992	1.951	1.969	1.985	1.947	1.980
Components											
msc	0.589	0.623	0.585	0.660	0.601	0.620	0.587	0.638	0.661	0.591	0.589
wm-phl	0.025	0.028	0.026	0.033	0.023	0.019	0.034	0.031	0.041	0.038	0.030
Al-cel	0.162	0.131	0.159	0.116	0.161	0.154	0.145	0.117	0.102	0.161	0.173
Fe-Al-cel	0.132	0.125	0.134	0.114	0.120	0.127	0.121	0.111	0.112	0.142	0.139
par	0.032	0.031	0.042	0.027	0.029	0.026	0.070	0.040	0.029	0.026	0.022
Ti-Mn-Ca-wm	0.061	0.063	0.054	0.051	0.067	0.054	0.044	0.064	0.056	0.042	0.047
xOH	0.984	0.999	0.985	0.999	0.997	0.996	0.976	0.984	0.993	0.973	0.990
sum_{O}	2.025	2.028	2.026	2.033	2.023	2.019	2.034	2.031	2.041	2.038	2.030
SiO_2	0.551	0.513	0.542	0.503	0.574	0.547	0.546	0.515	0.477	0.531	0.553
TiO_2	0.032	0.031	0.043	0.027	0.030	0.027	0.070	0.040	0.029	0.026	0.022
Al tot	2.272	2.337	2.284	2.401	2.294	2.325	2.345	2.389	2.400	2.265	2.251

Table A.6.

	64// Wm90	64// Wm91	64// Wm93	64// Wm94	64// Wm95	64// Wm96	64// Wm97	64// Wm98	64// Wm99	64// Wm100
SiO_2	47.58	47.64	47.44	47.61	46.90	46.37	47.75	47.05	47.03	48.12
TiO_2	0.95	0.96	1.11	1.00	1.06	0.77	1.06	1.16	1.04	0.97
Al_2O_3	28.76	28.67	29.63	28.75	28.76	30.89	29.10	29.90	29.81	28.28
FeO	3.43	3.63	2.89	3.03	3.01	2.92	3.07	3.13	3.47	2.99
MnO	0.00	0.01	0.00	0.00	0.00	0.00	0.00	0.00	0.00	0.00
MgO	2.22	2.11	1.95	2.05	1.99	1.56	2.00	1.80	1.80	2.18
CaO	0.03	0.02	0.00	0.03	0.01	0.00	0.00	0.03	0.07	0.00
Na_2O	0.18	0.21	0.28	0.17	0.24	0.30	0.20	0.25	0.20	0.23
K_2O	11.37	11.41	11.28	11.36	11.21	11.16	11.30	11.18	11.13	11.29
BaO	0.29	0.24	0.30	0.27	0.27	0.34	0.30	0.31	0.32	0.23
F^-	0.15	0.07	0.05	0.07	0.12	0.03	0.17	0.09	0.19	0.24
H_2O	4.32	4.35	4.38	4.34	4.28	4.36	4.32	4.36	4.31	4.27
Total	99.27	99.34	99.31	98.67	97.85	98.70	99.27	99.25	99.38	98.80
$Total_{c}$	99.21	99.31	99.29	98.64	97.80	98.68	99.19	99.22	99.30	98.70
Si	3.252	3.257	3.230	3.265	3.246	3.176	3.254	3.208	3.208	3.293
Al_{T}	0.748	0.744	0.771	0.735	0.754	0.824	0.746	0.793	0.792	0.707
Al_{O}	1.569	1.566	1.606	1.588	1.591	1.671	1.591	1.611	1.605	1.573
Ti	0.049	0.050	0.057	0.052	0.055	0.040	0.055	0.060	0.054	0.050
Fe^2	0.196	0.208	0.165	0.174	0.174	0.167	0.175	0.178	0.198	0.171
Mn	*b.d.l.*	0.001	*b.d.l.*	*b.d.l.*	*b.d.l.*	*b.d.l.*	*b.d.l.*	*b.d.l.*	*b.d.l.*	*b.d.l.*
Mg	0.226	0.215	0.198	0.209	0.206	0.159	0.203	0.183	0.183	0.223
Ca	0.002	0.002	*b.d.l.*	0.002	0.001	*b.d.l.*	*b.d.l.*	0.002	0.005	*b.d.l.*
Ba	0.008	0.007	0.008	0.007	0.007	0.009	0.008	0.008	0.009	0.006
Na	0.024	0.028	0.037	0.022	0.032	0.040	0.026	0.032	0.027	0.031
K	0.991	0.995	0.980	0.994	0.989	0.975	0.982	0.973	0.968	0.985
F	0.032	0.016	0.011	0.016	0.026	0.007	0.036	0.019	0.040	0.052
Cl	*b.d.l.*	*b.d.l.*	0.001	0.001	*b.d.l.*	0.002	*b.d.l.*	*b.d.l.*	*b.d.l.*	*b.d.l.*
H	1.968	1.984	1.989	1.984	1.974	1.991	1.964	1.981	1.960	1.949
Components										
msc	0.616	0.612	0.636	0.622	0.626	0.690	0.627	0.649	0.644	0.598
wm-phl	0.041	0.039	0.026	0.022	0.026	0.037	0.023	0.031	0.040	0.017
Al-cel	0.140	0.135	0.130	0.150	0.137	0.090	0.140	0.110	0.107	0.169
Fe-Al-cel	0.122	0.130	0.108	0.124	0.116	0.095	0.121	0.108	0.115	0.130
par	0.023	0.027	0.036	0.022	0.031	0.039	0.026	0.032	0.027	0.030
Ti-Mn-Ca-wm	0.058	0.058	0.065	0.061	0.063	0.049	0.063	0.070	0.067	0.056
xOH	0.984	0.992	0.994	0.992	0.987	0.996	0.982	0.990	0.980	0.974
sum_{O}	2.041	2.039	2.026	2.022	2.026	2.037	2.023	2.031	2.040	2.017
SiO_2	0.536	0.509	0.545	0.547	0.541	0.487	0.537	0.506	0.481	0.566
TiO_2	0.023	0.027	0.037	0.022	0.031	0.040	0.026	0.032	0.027	0.030
Al tot	2.317	2.310	2.377	2.323	2.345	2.494	2.337	2.403	2.397	2.280

APPENDIX - $^{40}Ar–^{39}Ar$ laserprobe analysis

Table A.7. $^{40}Ar–^{39}Ar$ laser step-heating data of biotite separates (sample D20-10-69, 0.50-0.25 mm, J = 0.00043459 ±0.00000117). Data completed through a MAP215-50 single-collector mass spectrometer. Instrumental sensitivity ~2.0E-11 mol/pA.

No.	laser power (W)	$^{36}Ar_{(atm)}$ pA	±2σ pA	$^{37}Ar_{(Ca)}$ pA	±2σ pA	$^{38}Ar_{(Cl)}$ pA	±2σ pA	$^{39}Ar_{(K)}$ pA	±2σ pA	$Ar_{(tot)}$ pA	±2σ pA	Age (Ma)	±2σ	$^{40}Ar^{*}$ (%)	$^{39}Ar_{K}$%	Ca/K	±2σ
8B	0.15	8.06E-01	2.47E-02	2.88E-01	1.76E+00	5.43E-02	2.85E-02	2.07E+00	1.36E-01	2.76E+02	1.46E+00	14.40	2.9	13.8	0.1	0.26	1.60
8C	0.3	7.08E-01	5.67E-02	2.74E+00	1.69E+00	5.05E-02	4.46E-02	5.13E+00	2.01E-01	3.19E+02	1.51E+00	16.71	2.6	34.4	0.3	1.01	0.63
8D	0.45	2.52E+00	7.60E-02	8.79E+00	1.92E+00	2.66E-01	6.77E-02	4.38E+01	3.80E-01	1.57E+03	2.92E+00	14.77	0.42	52.6	2.9	0.379	0.091
8E	0.55	1.45E+00	9.60E-02	6.44E+00	1.69E+00	4.93E-01	1.12E-01	1.09E+02	6.76E-01	2.38E+03	2.73E+00	13.95	0.22	81.9	7.2	0.111	0.031
8G	0.65	9.79E-01	7.28E-02	4.12E+00	1.77E+00	6.82E-01	1.33E-01	1.28E+02	5.49E-01	2.57E+03	3.85E+00	13.93	0.15	88.7	8.5	0.061	0.027
8H	0.75	5.87E-01	4.75E-02	2.99E+00	1.78E+00	4.64E-01	8.12E-02	1.21E+02	7.48E-01	2.32E+03	2.64E+00	13.80	0.12	92.5	8.0	0.047	0.028
8I	0.88	4.35E-01	3.81E-02	2.86E+00	1.95E+00	5.48E-01	9.52E-02	1.24E+02	5.70E-01	2.32E+03	3.99E+00	13.81	0.10	94.4	8.2	0.043	0.030
8K	1.03	3.47E-01	4.29E-02	3.35E+00	1.79E+00	6.32E-01	1.02E-01	1.14E+02	4.89E-01	2.14E+03	4.26E+00	13.94	0.11	95.2	7.5	0.055	0.030
8L	1.18	3.83E-01	3.06E-02	1.73E+00	1.80E+00	5.52E-01	7.86E-02	1.15E+02	6.37E-01	2.14E+03	3.33E+00	13.82	0.10	94.7	7.6	0.029	0.030
8M	1.35	3.93E-01	5.19E-02	2.10E+00	1.82E+00	6.26E-01	7.46E-02	1.24E+02	6.54E-01	2.32E+03	3.70E+00	13.83	0.12	94.9	8.2	0.032	0.028
8N	1.55	5.47E-01	5.59E-02	2.00E+00	1.85E+00	8.94E-01	1.74E-01	1.79E+02	7.13E-01	3.33E+03	5.39E+00	13.85	0.09	95.1	11.8	0.021	0.020
8Q	1.75	3.46E-01	3.11E-02	1.28E+00	1.79E+00	5.25E-01	1.30E-01	1.18E+02	5.65E-01	2.20E+03	2.96E+00	13.88	0.09	95.3	7.8	0.021	0.029
8R	2.05	4.66E-01	4.68E-02	1.59E+00	1.75E+00	6.84E-01	1.36E-01	1.49E+02	6.64E-01	2.78E+03	6.54E+00	13.91	0.10	95.0	9.8	0.020	0.022
8S	2.5	5.74E-01	5.03E-02	2.93E+00	1.90E+00	9.01E-01	1.82E-01	1.64E+02	7.69E-01	3.16E+03	5.50E+00	14.24	0.10	94.6	10.9	0.034	0.022
8U	3.5	1.72E-02	4.08E-02	8.50E-01	7.37E-01	1.75E-02	4.16E-02	9.00E+00	1.35E-01	2.28E+02	9.35E-01	19.30	1.08	97.7	0.6	0.18	0.16
8V	12	2.67E-02	2.13E-02	1.34E+00	5.79E-01	2.52E-02	4.10E-02	8.28E+00	1.83E-01	2.47E+02	8.36E-01	22.46	0.77	96.8	0.5	0.30	0.14
total gas age												**14.03**	**0.08**			0.089	0.027
age plateau (8E-8R)												**13.86**	**0.08**				

Table A.8. ^{40}Ar–^{39}Ar laser step-heating data of biotite separates (sample D18-10-64, 0.35-0.25 mm, J = 0.00020641 ± 0.00000155). Data completed through a MAP215-50 single-collector mass spectrometer. Instrumental sensitivity ~2.0E-11 mol/pA.

No.	laser power (W)	$^{36}Ar_{(atm)}$ pA	±2σ pA	$^{37}Ar_{(Ca)}$ pA	±2σ pA	$^{38}Ar_{(Cl)}$ pA	±2σ pA	$^{39}Ar_{(K)}$ pA	±2σ pA	$Ar_{(tot)}$ pA	±2σ pA	Age (Ma)	±2σ	$^{40}Ar^{*}$(%)	$^{39}Ar_{K}$%	Ca/K	±2σ
85B	0.15	1.09E+00	7.80E-02	2.12E-02	1.58E+00	6.07E-03	3.99E-02	1.23E+00	1.84E-01	3.47E+02	1.42E+00	7.26	7.0	6.9	0.2	0.03	2.4
85C	0.30	3.08E+00	6.63E-02	1.16E-01	1.52E+00	2.07E-02	8.80E-02	6.46E+00	2.89E-01	9.83E+02	2.70E+00	4.24	1.2	7.4	1.0	0.03	0.44
85D	0.45	1.51E+00	4.99E-02	2.07E+00	1.52E+00	2.06E-01	8.89E-02	2.78E+01	3.39E-01	1.23E+03	2.21E+00	10.53	0.24	63.8	4.3	0.14	0.10
85F	0.60	9.94E-01	6.49E-02	2.22E+00	1.52E+00	2.19E-01	1.82E-01	6.54E+01	6.23E-01	2.35E+03	4.86E+00	11.76	0.16	87.5	10.2	0.064	0.044
85G	0.75	8.69E-01	3.75E-02	1.05E+00	1.53E+00	2.32E-01	1.24E-01	8.00E+01	7.51E-01	2.69E+03	4.86E+00	11.34	0.12	90.4	12.5	0.025	0.036
85H	0.88	6.74E-01	4.26E-02	7.58E-01	1.52E+00	3.22E-01	1.10E-01	7.27E+01	7.82E-01	2.38E+03	5.00E+00	11.22	0.14	91.6	11.3	0.020	0.039
85J	1.03	8.51E-01	4.18E-02	1.07E+00	1.54E+00	2.57E-01	9.99E-02	9.18E+01	1.09E+00	3.03E+03	4.55E+00	11.30	0.14	91.7	14.3	0.022	0.032
85K	1.20	5.78E-01	6.37E-02	7.27E-01	1.59E+00	3.89E-01	1.73E-01	8.57E+01	9.48E-01	2.70E+03	5.38E+00	11.05	0.15	93.7	13.4	0.016	0.035
85L	1.40	3.73E-01	3.35E-02	2.72E-01	1.61E+00	2.73E-01	9.57E-02	8.03E+01	8.21E-01	2.49E+03	4.70E+00	11.04	0.12	95.5	12.5	0.006	0.038
85O	1.70	1.60E-01	3.04E-02	6.44E-02	1.57E+00	4.39E-02	6.56E-02	4.72E+01	2.58E-01	1.58E+03	3.11E+00	12.10	0.10	97.0	7.4	0.003	0.063
85P	2.2	1.19E-01	3.11E-02	7.44E-01	1.58E+00	8.46E-02	6.72E-02	4.29E+01	6.53E-01	1.45E+03	2.61E+00	12.31	0.20	97.6	6.7	0.033	0.070
85Q	3.0	1.29E-01	2.87E-02	1.25E+00	1.58E+00	9.16E-03	4.54E-02	3.25E+01	4.00E-01	1.12E+03	1.21E+00	12.47	0.18	96.6	5.1	0.073	0.092
85R	10.0	2.73E-02	2.52E-02	9.07E-01	1.58E+00	6.96E-03	3.71E-02	7.06E+00	1.62E-01	3.04E+02	9.53E-01	15.67	0.53	97.3	1.1	0.24	0.42
total gas age												**11.40**	**0.10**			0.033	0.017
isochron age (85F-85L, initial 40Ar/36Ar=471±28)												**10.68**	**0.12**				

Table A.9. ^{40}Ar–^{39}Ar laser *in-situ* analyses on rock chip (sample D20-10-49, J = 0.00575081 ± 0.00000288). Data completed through an ARGUS VI multi-collector mass spectrometer. Instrumental sensitivity ~5.0E-17 mol/fA.

No.	phase	$^{36}Ar_{(atm)}$ fA	±2σ fA	$^{37}Ar_{(Ca)}$ fA	±2σ fA	$^{38}Ar_{(Cl)}$ fA	±2σ fA	$^{39}Ar_{(K)}$ fA	±2σ fA	$Ar_{(tot)}$ fA	±2σ fA	Age (Ma)	±2σ	$^{40}Ar^{*}$(%)	Ca/K	±2σ
98B	Bt	2.98E-02	2.28E-03	3.16E-01	5.49E-02	0.00E+00	0.00E+00	9.13E+00	1.59E-02	2.02E+01	9.68E-01	13.00	0.79	55.8	0.065	0.0131
98C	WM S1	2.92E-03	1.10E-03	4.42E-01	7.44E-02	0.00E+00	0.00E+00	7.94E+00	1.20E-02	1.07E+01	4.72E-01	12.94	0.45	91.2	0.105	0.0206
98E	WM S1	3.04E-03	1.45E-03	1.39E-01	8.94E-02	0.00E+00	0.00E+00	1.13E+01	1.29E-02	1.46E+01	6.15E-01	12.68	0.41	93.1	0.023	0.0151
98F	Bt	9.66E-03	1.27E-03	2.98E-01	7.30E-02	3.22E-02	8.12E-02	1.06E+01	1.61E-02	1.54E+01	5.39E-01	12.29	0.38	80.7	0.053	0.014
98H	WM S2	4.58E-03	1.12E-03	1.23E-01	7.03E-02	0.00E+00	0.00E+00	6.38E+00	1.35E-02	9.34E+00	4.77E-01	13.12	0.56	84.8	0.036	0.0211
98I	WM S1	3.97E-03	1.22E-03	1.61E-01	6.92E-02	1.96E-03	9.25E-02	8.93E+00	1.26E-02	1.19E+01	5.17E-01	12.55	0.43	89.3	0.034	0.015
98K	Bt	5.86E-03	1.25E-03	3.05E-01	6.77E-02	1.18E-02	4.65E-02	1.35E+01	1.31E-02	1.81E+01	5.32E-01	12.75	0.30	89.7	0.043	0.0104
98L	WM S2	5.27E-01	4.43E-03	7.78E+01	2.37E-01	8.12E-03	5.11E-02	2.75E+01	1.76E-02	1.90E+02	1.92E+00	12.57	0.52	17.3	5.34	0.5343
98N	WM S1	5.73E-03	1.18E-03	4.33E-02	6.83E-02	0.00E+00	0.00E+00	1.01E+01	1.47E-02	1.37E+01	5.02E-01	12.45	0.37	86.9	0.008	0.0127
98O	Bt	7.07E-03	1.35E-03	2.07E-01	7.61E-02	0.00E+00	0.00E+00	1.26E+01	1.30E-02	1.75E+01	5.77E-01	12.76	0.34	87.3	0.031	0.0118
237E	WM S1	2.43E-03	1.37E-03	1.98E-01	1.36E+00	0.00E+00	0.00E+00	1.01E+01	1.39E-02	1.34E+01	5.80E-01	13.13	0.43	93.9	0.037	0.2537
237F	WM S1	6.50E-03	1.17E-03	4.88E-01	8.34E-01	2.73E-03	1.00E-01	1.01E+01	1.63E-02	1.43E+01	5.01E-01	12.86	0.37	85.8	0.091	0.1563
237H	WM S2	3.64E-03	1.39E-03	3.90E-01	9.46E-01	–		1.53E+01	1.52E-02	1.92E+01	5.92E-01	12.43	0.29	93.6	0.048	0.1168
237I	WM S2	6.00E-03	1.23E-03	1.60E-01	1.04E+00	1.82E-02	1.03E-01	1.43E+01	1.72E-02	1.85E+01	5.24E-01	12.28	0.28	89.6	0.021	0.1369
237K	Bt	1.49E-02	1.32E-03	6.47E-01	8.74E-01	–		1.49E+01	1.65E-02	2.20E+01	5.59E-01	12.38	0.28	79.2	0.082	0.1111
237L	WM S1	2.45E-03	1.39E-03	1.10E+00	8.63E-01	–		1.03E+01	1.48E-02	1.31E+01	5.89E-01	12.62	0.43	93.7	0.201	0.1597
237N	WM S1	2.51E-03	1.28E-03	1.07E+00	7.82E-01	2.80E-02	7.20E-02	8.76E+00	1.80E-02	1.19E+01	5.43E-01	13.32	0.47	93.0	0.231	0.1701
237O	WM S2	1.26E-02	1.75E-03	3.13E-01	7.77E-01	2.52E-03	5.72E-02	1.27E+01	1.86E-02	1.94E+01	7.43E-01	12.92	0.44	80.2	0.046	0.1155
237U	WM S1	3.15E-02	1.64E-03	3.38E-01	1.04E+00	–		1.21E+01	1.70E-02	2.45E+01	6.96E-01	13.11	0.43	61.3	0.053	0.1631
237V	WM S2	2.09E-02	1.57E-03	3.43E-01	1.06E+00	–		1.17E+01	1.25E-02	2.03E+01	6.66E-01	12.61	0.42	68.9	0.055	0.1715
237X	WM S2	2.41E-02	1.39E-03	3.41E+00	9.54E-01	3.58E-02	5.10E-02	9.89E+00	1.19E-02	1.92E+01	5.91E-01	12.75	0.44	62.2	0.652	0.1934
237Y	WM S1	4.11E-02	1.33E-03	1.15E-01	8.67E-01	–		1.32E+01	1.34E-02	2.83E+01	5.66E-01	12.69	0.32	56.4	0.016	0.1235
238A	Bt	1.82E-02	1.37E-03	5.17E-02	1.49E+00	–		7.30E+00	1.23E-02	1.42E+01	5.83E-01	12.61	0.60	61.4	0.013	0.386
238B	WM S1	2.11E-02	1.20E-03	3.46E-01	8.00E-01	–		1.14E+01	1.10E-02	2.02E+01	5.11E-01	12.72	0.33	68.3	0.057	0.1321
238D	WM S2	1.65E-02	1.33E-03	–		1.50E-03	8.75E-02	1.19E+01	1.62E-02	1.89E+01	5.65E-01	12.32	0.35	73.5	–	
238E	WM S1	2.75E-02	1.27E-03	4.68E-04	1.24E+00	–		1.53E+01	1.45E-02	2.64E+01	5.38E-01	12.48	0.26	68.5	6E-05	0.1527
238G	WM S1	5.84E-02	1.74E-03	6.81E-01	1.21E+00	2.43E-02	6.71E-02	1.66E+01	1.63E-02	3.88E+01	7.40E-01	13.50	0.33	54.8	0.077	0.1376
238H	WM S2	2.25E-02	1.33E-03	1.96E+00	1.56E+00	4.39E-02	6.32E-02	8.07E+00	1.58E-02	1.65E+01	5.66E-01	12.71	0.52	59.0	0.459	0.3685
238J	WM S1	3.38E-02	1.43E-03	1.07E+00	1.25E+00	3.46E-02	6.53E-02	9.21E+00	1.42E-02	2.11E+01	6.11E-01	12.51	0.50	51.9	0.219	0.2566
238K	WM S1	5.60E-02	1.59E-03	9.26E-01	1.05E+00	–		2.42E+01	1.55E-02	4.52E+01	6.76E-01	12.38	0.21	62.7	0.072	0.0825
238P	WM S2	3.71E-02	1.63E-03	1.22E+00	1.49E+00	3.46E-02	6.19E-02	7.45E+00	1.32E-02	2.01E+01	6.93E-01	12.76	0.69	44.9	0.309	0.3776
238Q	WM S2	1.75E-02	1.44E-03	1.12E-01	1.17E+00	2.62E-02	6.49E-02	7.23E+00	1.88E-02	1.49E+01	6.13E-01	14.09	0.63	64.7	0.029	0.3056
238S	WM S1	4.80E-02	1.55E-03	2.97E-01	1.68E+00	–		1.84E+01	1.37E-02	3.64E+01	6.60E-01	12.53	0.27	60.3	0.03	0.1716
weighted mean white mica (10/11), probability 0.095												**12.54**	**0.18**			
weighted mean biotite (6/6), probability 0.16												**12.57**	**0.24**			